DYNAMIC CHARACTERISTICS AND SEISMIC STABILITY OF EXPANDED POLYSTYRENE GEOFOAM EMBANKMENTS

by

Zahra A. Amini

A dissertation submitted to the faculty of
The University of Utah
in partial fulfillment of the requirements for the degree of

Doctor of Philosophy

Department of Civil and Environmental Engineering

The University of Utah

May 2014

The University of Utah Graduate School

STATEMENT OF DISSERTATION APPROVAL

The following faculty members served as the supervisory committee chair and members for the dissertation of_____Zahra A. Amini_____.

Dates at right indicate the members' approval of the dissertation.

_____Steven Bartlett _____, Chair	_8/23/2013_____ Date Approved
_____Ronald Bruhn_____, Member	_10/4/2013_____ Date Approved
_____Evert Lawton_____, Member	_8/23/2013_____ Date Approved
_____Chris Pantelides_____, Member	_8/23/2013_____ Date Approved
_____Aurelian Trandafir_____, Member	_10/26/2013_____ Date Approved

The dissertation has also been approved by__Michael Barber_____

Chair of the Department/School/College of_Civil and Environmental Engineering____

and by David B. Kieda, Dean of The Graduate School.

ABSTRACT

Expanded Polystyrene (EPS) geofoam has become a preferred material in various construction applications due to its light weight. Application of EPS accelerates the projects particularly on soft soils. The focus of this research is on the application of the EPS in embankments and its behavior mainly under harmonic vibration. The goal of this study was to investigate dynamic characteristics of freestanding vertical EPS geofoam embankment and address potential seismic issues that result from the distinguished dynamic behavior of such systems due to the layered and discrete block structure. A series of experimental studies on EPS 19 and a commercially available adhesive was conducted. Two-dimensional numerical analyses were performed to replicate the response of EPS geofoam embankment to horizontal and vertical harmonic motions.

The results of the analyses have shown that for some acceleration amplitude levels interlayer sliding is expected to occur in EPS geofoam embankments almost immediately after the start of the base excitation; however, as a highly efficient energy dissipation mechanism sliding ceases rapidly. Shear keys and adhesive may be used to prevent interlayer sliding if they cover the proper extent of area of the embankment. EPS blocks placed in the corners of the embankment and at the edges of the segment prohibited from sliding may experience high stress concentrations. The embankment may show horizontal sway and rocking once sliding is prevented.

To my beloved parents, Mostafa and Hamideh

TABLE OF CONTENTS

ABSTRACT iii

LIST OF TABLES vii

ACKNOWLEDGEMENTS viii

INTRODUCTION 1

REVIEW OF LITERATURE 3

Chapters

1. DYNAMIC CHARACTERISTICS OF FREE-STANDING EPS EMBANKMENT 13

- Methodology 14
  - Model Boundary Conditions and Properties 17
- Fundamental Period 20
  - Theoretical Approach 20
  - Numerical Approach 25
- Seismic Response Acceleration 29
- Conclusions 44

2. EXPERIMENTAL STUDY 47

- Uniaxial Compression Tests 53
  - Test Specimens 53
  - Test Specifications 54
  - Test Results 56
- Direct Shear Tests 60
  - Test Specimens 61
  - Test Specifications 62
  - Test Results 64
- Uniaxial Extension Tests 72
  - Test Specimens 72
  - Test Specifications 73
  - Test Results 75

Conclusions 80

3. INTERLAYER SLIDING OF THE EPS EMBANKMENT 82

Model Development and Properties 83
Interfaces 84
Interlayer Sliding Analysis 95
Harmonic Input Motion 102
Horizontal Input Motion 105
Vertical Input Motion 105
Input Motion with Horizontal and Vertical Components 106
Results 108
Horizontal Excitation 108
Horizontal and Vertical Excitation 115
Conclusions 123

4. INTEGRITY OF BLOCK ASSEMBLAGE IN THE EPS EMBANKMENT 125

EPS Embankment Layout 125
FLAC Model 127
Conclusions 134

5. INTERLAYER SLIDING PREVENTION STRATEGIES 136

Model Development 137
Application of Sliding Preventive Methods 137
Postsliding Remediation 139
Results 140
Conclusions 156

6. CONCLUSIONS 157

Appendices

A. EPS GEOFOAM EXPERIMENTAL DATA 159

B. DYNAMIC CHARACTERISTICS OF EPS EMBANKMENT 209

C. SLIDING ANALYSIS 215

D. STRESS DISTRIBUTION AFTER APPLICATION OF SLIDING REMEDIES 236

REFERENCES 262

LIST OF TABLES

1.1. EPS geofoam embankment system material properties 18

2.1. Summary of uniaxial compression test results 61

2.2. Summary of tensile test results 79

3.1. Mohr Coulomb properties of the EPS and EPS/EPS interfaces 102

A.1. Uniaxial compression test results of EPS specimens 180

A.2. Tensile test results of EPS specimens 208

B.1. EPS geofoam embankment system material properties 212

ACKNOWLEDGEMENTS

I would like to express the deepest appreciation to my committee chair, Dr. Bartlett, who continually conveyed valuable advice and review in regard to this research. Without his guidance this dissertation would not have been possible. I wish to thank professor Lawton for his continuous support and words of encouragement. I would like to express my sincere gratitude to my committee members, Professor Bruhn, Professor Pantelides and Dr. Trandafir, who provided me the opportunity to complete this dissertation. A special gratitude I give to InsulFoam® for providing funding that made the experimental part of this study possible. Finally, I would like to especially thank my fiancé, Alexis, who has been supportive throughout.

INTRODUCTION

Expanded Polystyrene (EPS) geofoam has emerged as the material of choice for embankment construction due to very low density and ease of application. In order to assess the seismic stability of the EPS embankment it is essential to fully understand the dynamic behavior of such a rather complex system. This could be challenging as the use of this material in construction of embankments is fairly recent (compared to soils) and thus case histories and full scale testing results are not abundant.

The study presented herein took up the challenge to address the shortcomings of the existing research on dynamic behavior and seismic stability of the EPS geofoam embankment system. This was done by performing two-dimensional numerical analyses using Fast Lagrangian Analysis of Continua (FLAC by Itasca, 2005) empowered by data obtained from experimental studies customized to this particular application of EPS geofoam as a part of this research.

Interlayer sliding is perhaps the first and most significant issue that defies the stability of the EPS geofoam embankment due to its layered structure. National Coorporative Highway Research Program (NCHRP) Web Document 65, which is probably the most commonly used reference for EPS geofoam applications in design and construction, addresses this issue based on assumptions that significantly influence the outcome of the study. Moreover specifics regarding interlayer sliding remedies and the

approach to applying such remedies are amongst the missing pieces of the similar studies puzzle. This research identifies the gaps in the existing knowledge about the dynamic characteristics of the freestanding vertical EPS geofoam embankment system and addresses the concerns regarding the seismic stability of such embankments through six main chapters.

Review of Literature is presented to clarify the motive and target of the research followed by an extensive experimental study of EPS 19 including uniaxial compression, extensional and direct shear testing. The experimental study was conducted on EPS geofoam samples treated with adhesive and environmental conditioning. The tests were specifically designed to include stresses similar to those present in a typical freestanding EPS embankment. The experimental stage of this research was funded by InsulFoam®. Further FLAC analyses conducted on various embankment models of different aspect ratios challenged the assumption of one-dimensionality in obtaining the fundamental period of the EPS embankment. Interlayer sliding was then investigated by applying both horizontal and vertical components of input motion to the EPS embankment model comprising of horizontal interfaces between the layers. Addition of vertical interfaces in the model replicate the vertical seams in the embankment and shed light on concerns about the integrity of the blocks during seismic excitation. Finally, recommendations were provided corresponding to when interlayer sliding remedies may be required, where in the embankment they should be applied and what the sufficient extent of application is.

REVIEW OF LITERATURE

Geofoam is a generic term that has entered the civil engineering vocabulary to describe foam materials used in geotechnical applications. The original definition of geofoam according to Horvath (1995) is any manufactured material created by some expansion process that results in a foam with texture of numerous closed, gas-filled cells. There are two significantly different processes for manufacturing foam from polystyrene. Therefore foams made from polystyrene can be Expanded Polystyrene (EPS) or Extruded Polystyrene (XPS) (Horvath 1995). EPS is used more extensively in civil engineering applications than XPS.

EPS is manufactured by first heating expandable polystyrene solid beads (with diameter ranging from 0.2 to 3.0 mm) to produce a bulk of cellular spheres containing numerous closed cells and having a diameter three to four times the diameter of the initial solid beads (Xenaki and Athanasopoulos, 2001). EPS geofoam can be made in rectangular-shaped blocks known as EPS-block or in application-specific shapes known as ESP-shape.

In geotechnical applications, geofoam has traditionally been used for thermal ground insulation and construction of light weight fills for more than 40 years. However, characterized by its low density, EPS geofoam has become the material of choice in a variety of geotechnical problems requiring lightweight fill such as slope stabilization,

embankments on soft soils, earth retaining structures, bridge approaches, bridge abutments, and buried pipes.

One of the newer innovations for constructing fills in an urban environment has been the use of lightweight materials. While such materials offer numerous benefits in a wide variety of conditions, they have proven to be advantageous in dealing with the many challenges presented by construction. In geotechnical structures such as fills, the gravity and seismic design loads are dominated by the mass of the fill material. Hence there has been a significant worldwide growth in the use of lightweight (low-density) materials in earthworks. Expanded Polystyrene (EPS) geofoam has emerged as the material of choice for most earthworks that utilize a lightweight material. The first use of EPS geofoam in its block-molded form as lightweight fill for transportation-related earthworks was in 1972 for a road stabilization project in Norway.

In summary, benefits of utilizing EPS geofoam in embankments include: (1) construction ease and speed, (2) placement in adverse weather conditions, (3) possible elimination of the need for preloading, surcharging, and staged construction, (4) reduction in maintenance costs due to less settlement from the low density of EPS geofoam, (5) reduction of the need to acquire additional right-of-way to construct flatter slopes because of the low density of EPS and/or the use of a vertical embankment because of the block shape of EPS, (6) decreased lateral stress on bridge approach abutments, (7) use over existing utilities that reduces or eliminates utility relocation, and (8) excellent durability (Stark et al, 2004). Use of EPS geofoam has been proven to be significantly cost efficient.

The density of EPS geofoam can be the most useful geotechnical index property

of this material, since the geotechnically relevant properties of EPS geofoam, such as strength, compressibility and thermal conductivity as well as cost, correlate well with its density. Density of EPS-block geofoam ranges from 8 kg/m^3 to 40 kg/m^3 where a density on the order of 20 kg/m^3 is the most commonly used for roadway construction purposes (Lingwall, 2011). This value is only about 1% of the density of soil, rock, and other materials that are traditionally used in geotechnical applications. This significantly low density is due to the fact that the void ratio of geofoam is between 40 and 100, implying that geofoam blocks are mostly consisted of air-filled voids.

Durability of EPS geofoam is another factor that drives more attention to using this material in construction. Being a non-biodegradable material, that does not dissolve, deteriorate, or change chemically in the ground and ground water makes EPS geofoam a very robust geosynthetic product. However, it can be chemically attacked by petroleum products, and protective measures are required to reduce the risk of potential exposure.

The knowledge of the mechanical properties of EPS in both the static and dynamic loading range is required for analysis and design of geotechnical applications involving EPS geofoam. The behavior of EPS geofoam under static loading conditions has been extensively studied using laboratory triaxial or uniaxial compression tests. Most of the compression testing results have been obtained under a strain rate of 10% per minute, which is a common rate characterizing rapid loading conditions (Athanasopoulos et al., 1999). EPS does not fail by a physical rupture of the material as traditionally known to be the case in solid materials used in construction. Nor does the EPS respond like soils where slippage takes place between the particles and a steady state or residual strength develops at large strains. Instead, the EPS collapses back to its original solid

polystyrene state, and the behavior at larger strain is strain hardening in nature. The stress-strain response of EPS geofoam can be divided into four zones consisting of initial linear response: (Zone 1), yielding (Zone 2), postyield linear work hardening (Zone 3), and postyield nonlinear work hardening (Zone 4) (Stark et al., 2004).

For low compressive strains (up to approximately 1%), the geofoam behaves linearly and an initial tangent Young's modulus of elasticity, E, can be defined, which shows an approximately linear correlation with the EPS geofoam density (Athanasopoulos et al., 1999). For compressive strains greater than 1%, the EPS geofoam behaves nonlinearly, and the Young's modulus value decreases with increasing strain (Duškov, 1997). Despite its uniquely low density, EPS has a remarkably high strength-to-density ratio and is capable of supporting long-term compressive stresses up to approximately 100 kPa (2000 lb/ft^2). This is comparable to many soils and, with proper design and construction, is more than adequate for supporting motor vehicles, trains, aircraft and even lightly loaded structures (Riad et al., 2003). The Young's modulus for geofoam ranges from about 4 MPa to 20 MPa depending on the geofoam's density (Negussey, 2006; Negussey and Anasthas 2001). Poisson's ratio, ν, of EPS geofoam in block form is typically measured using triaxial testing, and is generally found to be small (0.1 to 0.2) within the elastic range where its magnitude is greatest. This has led to the assumption that ν is equal to zero in many design applications (Stark et al., 2004). The mechanical properties of EPS geofoam may be influenced by factors such as specimen size, temperature, density, loading rate and confining stress.

Despite the many advantages of EPS geofoam when compared with traditional construction materials in many aspects, the use of EPS in geotechnical structures

(especially to alleviate the intensity of loads caused by seismic events) has been limited. This is perhaps mostly due to the rather restricted knowledge on the dynamic behavior of this material. Researchers have conducted laboratory testing on EPS geofoam including resonant column, cyclic triaxial (Athanasopoulos et al., 1999, 2007; Trandafir et al., 2010; Ossa and Roma, 2011) and shake table testing (Zarnani and Bathurst, 2007).

Some researchers have experimentally studied the stress-strain behavior of the EPS geofoam under cyclic loading via strain-controlled tests (Athanasopoulos et al., 1999, 2007; Ossa and Roma, 2011) which has led to findings about the relationship of the damping ratio, dynamic moduli, number of cycles, loading frequency, confining pressure and the deviator stress. However, dynamic experimental studies employing stress-controlled tests are very limited (Trandafir et al., 2010; Ossa and Roma 2011). The two approaches agree on degradation of shear modulus with strain.

Expanded Polystyrene (EPS) geofoam has emerged as the material of choice for embankment construction due to very low density and ease of application. It is essential to follow appropriate procedure in order to assess the global and internal stability of the EPS embankment. This could be challenging as the use of this material in construction of embankments is fairly recent (compared to soils) and thus case histories and full scale testing results are not abundant.

Since interlayer sliding of the EPS geofoam embankment due to seismic loads is one of the mechanisms that can affect the internal stability of the entire system, it is important to fully understand if and when sliding occurs during earthquake.

National Coorporative Highway Research Program (NCHRP) has addressed the seismic stability of the EPS embankments that includes global stability and interlayer

sliding in their Web Document 65 titled "Geofoam Application in the Design and Construction of Highway Embankments" (Stark et al., 2004). This document is perhaps the most commonly used reference for practical purposes associated with EPS geofoam applications in design and construction. However, major improvements are warranted in regards to seismic stability analysis procedures suggested in this document. Some of the concerns about the NCHRP document 65 procedure for stability analysis of EPS embankment are as the following:

- Pseudo-static approach is suggested in the NCHRP document 65 for internal and global stability analyses. However, more elaborate methods may be required to address the complexity of the EPS embankment behavior under seismic loading.
- NCHRP document 65 offers two methods to obtain the accelerations at the base of the EPS embankment: (1) conducting a one-dimensional site response analysis where the ground motion is applied at the bedrock elevation and propagated vertically through the overlying soil to estimate the acceleration at the base of the geofoam embankment or (2) using empirical relationships that relate the bedrock acceleration to the ground surface acceleration for different soil types. Both of these methods ignore the EPS/soil interaction and the fact that the EPS embankment requires a two-dimensional analysis. The role of the EPS embankment as a flexible mass that potentially amplifies the earthquake accelerations due to its response is very important when obtaining the accelerations on top of the EPS embankment. Since the pavement placed on top of the EPS embankment has a large weight, the EPS embankment-

pavement system behaves like a single degree of freedom system where the seismic forces are maximal on top of the system. Furthermore the recommended empirical relationships are specific to soils not EPS geofoam.

- The dynamic properties of the EPS geofoam and its rather complex dynamic behavior have not been taken into account in the NCHRP document 65 and the EPS has essentially been treated like soils.
- This document suggests linear interpolation between the top and base accelerations in order to obtain seismic accelerations at the center of the embankment or any other point within the embankment. This has not been validated for EPS embankments.
- The document does not address the vertical component of the seismic acceleration.

Limited research has been done on seismic stability analysis of the EPS geofoam embankment. Kuroda and Hotta (1996) conducted full-scale shake table tests on EPS geofoam embankment where the test results reported separation of the EPS blocks. The amount of displacements during shaking has also been presented in their work which makes a significantly valuable platform for further numerical studies. The authors attempted to model the behavior of the EPS embankment using Finite Element Method (FEM) and Distinct Element Method (DEM). The FEM analysis was unable to reproduce the decrease in the amplification factor as the input acceleration increased as was observed in the test results. As stated by the authors, the reason lies in the assumption of linearity of EPS response. The linear approach caused the model not to capture the damping correctly. The authors then artificially increased the apparent damping

coefficient of EPS block in order to take friction damping between EPS block into account. The damping coefficient that brought the analysis values into agreement with the test results was 5%.

The authors also attempted to model the embankment using Distinct Element method (DEM) where the model predicted the separation of blocks well; however, the model over predicted the residual displacement of the blocks compared to the shake table test. This is partially because the coefficient of friction changes during sliding and thus it should be considered in the model to depend the coefficient of friction on the sliding speed.

Bartlett and Lawton (2008) recommended an approach using a finite difference numerical model implemented in FLAC to evaluate the dynamic and deformation response of the geofoam embankment undergoing interlayer sliding and horizontal sway with rocking. They introduced interfaces in the model where EPS block sliding could occur. Friction angles assigned to such interfaces were intermediate values between the peak and residual friction angle also based on FLAC user's manual recommendation the normal and shear interface stiffness were set to ten times the stiffness of the neighboring zone. However, this interface stiffness may be too large and can interfere with the dynamic response of the embankment. It was concluded that ignoring the vertical component of strong motion when estimating sliding displacement is generally unconservative, but its inclusion is less important when the interlayer sliding displacement is well developed. The numerical model also suggested that other modes of failure such as rocking and sway can cause local tensile yielding of some blocks within the embankment, usually near the base which could in some cases propagate upward and

cause the embankment to begin to decouple dynamically.

Where sliding is predicted to be a potential problem, strategies to prevent the movement of the interlayers such as the following may be employed:

- Geometrical Precautions: Staggering the EPS blocks with a 90 degree rotation in orientation on each successive layer. Also the strategic placement of shear keys will require the potential sliding surface to shear through a select number of EPS geofoam blocks and ultimately this pattern of placement will disrupt the failure surface and greatly improve the sliding resistance (Bartlett and Lawton, 2008). A shear key is essentially an EPS geofoam block that is installed within two layers and breaks the isolation plane between each layer. The shear keys are placed periodically throughout the embankment for lateral stability as recommended by the design engineer. Shear keys have been used in Utah light rail system embankments.
- Mechanical Controls: Adhesion bond (i.e., glue) or barbed connector plates may be used to prevent the EPS blocks from sliding. However, according to Barrett and Valsangkar (2009) barbed connectors do not have a significant effect on the shear resistance of the blocks.
- Structural Measures: Casing, cabling, installing walls to restrain the blocks from moving freely on the edges may also be considered.

Since geometrical precautions can be applied at no cost and using an adhesive to bond the EPS blocks can be conducted at lower costs compared to structural measures, these two strategies are chosen to be studied within the scope of the proposed research. Although employing such methods can help to prevent sliding it is essential to study their

influence on the dynamic response of the EPS geofoam embankment as a unified mass. Altering the layout of the EPS embankment system in such ways could introduce other modes of failure (i.e., rocking and sway) to the embankment at high levels of ground motion.

CHAPTER 1

DYNAMIC CHARACTERISTICS OF FREE-STANDING EPS EMBANKMENT

Seismic behavior and design of a geosystem is primarily based on the response of that system to the strong motion resulting from a particular earthquake. For embankment systems, the nature of the seismic wave propagation through the embankment and the response of that embankment are key issues for evaluating their external and internal seismic stability. For Expanded Polystyrene (EPS) geofoam embankments, guidelines for dynamic evaluations in slope stability projects have been published in NCHRP projects 24-11 (Stark et al., 2004) and 24-11-02 (Arellano et al., 2011). These reports present recommendations for determining the fundamental period of the embankment system and the acceleration response at different points within the embankment. This chapter focuses on validating some of the assumptions and simplifications used in the NCHRP reports. It also discusses some of the ramifications of the NCHRP analytical approach by means of performing and evaluating several numerical simulations performed and discussed herein. Embankment fundamental period and acceleration response at different levels of EPS geofoam embankment obtained from the numerical simulation are discussed in this chapter.

Methodology

Figure 1.1 shows a photo of a typical free-standing EPS geofoam embankment with vertical walls as constructed in the Salt Lake Valley, Utah for the light-rail system. Figure 1.2 illustrates a typical cross-section of a free-standing EPS geofoam embankment when used for highway embankment. This typical drawing is from the I-15 Reconstruction Project in Salt Lake City where geofoam was extensively used to mitigate the potential for large and damaging consolidation settlement (Bartlett and Lawton, 2008).

EPS embankment construction consists of placing large geofoam blocks in horizontal layers and staggering the edges of each row of blocks so there are not continuous vertical seams. In addition, with the placement of each successive layer, the rows of blocks are oriented 90 degrees from the underlying layer to further interrupt the vertical seams. This method of block layout avoids continuous vertical joints and enhances interlocking of the geofoam mass. The lowermost layer of EPS block is placed on a level, bedding sand; the uppermost layer is often capped by reinforced concrete Load Distribution Slab (LDS) and pavement section (i.e., road base and pavement). The sides of the EPS embankment are often protected by a precast, concrete fascia (i.e., non-structural) panel wall that is typically placed a short distance (0.2 m) from the face of the EPS blocks to prevent interaction. The panel wall is supported by a concrete slot footing and is connected to the LDS to prevent horizontal movement at the top of the wall. The lowermost layer of EPS geofoam is placed directly against the slot footing, and constructed as such; the footing constrains the horizontal movement of the EPS block in its lowest layer (Bartlett and Lawton, 2008). The recommended density of EPS geofoam

Figure 1.1. Typical freestanding EPS embankment (Utah Transit Authority Light Rail System, Salt Lake City, Utah)

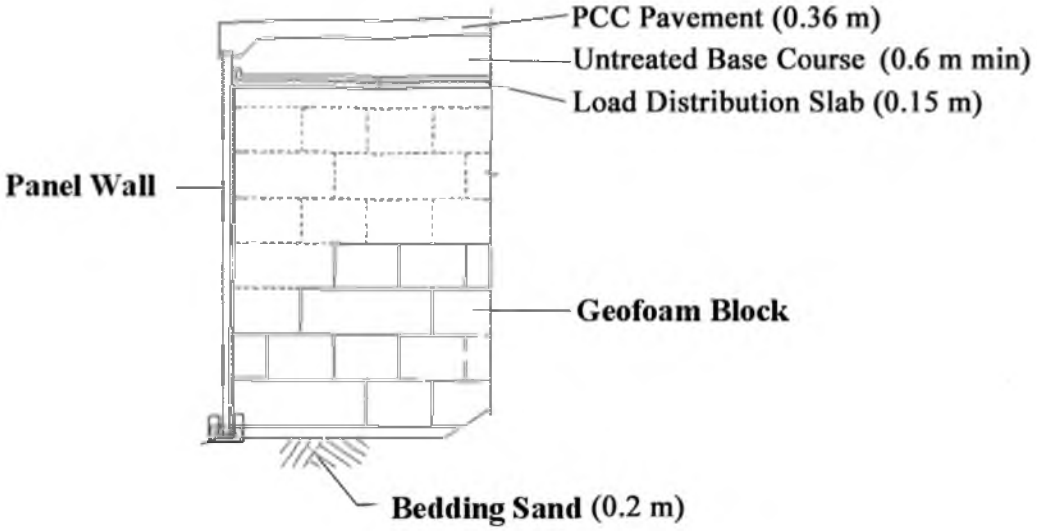

Figure 1.2. Typical EPS embankment cross-section used for the I-15 Reconstruction Project (after Bartlett and Lawton, 2008)

for roadway applications is that of EPS19 (19 kg/m^3) based on the evaluations performed on the I-15 Reconstruction Project.

Dynamic behavior of the vertical, free-standing, EPS geofoam embankment discussed above was simulated using the Finite Difference Method (FDM) as incorporated in the commercially-available two-dimensional computer program named FLAC (Itasca, 2005). Because the potential interaction of the panel wall with the geofoam embankment is relatively minor due to the design and construction detailing of the two systems, for simplicity, the panel wall is not included in the numerical model. In addition, the other components including the LDS, road base and concrete pavement are modeled as a lumped mass atop the EPS geofoam embankment. Interlayer sliding between the block and overlying and underlying systems is not considered at this stage of the study; therefore no interfaces were introduced to the model (The influence of interfaces will be treated in later sections of this report.) Hence, the geofoam was considered to be a coherent, homogeneous mass.

Because the design ground motion is usually specified as a free-field motion at the ground surface, the input wave in the numerical model was applied at the ground surface (i.e., base of the EPS embankment). This approach assumes that there is minimal soil-structure interaction between the EPS embankment and the underlying soil. This is a reasonable assumption because of the relatively low mass of the EPS system, which minimizes inertial interaction, and the shallow embedment of the basal blocks, which minimizes kinematic interaction. In addition, this approach does not require site-specific, soil response analyses and the associated deconvolution analysis (Bartlett and Lawton, 2008), which adds more complexity to the evaluations.

At this preliminary stage of the study, the ground motion is applied at the base of the embankment as velocity time history using simple harmonic wave. In addition, only the horizontal component of the wave is imposed to the model.

Model Boundary Conditions and Properties

The EPS geofoam embankment system is a "top-heavy" system due to the combined weights of the LDS and pavement systems, which are represented as a combined 1-m thick, non-deformable, lumped mass system. Below this, is the flexible EPS body, which is modeled with various width-to-height aspect ratios to examine this effect. The lowermost boundary of the embankment is fixed in the y direction and the nodes are "slaved" together in the x direction making this boundary behave rigidly in terms of wave propagation. Such a boundary condition has the potential of trapping reflected waves in the model, especially when vertical component of the ground motion is introduced to the model. However, for the preliminary modeling, this boundary condition is not unreasonable because of the relatively high impedance ratio between the EPS and a hypothetical foundation soil. For instance, if the foundation soil were to be modeled as medium to medium-stiff clay, similar to the study performed by Bartlett and Lawton (2008), the impedance ratio would be relatively high for the waves propagating down through the EPS geofoam embankment and reflecting at EPS-soil boundary. Therefore the stress amplitude of the reflected wave would be a large portion of the incident wave (Kramer, 1996). No boundary condition is assigned to the vertical sides of the EPS embankment system allowing free movement of the embankment in both the horizontal and vertical direction.

Table 1.1 presents the elastic moduli and properties of the EPS19 and the lumped mass used in the model. EPS19 has a density of 19 kg/m^3 and Young's modulus (E) of about 7 MPa as obtained from the uniaxial compression tests (Chapter 2). The properties of the lumped mass are adopted from work of Bartlett and Lawton (2008). Figure 1.3 illustrates an EPS geofoam embankment system FLAC model in which the EPS geofoam embankment is 8-m high, 16-m wide and is topped with a 1-m thick lumped mass. The grid spacing is 1 m by 1 m and the fixed boundary is shown at the base of the embankment system. According to the FLAC manual (Itasca, 2005) the zone length (grid spacing) must be within 1/10 of the longest wave length, in order to provide accurate wave transmission. The wave length is calculated by: $\lambda = \sqrt{G/\rho}/f$. Substituting G and ρ from Table 1.1 and fundamental frequency of the embankment f with 2 Hz (which is the largest fundamental frequency value associated with one of the embankment geometries used in this study), the value of wave length is approximately 204 m which is about 200 times the grid spacing used in the analyses. Therefore 1 m grid spacing is appropriate to use.

Table 1.1. EPS geofoam embankment system material properties

Material	ρ	E	υ	G	K
----------	kg/m^3	MPa	----------	MPa	MPa
EPS	19	7	0.1	3.2	2.9
Lumped Mass	2321	30000	0.2	12712	15625

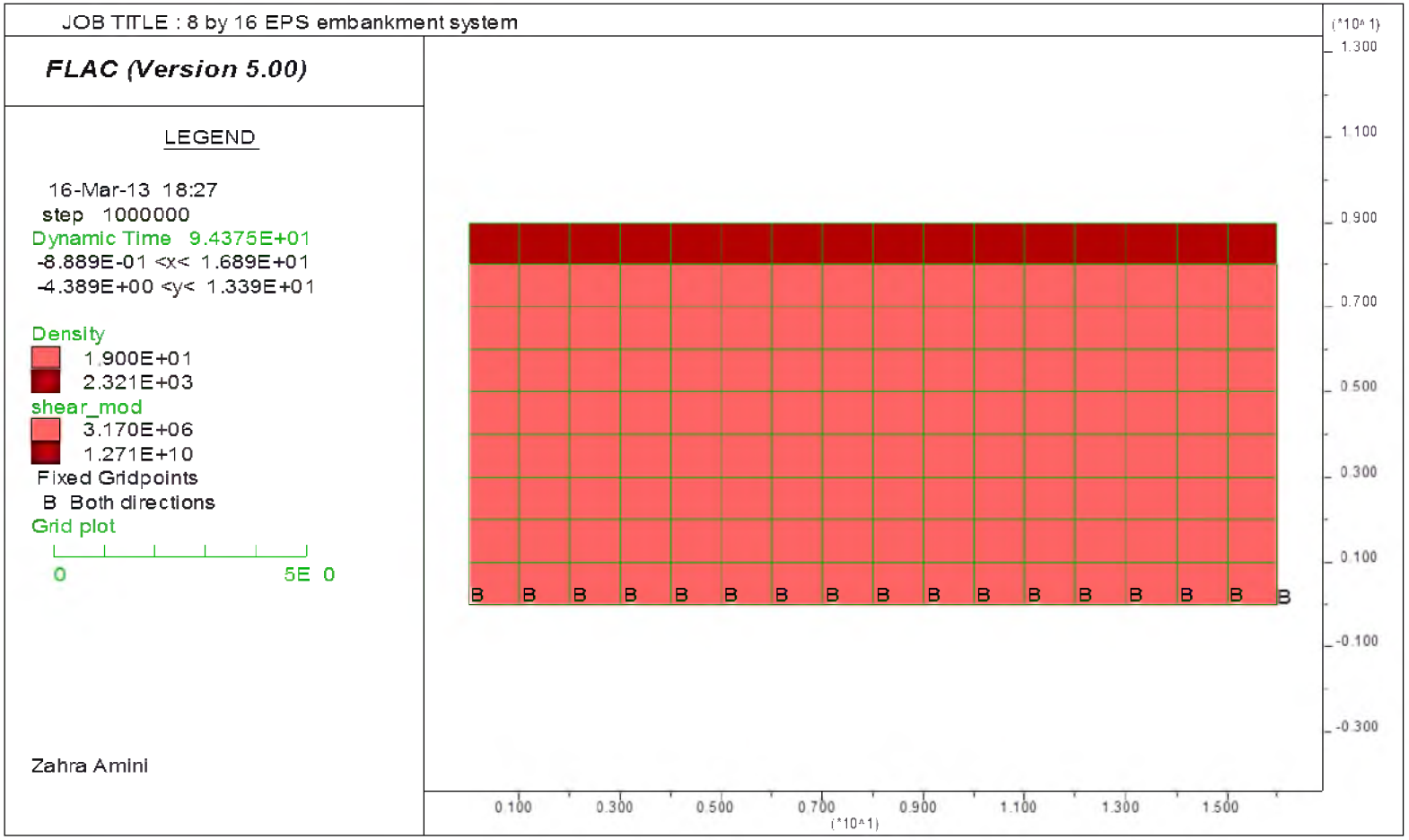

Figure 1.3. An 8 m by 16 m EPS embankment system in FLAC

Fundamental Period

The seismic analysis of any system requires the knowledge of its fundamental period or natural frequency of vibration. Embankment systems generate the maximum displacement response when excited at their fundamental period (Makdisi and Seed, 1978). In order to evaluate this parameter numerically for a free-standing EPS embankment system, simple models were exercised and compared with analytical solutions.

The EPS geofoam has a very low mass density thus the vast majority of the mass in an EPS geofoam embankment is located at the top of the EPS flexible body. Because of this, the top of the embankment experiences the largest displacements when exposed to harmonic motion inputted at the base. The potential for amplification of the base motion within the EPS embankment at its fundamental period has led researchers to model the system as a classical Single-Degree-Of-Freedom (SDOF) system (Horvath, 1995, Riad and Horvath, 2004). In such an approach, the EPS geofoam embankment system is generally modeled as a fixed-end cantilevered beam with a mass on top and where both flexure and shear components of displacement are considered. This simplifies the EPS geofoam embankment to a cantilevered Timoshenko beam, the length and width of which are equal to the height and width of the EPS geofoam embankment, respectively (Horvath, 2004).

Theoretical Approach

The current state-of-art equation for calculating the fundamental period of an EPS embankment system was published by Stark et al. (2000), and was later adopted in the

seismic stability evaluation procedure for EPS geofoam embankment systems in NCHRP project reports (2004 and 2011). The current use of this equation is the form of:

$$T_0 = 2\pi \left\{ \frac{\sigma'_{v_0} H}{E_{t_i} g} \left[4 \left(\frac{H}{B} \right)^2 + \left(\frac{12}{5} \right) (1 + \nu) \right] \right\}^{0.5} \tag{1.1}$$

where B and H are width and height of the embankment, respectively. σ'_{v_0} is vertical effective stress acting on top of the EPS, E_{t_i} and ν are the initial tangent Young's modulus and Poisson's ratio of the EPS, respectively, and g is the gravitational constant (i.e., 9.81 m/s^2). The derivation of Equation 1.1 can be explained by starting with the general fundamental period equation for a single degree of freedom where both components of flexural and shear stiffness are considered (Horvath, 2004):

$$T_0 = 2\pi \left[m \left(\frac{1}{k} \right) \right]^{0.5} \tag{1.2}$$

$$\frac{1}{k} = \frac{1}{k_f} + \frac{1}{k_s} \tag{1.3}$$

where m and k represent the mass and equivalent stiffness of the SDOF. k_f and k_s are flexural and shear components of the stiffness, respectively, and are defined as the following:

$$k_f = \frac{3EI}{L^3} \tag{1.4}$$

$$k_s = \frac{5}{6}\frac{GA}{L} \tag{1.5}$$

where E is the young's modulus, I is the moment of inertia, L is the length, A is the cross-sectional area and G is the shear modulus of the beam.

Applying these terms to the EPS embankment, one can obtain: $L = H$, $E = E_{t_i}$, $I = B^3/12$ and $A = B$ per unit length of the embankment. Also shear modulus can be written in terms of Young's modulus: $G = E_{t_i}/2(1+\nu)$. By substituting these terms into Equations 1.4 and 1.5, which will be substituted in Equation 1.3 and subsequently in Equation 1.2, Equation 1.2 can be rewritten as:

$$T_0 = 2\pi\left[m\left(\frac{4H^3}{E_{t_i}B^3} + \left(\frac{12}{5}\right)\frac{H(1+\nu)}{E_{t_i}B}\right)\right]^{0.5} \tag{1.6}$$

factoring out H/BE_{ti} Equation 1.6 will have the following form:

$$T_0 = 2\pi\left[\left(\frac{mH}{B}\right)\left(\frac{1}{E_{t_i}}\right)\left(\frac{4H^2}{B^2} + \left(\frac{12}{5}\right)(1+\nu)\right)\right]^{0.5} \tag{1.7}$$

in which the term (m/B) is σ'_{v_0}/g per unit length of the embankment. Therefore Equation 1.7 can be written as:

$$T_0 = 2\pi \left[\left(\frac{\sigma'_{v_0} H}{g E_{t_i}} \right) \left(4 \left(\frac{H}{B} \right)^2 + \left(\frac{12}{5} \right) (1 + \nu) \right) \right]^{0.5} \tag{1.8}$$

which is the same as Equation 1.1.

There are two alternatives to this equation, one of which is a more rigorous solution where the coefficient 5/6 in Equation 1.5 is replaced by a theoretically more rigorous factor in the form of: $10(1 + \nu)/(12 + 11\nu)$ (Horvath, 2004). Rewriting Equation 1.8 using this factor gives:

$$T_0 = 2\pi \left[\left(\frac{\sigma'_{v_0} H}{g E_{t_i}} \right) \left(4 \left(\frac{H}{B} \right)^2 + \left(\frac{12+11\nu}{5} \right) \right) \right]^{0.5} \tag{1.9}$$

The other alternative for calculating the fundamental period of the EPS geofoam embankment system, known as the Japanese Design Equation, is:

$$T_0 = 2\pi \left[\left(\frac{\sigma'_{v_0} H}{g E_{t_i}} \right) \left(4 \left(\frac{H}{B} \right)^2 + \left(\frac{12}{5} \right) (1 + \nu) + 1 \right) \right]^{0.5} \tag{1.10}$$

Equation 1.10 is different from Equation 1.1 only in one term, which has a value of 1 added at the end of the equation. This term shows that according to the Japanese Design Equation there is a third component in the structure of the stiffness factor (other than the flexural and shear components discussed previously). A closer look at the Equation 1.10 gives the third component of stiffness as: $E_{t_i}B/H$. There has not been a clear explanation for this term in the literature, and most papers on seismic stability evaluation of the EPS geofoam embankment systems simply omit this term in calculating the fundamental period. For example, Horvath (2004) states in his work on investigation of the fundamental period calculation for the EPS geofoam embankment: "It is not obvious what the additional term…is intended to represent as there are no other theoretical contributions to beam stiffness per se other than flexure and shear."

However, because the EPS geofoam mass forms the body of the hypothetical beam, the flexibility and ability to axially deform is inherent in the beam analogy. The axial component of the stiffness for a beam that can undergo axial displacement is:

$$k_a = \frac{EA}{L} \tag{1.11}$$

Substituting terms *E*, *A* and *L* with those corresponding to the EPS embankment the following is obtained:

$$k_a = \frac{E_{t_i}B}{H} \tag{1.12}$$

which is similar to the extra term found in the Japanese Design Equation for the fundamental period of the EPS geofoam embankment. Therefore, it is likely that flexibility of the EPS in both x and y direction as an isotropic material was considered in the Japanese equation by addition of a third stiffness component representing the axial stiffness of the EPS geofoam.

Numerical Approach

To shed more light on the difference between Equations 1.1 and 1.10, a series of FLAC analyses were performed to obtain the fundamental period of EPS geofoam embankments with various base to height aspect ratios independent of the discussed formulations for such embankments and the results were compared.

EPS geofoam embankments were modeled in two-dimensional FLAC with eight different heights including 5, 6, 7, 8, 9, 10, 12 and 15 m high models at base to height aspect ratios of 0.6, 0.8, 1, 1.5, 2, 2.5 and 3, respectively. A 1-m thick, relatively stiff mass was modeled atop the EPS embankment body representing the LDS and pavement section. The EPS geofoam body of the embankment was modeled as a coherent mass (i.e., no horizontal and vertical interfaces) at this stage of the study rather than as individual blocks. Material properties indicated in Table 1.1 were used and a harmonic velocity wave comprising of only the horizontal component of motion was imposed at the base of the embankment. The input wave was set up in a way that at time zero, zero velocity would be applied to the model. No material damping was assigned to the model; thus for these initial analyses, the system is undergoing forced, undamped vibration to find the fundamental period of the EPS embankment(s).

A trial-and-error method was used to find the fundamental period of the EPS geofoam embankment. The procedure included manually changing the period of the input wave in the FLAC code and monitoring the displacement of the embankment at the uppermost nodes (i.e., top of the lumped mass). In the absence of damping, the system is expected to display an ever-increasing displacement at resonance. Once this behavior was observed for each model, the assigned input wave period was recorded as the fundamental period of the EPS geofoam embankment system. Figure 1.4 illustrates the displacement time history of the mid-uppermost node of a 10-m high and 15-m wide EPS geofoam embankment excited at its fundamental period. It is noteworthy that the FLAC model gives a fundamental period of 0.81 s for this system, whereas Equation 1.1 (i.e., used in NCHRP report) gives a value of 0.76 s, and Equation 1.10 (i.e., Japanese Design Equation) calculates this value as 0.84 s. The results obtained by using Equation 1.9 were also monitored to evaluate the more rigorous alternate to Equation 1.1.)

The results of 56 analyses of EPS embankments with various geometries are presented in Figure 1.5. In order to compare the results of the equations discussed above with those of the numerical modeling, the percent error of fundamental period values was calculated and normalized to the numerical results as follows:

$$\left[\frac{T_{Theoretical}-T_{FLAC}}{T_{FLAC}}\right] \times 100 \qquad (1.13)$$

The FLAC results were selected as the "baseline" to compare the theoretical results because in two-dimensional analysis flexural, shear and axial stiffness

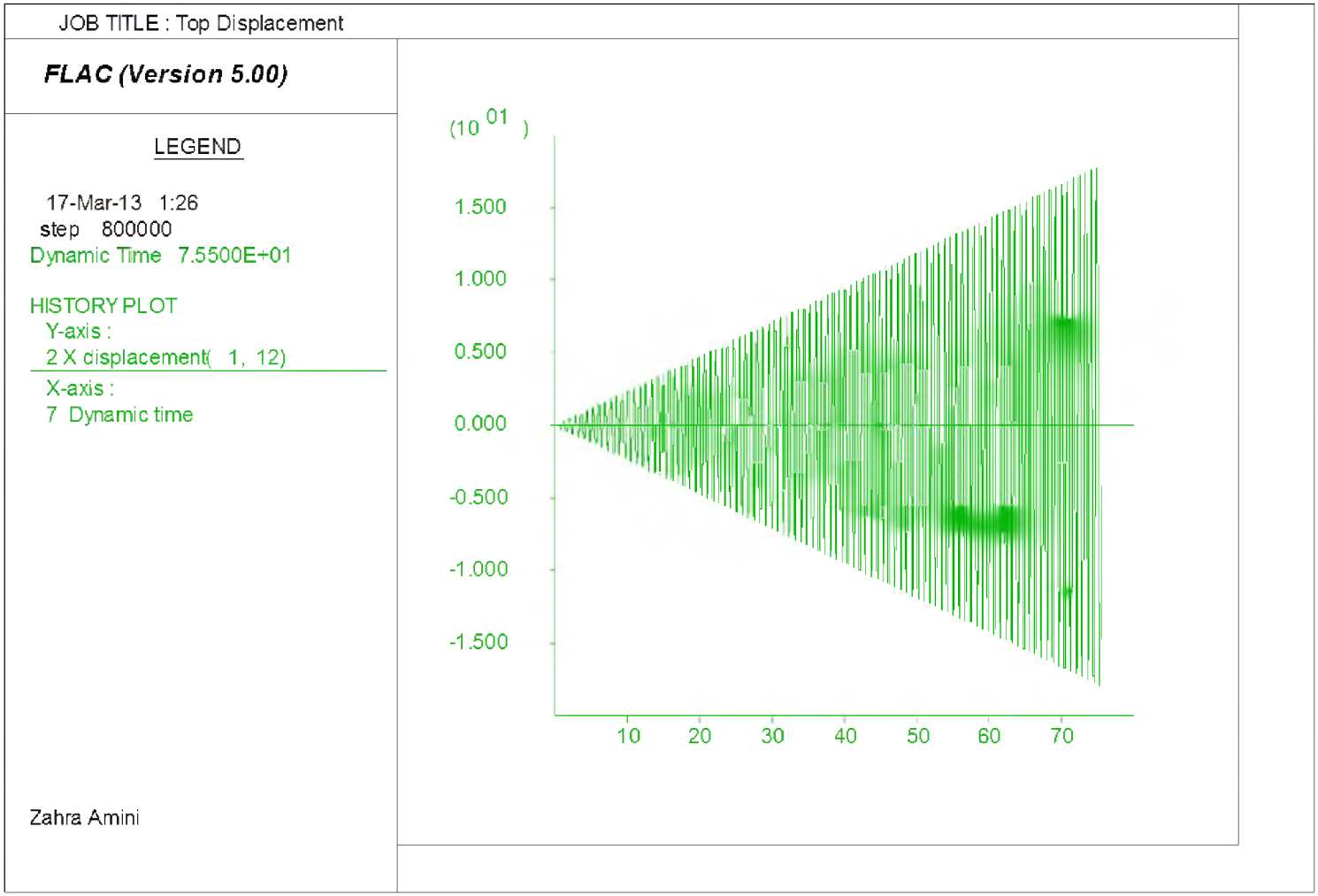

Figure 1.4. Displacement time history of the top of a 10 m by 15 m EPS embankment at resonance

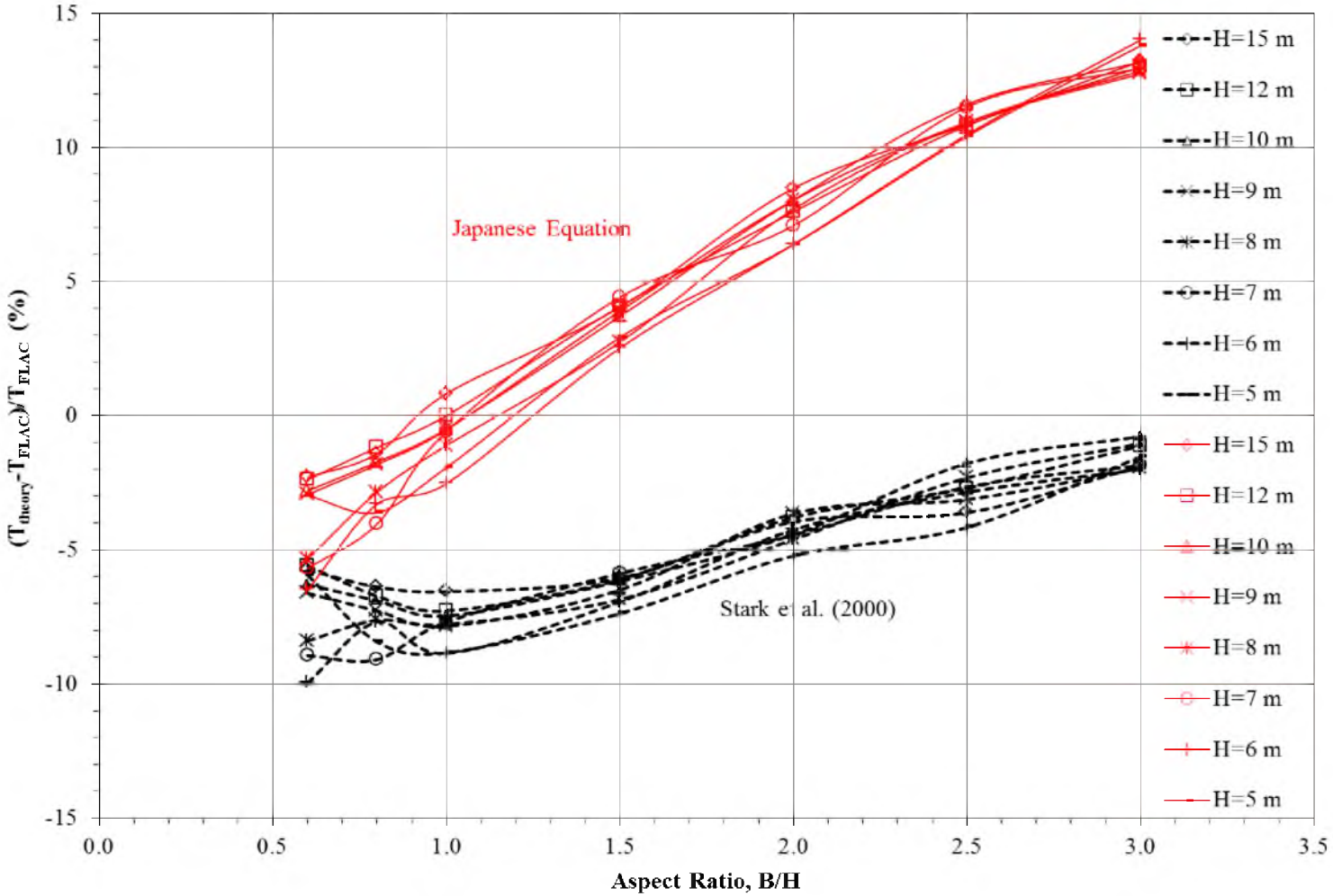

Figure 1.5. Comparison of fundamental period results obtained from two theoretical methods and FLAC analysis

components are included.

Based on the comparison with the FLAC analyses, it was concluded that Equation 1.9 gives very similar results to those obtained from Equation 1.1. In fact for, the vast majority of the fundamental period values calculated using these two equations agreed to the second decimal place. Thus, for final comparison the results from Equation 1.9 are not presented. More importantly, Figure 1.5 shows the percent error obtained from the comparison of Equations 1.1 and 1.10 with the two-dimensional FLAC results. Equation 1.1 appears to underestimate the fundamental period value for all aspect ratios, whereas Equation 1.10 (Japanese Design Equation) generally overestimates the values of fundamental period for aspect ratios greater than 1. Based on this figure, it was concluded that Equation 1.10 agrees well with the FLAC results for aspect ratios of about 1.5, or less; whereas Equation 1.1 results are generally in reasonable agreement with FLAC results for aspect ratios greater than about 2 to 3. Thus, it was concluded that the two-dimensional FLAC analysis captures the effect of the axial stiffness component included in Equation 1.10 very well, especially for square-shaped cross-sections and those with more slender (smaller) aspect base to height ratio less than 1. Based on the numerical modeling, it is recommended that Equation 1.10 be used for base to height aspect ratios of 1.5 or lower, whereas Equation 1.1 is more likely to give better results for wider EPS embankments with aspect ratios of about 2 or higher.

Seismic Response Acceleration

Simplified external and internal seismic stability evaluations of the EPS geofoam embankment require the knowledge of magnitude and distribution of the maximum

acceleration response in the embankment. Also, in order to address interlayer sliding, using simplified methods, the relation of the acceleration response at various depths (i.e., horizontal interlayers) of the EPS embankment is needed as well.

Both NCHRP projects (i.e., 24-11 and 24-11-02) are similar in their analytical approach in which they decouple the determination of the overall acceleration response of the EPS geofoam embankment system into: (1) an evaluation of the acceleration response at the existing ground surface (i.e., peak ground acceleration) located at the interface of the ground and the base of the EPS geofoam embankment and (2) an evaluation of the acceleration response of EPS geofoam embankment itself, including the acceleration at the top of the embankment. In the 24-11 (2004), the recommended procedure is to determine the top acceleration of the EPS geofoam embankment by approximating the EPS geofoam mass as a soil. This is done for convenience sake in order to essentially be able to utilize existing empirical site response relationships for soils to estimate the top acceleration of the EPS geofoam embankments as a function of the embankment's basal peak ground acceleration. Note that prior to this step, it is recommended that the base acceleration be obtained using either a one-dimensional site response analysis or empirical attenuation relationships. For the one-dimensional analysis, a one-dimensional ground response computer program is recommend to perform a one-dimensional soil response analysis for the foundation soils. In this analysis, a representative earthquake record is selected for the input motion at depth and is propagated vertically through the overlying soil deposit to the ground surface to estimate the peak ground acceleration at the base of the EPS geofoam embankment. In contrast, the empirical attenuation relationship approach is recommended and used to relate the input, basal, bedrock

acceleration to peak ground acceleration for different soil types. However, in regards to evaluating the top acceleration of the EPS geofoam embankment system, there are some discrepancies in the procedures as published in the NCHRP project 24-11 and 24-11-02 reports. For example, stating that the maximum acceleration on top of the EPS geofoam embankment system is different from those at the base (i.e., pga), NCHRP 24-11 suggests that: "it is anticipated that the top acceleration will be less than the base acceleration." The cause of which is further explained as the potential for shear deformation to occur between geofoam blocks as a result of vertical propagation of the seismic shear waves. Furthermore, NCHRP project 24-11 uses the rationale that if the EPS geofoam is approximated as a one-dimensional, deep cohesionless soil column, this situation often produces accelerations at top of the domain which are less than those incurred at the base. (However, it is noted herein that this may not be the case for a two-dimensional body such as an EPS embankment where the top acceleration is heavily influenced by the magnitude of the basal, input motion and the potential for nonlinearity and damping resulting from such motion in the EPS body.)

In contrast to NCHRP project 24-11, NCHRP project 24-11-02 report introduces a simplified seismic response method that treats the EPS geofoam embankment system as a SDOF with flexible body, where the assemblage of the EPS blocks are considered as one coherent mass that can amplify the ground motion in such a way that higher response accelerations are expected at the top of the embankment compared to those at the base. This simplified method is consistent with Japanese practice which also considers the EPS geofoam fill as a flexible structure with an amplification of surface motion (EPS Construction Method Development Organization, 1994). It is noted herein that the

NCHRP 24-11-02 approach is more consistent with conventional embankment response analysis (Makdisi and Seed, 1978).

In order to determine the response acceleration of the EPS geofoam embankment at different elevations or levels within the embankment, both NCHRP project reports suggest linear interpolation between the base and top accelerations.

The above assumption regarding the distribution of the acceleration response at various levels within the EPS geofoam embankment system was investigated herein using FLAC. Two-dimensional analyses were performed to determine how similar the behavior of the EPS geofoam embankment is to that of a SDOF and to determine the acceleration response at various levels. The results of this section of the study address the questions: (1) Where does the EPS geofoam embankment show the maximum response? (2) Does the acceleration response change linearly from base to top at the various levels found in the embankment? (3) Are higher modes of vibration involved (other than the fundamental mode), and do these modes significantly affect the acceleration response?

For the purpose of this study, three aspect ratios of EPS geofoam embankments were incorporated in the evaluations. The selected EPS geofoam embankments for the FLAC modeling had a height of 8 m with aspect ratios of 1, 2 and 3, respectively. The studies were performed in the elastic mode and the properties presented in Table 1.1 were used.

The EPS geofoam embankment body was modeled as a coherent mass with a damping ratio of 2%, which was input as Rayleigh damping applied to EPS geofoam material. This value of damping was chosen as a typical elastic range value in accordance with the results of torsional resonant column performed on specimens of block-molded

EPS geofoam under zero confining pressure as published by Athanasopoulos et al. (1999). The 2% damping is associated with the upper ranges of torsional resonant column test results and lower ranges of cyclic uniaxial test results at 1% shear strain which is believed to be the boundary of elastic behavior of the EPS geofoam. Above 1% shear strain, Athanasopoulos et al. (1999) reported strong nonlinearity developing in the specimens.

A horizontal harmonic input motion was imposed to the base of the model as a velocity time history associated with a maximum horizontal acceleration of 0.1 g. The frequency of the input motion was chosen in order to create frequency ratios of 0.5, 1 and 2 where the frequency ratio is defined as the ratio of the basal input frequency to the fundamental frequency of the EPS geofoam embankment system (f_{input}/f_0). The frequency ratio of higher than 1 was considered in order to investigate the possibility of higher modes of vibration than just the primary mode. The response accelerations throughout the EPS geofoam embankment were recorded at 1 m intervals and are presented in Figure 1.6. The results are presented in the form of normalized maximum accelerations where the maximum response acceleration at each depth was normalized to the maximum base acceleration $(a_{z,max}/a_{b,max})$ and was plotted against the normalized depth defined as the depth of the point of interest divided by the total height of the EPS geofoam embankment system.

Figure 1.6 (a) shows that for embankments excited at the fundamental period, the amplitude of the acceleration response increases as the horizontal shear wave propagates vertically. The EPS geofoam embankment shows a maximum response at its top. Similar behavior is obtained in all three embankments with different aspect ratios. For f_{input}/f_0

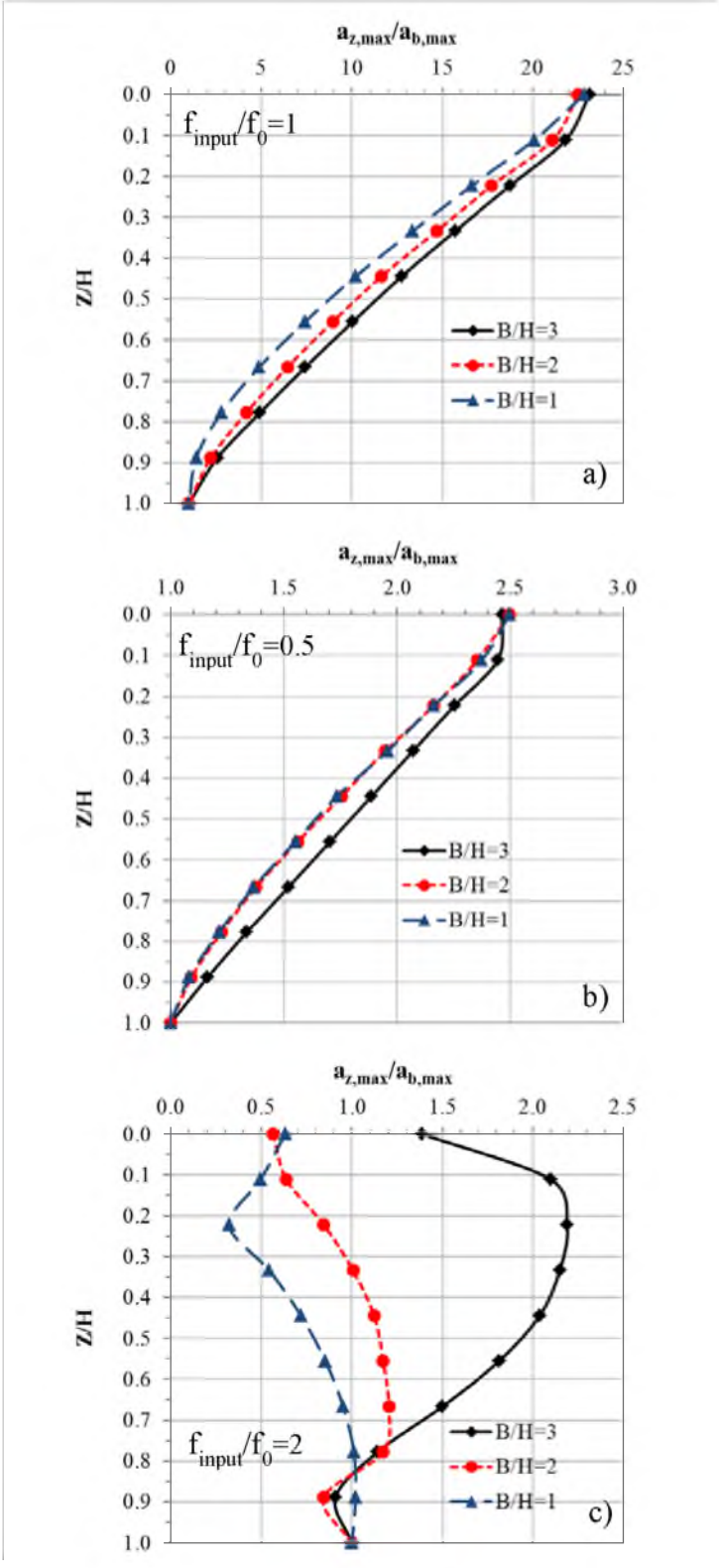

Figure 1.6. Response accelerations of embankments with different aspect ratios at frequency ratios of a) 1, b) 0.5 and c) 2

equals 1 (i.e., the forcing function at the resonance frequency), the maximum response acceleration at the top of the embankment ranges from 22 to 23 times larger than the harmonic acceleration input at the base.

Figure 1.6 (b) for f_{input}/f_0 of equal to 0.5 shows a similar trend with response accelerations increasing from base to top of the embankment with the maximum acceleration found at the top of the embankment. However, because this series of analysis was performed at a frequency ratio smaller than the 1 (i.e., the frequency of the input motion being half of the fundamental frequency of the EPS geofoam embankment system), the maximum acceleration response at the top of the embankment is only about 2.5 times the maximum basal acceleration when compared the 22 to 23 times obtained for the resonance case.

Both Figures 1.6 (a) and (b) illustrate that a linear approximation for the acceleration response which increases from base to top of the embankment is a reasonable approximation of the FLAC modeling results. However, as shown in Figure 1.6 (c), when the EPS geofoam embankment is excited with an input motion at frequencies higher than the fundamental frequency of the system, it displays an acceleration response behavior that is far from linear. The trend illustrated in Figure 1.6 (c) shows that the acceleration response can be de-amplified at certain aspect ratios and slightly amplified at others. Nonetheless, when one compares the magnitude of the amplification at the fundamental period (Figure 1.6 (a)) with that at higher frequencies (Figure 1.6 (c)) it is clear that excitation at the fundamental period produces amplification that is approximately 10 to 20 times greater than that at frequencies above the fundamental period. Hence, from an analytical standpoint, the fundamental frequency

controls the acceleration response of the embankment for the aspect ratios tested by the FLAC modeling.

In order to verify that the acceleration response is relatively linearly distributed throughout the embankment for excitation at the fundamental period (i.e., resonance) as suggested by NCHRP, the results in Figure 1.6 (a) are plotted in Figure 1.7 for the three aspect ratios investigated. This figure shows the goodness of fit for the linear approximation of the acceleration response plotted from base to top of the embankment. Although the analysis results show a slight curvature, R^2 values of 0.97%, or higher, all aspect ratios indicate that the linear approximation is reasonable for simplified analyses. The results in Figure 1.7 also indicate that higher aspect ratios (i.e., wider embankments) have a more linear distribution throughout the embankment as indicated by the higher R^2 values.

Based on the results in Figure 1.7, it is concluded that the procedure of determining the distribution of the acceleration response by using linear interpolation between the base and top accelerations is reasonable for basal excitation input at the fundamental period. However, it must be noted that this linear distribution has only been validated by the FLAC analysis when the EPS geofoam embankment is in the elastic mode where no yielding or permanent deformations have occurred.

The EPS geofoam embankment with a base to height aspect ratio of 3 was chosen to investigate further the effects of the second mode of vibration. A trial and error process, similar to that used in finding the fundamental period of the embankment, was used in FLAC to determine the second natural frequency of the system. The results of the analyses showed that the frequency ratio of 2 (i.e., the frequency ratio used in obtaining

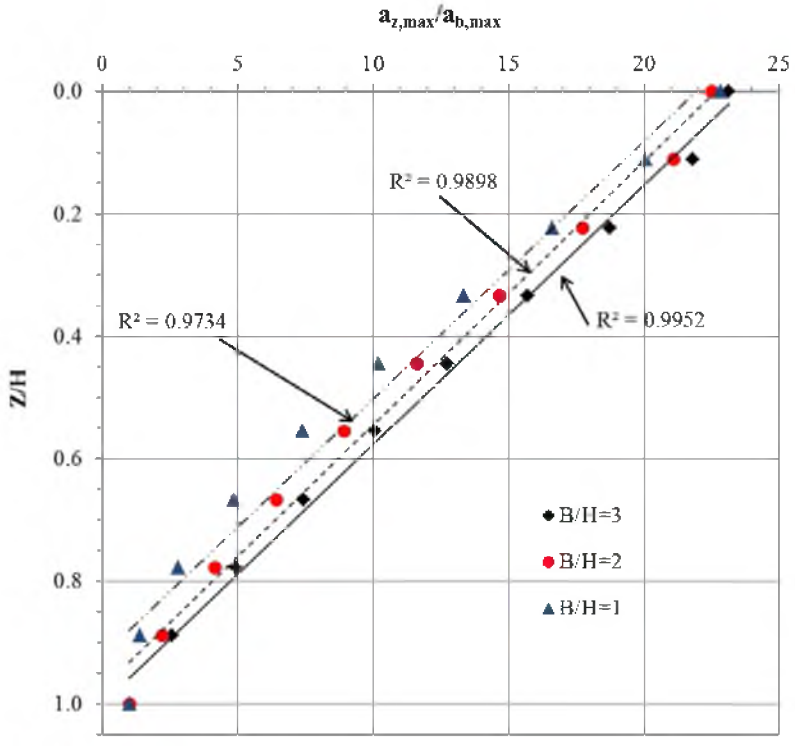

Figure 1.7. Linear regression fitted to the response accelerations at different depths of EPS geofoam embankments with different aspect ratios

the results presented in Figure 1.6 (c) for embankment with aspect ratio of 3) corresponds to the second mode of vibration for horizontal excitation of the embankment. Figure 1.8 illustrates the behavior of the EPS geofoam embankment system at the uppermost layer when the input motion is applied at a frequency ratio of 2. As shown in Figure 1.8, the response of the embankment is similar to that at the fundamental period with the exceptions that in this case the 2% damping assigned to the system inhibits the accelerations from becoming ever-increasing with time. Also, this figure indicates that when the acceleration reaches a maximum value, the system maintains this value with subsequent excitation. Also, the maximum acceleration response within the EPS

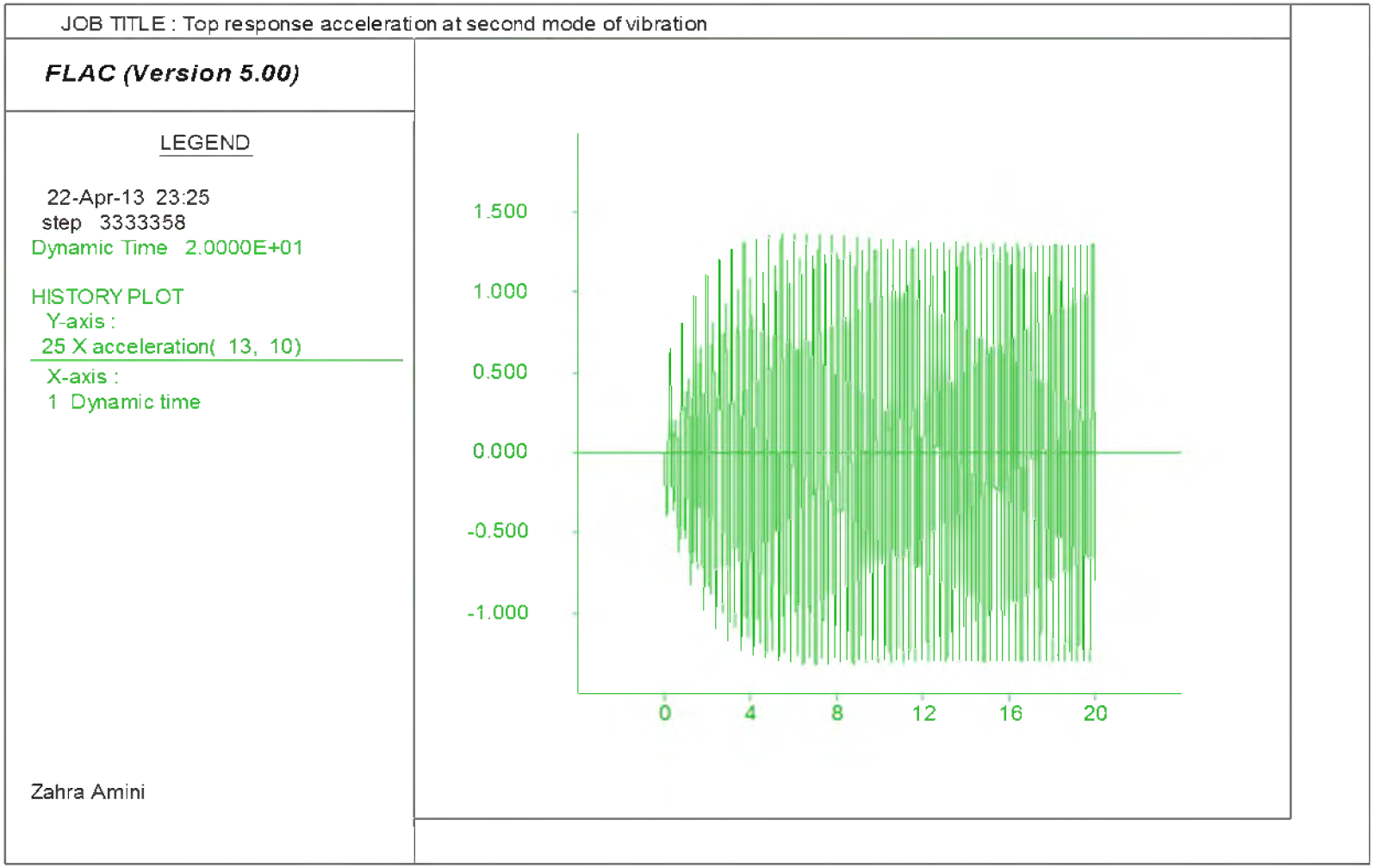

Figure 1.8. Response acceleration time history of the top of an 8 m by 24 m EPS embankment in the second mode of vibration

geofoam embankment for the second mode is much smaller; it is about 10% of the value obtained for the fundamental mode and does not occur at the top. Hence, for practical purposes when compared with the fundamental model of vibration, the second mode of vibration makes a relatively small contribution to the overall acceleration response of the embankment undergoing horizontal acceleration.

In current state of practice for EPS embankment design, there are no guidelines regarding how to calculate the frequency of vibration for the second mode. To estimate this value, the method to calculate the second natural frequency of an earth embankment derived from one-dimensional shear slice theory (Seed and Martin, 1966) is combined with that developed for a cantilever beam. For an earth embankment, where typically only shear forces and deformations due to these forces are considered, the embankment has a rigid base and is infinitely long the second natural circular frequency of the embankment is calculated using the following (Das, 1993):

$$\omega_{s2} = \frac{5.52}{H}\sqrt{\frac{G}{\rho}} \tag{1.14}$$

where ρ is the density of the embankment which equals m/B per unit length of embankment for the EPS embankment configurations described in this study. If Equation 1.14 is written in a simple form of:

$$\omega_{s2} = \sqrt{\frac{k_{s2,eq}}{m}} \tag{1.15}$$

the equivalent shear stiffness for the second mode of vibration would be:

$$k_{s2,eq} = 5.52^2 \frac{GB}{H^2} \tag{1.16}$$

For a cantilever beam the second natural circular frequency is calculated via Equation 1.17 (Chopra, 2007):

$$\omega_{f2} = \frac{22.03}{\sqrt{L}} \sqrt{\frac{k}{m}} \tag{1.17}$$

According to Equation 1.4 for the EPS geofoam embankment system the flexural component of stiffness is: $3EI/L^3$. Substituting appropriate terms for E, I and L Equation 1.17 can be rewritten as:

$$\omega_{f2} = \frac{22.03}{\sqrt{H}} \sqrt{\frac{3E_{t_l}B^3}{12H^3m}} \tag{1.18}$$

If Equation 1.18 is written in the simple form of:

$$\omega_{f2} = \sqrt{\frac{k_{f2,eq}}{m}} \tag{1.19}$$

then the equivalent flexural component of stiffness could be rewritten in the following form:

$$k_{f2,eq} = 22.03^2 \frac{E_{t_i} B^3}{4H^4} \tag{1.20}$$

With the two flexural and shear components of the stiffness, the total equivalent stiffness that can be used to calculate the second natural frequency of the embankment system can be obtained by:

$$\frac{1}{k_{2,eq}} = \frac{1}{k_{f2,eq}} + \frac{1}{k_{s2,eq}} \tag{1.21}$$

Substituting $k_{s2,eq}$ and $k_{f2,eq}$ with Equations 1.16 and 1.20 and simplifying, the following will be obtained:

$$k_{2,eq} = \frac{121\ G\ E_{t_i}\ B^3}{H^2(G\ H^2+4\ E_{t_i}\ B^2)} \tag{1.22}$$

Therefore the second natural circular frequency of the EPS embankment system can simply be derived from:

$$\omega_2 = \sqrt{\frac{k_{2,eq}}{m}} \tag{1.23}$$

Replacing $k_{2,eq}$ with Equation 1.22 and m with $\sigma'_{v_0}B/g$ Equation 1.24 will be obtained:

$$\omega_2 = \sqrt{\frac{121\ G\ E_{t_i}\ B^2 g}{\sigma'_{v_0}\ H^2(G\ H^2+4\ E_{t_i}\ B^2)}} \tag{1.24}$$

Using Equation 1.24, the second natural circular frequency for the EPS geofoam embankment with an aspect ratio of 3 (i.e., 8 m high and 24 m wide), that was numerically analyzed, was calculated; the value of which was approximately equal to $2\omega_0$ (ω_0 being the fundamental circular frequency of the embankment). As previously discussed, the FLAC analysis of this EPS geofoam embankment revealed that the second natural vibration mode is experienced at a frequency ratio of 2 (i.e., results shown in Figure 1.6 (c) and Figure 1.8). Since $f_b/f_0 = \omega_2/\omega_0$, it is concluded that Equation 1.24

can be used to approximate the second natural frequency of the EPS geofoam embankment.

A comparison of Figure 1.6 (a) and (c) shows that the maximum acceleration response of the EPS geofoam embankment for the second mode of vibration is relatively small when compared with the corresponding value for the fundamental mode of vibration, and the contributing accelerations from the second mode can probably be omitted in a simplified design approach. However, if one wishes to include the influence of the second mode, then the total acceleration from the first and second modes of vibration can be calculated at any level, z, within the EPS embankment using the square root of the sum of the squares:

$$a_{z,max,total} = \sqrt{a_{z,max1}^2 + a_{z,max2}^2} \tag{1.25}$$

where $a_{z,max,total}$ is the maximum total acceleration from the first two modes of vibration at depth z below the top of the embankment and $a_{z,max1}$and $a_{z,max2}$ are the maximum accelerations for the first and second modes of vibration, respectively, at depth z below the top of the embankment.

However, as shown in the following example, the second mode of vibration has a relatively small influence on the maximum acceleration response of the EPS embankment, For example, Equation 1.25 can be used to calculate $a_{z,max,total}$ at the top of the embankment (z = 0) for the first two modes of vibration using the results shown in

Figure 1.6 for an embankment with *B/H* equal to 3. For the first mode of vibration (i.e., fundamental mode), $a_{z,max}/a_{b,max}$ is about 23. For the second mode of vibration, $a_{z,max}/a_{b,max}$ is about 1.4. Thus, the $a_{z,max}/a_{b,max}$ ratio for the first two modes of vibration is $[23^2 + 1.4^2]^{1/2} = 23.04$. Hence, because 23.04 is approximately equal to 23, it is reasonable to neglect the maximum acceleration contribution from the second mode of vibration for practical purposes when calculating the maximum acceleration at the top of the EPS embankment. Further, the maximum acceleration response for the first two modes of vibration at the center of the same embankment is: $[9^2 + 1.9^2]^{1/2} = 9.1984$. Thus, because 9.1984 is approximately equal to 9, it is reasonable to neglect the maximum acceleration contribution from the second mode of vibration for practical purposes when calculating the maximum acceleration in the middle of the EPS embankment.

Conclusions

The results of undamped, two-dimensional, numerical, FLAC analysis for EPS geofoam embankments with various base to height aspect ratios excited with basal harmonic motion show that the Japanese Design Equation gives better estimates of the fundamental period for aspect ratios of 1.5, or lower; whereas the equation published in NCHRP reports (Stark et al., 2000) gives better results for wider EPS geofoam embankments (i.e., those with aspect ratios of 2 or higher). The difference between the two equations results from the assumptions found in their development. The NCHRP equation appears to have been established for a one-dimensional SDOF system. Such assumption leads to disregarding the vertical stiffness of the system in the derivation of the equation. In contrast, the Japanese Design Equation derivation appears to have

included the vertical stiffness of the system; therefore it is capable of capturing the two-dimensional effects, such as axial stress and strain in the vertical direction. Because FLAC is a two-dimensional analysis tool, it also captures the vertical as well as horizontal strains that developed in the embankment system. The results of the FLAC analysis suggest that higher vertical strain values will most likely develop in relatively slender embankments when compared with those produced in wider embankments.

Modeling results of the acceleration response throughout the EPS geofoam embankment show a relatively linear distribution of horizontal acceleration at different levels within the embankment for the fundamental mode of vibration. The basal acceleration was equal to the acceleration of the input harmonic motion, and the maximum acceleration occurred at the top of the embankment. When excited at the fundamental period and with 2% damping present in the EPS embankment, the acceleration response reached values that were about 22 to 23 times higher than the basal acceleration. However, when excited at frequency ratios higher than 1, the distribution of the horizontal acceleration was highly nonlinear, suggesting that higher modes of vibration were being partially realized.

Subsequently an analytical approach was developed to estimate the frequency of vibration associated with the second mode of vibration of the EPS geofoam embankment and compared with FLAC analysis. The FLAC results were used to estimate the maximum acceleration response for the second mode of vibration and compared with the corresponding values obtained from the fundamental mode. This comparison showed that contribution from the second mode of vibration to the overall maximum acceleration response was relatively small. Therefore, it is generally recommended that when

performing simplified dynamic stability evaluations of EPS geofoam embankments, the modal contribution of higher modes of vibration to the maximum acceleration response be neglected, and the maximum acceleration within the EPS embankment be estimated only from the acceleration associated with the fundamental mode.

CHAPTER 2

EXPERIMENTAL STUDY

This chapter focuses on evaluating the strength and effectiveness of a commercially available adhesive for application in EPS geofoam embankment construction to prevent interlayer sliding. Laboratory testing was performed to evaluate the bond strength of the Flexible Fast™ urethane adhesive and other pertinent EPS geofoam properties for different types of loading conditions imposed on both bonded and intact EPS geofoam specimens. The types of laboratory testing performed on the bonded and intact specimens included: uniaxial compression, direct shear and uniaxial extension (i.e., tensile) tests. Uniaxial compression and extension tests were chosen because of the relatively small to negligible confining pressure that develops in most above-ground EPS embankment applications.

In order to address the internal and external stability of the EPS geofoam embankment, an investigation of the material properties of the EPS is required. Two main aspects of material properties of the EPS geofoam that are of significance for embankment applications are properties associated with compression (i.e., axial) loading and shearing of the EPS. Because EPS geofoam embankment may be exposed to vertical and horizontal live and dead loads, it is important to investigate the behavior of the

EPS geofoam under compressional and shear loadings. Information such as the type of response (e.g., elastic or plastic), the amount of permanent deformation and maximum allowable stress can be obtained from the stress-strain response of the EPS specimen resulting from uniaxial compression tests. In the event of exposure to horizontal loading such as seismic forces, the internal shear properties of the EPS geofoam itself and those of the interfaces between the EPS geofoam blocks are of interest to evaluate the dynamic stability of the embankment. In addition, during seismic excitation, it is possible for the EPS geofoam embankment to undergo other modes of excitation that induce extensional (i.e., tensile) stresses particularly when the EPS geofoam embankment system undergoes horizontal sway, rocking or uplift modes (Bartlett and Lawton, 2008). Therefore properties of the EPS geofoam obtained from extensional testing may be required in stability analysis of the embankment.

Nonetheless, the potential for interlayer sliding is the primary issue concerning the internal seismic stability of the EPS geofoam embankment constructed of blocks stacked atop each other. For cases where EPS geofoam embankments may be subjected to high levels of earthquake motion and sliding is expected to be a performance issue, mechanical or structural countermeasures to prevent interlayer sliding may be employed. For example, an adhesive bond (i.e., glue) or barbed connector plates placed between the blocks has been proposed to inhibit interlayer sliding.

Barrett and Valsangkar (2009) have shown that barbed connectors (i.e., gripper plates) do not have a significant effect on the shear resistance of the blocks and therefore may not lead to adequate stability. However, their evaluation of adhesive was shown to be effective in bonding the EPS geofoam blocks together, thus eliminating the potential

for horizontal interlayer sliding between blocks.

Another alternative for preventing interlayer sliding is the potential use of shear keys. The shear key is essentially an EPS geofoam block that is installed within two layers that interrupts the continuous plane between layers. The shear keys are placed periodically throughout the embankment for lateral stability as recommended by the design engineer. According to Bartlett and Lawton (2008), the strategic placement of shear keys will require the potential sliding surface to shear through a select number of EPS geofoam blocks, and ultimately this pattern of placement will disrupt the failure surface and greatly improve the sliding resistance.

In addition, some researchers and practitioners have suggested mechanical / structural remedies such as tie-back wall or anchored systems where the panel wall on each side of the EPS is restrained in some manner. Although initially attractive, these alternatives have design issues related to determining the magnitude of the seismic loadings to wall and its connections, and the potential for higher design and construction costs.

The use of an adhesive bond between the EPS blocks appears to be one of the more straightforward ways of addressing interlayer sliding. The primary goal of this study is to test bonded specimens to evaluate whether or not the Flexible Fast™ adhesive bond was capable of withstanding various loading conditions applied to the bonded interface without debonding. Uniaxial compression tests were performed to evaluate the compressive resistance of EPS geofoam (InsulFoam® GF19) samples at various levels of axial strain. This test setup replicates the state of stress that develops in EPS blocks associated with a vertically loaded, freestanding, embankment. In addition to testing

intact specimens, a bonded interface plane that was oriented at a 45-degree angle from the horizontal was tested. For purely cohesive materials, this 45-degree plane is the plane upon which the theoretical maximum shear stress develops during uniaxial compression. This orientation of the bonded plane ensures that the shear bonding is tested at its maximum value.

The direct shear device was used to measure the following: (1) cohesive shear strength of intact specimens, (2) cohesive interface shear strength of Flexible Fast™ bonded specimens, and (3) frictional interface shear resistance of unbonded (intact) specimens. In the direct shear test, the horizontal shear force is concentrated on a discrete horizontal plane that is found between the two halves of the rigid shear box. As such, this test is best for determining interface properties of unbonded (intact) and bonded specimens for use in interlayer sliding evaluations. It is noted that the internal shear strength of intact specimens has often been obtained from the ASTM C273 test by the EPS industry. This test determines the shear strength properties of sandwich construction core materials associated with shear distortion of planes parallel to the facings. The properties determined are the shear strength parallel to the plane of the sandwich, and the shear modulus associated with strains in a plane perpendicular to the facings (ASTM C237). However, it is deemed that the direct shear test may better represent the mode by which the shear forces are transferred and distributed through an EPS geofoam block used as a shear key in a full-sized EPS embankment. For example, at the initiation of horizontal loading, the horizontal sliding force is resisted by interlayer friction at the contact surfaces between the block and by the shear strength of the shear key. As shearing initiates, the potential shear plane will most likely develop along a horizontal

plane. Shear stress will be reasonably concentrated along a horizontal plane within the shear key; hence the direct shear test provides a reasonable representation of this situation.

Nonetheless, very little information is available regarding the nature of the shear stress concentration along and near this plane and the peak shear resistance that develops in the shear key. Although not a complete representation of the field case, it is hoped that the results of these direct shear tests on intact specimens can provide a lower bound estimate regarding the potential magnitude of localized shear resistance that develops in shear keys. The results of this study are lower bound estimates because of the highly concentrated shear plane that develops in the direct shear test when compared with the field situation, and because of the relatively small size of the samples tested in this program, which are known to produce conservative (i.e., low) estimates of shear strength when compared with full-sized block.

Uniaxial extension (i.e., tensile) testing was performed on intact and Flexible Fast™ bonded EPS specimens. This was done to estimate the tensile strength of EPS block subject to horizontal sway, rock and uplift forces. For example, Bartlett and Lawton (2008) have suggested that internal deformation resulting from rocking and swaying modes can cause local tensile yielding of some blocks within the embankment when horizontal interlayer sliding of block is prohibited. For bonded EPS specimens tested in the laboratory, the bonded plane was positioned horizontally which maximizes the developed tensile stress on the bond when the specimen was placed in uniaxial extension.

Additionally, the potential effect of extreme temperature changes on the

properties of the EPS geofoam and the Flexible Fast™ bonding adhesive was studied. A set of laboratory tests was performed on intact and bonded samples that were environmentally conditioned through various freeze-heat cycles, and the results were compared against those of unconditioned samples.

In order to explore the properties and effectiveness of the Flexible Fast™ adhesive to prevent interlayer sliding of the EPS geofoam embankment during installation and from seismic events, the types of testing previously discussed were completed on bonded and homogeneous, intact samples to determine the bond strength. The test program was carried out solely on InsulFoam® GF19 (EPS 19) because this density of EPS is commonly used in roadway and embankment construction in the U.S. and Europe.

For the bonded samples, the specimens were adhered using Flexible Fast™ adhesive which was applied and cured by InsulFoam and shipped to the University of Utah. In addition, InsulFoam provided all the specimens in the cylindrical forms used in the testing program. The samples were tested to failure in the Soil Mechanics Laboratory at the University of Utah in the manner previously discussed.

Additionally, because EPS geofoam embankments can be installed in adverse climates and exposed to freeze-heat cycles (e.g., I-15 Reconstruction project in Salt Lake City, Utah), environmental conditioning was done to address potential concerns about the integrity of the Flexible Fast™ adhesive bond in such conditions. The laboratory testing was done on environmentally conditioned samples consisting of both bonded and intact specimens. For this purpose, a subset of specimens was placed in an environmental chamber at the University of Utah and exposed to several hundred freeze-heat cycles. The

chamber introduced 8 to 12 freeze-heat cycles per day to the EPS samples by changing the temperature between 0 and 40 degrees Fahrenheit over a period of 6 months. The samples were removed from the environmental chamber, and shear testing was performed at room temperature to quantify any potential effects resulting from the environmental conditioning.

Uniaxial Compression Tests

Compression under gravity loading is the predominant mode of loading in embankment applications; hence the mechanical properties of the EPS geofoam associated with this type of loading are of most important. The compression testing was performed uniaxially (i.e., no confining stress applied to the specimens), which is consistent with NCHRP (2004) guidelines. In addition, such testing requires consideration of factors such as: specimen size and dimensions, type of loading (strain-controlled versus stress-controlled), loading rate and temperature, which will be discussed in the following sections.

Test Specimens

The specimens used in the uniaxial compression tests were cylindrically shaped with a height of 127 mm (5 in.) and a diameter of 63.5 mm (2.5 in.). A total of 20 specimens were tested consisting of 13 bonded and 7 intact specimens, where 3 of the bonded and 2 of the intact specimens had been environmentally conditioned. The bonded specimens were cut at a 45-degree angle and glued together with the adhesive.

Figure 2.1 shows the intact and bonded specimens used in uniaxial compression testing. Specimens were examined for potential gaps in the cut area.

Test Specifications

The specimens were vertically loaded under zero confining pressure using the GeoComp LoadTrac™ frame shown in Figure 2.2 and in accordance with ASTM D2166. The vertical force was applied to the specimen and measured via a pressure transducer connected to the cross-bar of the load track frame.

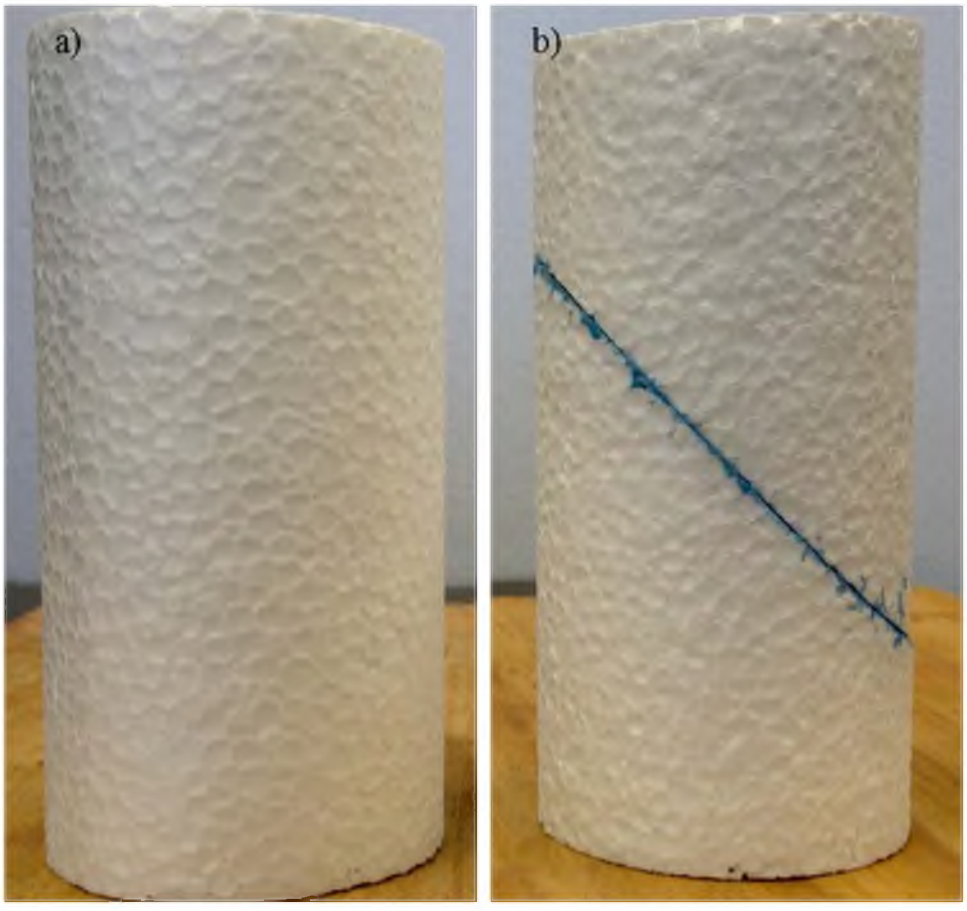

Figure 2.1. EPS specimens for uniaxial compression test: a) Intact and b) Bonded

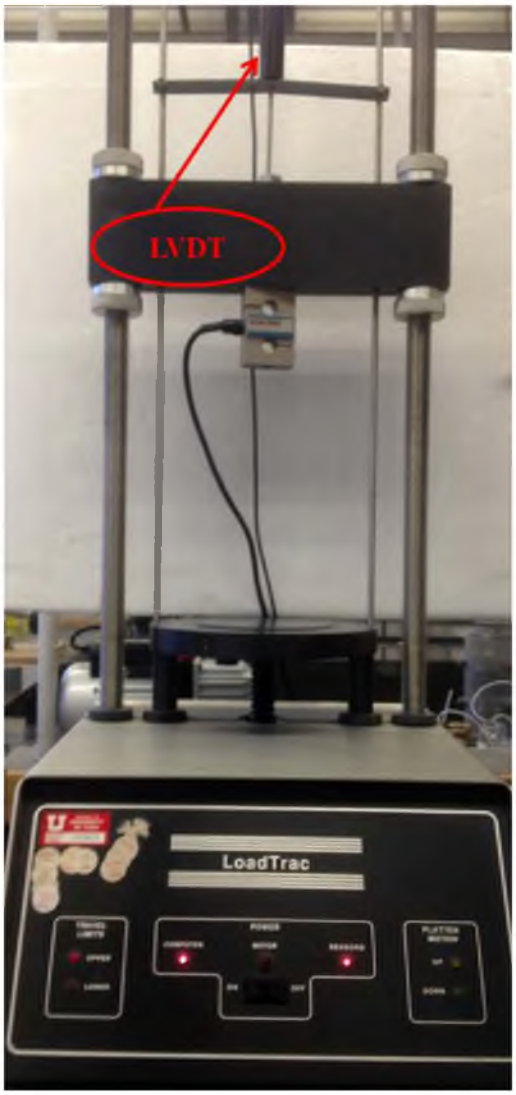

Figure 2.2. GeoComp LoadTrac™ device used for uniaxial compression testing

A Linear Velocity Displacement Transducer (LVDT) (shown in Figure 2.2) measured the vertical displacement of the specimen as the axial force was applied. The data acquisition system for the LoadTrac recorded the force and displacement values at predetermined time intervals.

The specimens were subjected to strain controlled loading with a rate of 10% axial strain per minute. The 10%/min rate is in accordance with NCHRP (2004)

guidelines. Furthermore, an experimental study by Doskov (1997) showed that the effects of loading rate in lower ranges of strain (where the initial tangent modulus is measured) were negligible. The uniaxial compression testing was performed at room temperature, which was approximately 22 degrees C. The GeoComp LoadTrac™ device is available at the Geotechnical Engineering Laboratory at the Department of Civil and Environmental Engineering.

Test Results

Figure 2.3 shows the typical stress-strain behavior of the intact EPS specimens and environmentally conditioned intact specimens. Figure 2.4 presents the response of the bonded (glued) EPS specimens and the environmentally conditioned bonded EPS specimens under uniaxial compression. It can be observed that over a small range of strain (i.e., generally less than 1%), the intact and bonded EPS specimens display a linearly elastic stress-strain behavior under uniaxial compression. This is true regardless if the specimens were or were not environmentally conditioned. The initial tangent Young's modulus of the EPS can be obtained using the following:

$$E_{t_i} = \frac{\Delta\sigma}{\Delta\varepsilon} \tag{2.1}$$

where E_{t_i} is the initial tangent Young's modulus, $\Delta\sigma$ and $\Delta\varepsilon$ are the compressive stress and strain intervals corresponding to the linear elastic range. It is important to quantify the limits of the linear elastic range therefore as part of the results of the uniaxial

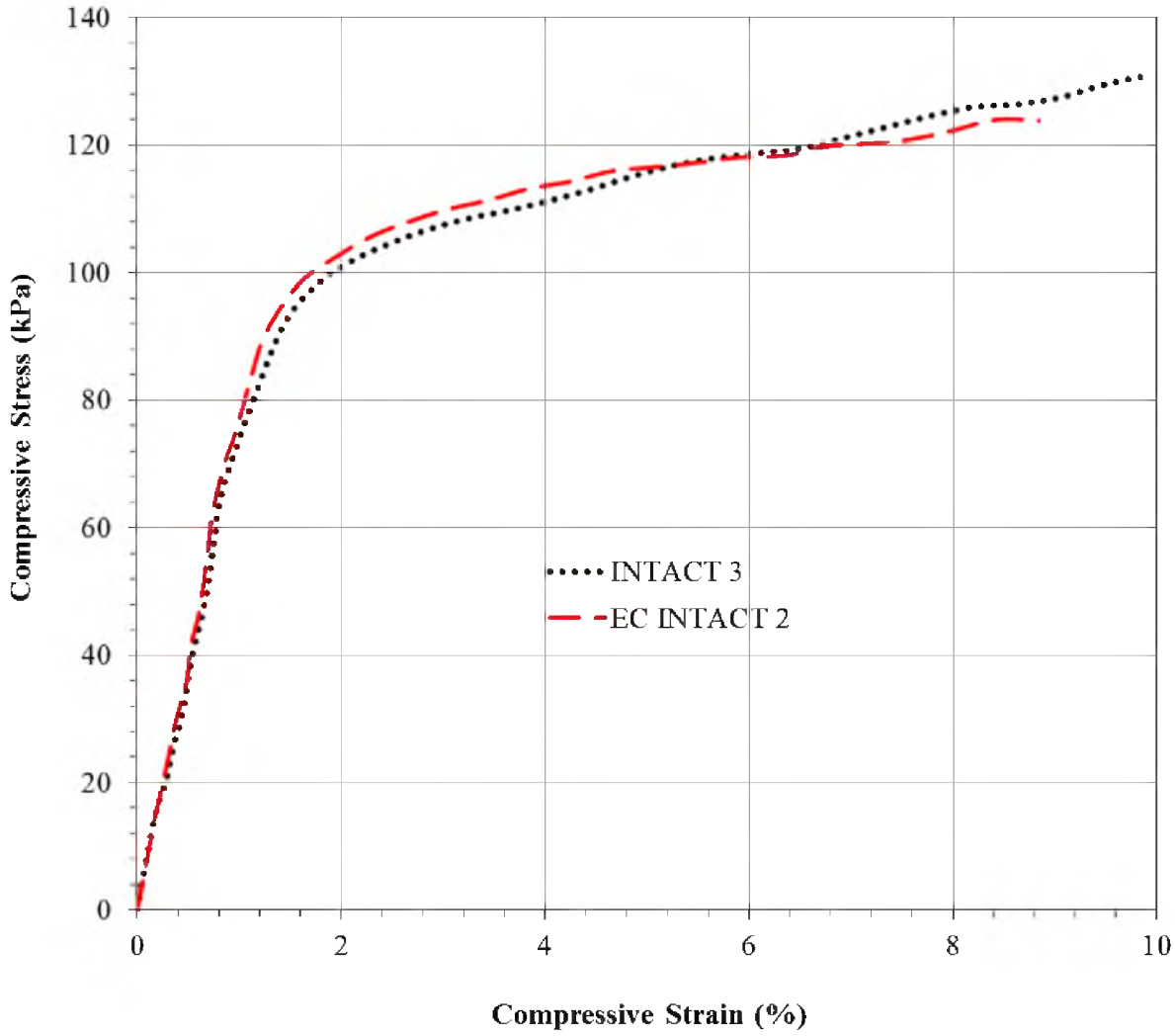

Figure 2.3. Stress-strain behavior of an intact and an environmentally conditioned intact EPS specimen

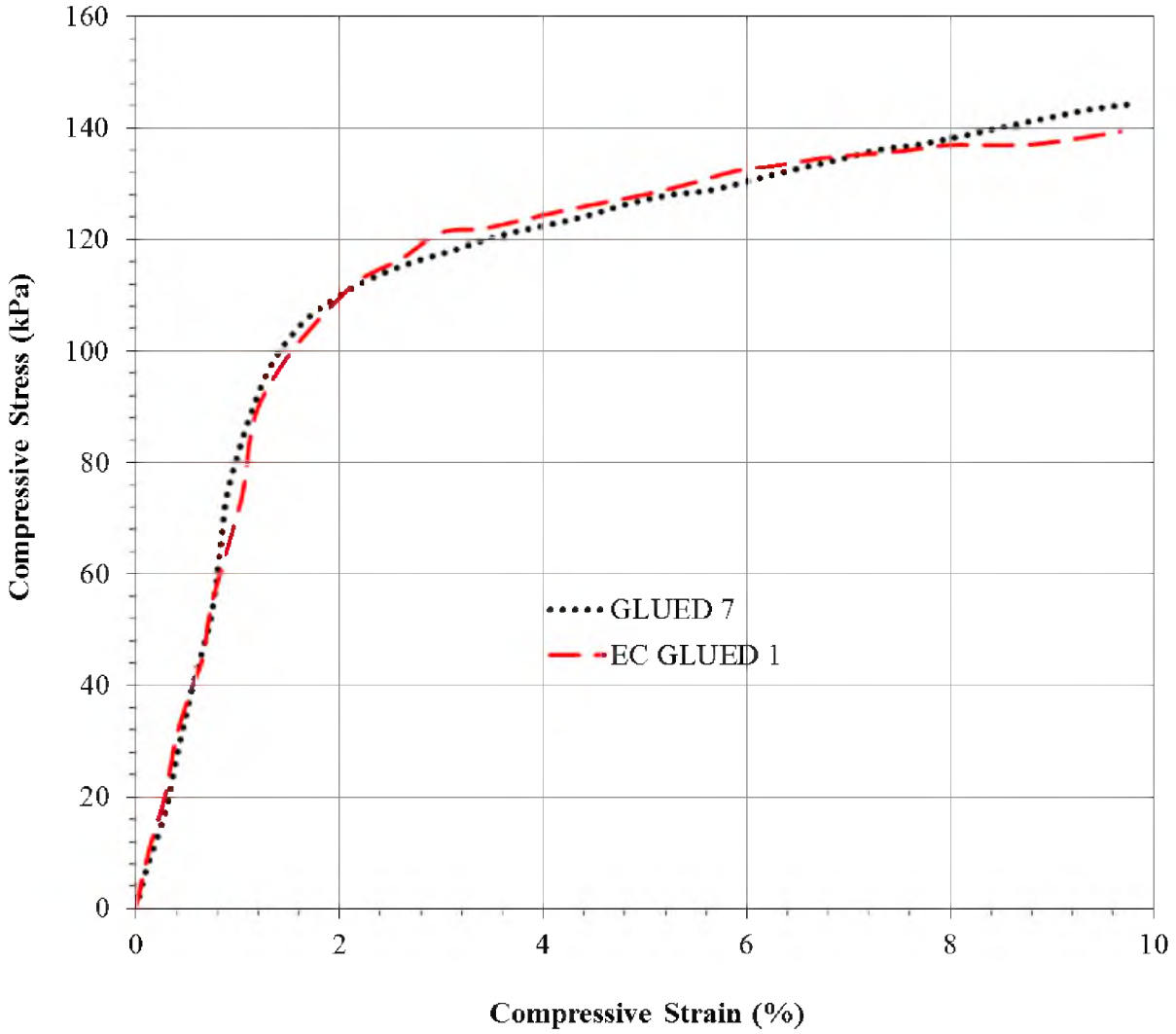

Figure 2.4. Stress-strain behavior of a glued and an environmentally conditioned glued EPS specimen

compression tests values of elastic limit stress (σ_e) and elastic limit strain (ε_e) are reported. It is noteworthy that NCHRP guidelines indicate that as a rule of thumb ε_e is generally 1% and therefore the value of σ_e corresponds to 1% strain. However, in this study the linear elastic range of the EPS specimen behavior was closely monitored for each test and thus the elastic limit values are reported on a case by case basis. Therefore the elastic limit strain values may deviate from 1% depending on the results of each specific test. As shown in Figures 2.3 and 2.4, the EPS does not fail in the traditional pattern of other solid construction materials (e.g., metals and concretes). No physical rupture of the EPS specimen is observed. Rather, the EPS essentially collapses back to its original solid polystyrene state, and the behavior is continuously strain hardening in nature (Stark et al., 2004). However, even though EPS does not fail in the traditional sense of a physical rupture under compression, it is common to define compressive strength of the EPS (σ_c) as the compressive stress at some arbitrary strain level. Since there is no universal agreement on this strain level, for this study the value of σ_c is the compressive resistance associated with an axial strain of 5%. No rupture or failure of any kind was observed alongside the plane on which the adhesive was applied to the specimen. The integrity of all bonded specimens was preserved regardless of environmental conditioning.

An initial slightly curved, concave upward, response was observed in the results of the compression test on one of the bonded samples (Appendix A). This curvature may be resulting from a gap introduced to the specimen in the process of gluing the pieces of EPS together. Errors related to seating of the pieces of the EPS in bonded samples were not observed in other specimens. The stress-strain behavior of all the specimens are

presented in Appendix A. Table 2.1 summarizes the results of the uniaxial compression tests in terms of the minimum and maximum values of the variables of concern where the environmentally conditioned specimens are indicated with the prefix "EC." More detailed results are tabulated and presented in Appendix A. It can be concluded that freeze-heat cycle treatment may have a small stiffening effect on the EPS specimens as such samples are associated with a slightly higher average Young's modulus, as noted in Table 2.1. However, this stiffening effect seems small enough to be neglected. Bonded specimens generally show a higher maximum value of compressive strength compared to intact samples whether environmentally conditioned or not. Also, the maximum compressive strength does not show a considerable change due to environmental conditioning. Intact specimens show a linear elastic behavior up to 0.68% strain and a maximum elastic limit stress of about 53 kPa while the bonded specimens show an elastic limit stress of up to 68 kPa at 0.95% strain. The compressive strength varies from 90 to 118 kPa for intact and 95 to 133 kPa for bonded specimens. Young's modulus of the tested EPS geofoam is estimated to be around 7 MPa.

Direct Shear Tests

In the event of horizontal loading imposed to the EPS geofoam embankment such as in earthquakes, shear forces will be introduced to the EPS geofoam; hence the shear mode is a potential failure mode. Such shear forces may result in interlayer sliding at the boundary of the EPS blocks where bonding does not exist, and shear deformations withinthe EPS geofoam blocks. Moreover, when sliding remedies such as adhesive bond and shear keys are applied, it is important to investigate the response of these measures to

Table 2.1. Summary of uniaxial compression test results

Specimen ID	$\varepsilon_{e,min}$	$\varepsilon_{e,max}$	$\sigma_{e,min}$	$\sigma_{e,max}$	$E_{ti,min}$	$E_{ti,max}$	$E_{ti,avg}$	$\sigma_{c,min}$	$\sigma_{c,max}$
----------	*(%)*	*(%)*	*(kPa)*	*(kPa)*	*(MPa)*	*(MPa)*	*(MPa)*	*(kPa)*	*(kPa)*
INTACT	0.42	0.68	30.0	49.6	6.9	7.6	7.2	89.8	117.5
GLUED	0.45	0.87	26.6	60.5	6.0	7.5	6.2	94.6	133.2
EC INTACT	0.44	0.66	32.9	52.7	7.7	7.8	7.8	114.3	116.5
EC GLUED	0.61	0.95	42.4	68.1	6.8	7.2	7.0	94.7	128.1

the shear loading. The results of direct shear testing give an insight about the cohesive shear strength of the EPS geofoam and the interface friction angle of EPS sliding on EPS.

Test Specimens

Cylindrical specimens of InsulFoam® GF19 (EPS 19) that were 63.5 mm (2.5 in.) in diameter were used for direct shear testing. The specimens were prepared in three different forms. The first group that was used to determine the cohesive shear strength of the EPS consisted of 33 mm (1.3 in.) high uniform intact EPS cylinders. The second group used to determine the bond strength resulting from application of the adhesive, were prepared by assembling two cylindrical EPS specimens atop each other and adhered in the middle to build a cylindrical specimen with a total height of 33 mm (1.3 in.). Figure 2.5 illustrates the intact and bonded specimens used in cohesive testing. Finally, the specimens used to evaluate the EPS/EPS frictional resistance included two separate

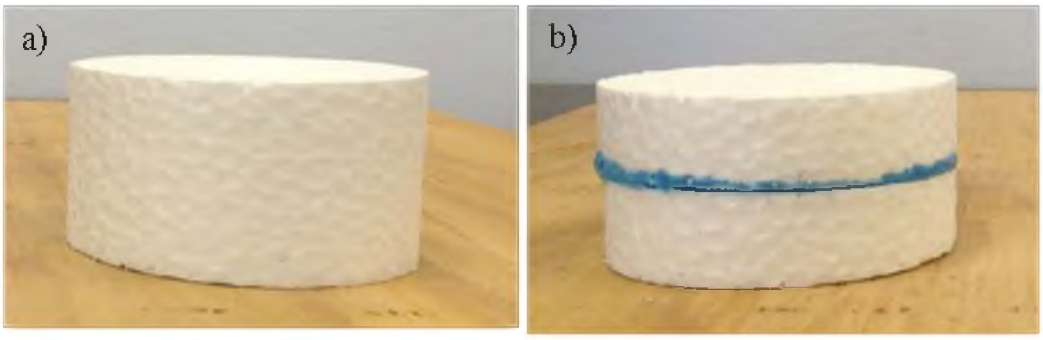

Figure 2.5. Specimens used in direct shear testing: a) Intact and b) Glued

15 mm (0.6 in.) high cylindrical specimens that were set atop each other in the direct shear device. A total of 26 specimens were tested including 9 intact and 9 bonded specimens used for cohesive testing and 8 specimens used for frictional testing. From each group of specimens 3 were environmentally conditioned.

Test Specifications

The specimens were horizontally loaded using the direct shear device and in accordance with ASTM D3080. Figure 2.6 shows the direct shear equipment available at the Department of Civil and Environmental Engineering of the University of Utah used for testing. The interface between the two pieces of the specimens in each test was carefully aligned with the small gap between the top and bottom rings of the direct shear box. The unconditioned specimens were tested under normal stresses of 10, 15, 20, 25 and 30 kPa and the environmentally conditioned specimens were tested under 10, 15 and 25 kPa. As Horvath (1995) recommends, relatively rapid loading rates for shearing the EPS specimen were used to conduct the direct shear tests. The applied loading rate for

Figure 2.6. University of Utah direct shear device manufactured by ELE International

direct shear testing was 1%/min. However, in order to study the effect of loading rate on the shear behavior of the EPS specimens 1 intact and 1 bonded specimen were tested with a loading rate of 2%/min, under 15 kPa normal stress and the results were compared with those tested with 1%/min loading rate under the same normal stress. The incremental horizontal displacement of the each sample and the shear force were recorded throughout the testing.

Test Results

Figure 2.7 shows an intact and a bonded sample after the direct shear testing. Visual inspection of the bonded samples after the tests confirmed that the interface bond was not broken between the two pieces of EPS, instead the shear deformation occurred locally between a fine layer of EPS immediately above the adhesive layer and the top portion of the specimen. Figure 2.7 (b) shows that beads of EPS were still embedded in the adhesive suggesting that the failure was a localized cohesive failure and not adhesive failure of the interface bond. Inspection of the bonded samples, regardless of normal stress and environmental conditioning showed that the adhesive withstood shear loading and the shear failure took place in the EPS material.

Figure 2.8 shows the shear response of the intact, bonded and environmentally conditioned EPS samples tested under 15 kPa normal stress. The intact and bonded samples that were not environmentally conditioned show very similar stress paths; and the maximum shear stress, which is representative of the cohesive shear strength of the EPS under this normal stress, is about 60 kPa for these samples. This similarity shown in the behavior of the bonded and intact samples provides more evidence for the local shear failure occurring within the EPS material and not the adhesive. The environmentally conditioned samples, however, show a cohesive shear strength of about 74 kPa which is 23% higher than that of unconditioned samples. This effect may be a result of alteration of EPS cell connections in a way that favors the strength of the material when exposed to shear loading. The results for bonded, intact and environmentally conditioned EPS samples for all the normal stresses are presented in Appendix A.

The results of the direct shear testing of all groups of samples at each normal

Figure 2.7. EPS specimens after direct shear testing: a) Intact and b) Glued

stress is summarized in Figure 2.9 in terms of the relation between the cohesive shear strength and the normal stress. According to this figure there is a very slight increase in the shear strength of all the groups of samples as the normal stress increases where the bonded samples are associated with shear strength very similar to those corresponding to intact samples. The effect of environmental conditioning the samples is very evident in terms of increasing the shear strength. The effect of loading rate was studied on bonded and intact samples at 15 kPa normal stress. Figure 2.10 shows the shear stress versus displacement for samples tested at 1%/min and 2%/min loading rates.

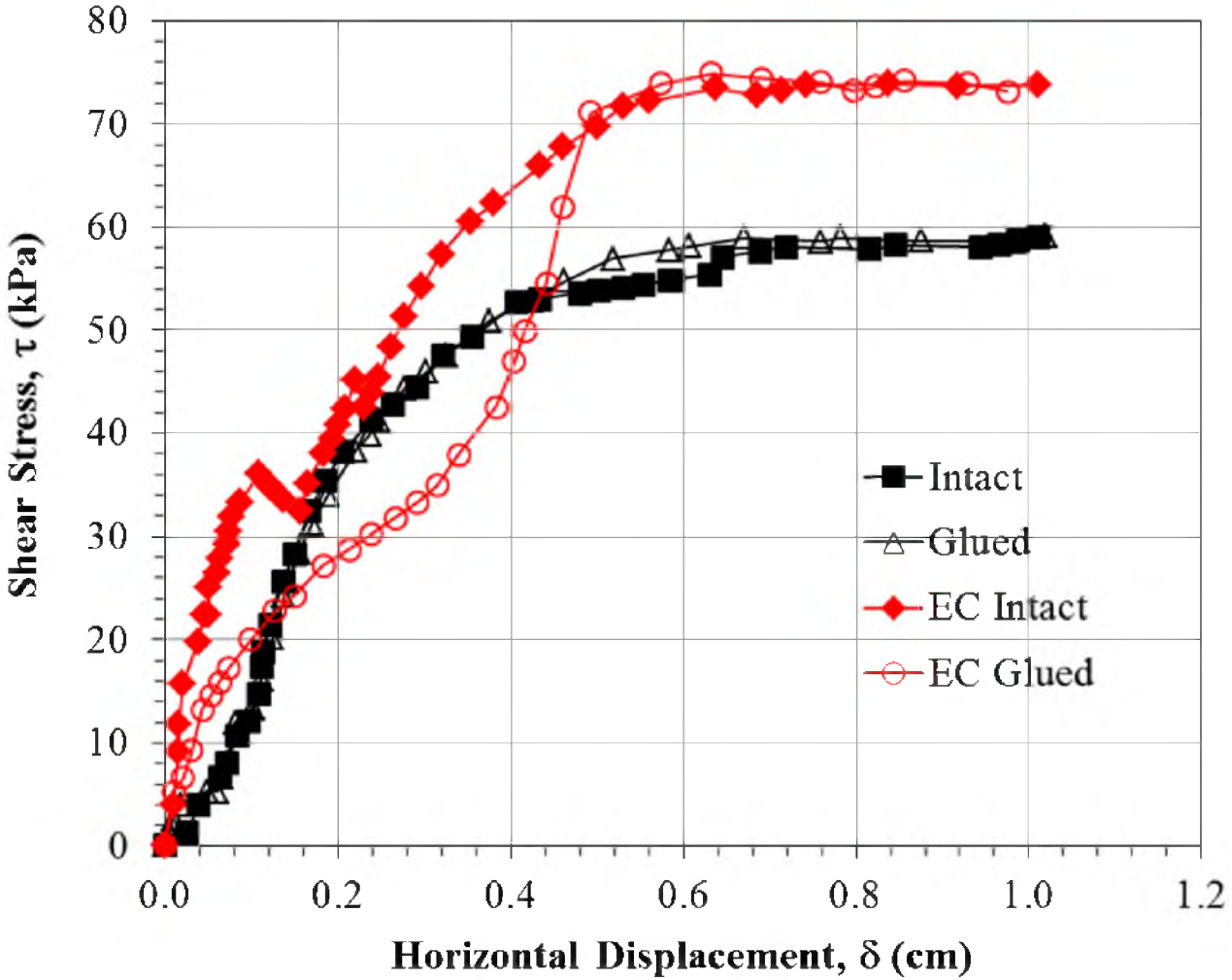

Figure 2.8. Shear stress vs. displacement of EPS specimens under 15 kPa normal stress

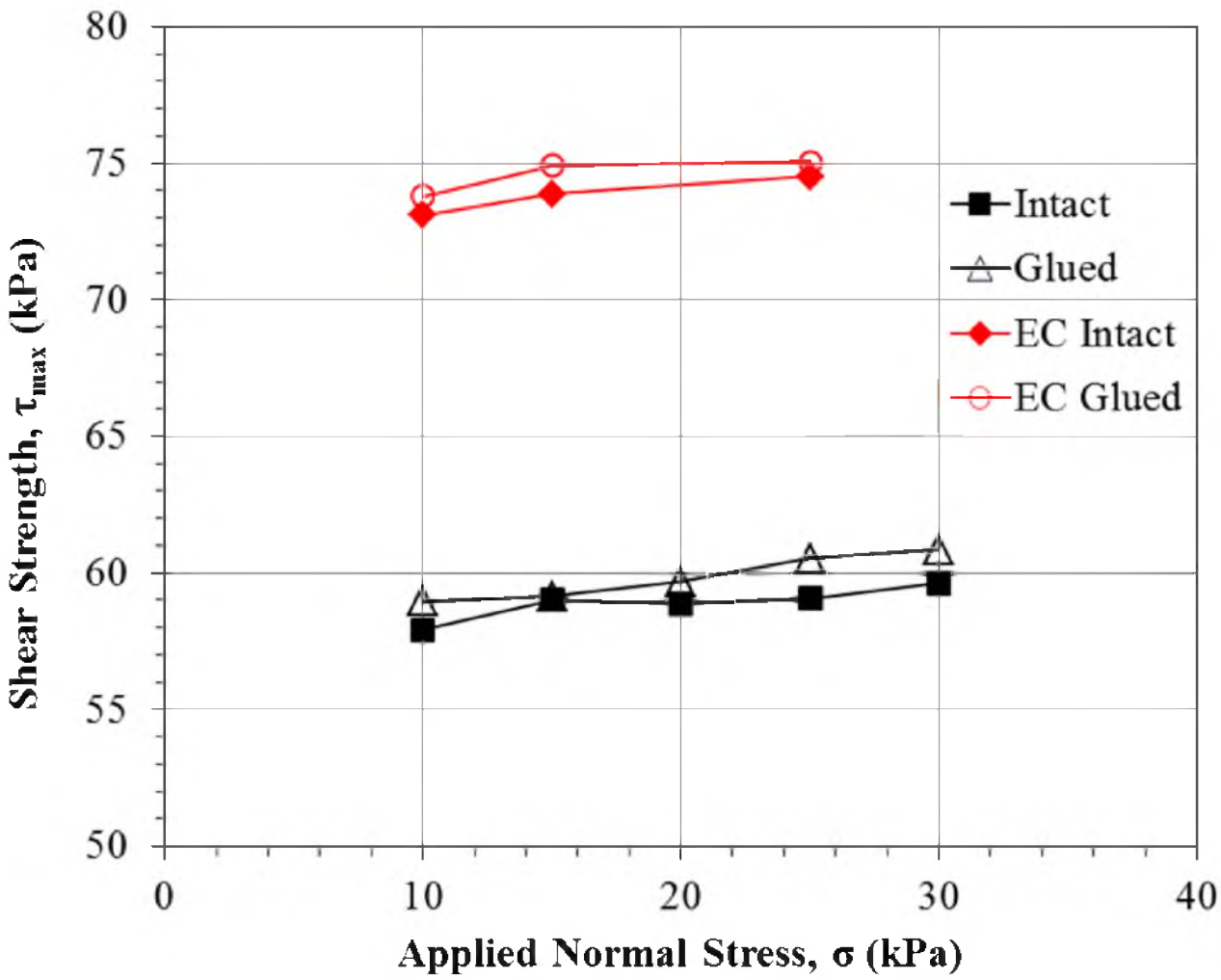

Figure 2.9. Shear strength vs. applied normal stress

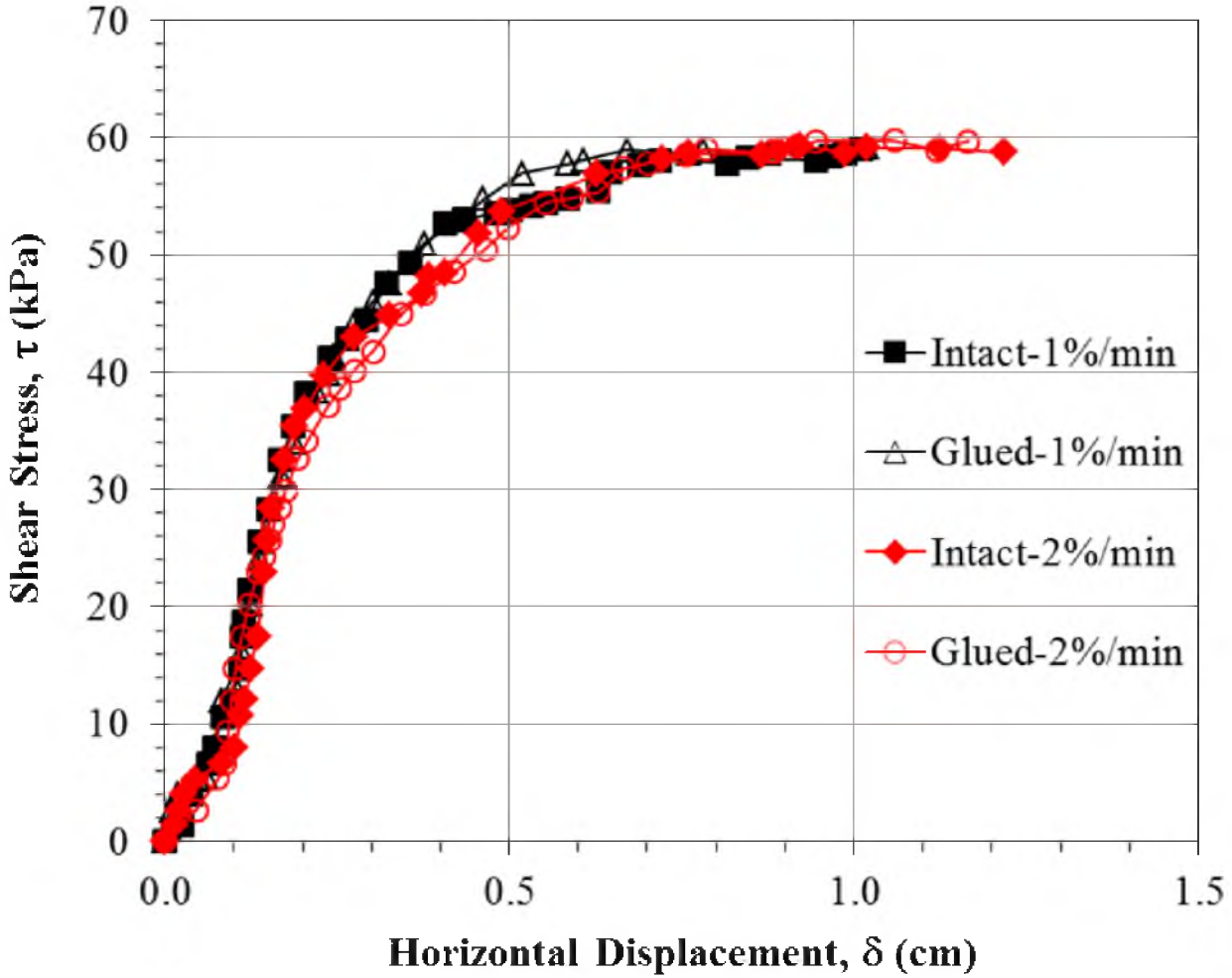

Figure 2.10. Shear stress vs. displacement of EPS specimens under 15 kPa normal stress at different loading rates

It is apparent that doubling the loading rate has no significant influence on the shear response of the samples. Both stress path and maximum shear stress observed for the two loading rates are greatly similar. However, these results do not imply that the shear response of EPS is independent of the loading rate; rather, it may be concluded that at relatively rapid rates of loading, minor changes in loading rate may not significantly affect the test results. Horvath (1995) quantifies "relatively rapid" loading rate with a value of 0.5%/min, which is lower than loading rates used in this study, therefore the effect of lower loading rates (i.e., loading rates lower than 0.5% /min) must be evaluated if such rates were to be applied.

Further, the frictional shear strength of the two EPS specimens sliding atop each other was studied. Figure 2.11 compares the results of the test on intact and environmentally conditioned samples under 15 kPa normal stress. From the great similarity of the stress paths and maximum shear stresses shown in Figure 2.11, it is perceived that environmental conditioning does not have a substantial effect on the surface of the specimens. While the results of frictional shear testing of the specimens under various normal stresses are presented in Appendix A in the form of shear stress versus the displacement graphs, Figure 2.12 summarizes the results of these tests. The maximum shear stress versus the corresponding normal stress was plotted to obtain the peak friction angle for intact and environmentally conditioned specimens. The intact and environmentally conditioned specimens show friction angles of 35.0 and 35.6 degrees corresponding to 0.70 and 0.71 coefficients of friction, respectively. Coefficient of friction is defined as tangent of friction angle. It is evident that environmental conditioning does not have an important influence on the friction angle of the EPS.

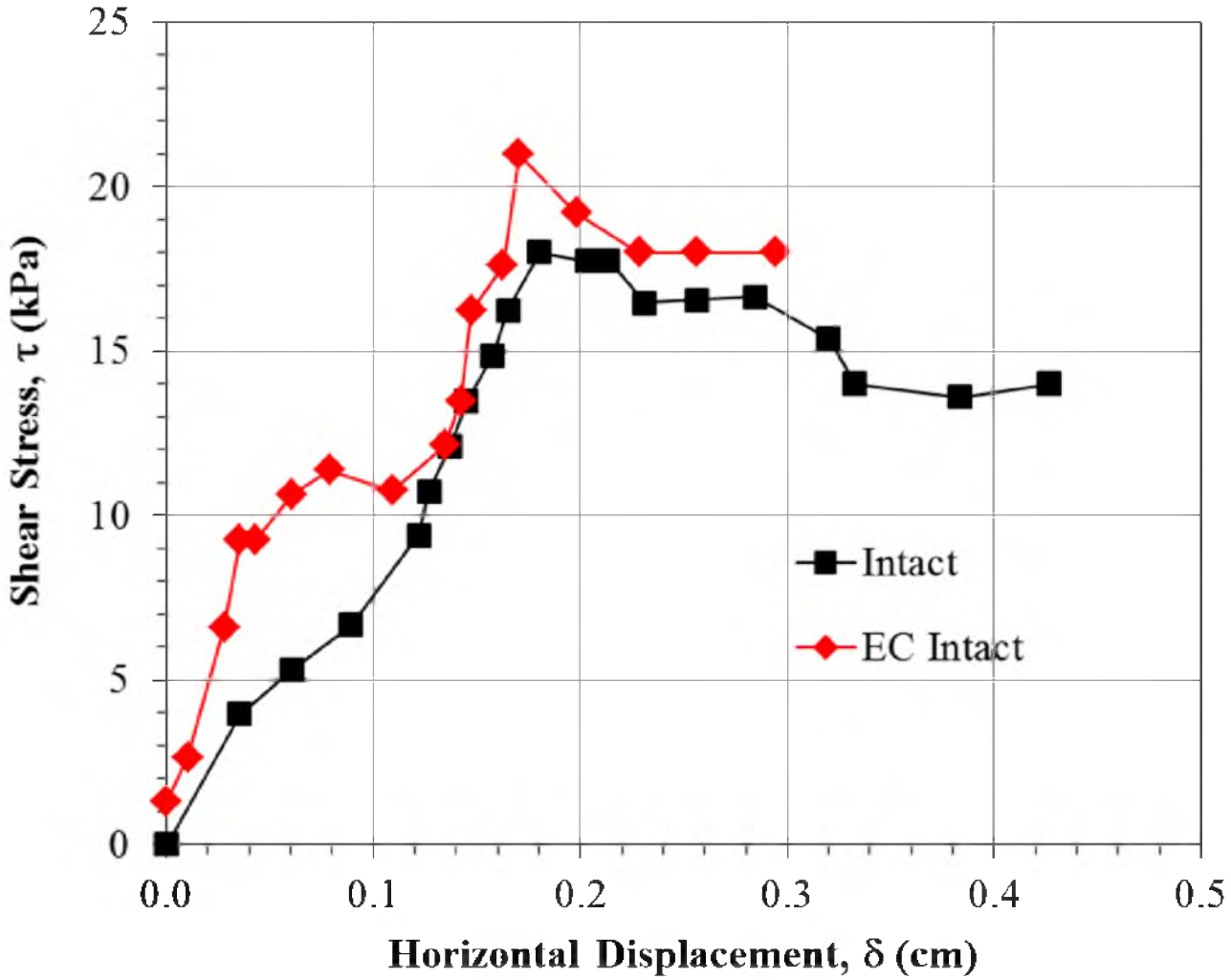

Figure 2.11. Shear stress vs. displacement of intact and environmentally conditioned EPS specimens under 15 kPa normal stress

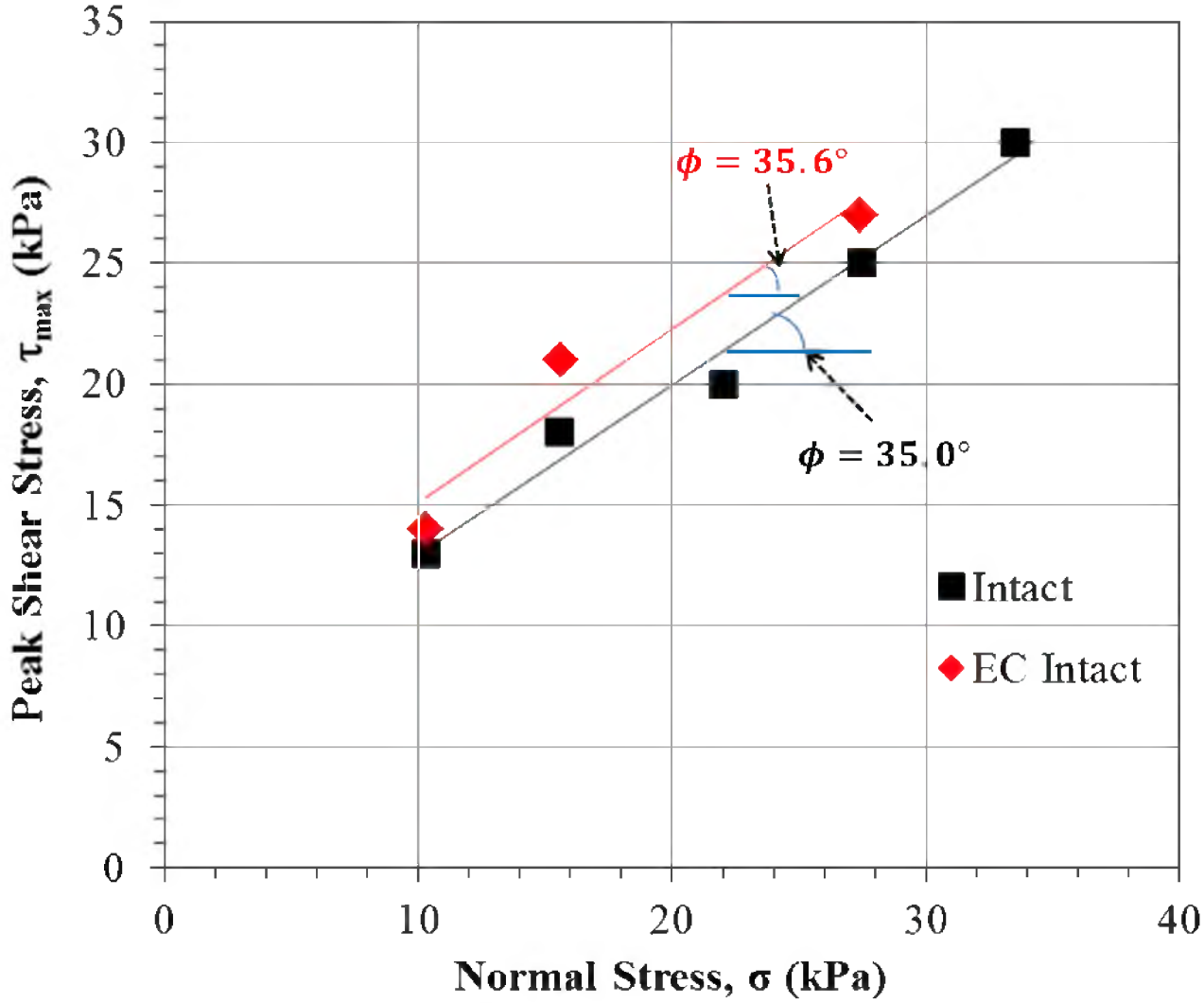

Figure 2.12. Peak shear stress vs. normal stress of intact and environmentally conditioned EPS specimens

Uniaxial Extension Tests

Tensile strength of the EPS geofoam is an index of its quality. Tensile strength of the EPS geofoam varies depending on the EPS density and how well the prepuff was fused during the molding stage of EPS manufacturing (Horvath, 1995). EPS geofoam may experience tensile stresses particularly when the EPS geofoam embankment system undergoes sway or rocking modes (Bartlett and Lawton, 2008). Therefore tensile properties of the EPS geofoam such as tensile strength may be useful in stability analysis of the embankment. There is an ASTM test method (C 1623) for obtaining the tensile strength of EPS geofoam that requires hourglass shaped samples. However, this extension testing is not typically performed because of the difficulty in fabricating the EPS samples. In this study cylindrical EPS geofoam samples were axially exposed to tension in the absence of confining pressures until rupture occurred.

Test Specimens

The specimens used in tensile tests were in cylindrical shapes with a height of 203 mm (8 in.) and a diameter of 63.5 mm (2.5 in.). A total of 21 specimens were tested consisting of 14 bonded and 7 intact specimens where 2 of the bonded and 2 of the intact specimens were exposed to environmental conditioning. The bonded specimens were cut horizontally in the middle and bonded together with use of adhesive. This was done in order to maximize the developed tensile stress on the bond when the specimen was placed in uniaxial extension. Figure 2.13 shows the intact and bonded specimens used in tensile testing.

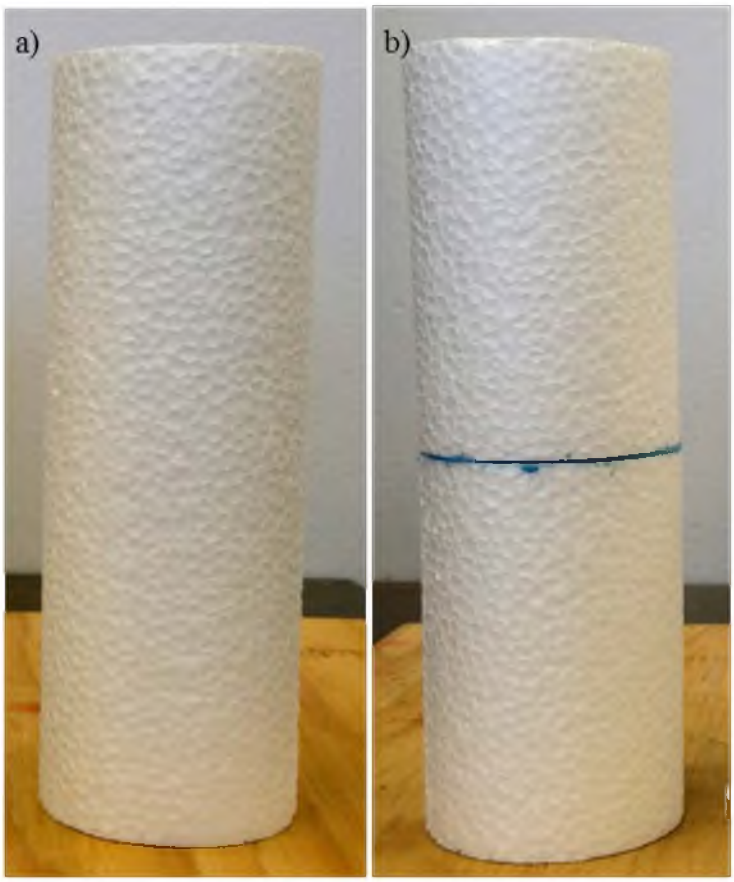

Figure 2.13. EPS specimens for tensile test: a) Intact and b) Glued

Test Specifications

The GeoComp LoadTrac™ equipment shown in Figure 2.2 was used for uniaxial extension testing. Since to load the EPS in tension the top and bottom of the specimens had to be fixed to the load actuator and base plate of the LoadTrac, respectively, the specimens were glued to wood plates at both ends and then clamped to the a wood plate screwed on to the load actuator and the base plate. In order to completely secure the EPS specimen to the wood plates, both ends of the EPS specimens were embedded in the wood plate and bonded using wood glue. Figure 2.14 shows the test setup for intact and bonded specimens. As seen in Figure 2.14 the specimens were tested in an unconfined

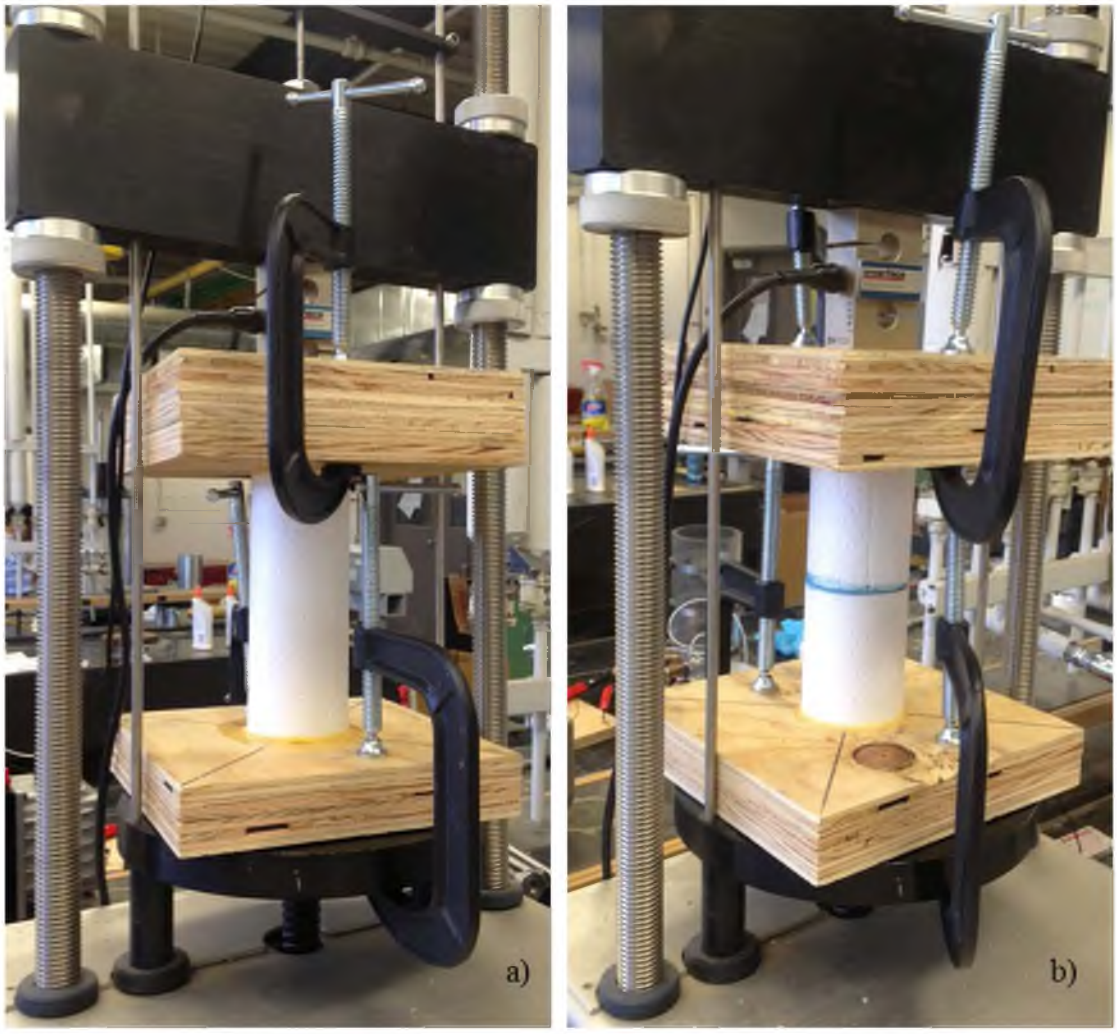

Figure 2.14. Tensile test setup for EPS specimens: a) Intact and b) Glued

condition. During the test the lower LoadTrac plate was lowered at a rate of 2%/min while the tensile force and displacement were monitored and recorded at predetermined time increments. The loading was continued until the specimen was ruptured. The location of rupture was closely observed, particularly in the case of bonded specimens. Embedment of specimens in the wood plates ensured the displacement occurred within the specimens.

Test Results

Figure 2.15 shows the tensile failure that occurred in the EPS specimens in the form of EPS material rupture. Bonded specimens also showed a rupture within the EPS material and not the adhesive. The rupture cross section was carefully inspected for each bonded specimen and it was confirmed that no bond breakage occurred during the uniaxial extension testing. Figure 2.16 shows the rupture cross section in a bonded specimen. As apparent in Figure 2.16 the location of rupture was away from the location of the adhesive plane in the middle of the specimen and it is obvious that the rupture took place within the EPS material. The rupture typically occurred close to the top or the bottom of the specimens and not in the middle or near the bonded plane. Figure 2.17 shows the tensile stress-strain behavior of the intact EPS specimens and environmentally conditioned intact specimens while Figure 2.18 illustrates the response of the Flexible Fast™ bonded (glued) EPS specimens, and the environmentally conditioned EPS specimens under tensile stress. It is shown that over a small range of strain (i.e., generally less than 1%) the EPS specimens, regardless of being intact or bonded and environmental conditioning, display a linearly elastic stress-strain behavior. Consequently the values of elastic limit stress (σ_e) and elastic limit strain (ε_e) are reported. The tensile stress that causes the rupture is referred to as tensile strength of the EPS (σ_t). This value along with the maximum tensile strain (ε_t) corresponding to the tensile strength is also reported as an average value for specimens of all groups. The tensile stress-strain behavior of all the specimens are presented in Appendix A. Table 2.2 summarizes the results of the tensile tests in terms of the minimum, maximum and average values of the variables of concern. More detailed results are tabulated and presented in Appendix A. It can be concluded that

Figure 2.15. Tensile rupture in EPS geofoam specimen

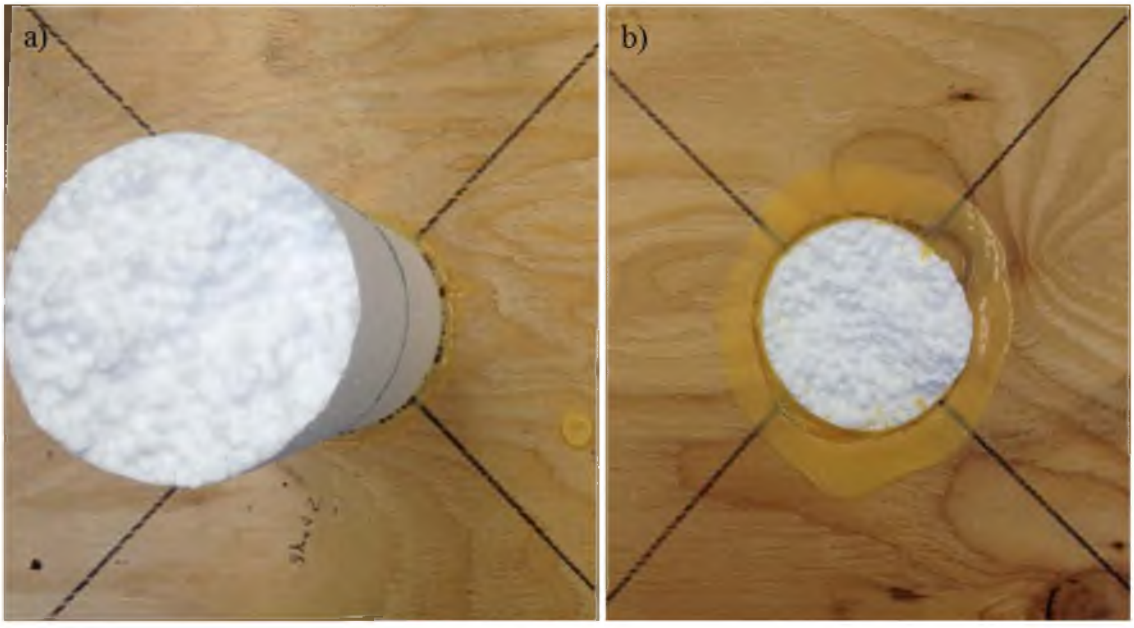

Figure 2.16. Rupture cross section in glued EPS geofoam specimen: a) Top of the specimen and b) Bottom of ruptured piece

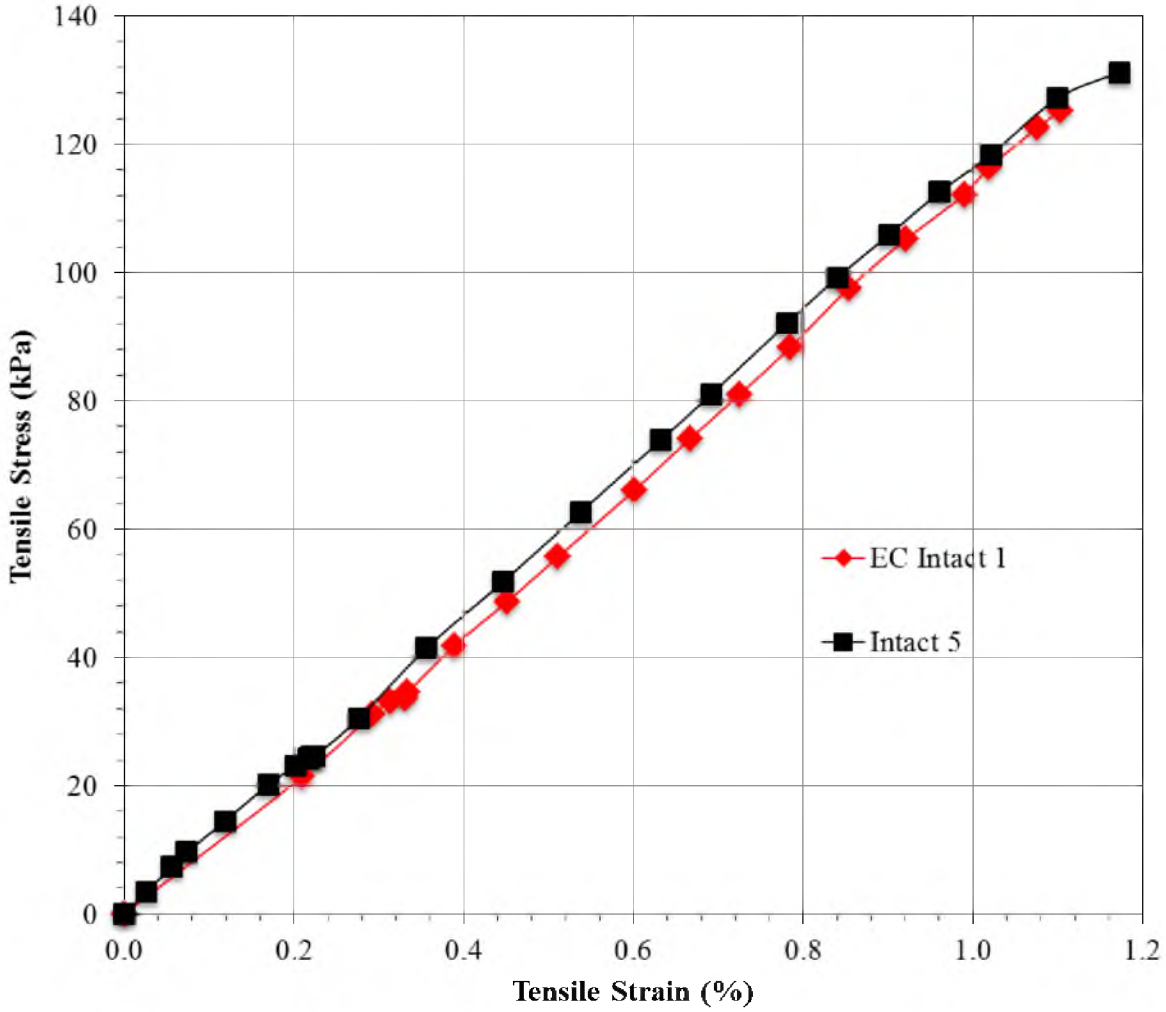

Figure 2.17. Tensile stress-strain behavior of intact and environmentally conditioned EPS specimens

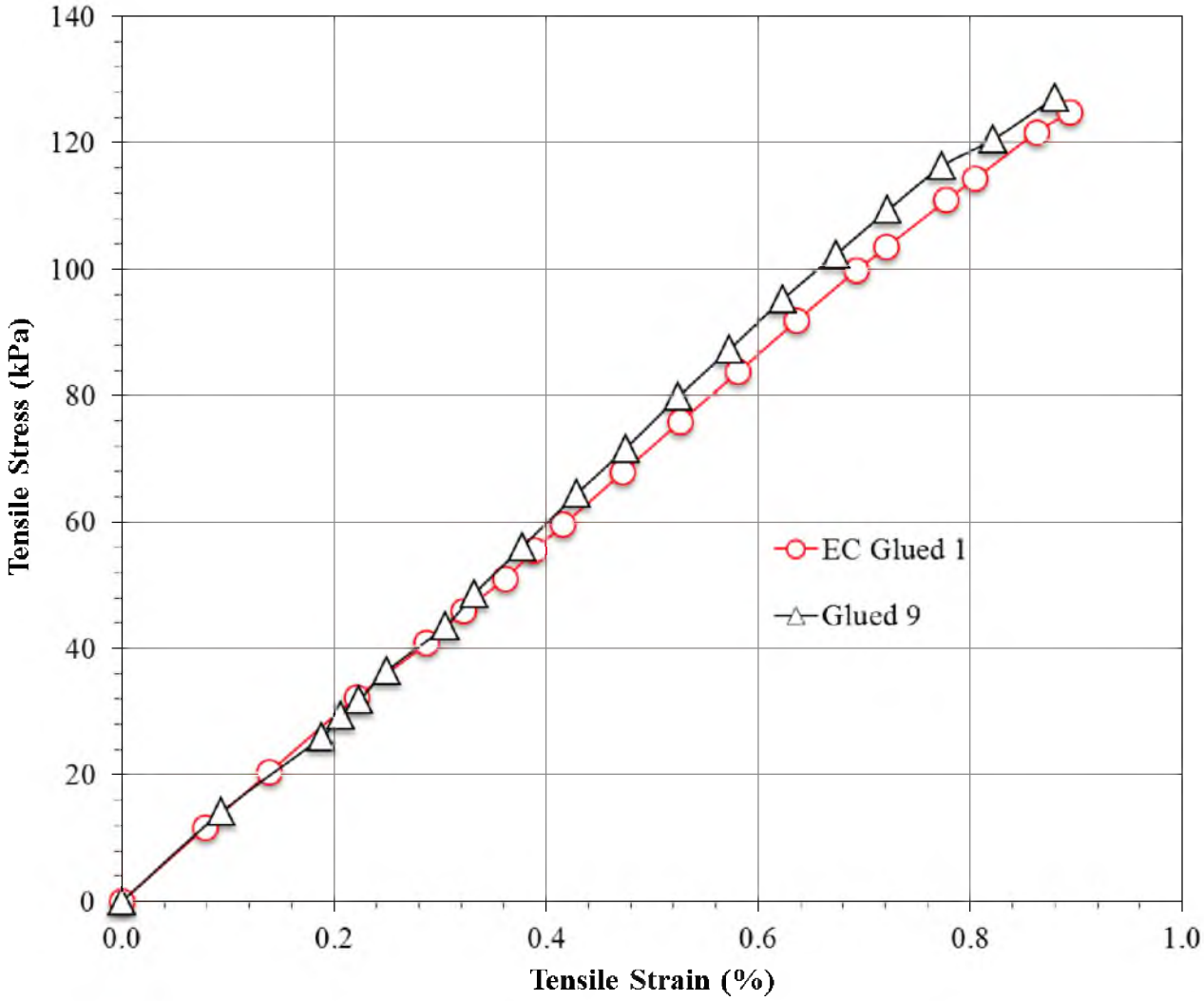

Figure 2.18. Tensile stress-strain behavior of glued and environmentally conditioned EPS specimens

Table 2.2. Summary of tensile test results

Specimen ID	$\varepsilon_{e,min}$	$\varepsilon_{e,max}$	$\sigma_{e,min}$	$\sigma_{e,max}$	$\sigma_{t,min}$	$\sigma_{t,max}$	$\sigma_{t,avg}$	$\varepsilon_{t,avg}$
----------	*(%)*	*(%)*	*(kPa)*	*(kPa)*	*(kPa)*	*(kPa)*	*(kPa)*	*(%)*
INTACT	0.62	1.00	106.7	128.3	131.2	186.3	156.5	1.28
GLUED	0.40	0.99	34.4	135.3	124.3	185.2	159.7	1.27
EC INTACT	0.92	1.00	105.2	108.2	125.3	127.8	126.6	1.14
EC GLUED	0.86	0.90	115.4	121.6	115.4	124.8	120.1	0.90

freeze-heat cycle treatment may have an effect on the EPS specimens as such samples are associated with a lower average tensile strengths as is noticeable in Table 2.2. However, this effect must be further studied by increasing the number of environmentally conditioned specimens subjected to tensile testing as the minimum values of tensile strength associated with conditioned and unconditioned samples do not show a great difference (Table 2.2). The conditioned specimens are associated with similar tensile strains as those of unconditioned specimens. Bonded specimens generally show similar values of tensile strength compared to intact samples regardless of environmental conditioning, further confirming the occurrence of rupture within the EPS material. Intact specimens showed a linear elastic behavior up to 1% strain and a maximum elastic limit stress of 128 kPa. Bonded specimens showed an elastic limit stress of up to 135 kPa at 0.99% strain. The tensile strength varied from 124 to 186 kPa for unconditioned specimens and from 115 to 128 kPa for environmentally conditioned samples.

Conclusions

The results of uniaxial compression, direct shear and uniaxial extension (i.e, tensile) testing of intact and Flexible Fast™ bonded InsulFoam EPS geofoam specimens, some of which were environmentally conditioned through imposing of freeze-heat cycles, show that the Flexible Fast™ adhesive bond has adequate strength to withstand these types of loading. No breakage or failure was observed within the adhesive bond and in all cases the location of failure was determined to be within the EPS material.

The freeze-heat cycle treatment did produce a slight effect on the results of the uniaxial compression tests. Bonded specimens generally show a higher maximum value of compressive strength compared to intact samples. The compressive strength varied from 90 to 118 kPa for intact and 95 to 133 kPa for bonded specimens. The Young's modulus of the EPS geofoam tested was estimated to be around 7 MPa.

For the direct shear results, environmentally conditioned samples showed a cohesive shear strength value 23% higher (about 74 kPa) than that of unconditioned samples (about 60 kPa). This effect may be a result of alteration of EPS cell connections in a way that favors the strength of the material when exposed to shear loading. However, environmental conditioning did not have a substantial effect on the surface of the specimens and therefore did not influence the EPS/EPS coefficient of friction which was calculated to be about 0.70.

While uniaxial extension (tensile) strength values of environmentally conditioned EPS specimens were similar to the minimum values of tensile strength corresponding to unconditioned samples, further investigation is recommended to evaluate the influence of freeze-heat cycle treatment on the tensile strength of EPS geofoam. The tensile strength

varied from 124 to 186 kPa for unconditioned EPS specimens and from 115 to 128 kPa for environmentally conditioned samples. The maximum tensile strain was around 1.3% for unconditioned and about 1.0% for conditioned samples.

CHAPTER 3

INTERLAYER SLIDING OF THE EPS EMBANKMENT

The potential for interlayer sliding between layers of blocks in EPS geofoam embankments is of concern for moderate to high levels of earthquake strong motion (Bartlett and Lawton, 2008). Internal sliding evaluations are required to evaluate the internal stability of an EPS embankment for seismic and other horizontal loadings.

Most studies that address the seismic stability of the EPS geofoam embankment (e.g., NCHRP design guidelines) simplify the complex, layered structure of the embankment to a unified mass by disregarding the horizontal discontinuity between the block layers. However, this study recognizes the presence of such layers and the potential for interlayer sliding upon imposition of the seismic loading.

This chapter is dedicated to investigating the potential of interlayer sliding in EPS geofoam embankment under harmonic loading resulting from both solely horizontal motion and the combination of horizontal and vertical motion. The study was performed by simulating the layered EPS geofoam embankment topped with a typical pavement system using the FLAC computer program. In the study, various amplitudes of harmonic motion were imposed on the embankment systems at its fundamental period.

Only horizontal layers and interfaces were considered at this stage of the study;

vertical interfaces were disregarded, but will be addressed in subsequent chapters. EPS 19, which is commonly used in roadway construction, was chosen for the modeling exercises, the properties of which were obtained in the experimental part of this study. The results of the two-dimensional FLAC simulation were then used to compare the response of a layered EPS geofoam embankment with that of uniform, homogeneous embankment without layers.

In addition, the influence of including the vertical component of harmonic motion in the analysis was also investigated. Therefore, the results of this chapter provide a basis for the potential improvement of the current design guidelines by investigating some of the important assumptions that form the foundation of these guidelines.

Model Development and Properties

A procedure similar to that used in Chapter 1 was followed in order to develop the model to simulate the potential sliding phenomenon within the EPS geofoam embankment. A model similar to that shown in Figure 1.3 was developed with an EPS geofoam body 8 m in height and 20 m in width topped with a 1-m high load distribution slab and pavement system. The foundation soil was not included in the model because the focus of this part of the study is to evaluate the response of the EPS geofoam embankment itself to a known basal motion which includes the local soil response. Also, soil-structure interaction effects are expected to be minimal due to the light weight nature and shallow embedment of the EPS embankment; hence the soil was not included in the numerical model. Nevertheless, disregarding such potential interaction is conservative as discussed in Appendix B. The lowermost boundary of the embankment is fixed in the y

direction and the nodes are "slaved" together in the x direction making this boundary behave rigidly in terms of wave propagation. This type of boundary condition was chosen considering the high impedance ratio between the boundary of the hypothetical foundation soil and the EPS geofoam. For instance, if the foundation soil were to be modeled as medium to medium-stiff clay, similar to the study performed by Bartlett and Lawton (2008), the impedance ratio would be extremely high for the waves propagating down through the EPS geofoam embankment and reflecting from the boundary of soil and EPS. Thus, the stress amplitude of the reflected wave would be a large portion of the incident wave as discussed in Kramer (1996). No boundary condition is assigned to the vertical sides of the EPS embankment system, accommodating free movement of the embankment in both the horizontal and vertical direction. The elastic material properties presented in Table 1.1 were incorporated in the model. However, horizontal interfaces were required between the EPS blocks to estimate the potential for interlayer sliding. It should be noted that such interlayers are neglected in existing seismic design guidelines. FLAC provides interfaces that are characterized by Coulomb sliding and/or tensile separation where interface properties such as friction, cohesion, dilation, normal and shear stiffness, and tensile strength are assigned. The choice of interface type and properties is critical for this part of study; therefore it is necessary to provide a brief background on the characteristics of interfaces in FLAC.

Interfaces

As shown in Figure 3.1, an interface is represented by normal and shear stiffnesses that act between the two contacting planes. As indicated in the user's manual

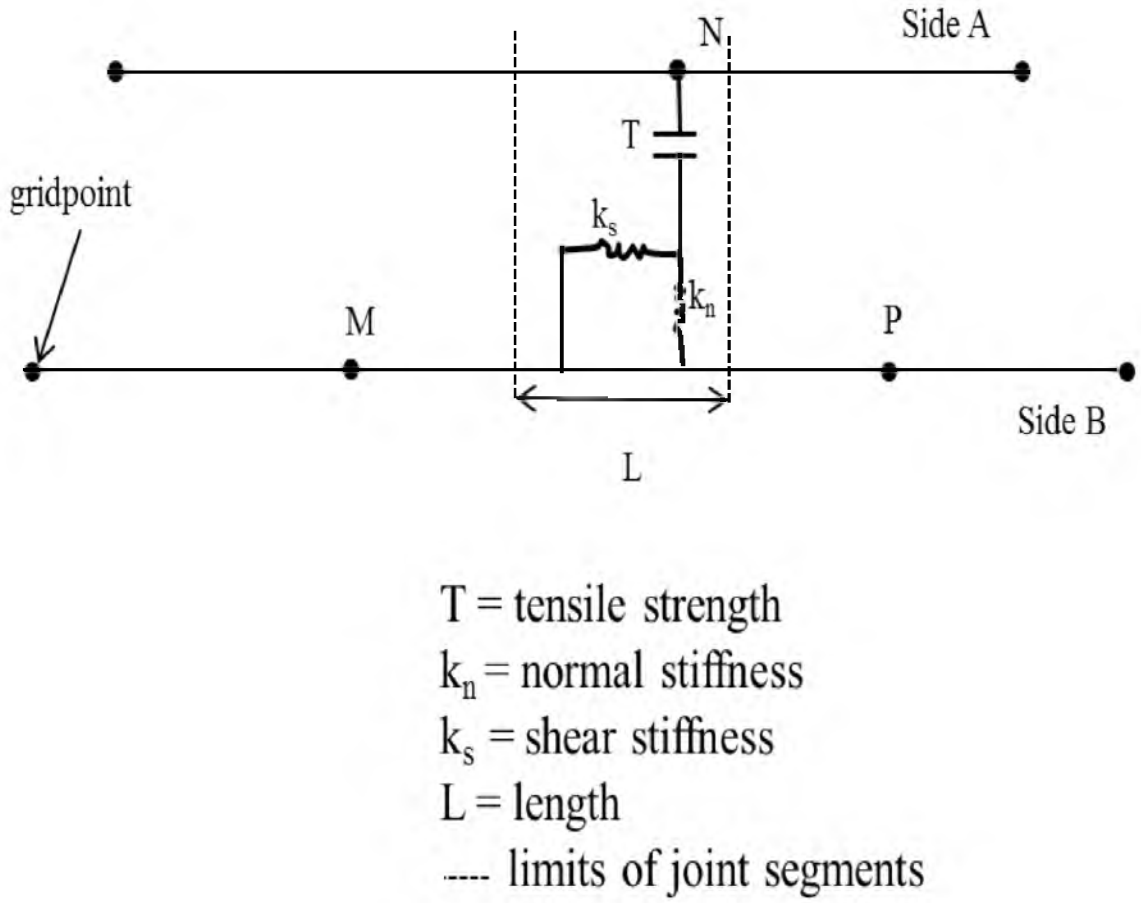

Figure 3.1. An interface represented by sides A and B, connected by shear (k_s) and normal (k_n) stiffness springs (modified after Itasca, 2005)

(Itasca, 2005), FLAC uses a contact logic, which is similar in nature to that employed in the distinct element method, for either side of the interface.

A list of the gridpoints that lie on each side of any surface is stored in the FLAC code. Each gridpoint is then checked for contact with its closest neighboring point on the opposite side of the interface. For instance, as shown in Figure 3.1, gridpoint *N* is checked for contact on the segment between gridpoints *M* and *P*. In case of contact, the normal vector, to the contact gridpoint, *N*, is computed. Contact length, *L*, is half the distance to the nearest gridpoint to the left of *N* plus half the distance to the nearest

gridpoint to the right. Thus, the entire interface is divided into contiguous segments, each controlled by a gridpoint. During each timestep the velocity and consequently the incremental displacement for each gridpoint is determined. The incremental relative displacement vector at the contact point is resolved into the normal and shear directions, and total normal and shear forces are determined by:

$$F_n^{(t+\Delta t)} = F_n^{(t)} - k_n \Delta u_n^{(t+1/2t)} L \tag{3.1}$$

$$F_s^{(t+\Delta t)} = F_s^{(t)} - k_s \Delta u_s^{(t+1/2t)} L \tag{3.2}$$

where k_n and k_s are the normal and shear stiffnesses with the units of stress/displacement; and Δu_n and Δu_s are normal and shear displacements, respectively. Three types of interface are available in FLAC:

1. Glued Interfaces: No slip or opening is allowed in glued interfaces, but elastic displacement still occurs, according to the given stiffnesses.

2. Coulomb Shear Strength: The Coulomb shear-strength criterion limits the shear force by a maximum force that depends on cohesion along the interface, effective contact length, and the friction angle of interface surfaces.

3. Tension Bond: While normal tensile stress is smaller than bond strength of the interface, the interface acts as if it is glued otherwise separation and/or slip can occur.

The value of shear stiffness should be obtained from laboratory testing. In order to

eliminate the potential for specimen size effects, the large scale EPS block sliding test results obtained by Barrett (2008) were used. In these tests, large block sliding shear tests were completed with a computer controlled actuator on 1200 mm x 600 mm x 300 mm EPS specimens under normal pressures of 9 kPa, 18 kPa and 27 kPa. The shear stress-horizontal displacement relationships were provided by Barrett (2008) as a result of the experimental study (Appendix C). Shear stiffness corresponding to EPS/EPS sliding was back calculated from these results (i.e., the slope of the stress-displacement line). Figure 3.2 shows the relationship of the EPS/EPS interface shear stiffness (back-calculated from Barrett (2008) experimental results) and applied normal stress. Based on this figure, the value of the EPS/EPS interface shear stiffness is 2.6 MPa at a normal

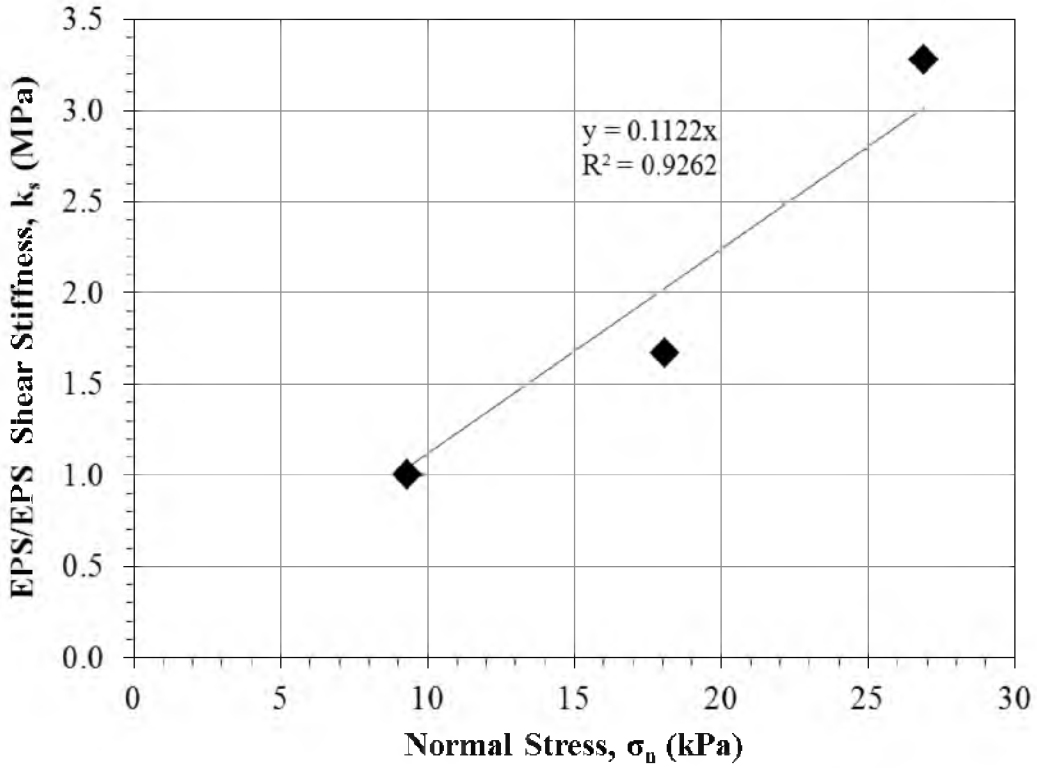

Figure 3.2. EPS/EPS shear stiffness relationship with normal stress (based on Barrett's (2008) experimental results)

stress of 23 kPa, which is a typical normal stress used in this study and resulting from the weight of the pavement section and EPS.

To further verify and model the back-calculated shear stiffness values shown in Figure 3.2, a direct shear test was simulated in FLAC. In this simulation, two EPS blocks having the same dimensions and density as those used in Barrett's test were subjected to horizontal sliding. The values of back calculated shear stiffness were applied at corresponding normal stresses. Figures 3.3, 3.4 and 3.5 show the relationship of the shear stress (Pa) and displacement (m) for normal stresses of 9 kPa, 18 kPa and 27 kPa, respectively. Based on these simulations, the selected shear stiffness relation used for the FLAC modeling produces results similar to those of Barrett's experimental study with a reasonable level of accuracy. The FLAC code developed for these sliding simulations is presented in Appendix C.

The normal stiffness of the interface is equal to the apparent stiffness (expressed in stress-per-distance units) of a zone in the normal direction. This normal stiffness is defined as: $(K + 4/3\,G)/\Delta z_{min}$ according to the FLAC manual (Itasca, 2005). The values of K and G are the bulk and shear moduli, respectively; and Δz_{min} is the smallest width of an adjoining zone in the normal direction. In this case, shear stiffness properties have been derived from tests on geofoam block with suitable scale to account for potential size effects; hence the normal stiffness will also be calculated from the EPS physical properties given in Table 1.1.

Other required interface properties include: interface friction, cohesion, tensile bond strength, and dilation. Values of zero cohesion and dilation were assigned at the interfaces. The tensile bond strength was also assigned as zero because the lack of tensile

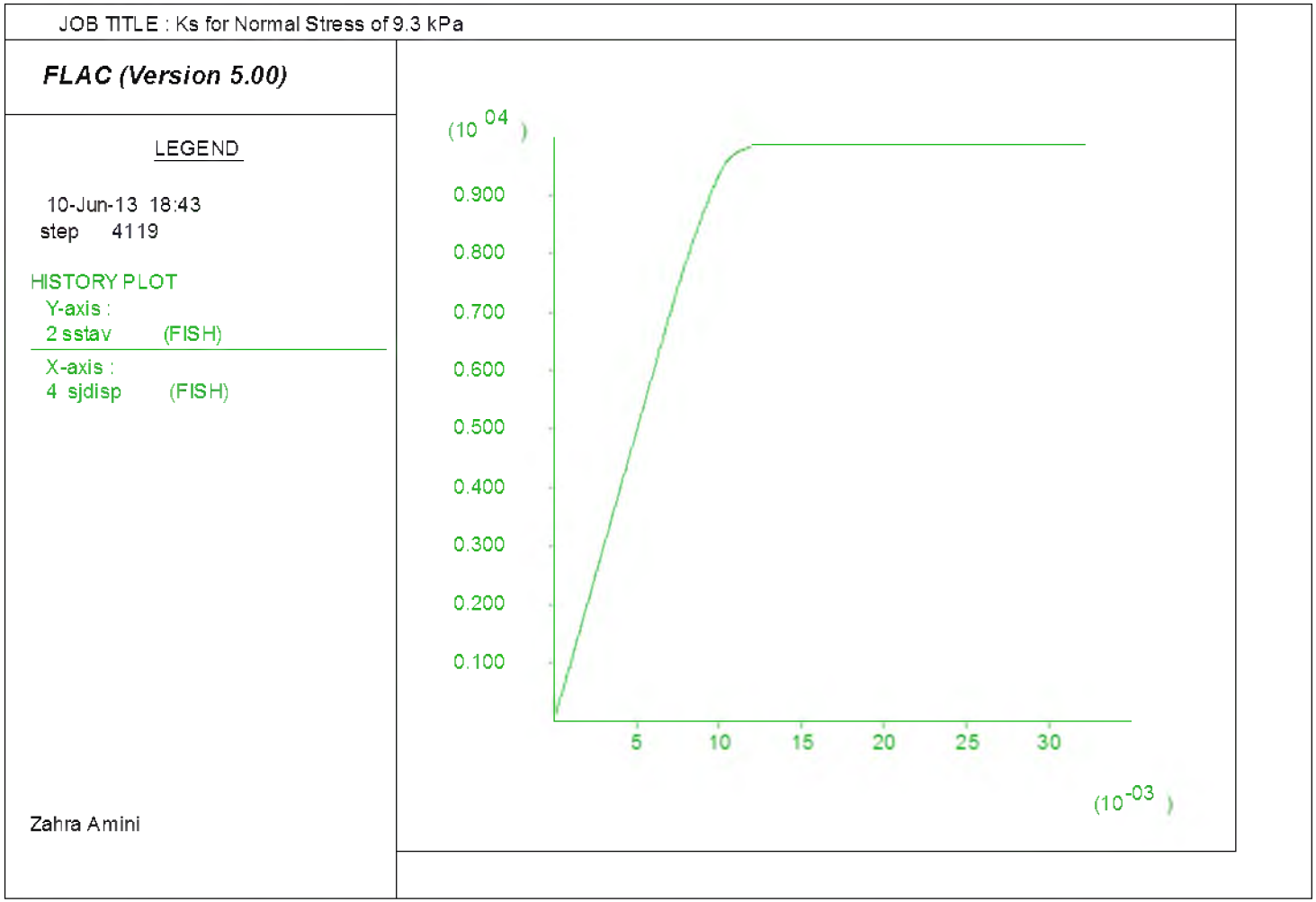

Figure 3.3. Shear stress-displacement of EPS/EPS sliding under normal stress of 9 kPa simulated in FLAC

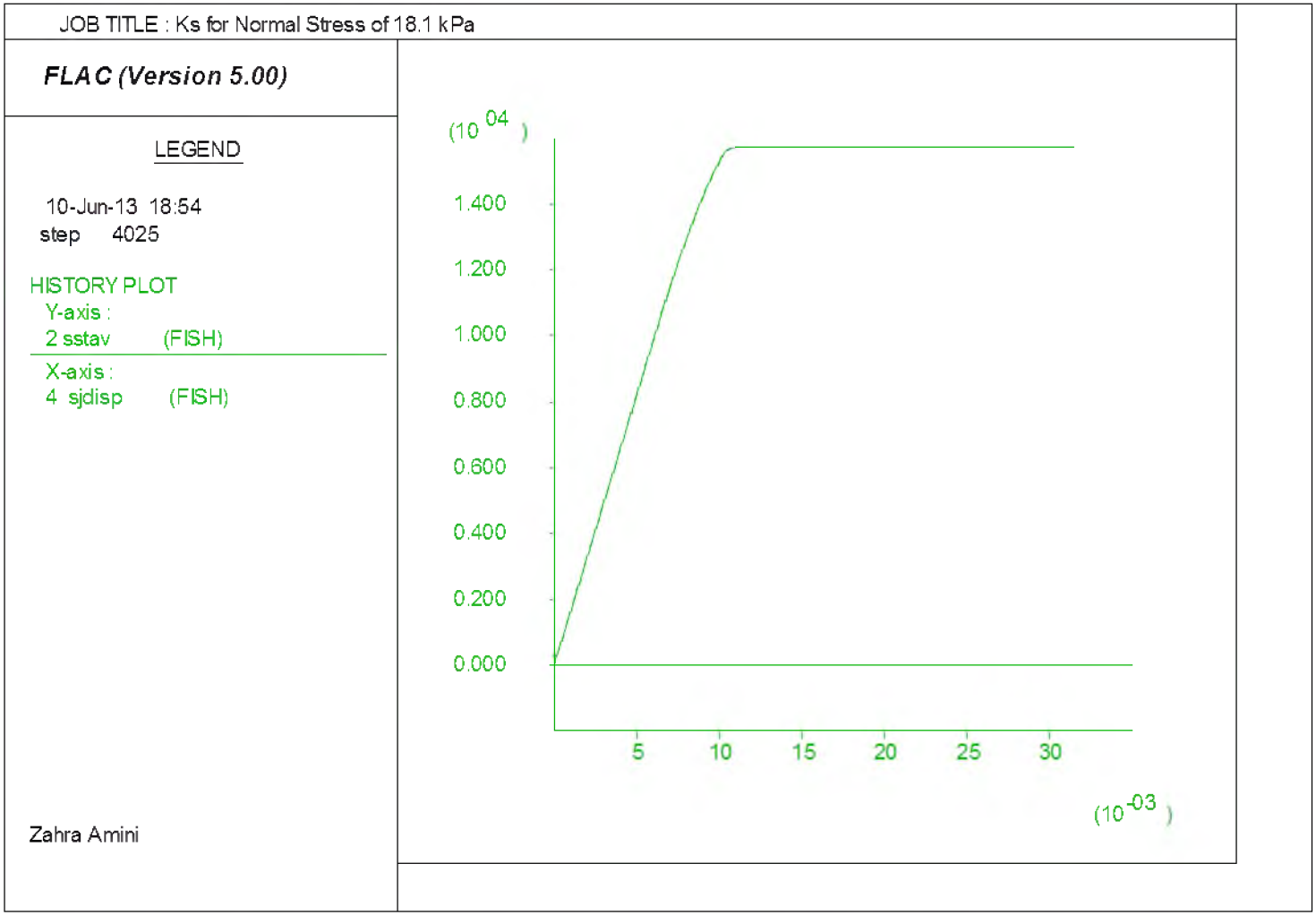

Figure 3.4. Shear stress-displacement of EPS/EPS sliding under normal stress of 18 kPa simulated in FLAC

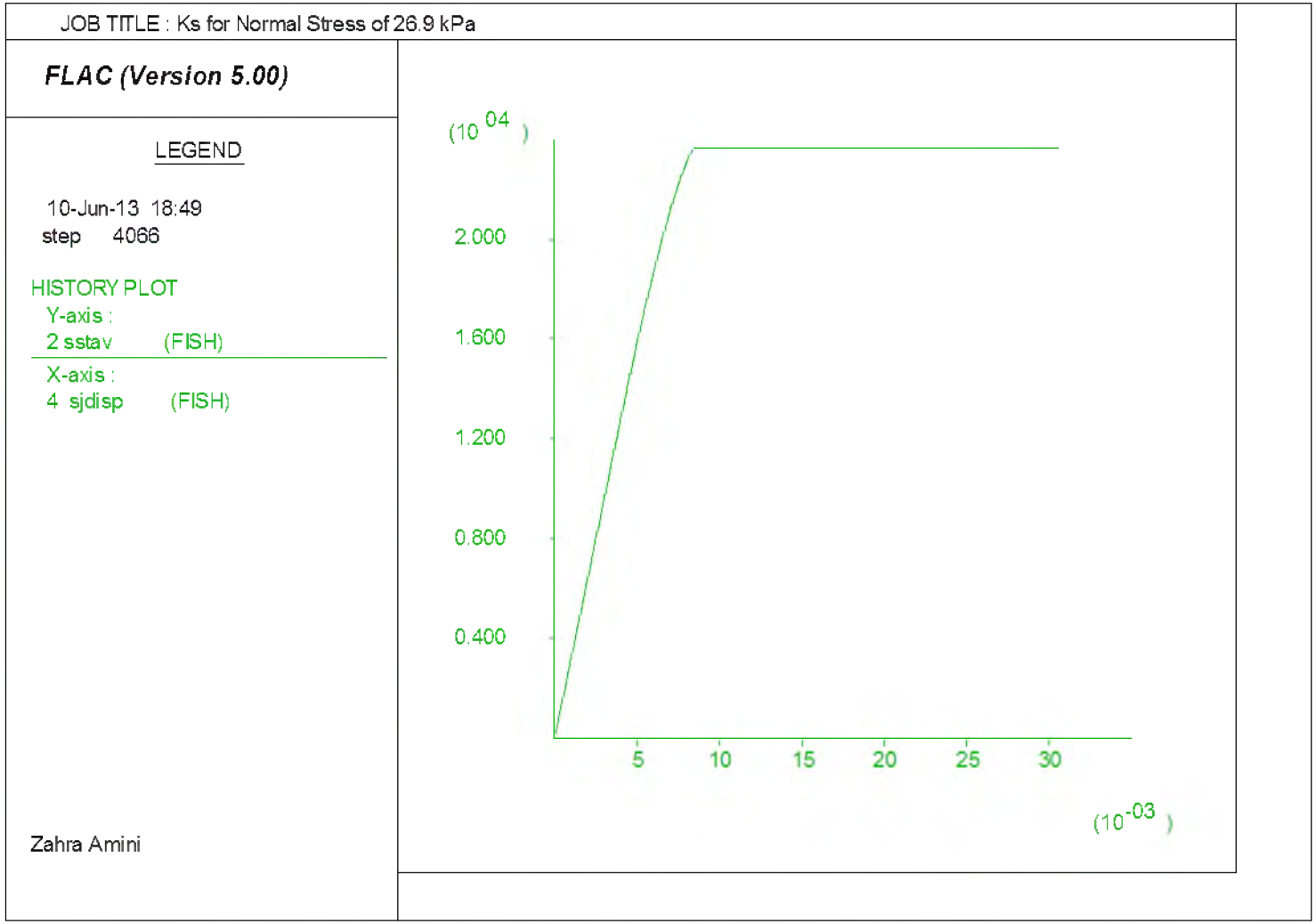

Figure 3.5. Shear stress-displacement of EPS/EPS sliding under normal stress of 27 kPa simulated in FLAC

bond strength allows for separation between the geofoam layers during excitation. The interface (sliding) friction angle was assigned as 41 degrees, which is the peak friction angle at 23 kPa normal stress based on large EPS block sliding tests results (Barrett, 2008). It is noteworthy that because the initiation of sliding is being addressed by this part of the study, the use of peak values of interface friction angle is more applicable than the use of residual values. Moreover, the barbed plates, which may be placed between EPS geofoam blocks during construction, are not considered a significant source of sliding resistance due to their relatively small size (Barrett and Valsangkar, 2009) and were not incorporated into these analyses. Finally, only sliding friction was used at the interface of the uppermost layer of EPS and the lumped mass representing both the load distribution slab and pavement section. However, in practice the concrete load distribution slab is usually poured directly atop the geofoam, resulting in bonding at this interface that has some amount of tensile and shear capacity (Bartlett and Lawton, 2008). Nonetheless, the assumptions made for these analyses are conservative in that they disregard any additional strength from gripper plates or concrete bonding. Figure 3.6 illustrates FLAC model developed for this stage of the study incorporating the interfaces between the EPS blocks.

The presence of horizontal layer interfaces in the numerical model does affect the dynamic behavior of the numerical model compared to the homogeneous, intact mass case when excited by horizontal waves. This is true, even before sliding is initiated at the interface due to elastic shear displacement that occurs parallel to the interface as governed by the assigned value of the interface shear stiffness k_s. The behavior of layered EPS mass with interface properties will be further evaluated in Chapter 4.

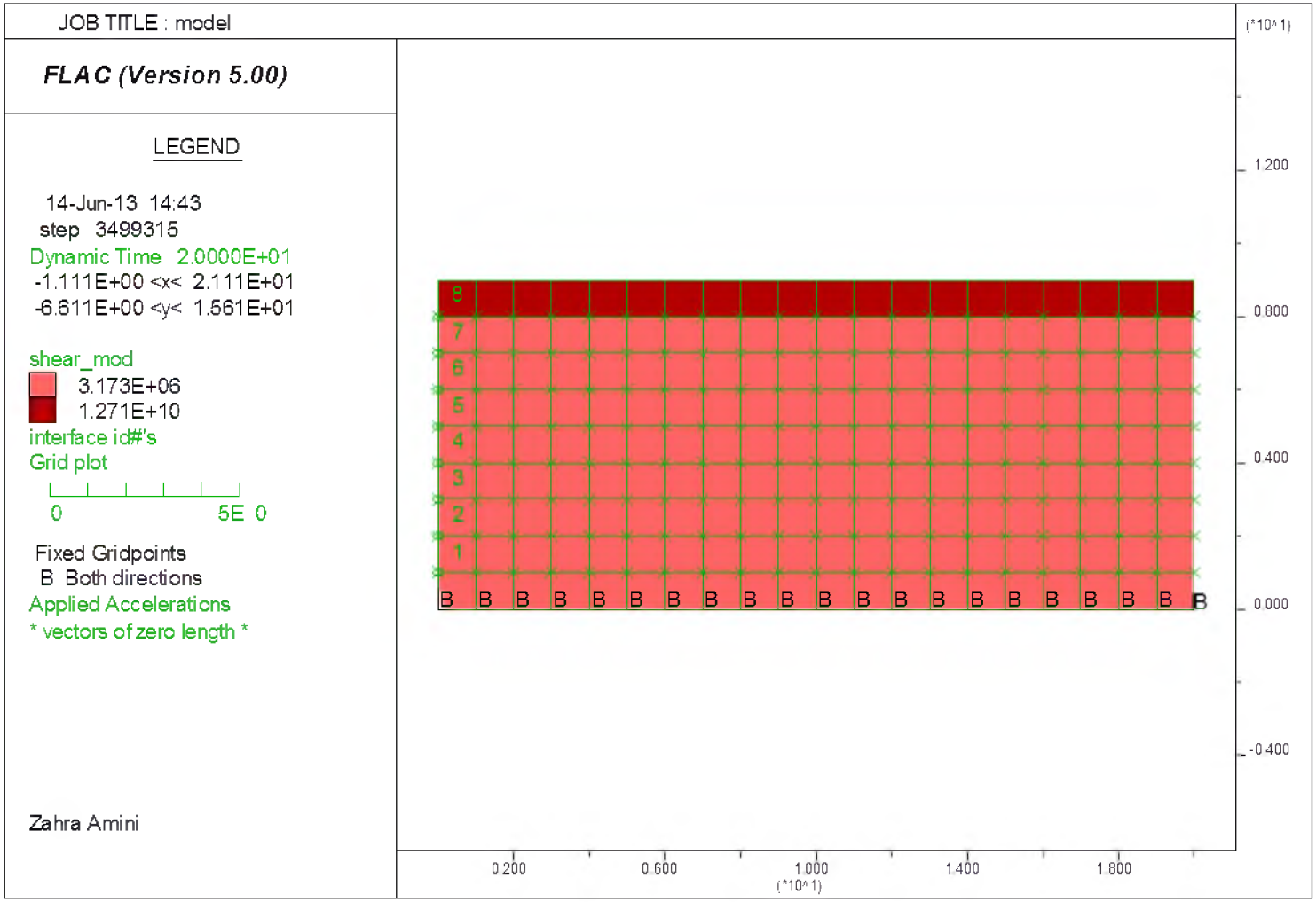

Figure 3.6. Twenty meter wide and 8 m high EPS embankment FLAC model including horizontal interfaces

Lastly, to check the behavior of the numerical algorithm of FLAC with glued interfaces present, a parametric study was done to see if a model with glued interfaces could produce the same results as the homogenous (no layer) case. It is anticipated that some layers in the subsequent modeling may be "gluded" together to represent a potential remedial strategy for the EPS embankment. The gluing will be accomplished using a commercial adhesive (Chapter 2) and "gluing" of an interface in the numerical model will be done to represent this remediation in subsequent chapters of this dissertation.

To represent gluing, the values of k_n and k_s need to be arbitrarily increased so they no longer play a role in the dynamics of the system. The FLAC manual suggests that for cases where the real interface properties are unknown but slip and separation is desired, stiffness values be set to ten times the apparent stiffness of a zone in the normal direction $[10(K + 4/3\,G)/\Delta z_{min}]$ in order to develop stiff, artificial interfaces.

To test this recommendation, the interfaces were glued (in order to prevent sliding) while the shear and normal stiffness values were increased. By doing so, the glued interface while still present, does not provide a discontinuity to accommodate slip and separation; rather, it serves as an artificial device to connect two subgrids together. However, it will still allow for elastic deformation at the interface associated with preslip or preseparation behavior as governed by the values of k_n and k_s assigned to the interface.

A trial and error process was used to test the numerical behavior of the glued interfaces. In this test, embankment models with and without glued interfaces were subjected to the same harmonic motion in the horizontal direction. The selected motions were associated with acceleration amplitudes of 0.1 g and 0.5 g and were applied at the

fundamental period of the embankment (i.e., 0.6 s). The results in Figures 3.7 and 3.8 show the acceleration response of EPS geofoam embankments without interfaces and with glued interfaces, respectively, to 0.1 g amplitude base motion. Each figure presents the acceleration values at midwidth of the embankment and at the bottom of each layer with the base marked as point 1 and the top of the pavement system as point 18 in the figure legend. The acceleration response was captured within the first 5 s of motion.

Figures 3.9 and 3.10 illustrate very similar acceleration response plots corresponding to an input base motion with amplitude of 0.5 g. The comparison of acceleration response of embankment with no interface and embankment with glued interfaces confirms that presence of glued interfaces in the model does not alter the fundamental dynamics of the system, if the values of k_n and k_s are increased to 50 times their real values. Thus it was determined that recommendation of the FLAC of ten-fold increase of the glued interface stiffness properties still leads to some energy loss (i.e., some amount of damping) in the system, and such energy loss decreases the amplitude of the harmonic response. However, when k_n and k_s were increased to 50 times their real values, this value was found to be appropriate in terms of energy conservation and numerical stability. This finding will be used later in the dissertation when potential remediation of sliding by gluing is introduced in the numerical modeling.

Interlayer Sliding Analysis

The potential for interlayer sliding is perhaps the most significant potential performance issue for EPS embankments undergoing earthquake shaking. This is because potential continuous horizontal sliding planes are created in most EPS embankments due

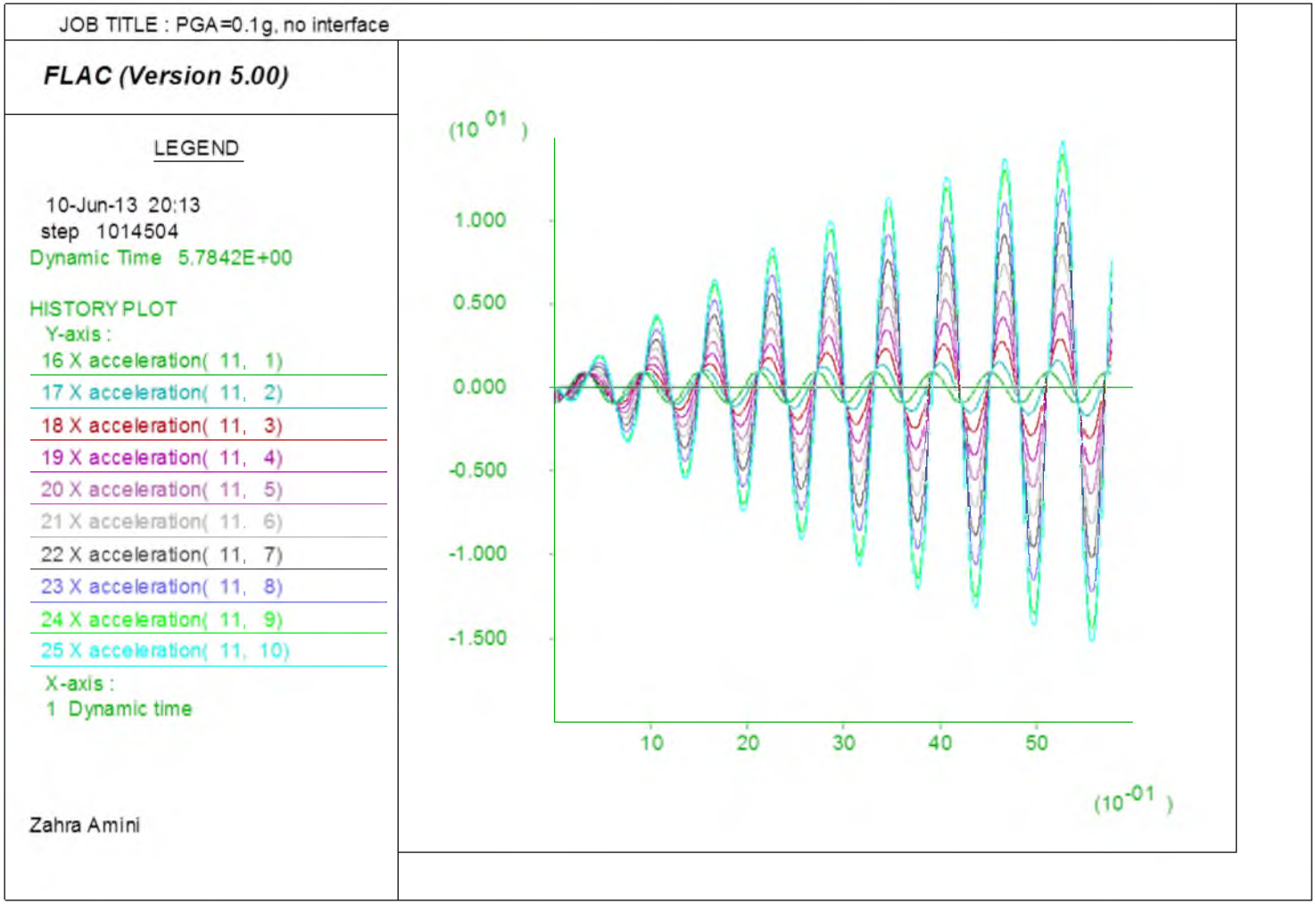

Figure 3.7. Response acceleration of EPS embankment without interfaces due to 0.1g amplitude input motion

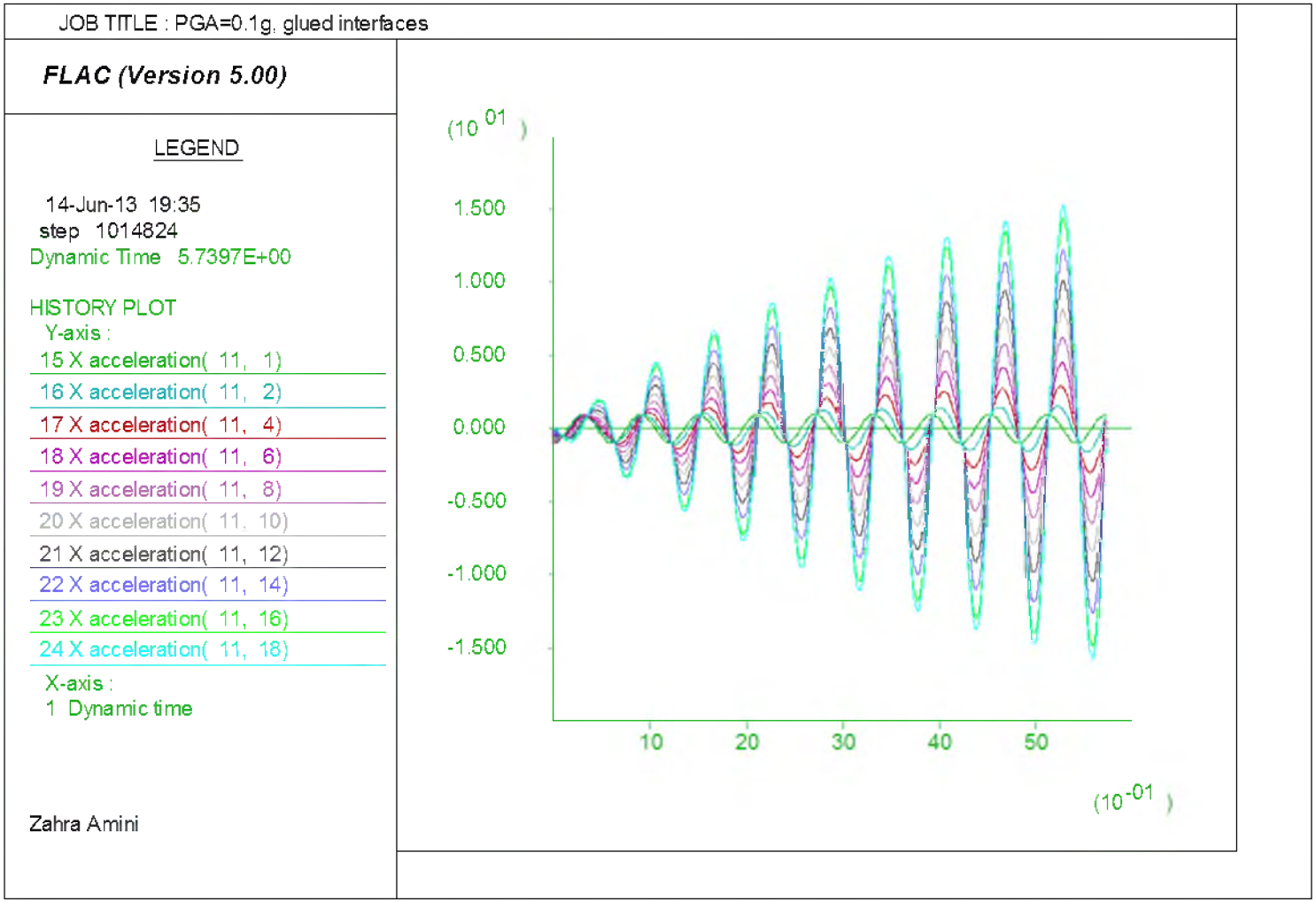

Figure 3.8. Response acceleration of EPS embankment with glued interfaces due to 0.1g amplitude input motion

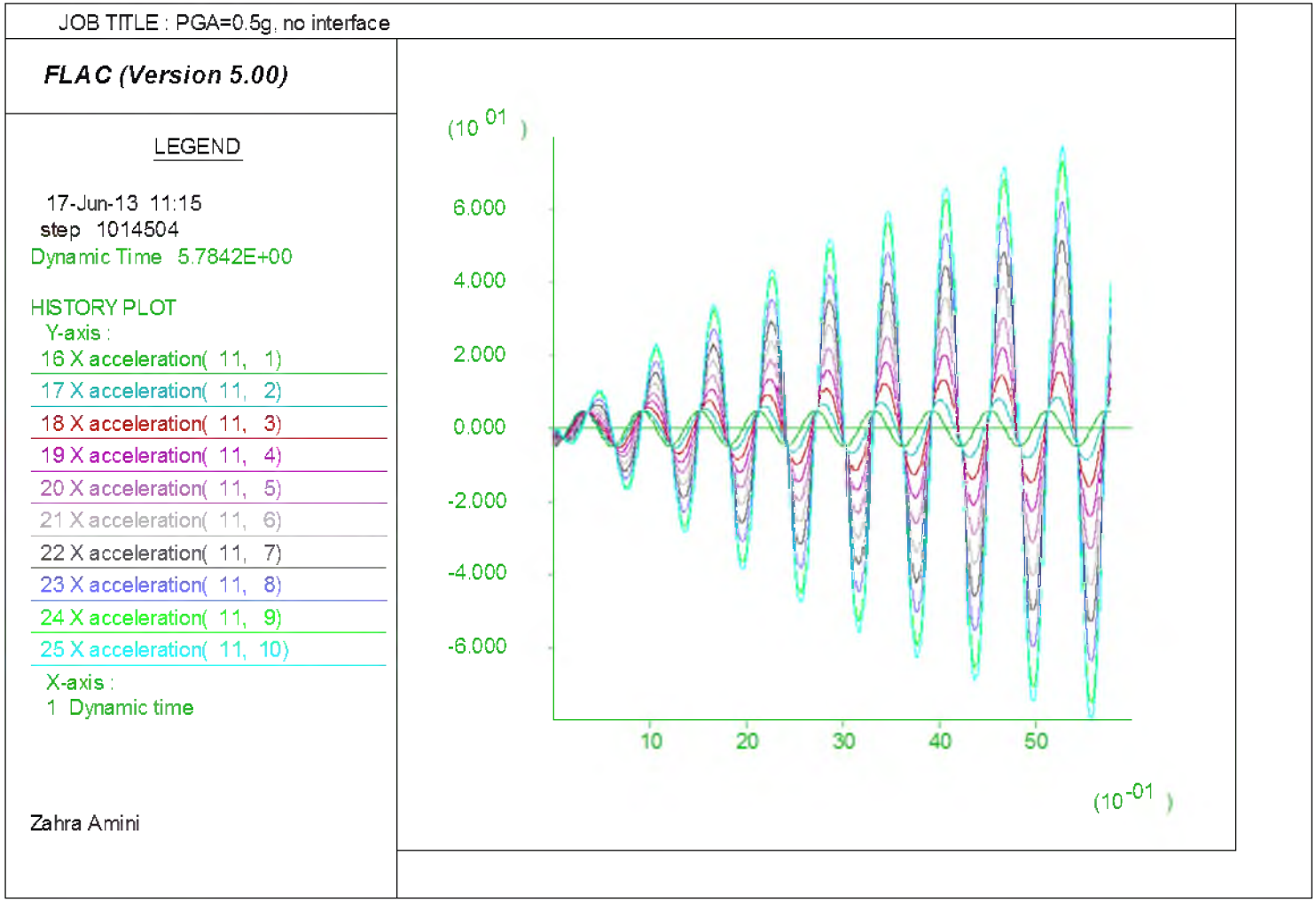

Figure 3.9. Response acceleration of EPS embankment without interfaces due to 0.5g amplitude input motion

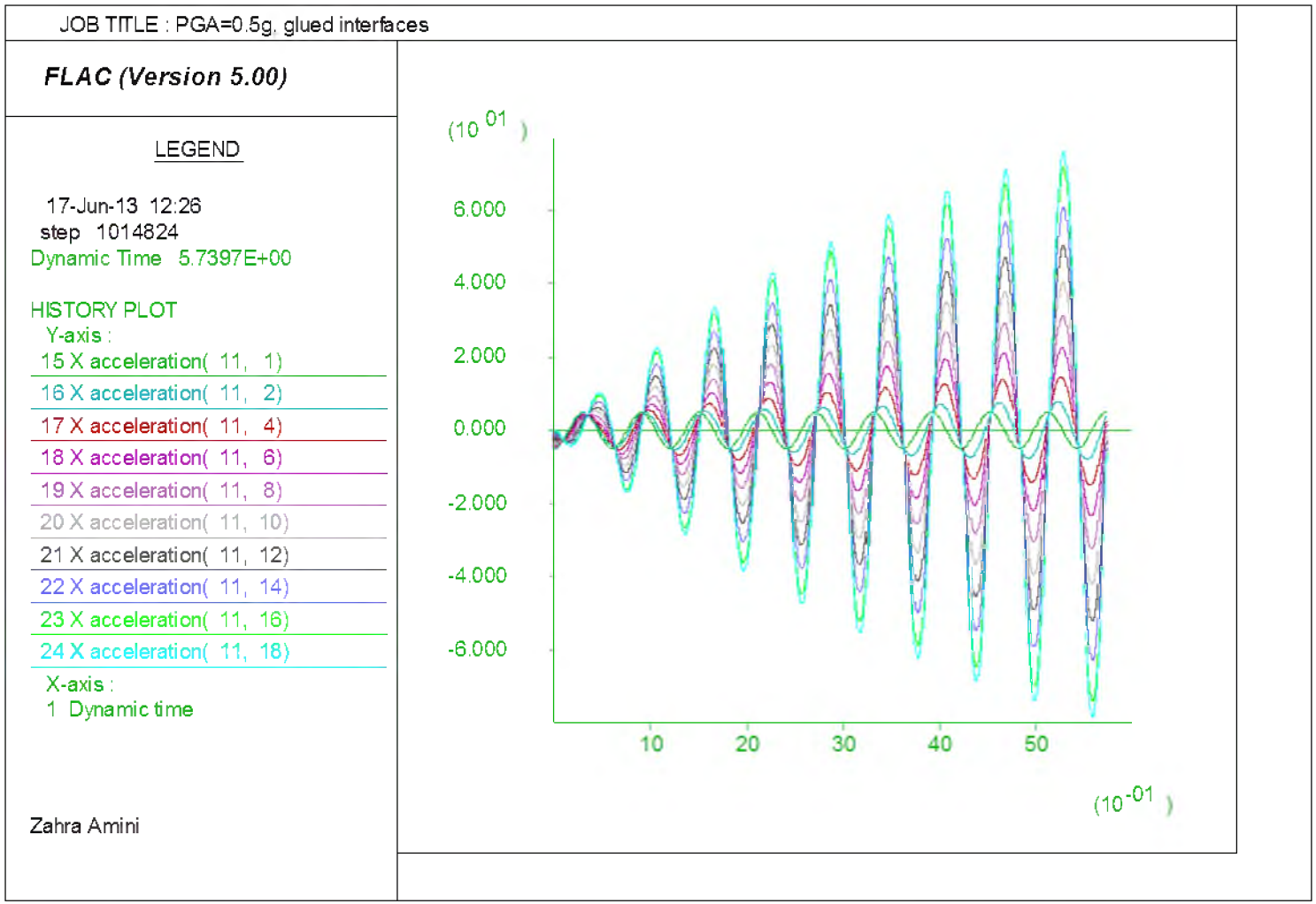

Figure 3.10. Response acceleration of EPS embankment with glued interfaces due to 0.5g amplitude input motion

to block placement procedures used in current construction practice. Therefore, the focus of this part of the study is to determine if interlayer sliding occurs under cyclic loading and when and where in the embankment it is initiated. The focus of this study is on the initiation of sliding and not estimating the final amount of sliding. For the purposes of this study, sliding will be considered as "initiated" when the combination of elastic deformation and sliding at any given interface exceeds 1 inch (i.e., 2.5 cm).

Knowledge of dynamic response type (elastic or plastic, linear or nonlinear) and the associated damping is required to model the interlayer sliding phenomenon. The interlayer sliding analysis was started based on the hypothesis that interlayer sliding is initiated while the EPS blocks within the embankment are primarily in their elastic state (i.e., before significant yielding or plastic behavior has occurred). If this is true, then the model properties for the EPS geofoam could be developed using elastic properties and a small amount of damping consistent with the shear strains that develop with the embankment.

To test this hypothesis, the EPS geofoam embankment models with horizontal interfaces for each layer were excited with horizontal harmonic motions of various amplitudes of 0.5 g, 0.6 g, 0.8 g and 1 g. For these analyses, elastic properties were applied with a constant damping ratio of 2%, which was applied as Rayleigh damping at the fundamental period of the embankment. This value of damping was chosen in accordance with the results of torsional resonant column tests and cyclic uniaxial tests on block-molded EPS geofoam specimens under zero confining pressure published by Athanasopoulos et al. (1999). The 2% damping is associated with the upper ranges of torsional resonant column test results and lower ranges of cyclic uniaxial test results at

1% shear strain.

The results of the analyses described above were closely monitored to determine when sliding was initiated between the EPS layers. Following this, the embankments with no interfaces were also subjected to the same base motion; however, Mohr Coulomb conditions were applied to the model to check for potential yielding. This latter set of tests was conducted to determine the state of the model (i.e., elastic or yield) at the time sliding was initiated.

To apply the Mohr Coulomb model in FLAC, properties such as cohesion, friction, dilation and tension were also required in addition to the elastic moduli. The values of friction and dilation were set to zero; whereas cohesion and tension values for the EPS block were assigned as 60 kPa and 158 kPa, respectively, as obtained from the laboratory testing results presented in Chapter 2. Table 3.1 summarizes the Mohr Coulomb properties and the interface properties used in these analyses.

The duration of shaking was set to be equal or greater than the time sliding was initiated in the models incorporating interfaces. Sliding was measured by calculating the relative displacement at each interface. A time history of relative displacement for each interface was recorded along a vertical centerline in the embankment model where the relative displacement was computed by differencing the displacement of the gridpoint on the lower side from that of the gridpoint on the upper side of the interface located on the vertical axis of the embankment. Figure 3.11 shows the time history of sliding at each interlayer for input amplitude of 0.6 g. The y axis represents amount of sliding in meters and the x axis represents time in seconds. As shown in this figure, sliding in the order of a few centimeters begins at less than about 0.5 s.

Table 3.1. Mohr Coulomb properties of the EPS and EPS/EPS interfaces

	Cohesion	Friction Angle	Dilation Angle	Tensile Strength	Shear Stiffness	Normal Stiffness
	MPa	Degree	Degree	MPa	MPa	MPa
EPS	0.06	0	0	0.16	---------	---------
Interfaces	0	41	0	0	2.6	7.2

The data in Figure 3.12 illustrates the state of the embankment model after one cycle (i.e., 0.6 s) of input motion was applied to the model. It is apparent that the majority of the model is still in the elastic range and only a small portion of the EPS material located at the corner of the embankment has yielded during the shaking. A similar condition was also observed in the case of other input motion amplitudes and the results are presented in Appendix C. Therefore, it is confirmed that the hypothesis is true, interlayer sliding is initiated when the EPS geofoam embankment is still in the elastic range. Thus, is recommended that sliding analysis be performed incorporating the elastic material properties, and a constant damping ratio value appropriate for the level of strain developed before sliding, as determined from a laboratory test program, or from relations published in the literature.

Harmonic Input Motion

Most of the studies on dynamic behavior of the EPS geofoam embankment focus solely on the horizontal component of ground motion and simply disregard the effects of

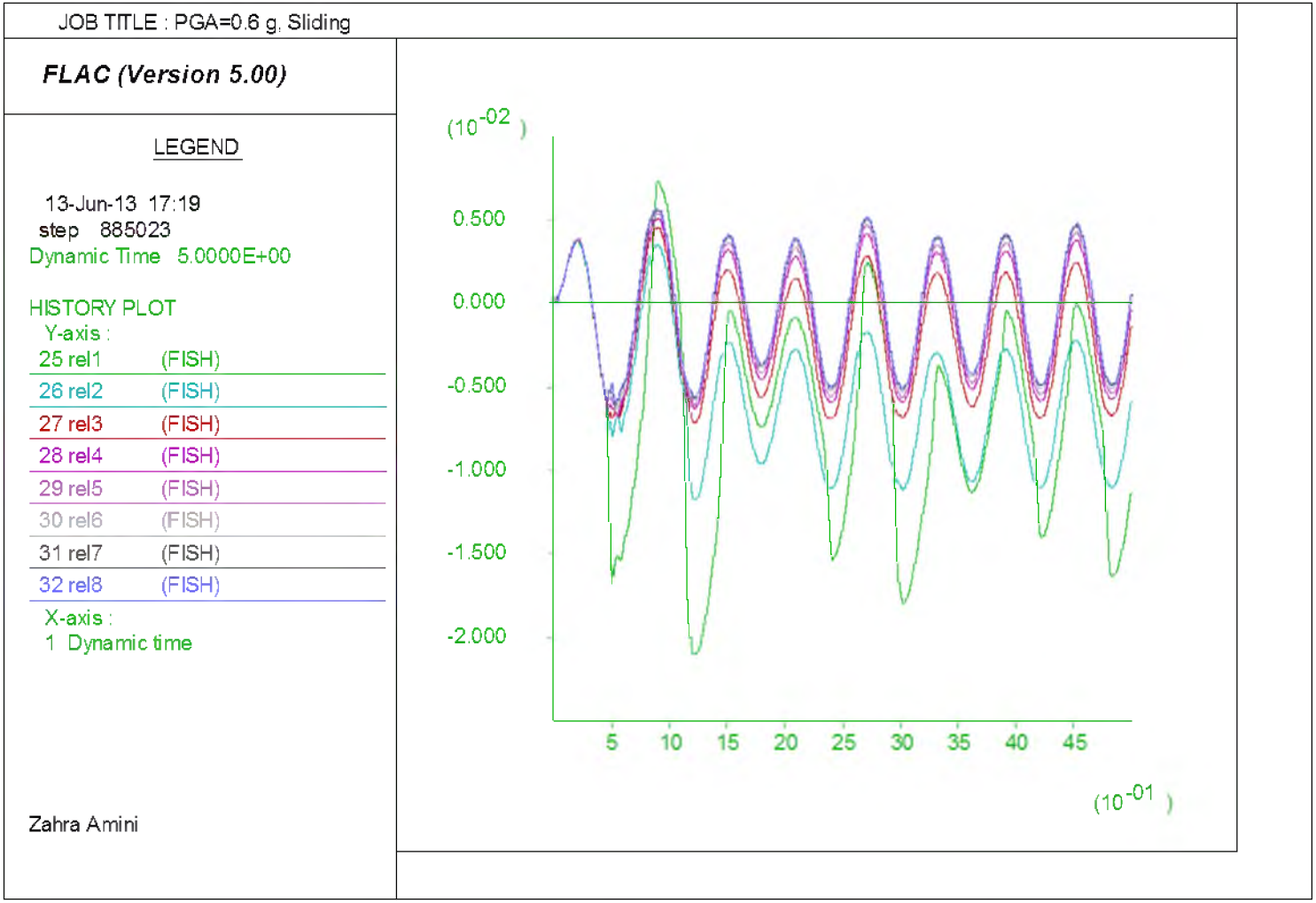

Figure 3.11. Interlayer sliding within the EPS embankment due to 0.6g amplitude horizontal input motion

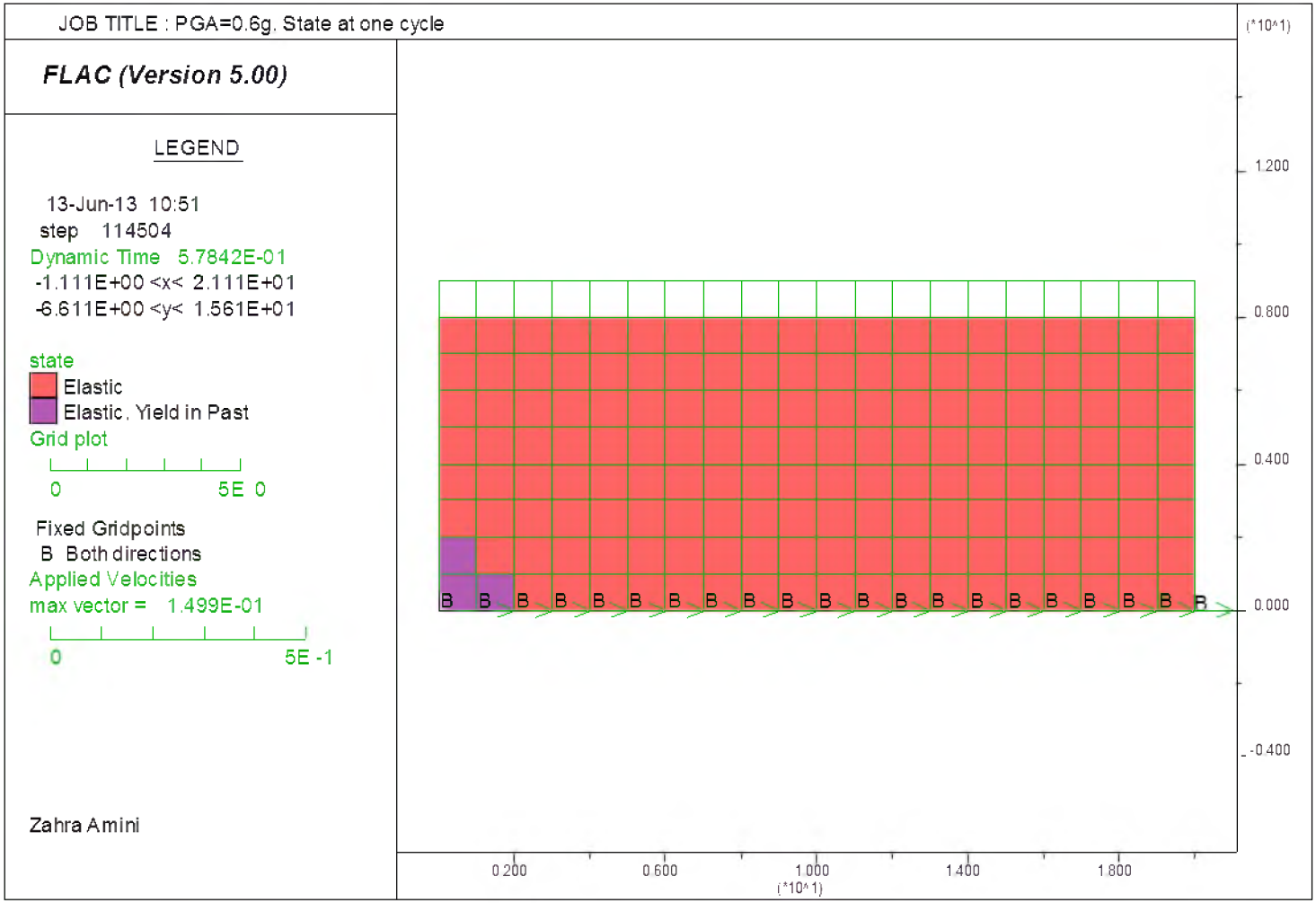

Figure 3.12. state of the EPS embankment after one cycle of 0.6g amplitude horizontal input motion

the vertical component. However, a modeling study performed by Bartlett and Lawton (2008) on the EPS geofoam embankment used the vertical component of strong ground motion as well as the horizontal component. This study concluded that neglecting the vertical motion of the seismic loading may not be conservative. This study further investigates the dynamic behavior of the EPS embankment geofoam under horizontal and vertical loading to determine the effect(s) that the vertical component has on interlayer sliding.

Horizontal Input Motion

A sinusoidal wave was applied at the base of the EPS embankment in the horizontal direction. In the first set of analyses, various acceleration amplitudes of 0.5 g, 0.6 g, 0.8 g and 1 g were applied at the fundamental period of the embankment. For these cases, no vertical motion was applied and the results of the analyses were obtained in terms of horizontal interlayer sliding throughout the embankment.

Vertical Input Motion

The frequency at which the vertical motion is most effective can be calculated using the following equation that applies to a cantilever beam exposed to a force perpendicular to its cross section.

$$f = \frac{1}{2\pi}\sqrt{\frac{k}{m}} \tag{3.3}$$

where $k = EA/L$ is the stiffness and m is the mass of the embankment. Using the parameters defined in Chapter 1 f can be calculated as 3.09 Hz, which gives a period of 0.32 s. In order to check this in FLAC a trial and error procedure similar to that discussed in Chapter 1 was followed. A harmonic wave was applied at the base of the embankment model without interfaces at different frequencies and the acceleration response was monitored within the embankment and at the top. Figure 3.13 shows the vertical acceleration at the top due to a vertical harmonic motion with amplitude of 0.1 g applied at a period of 0.32 s. Damping was not applied to the model. This period was shown to be the most vertical period therefore the vertical input motion was applied at a period of 0.32 s in the study thereafter.

Input Motion with Horizontal and Vertical Components

To study the effect of both horizontal and vertical components of ground motion on interlayer sliding both motions were applied at the base of the EPS geofoam embankment model with horizontal interfaces. Two sinusoidal waves were imposed to the model: one in the horizontal direction at a period of 0.6 s and one in the vertical direction at a period of 0.32 s. The horizontal input motion was characterized with amplitudes of 0.5 g, 0.6 g, 0.8 g and 1 g. However, in reality both components of ground motion are not likely to simultaneously be associated with the peak ground acceleration value, therefore the acceleration amplitude of the vertical component of the input motion was set to 40% of the horizontal wave amplitude for each case (ASCE, 1987).

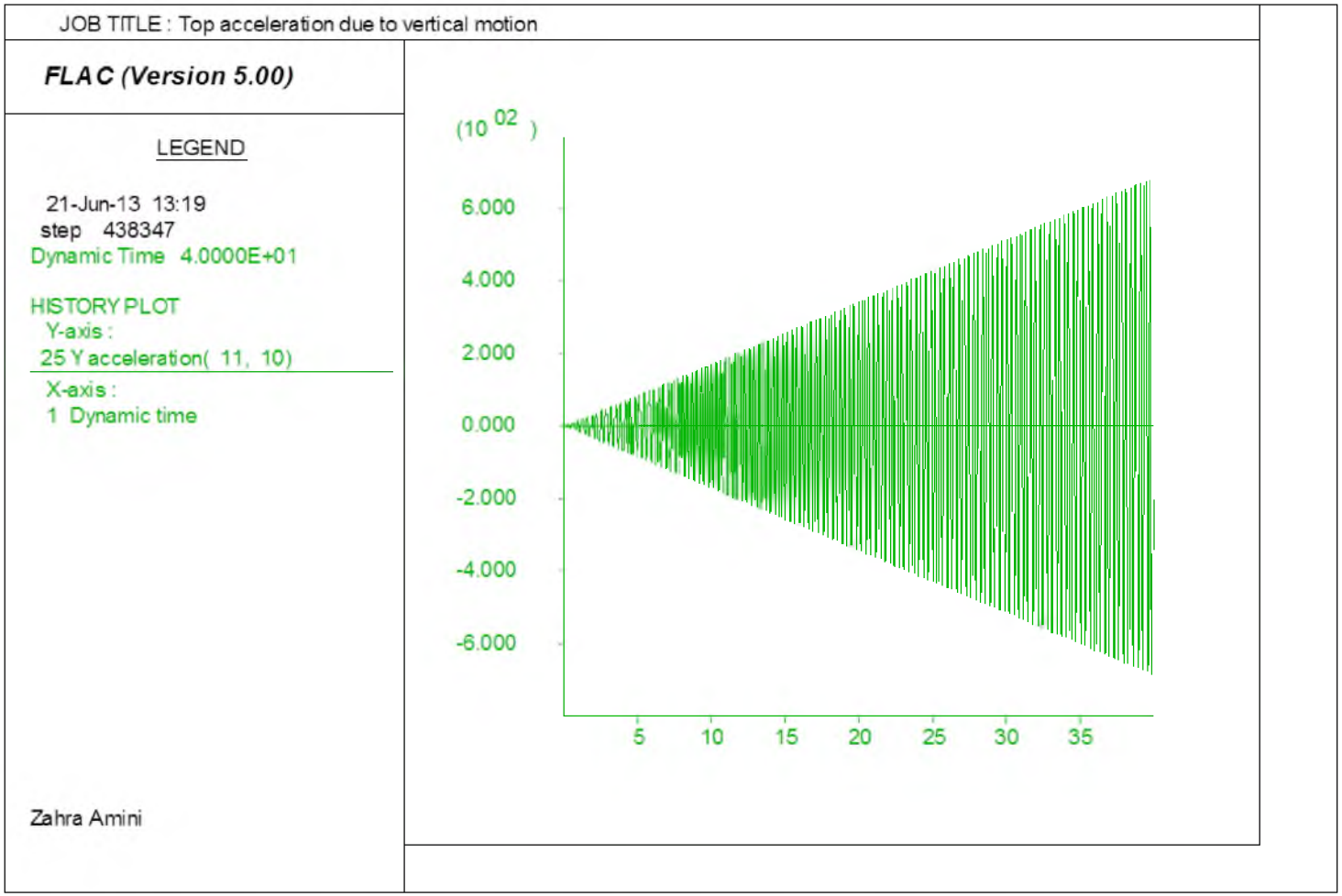

Figure 3.13. Response acceleration at the top of EPS embankment due to vertical input motion applied at a period of 0.32 s

Results

Horizontal Excitation

The results of the sliding analyses are shown in terms of time history of the amount of horizontal movement at each interface. The extent of horizontal movement was determined by obtaining the relative displacement of each interface. This was achieved by subtracting the displacement of the gridpoint located on the lower boundary of the interface from the displacement of the gridpoint located on the upper boundary of the interface. All time histories were recorded at the gridpoint on the midaxis of the embankment and at all the interfaces. The horizontal movement at interfaces comprises two kinds of displacement: one resulting from elastic deformation due to the fact the interfaces are characterized by a spring element and the other caused by separation of blocks at the interface, it is referred to as sliding. The horizontal movement between the EPS blocks at a very low extent may only include the elastic deformation, however, at greater values sliding is a more appropriate term to use. Sliding initiation at all interfaces, for the embankment model excited with a horizontal input motion of amplitude 0.6 g was previously shown in Figure 3.11. Figures 3.14, 3.15 and 3.16 show sliding results of the models that were excited with 0.5 g, 0.8 g and 1 g amplitude input motions, respectively. The horizontal axis in these figures represents time in seconds and the vertical axis represents relevant displacement at the interface in meters. The result corresponding to the first interface is associated with number 1, whereas the uppermost interface (i.e., the interface between the EPS and the pavement system) is assigned to number 8 in the legend.

The results of sliding analyses show that interlayer sliding is initiated fairly soon

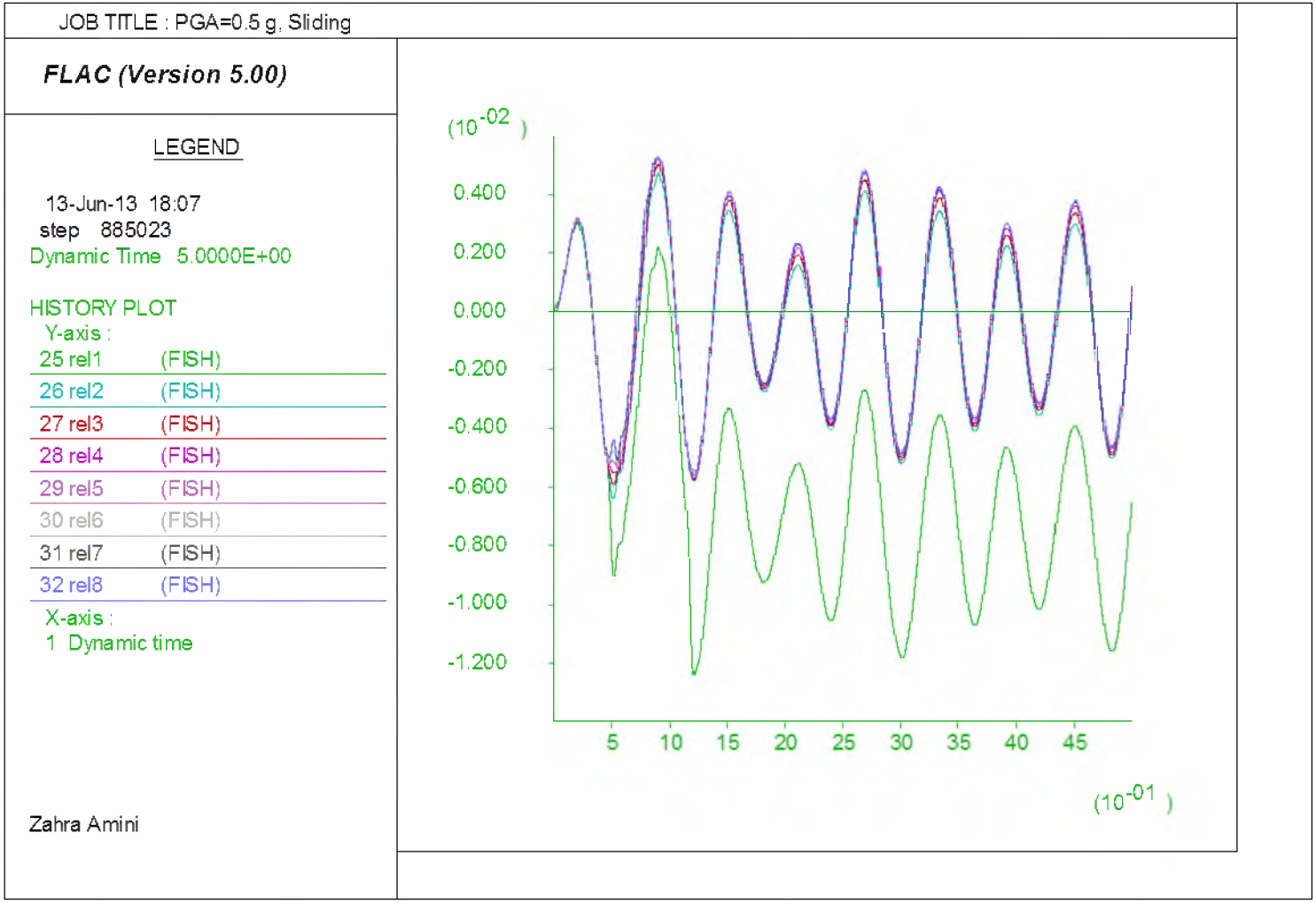

Figure 3.14. Interlayer sliding within the EPS embankment due to 0.5g amplitude horizontal input motion

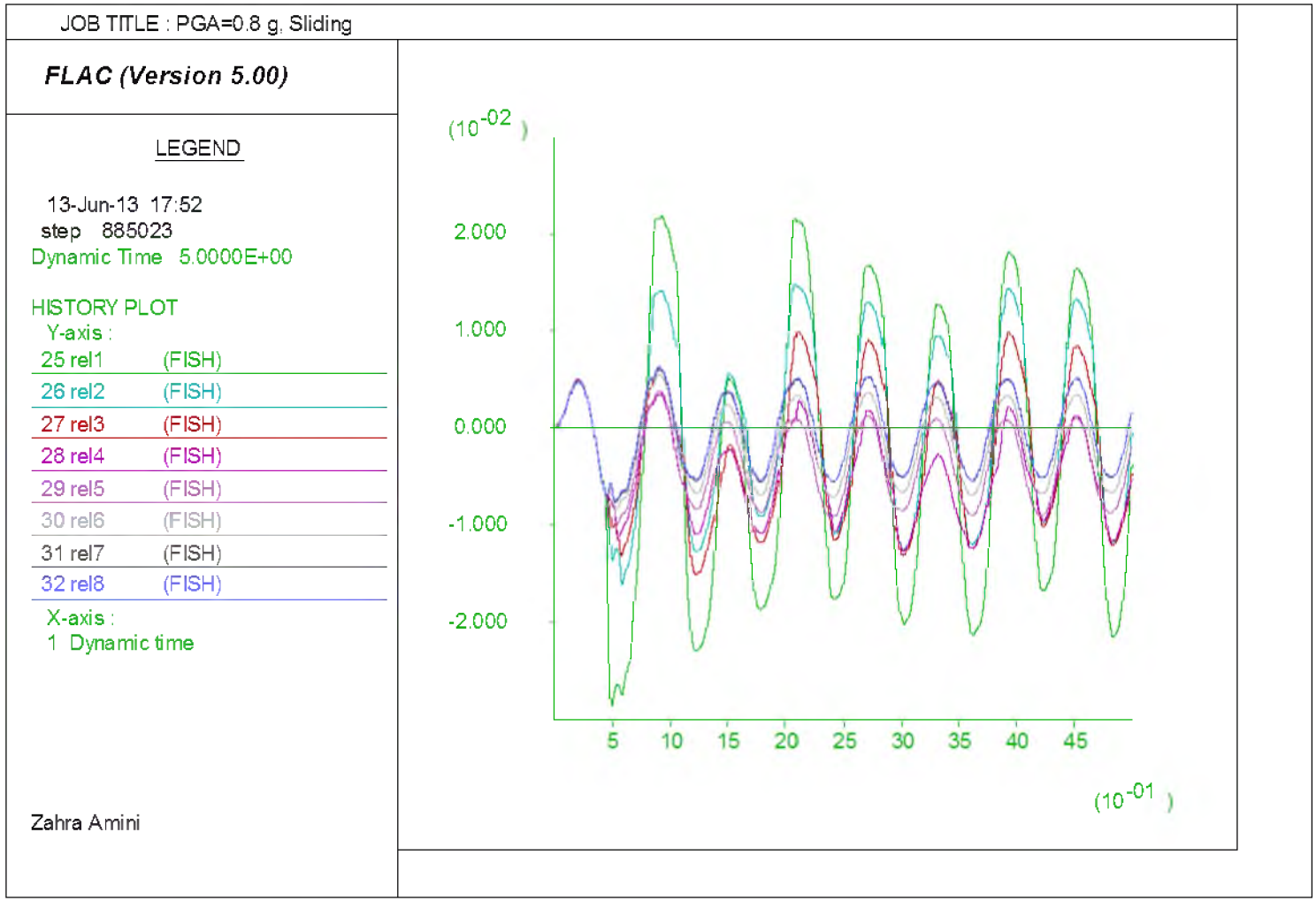

Figure 3.15. Interlayer sliding within the EPS embankment due to 0.8g amplitude horizontal input motion

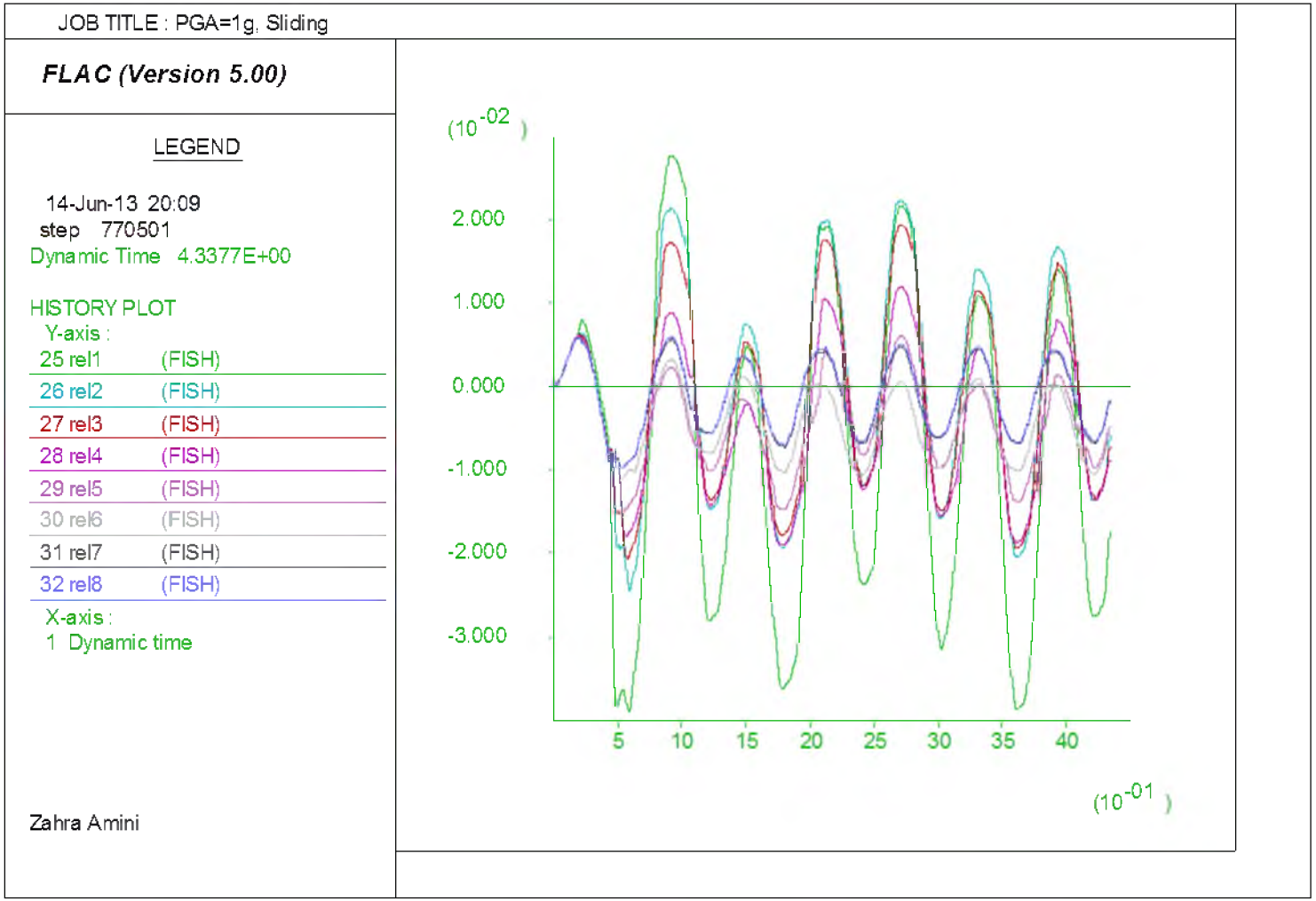

Figure 3.16. Interlayer sliding within the EPS embankment due to 1g amplitude horizontal input motion

after the ground motion is imposed to the model as the amount of relative horizontal movement increases up to the order of centimeters at times less than 0.5 s. The maximum amount of relative horizontal movement (sliding) increases with increasing the acceleration amplitude of the input motion and decreases with time as sliding is an energy dissipating mechanism. The lowermost interface seems to be the first interface to initiate movement and upper interfaces subsequently follow. The first (lowermost) interface is also associated with the most amount of sliding.

These results are very significant because the most commonly used design guidelines regarding dynamic evaluations of the EPS geofoam embankment, as published by NCHRP (Stark et al., 2004), assumes that the maximum accelerations occur at the top of the EPS embankment. However, when relative movement can occur between the layers due to the presence of horizontal discontinuities as represented by the interfaces between the EPS blocks, then the acceleration response within the embankment is significantly modified.

In order to evaluate this effect and determine the location of the maximum acceleration response, such response was monitored at all levels within embankment for cases with and without interfaces. This was performed for all input motion amplitudes discussed previously and the results are presented in Appendix C. In short, Figures 3.17 and 3.18 represent the acceleration response time history at the top of the EPS geofoam embankment with and without interfaces, respectively. The input motion amplitude was 0.6 g applied at the fundamental period of the embankment for these models and the acceleration values are shown in m/s^2 on the vertical axis while the horizontal axis represents time in seconds. It is shown that if interfaces are neglected and the EPS

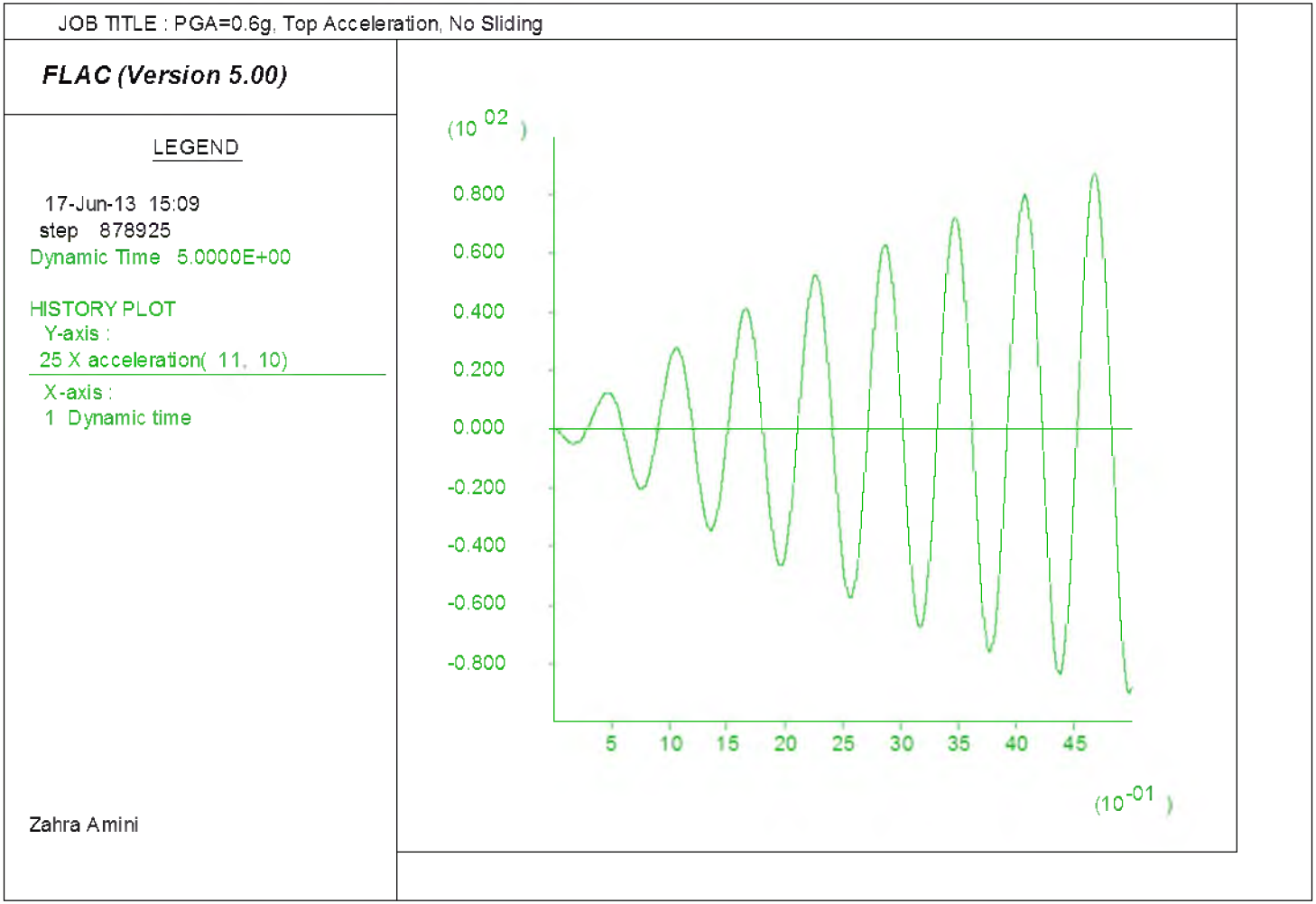

Figure 3.17. Response acceleration at the top of the EPS embankment without interfaces due to amplitude 0.6g input motion

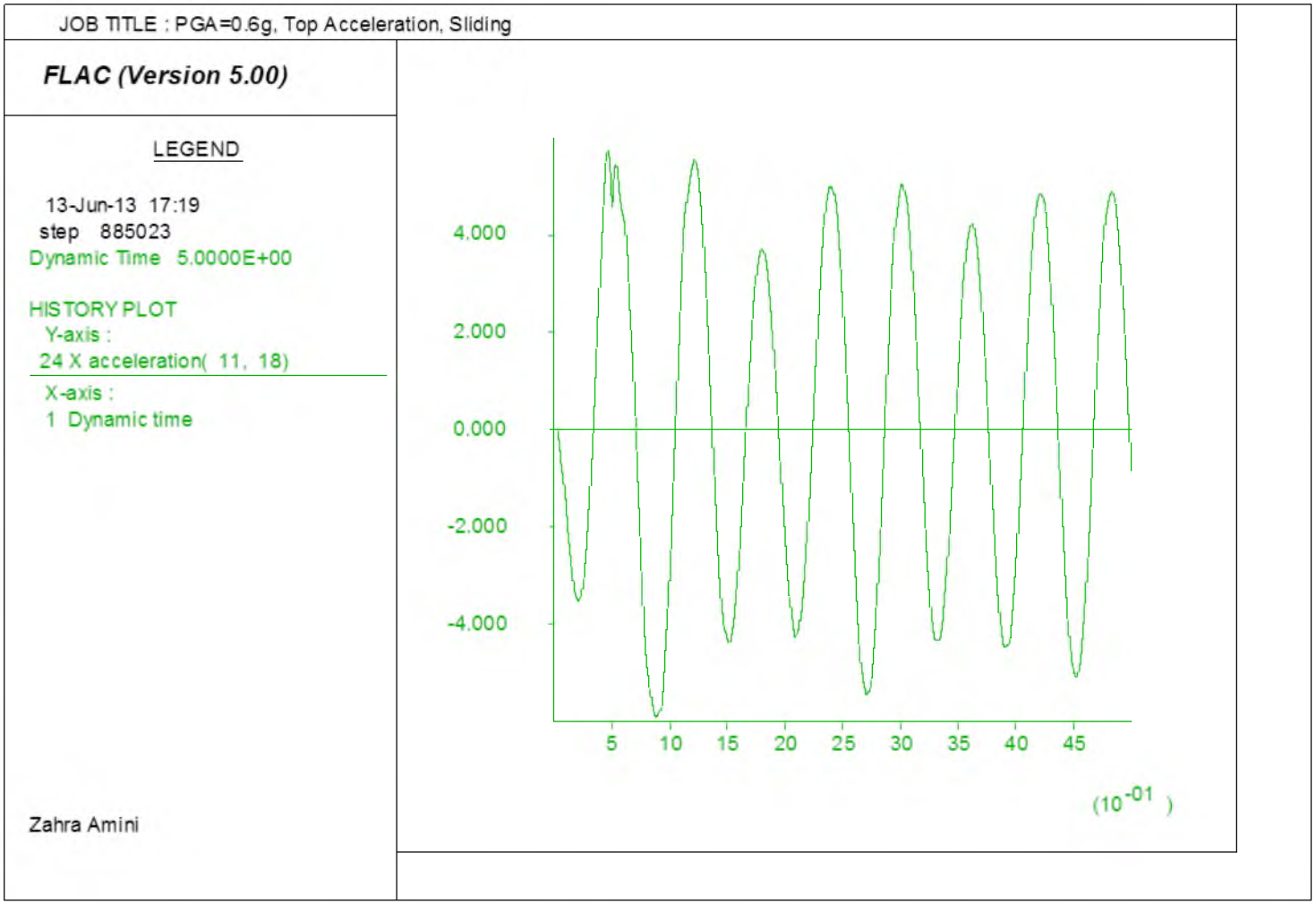

Figure 3.18. Response acceleration at the top of the EPS embankment with interfaces due to amplitude 0.6g input motion

geofoam is treated as a coherent mass, the acceleration response at the top of the embankment increases with time and reaches the value of about 85 m/s^2 (Figure 3.17).

However, when interfaces are included in the model (Figure 3.18), the maximum acceleration response at the top the embankment is about 5 m/s^2. This large difference between the maximum acceleration values calculated at the top of the EPS geofoam embankment is caused by the relative movement of the EPS at the interfaces, which appears to be a very efficient energy dissipating mechanism. This modeling also showed that once relative movement is initiated at the basal interfaces, this movement at these interfaces partially isolates the remaining part of the embankment from the high levels of acceleration.

Figure 3.19 illustrates the acceleration response contours within the embankment model that includes horizontal interfaces. Figure 3.19 is associated with an embankment model excited by a horizontal input motion of amplitude 0.6 g and at 1.8 s after excitation was initiated. It is shown that the layer closest to the base of the model is associated with the highest acceleration response. The response shows a decreasing trend as the height increases from the base to the top of the embankment system. At a location close to the middle of the embankment, the acceleration response becomes very small. These accelerations also show an increasing trend towards the top of the embankment (Figure 3.19).

Horizontal and Vertical Excitation

The sliding analysis results of the embankment models excited with both horizontal and vertical motions simultaneously were conducted in the manner explained

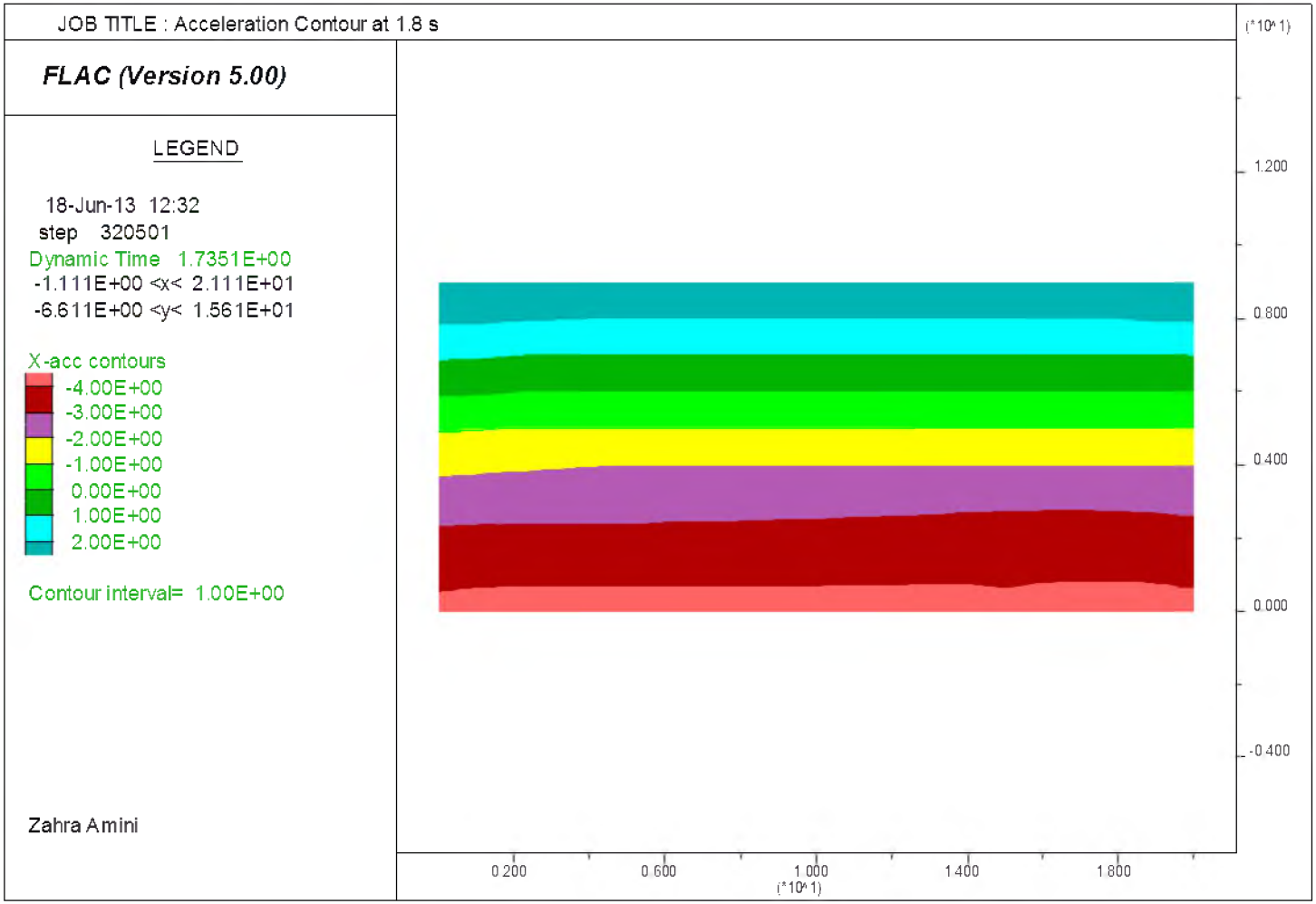

Figure 3.19. Response acceleration within the EPS embankment with interfaces due to amplitude 0.6g input motion

previously. The model was excited with 0.5 g, 0.6 g, 0.8 g and 1 g horizontal acceleration amplitudes while vertical acceleration amplitudes of 0.20 g, 0.24 g, 0.32 g, and 0.40 g were imposed, respectively. Figures 3.20 to 3.23 illustrate the extent of horizontal movement versus time at the interfaces of the EPS embankment correspondingly. It is shown that relative movement is initiated very soon after the input motion is imposed to the model, and the maximum amount of sliding increases with increasing values of vertical and horizontal acceleration. The results of the series of analyses performed incorporating both horizontal and vertical components of input motion differ from those corresponding to solely horizontal component of input motion in two main ways: first the maximum amount of sliding is larger and occurs earlier in the analysis when both vertical and horizontal harmonic components are considered compared to when only horizontal motion is applied. Secondly when the model is excited in the horizontal direction only the lowermost interface shows the largest amount of relative movement, which gradually decreases going upwards toward the top of the embankment. However, this subsequent decrease is not shown in the behavior when the vertical component is included as represented by the results shown in Figures 3.20 to3.23. In addition, the order of interfaces associated with subsequent levels of sliding is not necessarily from the bottom of the embankment to the top, particularly at higher acceleration amplitudes. This is more prominently observable in Figure 3.23 where the embankment was excited with 1 g horizontal and 0.4 g vertical amplitudes. Figure 3.23 shows that unlike in the horizontal input motion case, the uppermost interface shows the greatest amount of horizontal movement compared to the other interfaces. Figure 3.24 compares the maximum interlayer relative movement (sliding) between the two cases when only horizontal

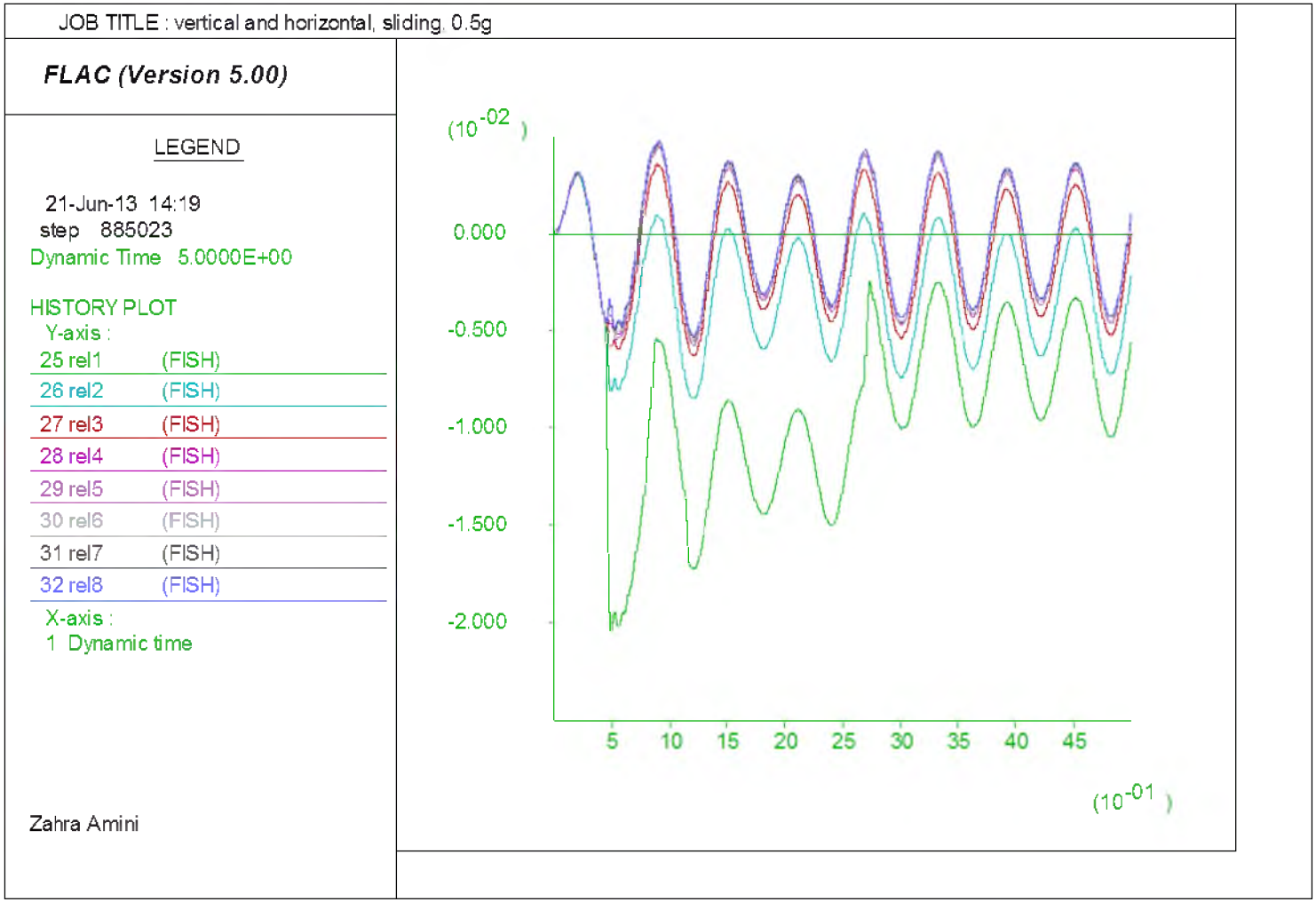

Figure 3.20. Interlayer sliding within the EPS embankment due to 0.5 and 0.2g horizontal and vertical amplitudes of input motion

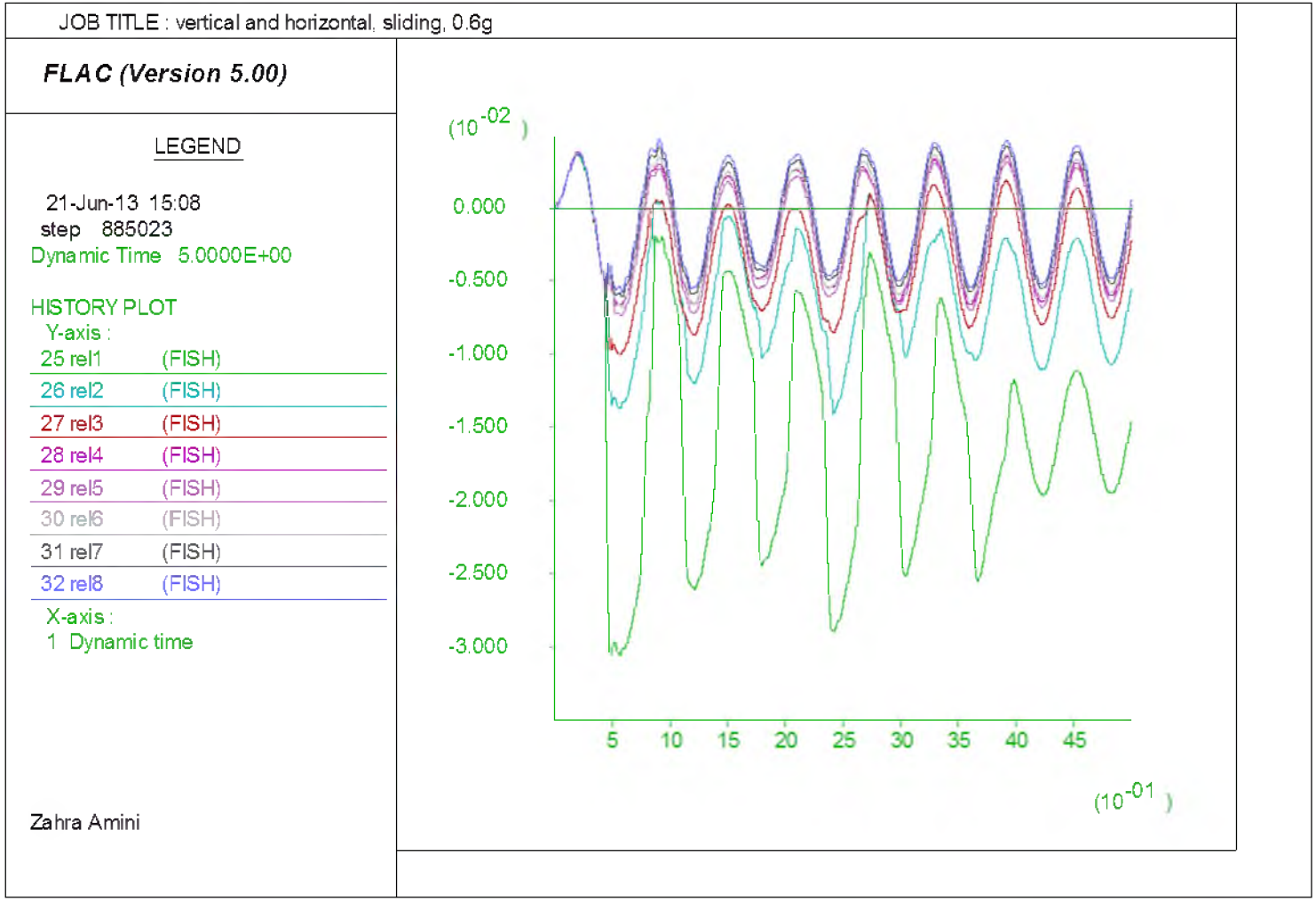

Figure 3.21. Interlayer sliding within the EPS embankment due to 0.6 and 0.24g horizontal and vertical amplitudes of input motion

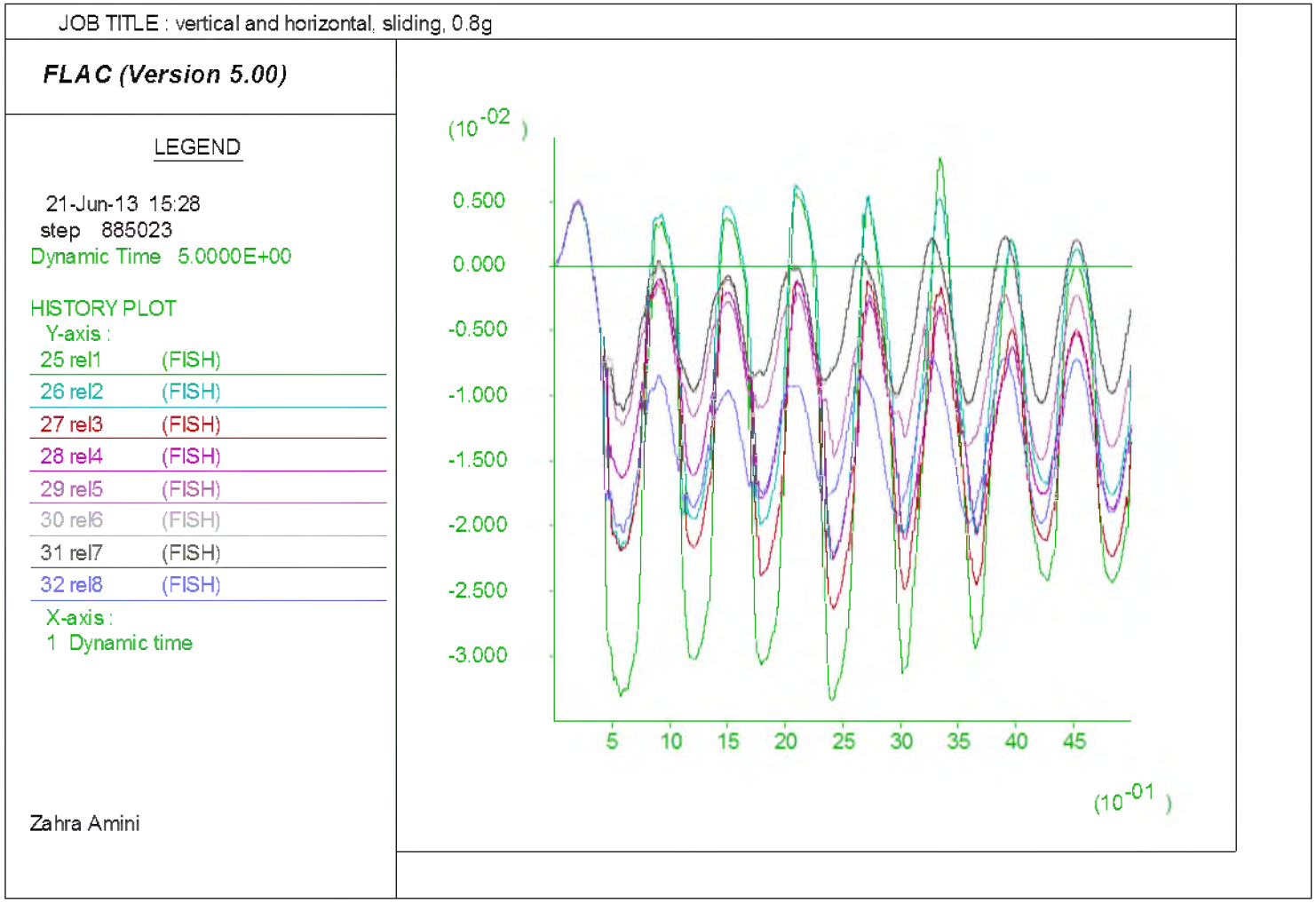

Figure 3.22. Interlayer sliding within the EPS embankment due to 0.8 and 0.32g horizontal and vertical amplitudes of input motion

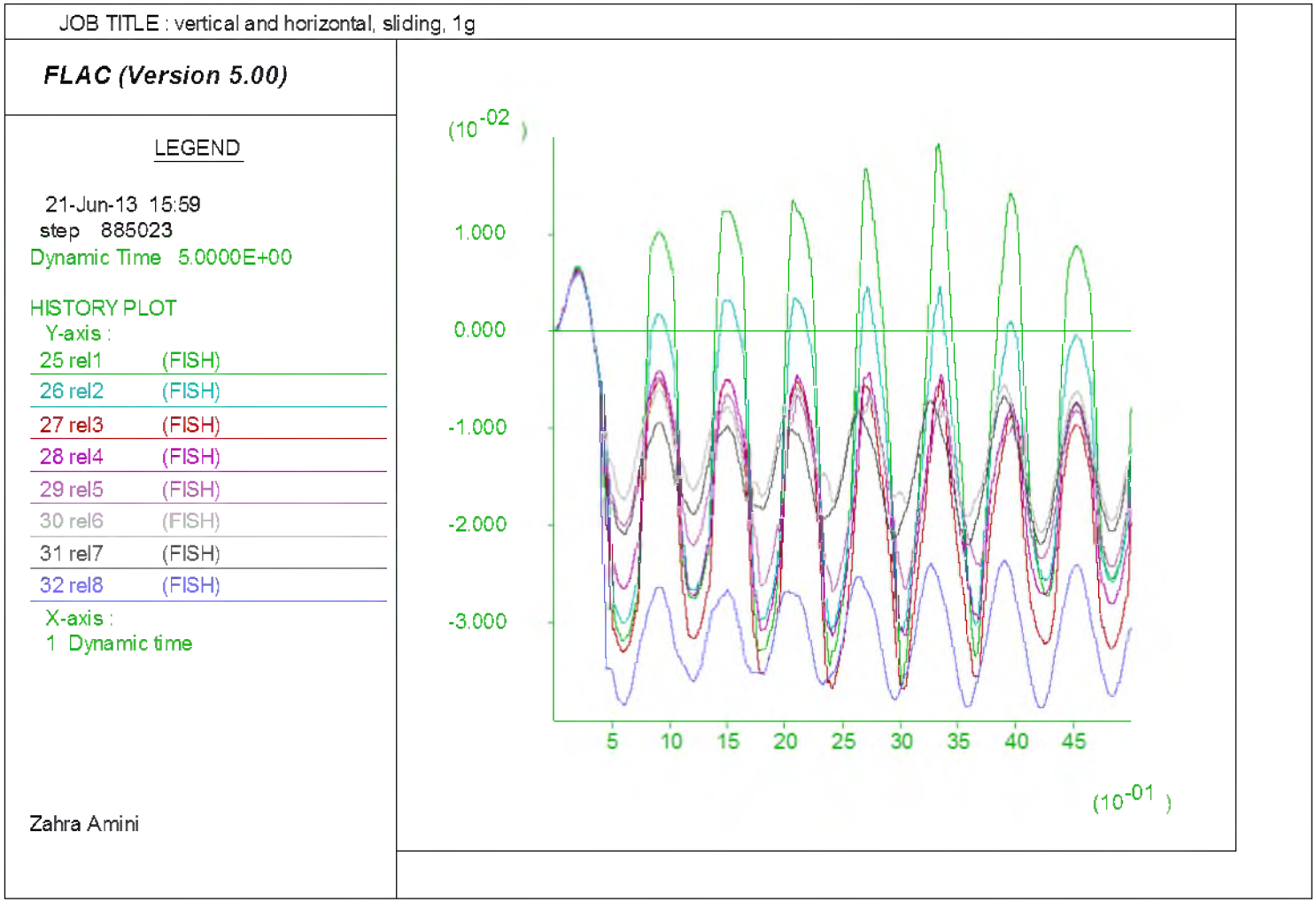

Figure 3.23. Interlayer sliding within the EPS embankment due to 1 and 0.4g horizontal and vertical amplitudes of input motion

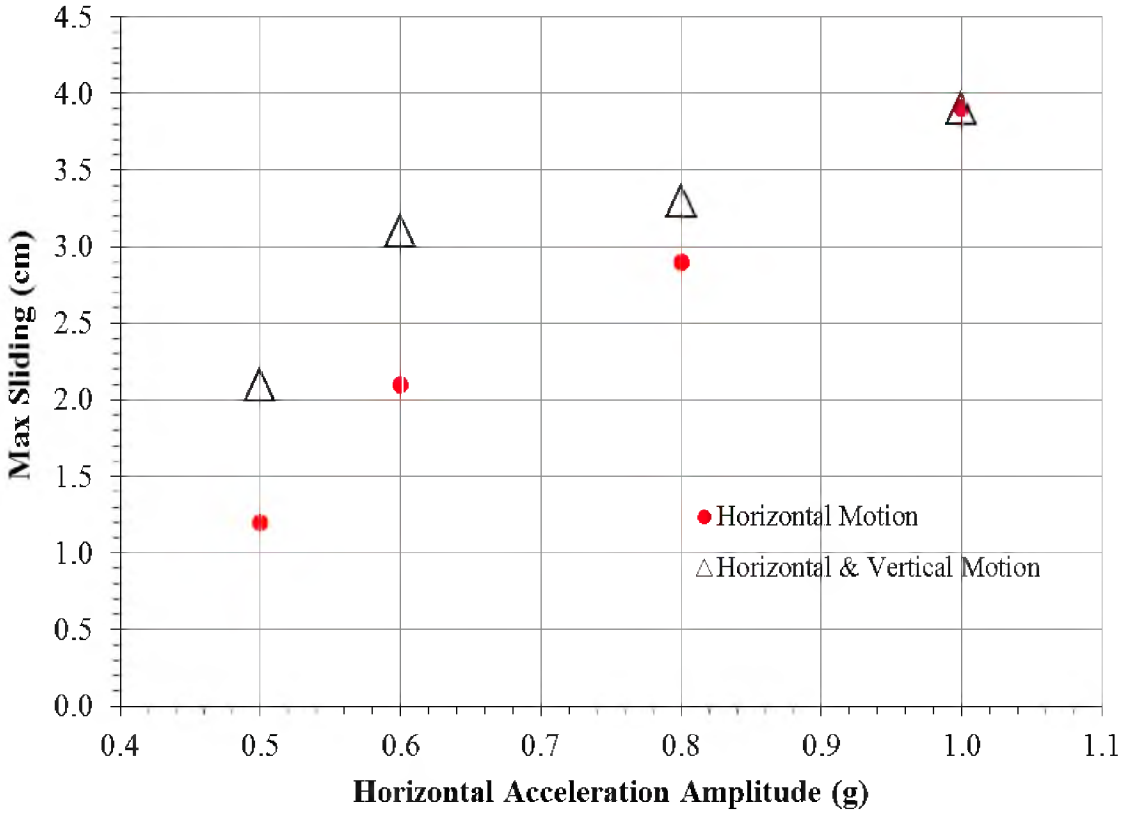

Figure 3.24. Comparison of maximum sliding extents in two cases of only horizontal and both horizontal and vertical input motion at different acceleration amplitudes

component of input motion is considered and when both horizontal and vertical components are included. It is shown that when both horizontal and vertical components of input motion are included the maximum sliding values are generally larger than those associated with only horizontal input motion. However, this difference decreases as the horizontal acceleration amplitude (and subsequently the vertical acceleration amplitude) increases, to the extent that at 1 g amplitude inclusion of vertical component of input motion does not affect the maximum amount of sliding. Nonetheless, the maximum sliding occurs at different locations depending on whether the vertical component of the input motion is considered or not.

To quantify the difference between the maximum sliding in these two cases it can be shown that for horizontal acceleration amplitudes of 0.5, 0.6 and 0.8 g, the amount of maximum sliding is 75, 48 and 14% higher when the model is both horizontally and vertically excited compared to when it is only excited in the horizontal direction. At the horizontal acceleration amplitude of 1 g the maximum sliding values are similar though occurring at the opposite sides of the embankment (i.e., when the model is excited horizontally at 1 g acceleration amplitude, the lowermost interface shows the maximum sliding extent, whereas when the vertical component of the input motion is also applied to the model a similar extent of maximum sliding takes place at the uppermost interface of the EPS embankment model, which is the interface between the last layer of EPS blocks and the pavement system.). Therefore exclusion of the vertical component of the seismic input motion does not appear to be conservative for a large spectrum of input acceleration amplitudes.

Conclusions

It is concluded that in order to predict the full dynamic behavior of the EPS geofoam embankment it is necessary to consider the layered structure of the EPS geofoam embankment where, if the EPS blocks are not glued some amount of interlayer relative movement is inevitable at moderate to high levels of horizontal motion. Once interlayer sliding is initiated, the EPS embankment ceases to behave as a coherent mass unlike what is assumed in the current NCHRP design guidelines.

The results of interlayer sliding analyses show that relative horizontal movement occurs relatively early in the analysis along the interfaces when the model is in the elastic

mode. This relative movement is generally initiated at the lowermost interlayer and propagates upwards to the top of the embankment. However, relative movement at the interfaces appears to be a very efficient energy dissipating mechanism. Not only does it decrease the extent of sliding with time, but also once initiated, it isolates the higher levels from large accelerations and the larger movement associated with these accelerations. This effect was mostly observed when the model is excited with horizontal seismic forces.

The addition of the vertical component of input motion leads to larger values of interlayer sliding when compared to those obtained with only the horizontal acceleration present for the majority of cases. Only at very high amplitudes (i.e., 1 g), does the vertical component of seismic motion appear not to alter the maximum amount of sliding.

However, at this high level of acceleration, the uppermost interface (i.e., the interface between the EPS and the pavement system) is associated with the maximum sliding. In contrast, when excited at the same amplitude of horizontal motion without the vertical component, the first (i.e., basal) interface shows the largest amounts of relative movement.

Therefore it is concluded that disregarding the vertical component of the input motion does not appear to be conservative in predicting both the maximum extent of sliding and its location for high levels of input acceleration.

CHAPTER 4

INTEGRITY OF BLOCK ASSEMBLAGE IN THE EPS EMBANKMENT

Vertical seams are avoided in EPS embankment construction by placing large geofoam blocks in horizontal layers and staggering the edges of each row of blocks. In addition, with the placement of each successive layer, the rows of blocks are oriented 90 degrees from the underlying layer to further interrupt the vertical seams. Although this method of block layout prevents continuous vertical joints within the embankment and enhances interlocking of the geofoam mass, there are concerns regarding stability of the EPS blocks placed on the vertical edges of the embankment. This chapter investigates the potential of "block walk-out" by including the vertical interfaces where appropriate.

EPS Embankment Layout

In order to clarify the potential for "block walk-out" it is necessary to illustrate the assemblage of the blocks in an EPS geofoam embankment in each layer. Figure 4.1 shows the layout of an EPS geofoam embankment in cross section and plan views. Figure 4.1 (a) shows an EPS geofoam embankment consisting of five layers of

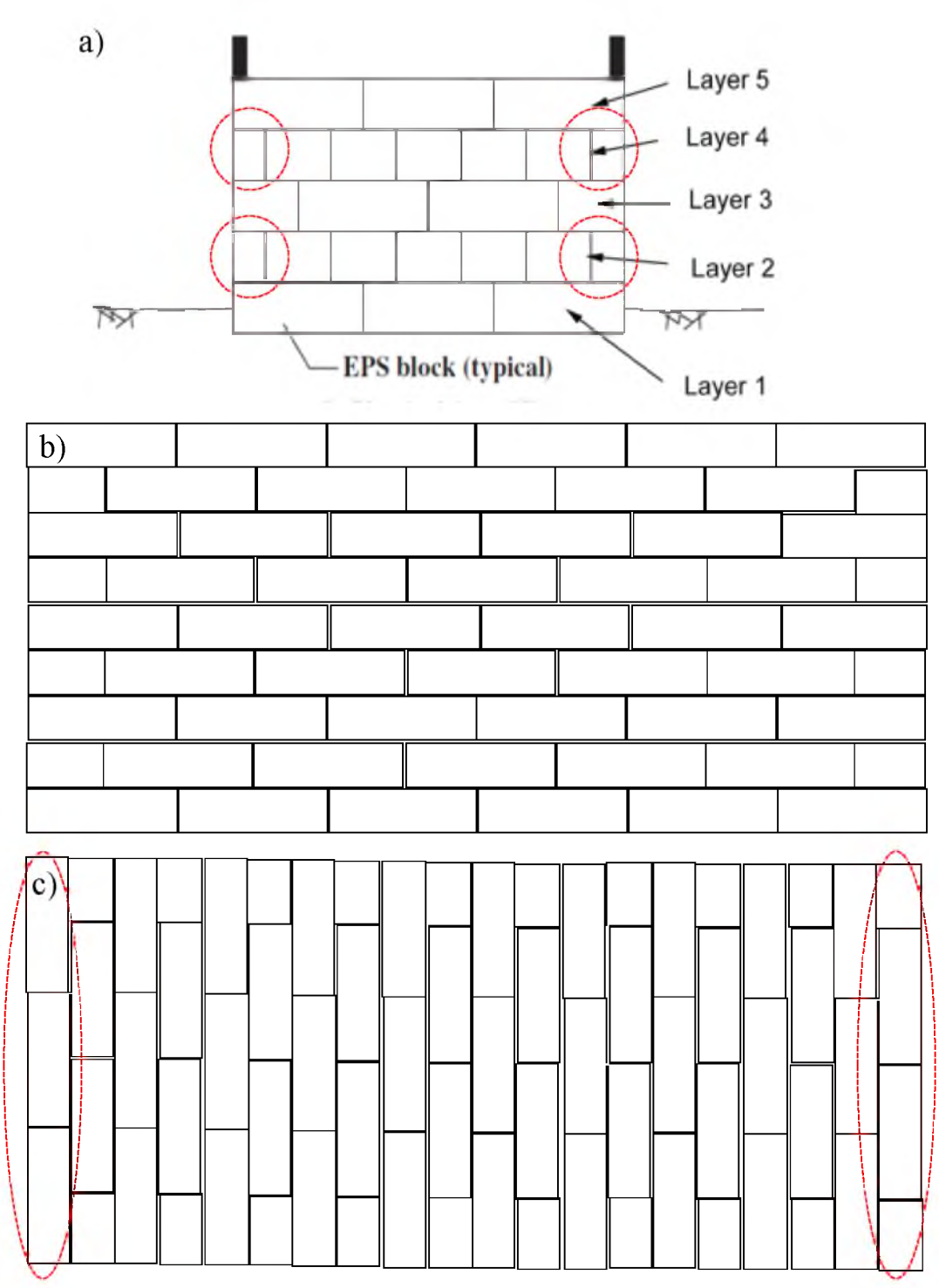

Figure 4.1 EPS geofoam embankment's a) Cross section (modified after Stark et al., 2004), b) Plan view of layer 1 and c) Plan view of layer 2

EPS geofoam blocks placed atop each other. Figure 4.1 (b) shows the plan view of the first layer where the blocks are laid out with the longest dimension parallel to the cross section of the embankment. The second layer of the EPS geofoam blocks is placed atop the first layer with a 90 degree rotation in the orientation where the longest dimension of the blocks are parallel to the sides of the embankment. This is done in a fashion that prevents vertical edges of the EPS from aligning between layers. The 90 degree rotation of the blocks is applied to each successive layer resulting in layers 1, 3 and 5 with the same layout and layers 2 and 4 with similar block placement pattern.

Because vertical seams are avoided through the embankment, vertical separation of the blocks within the embankment is not of concern. However; when the blocks are placed with their longest dimension parallel to the sides of the embankment at the edges such as marked in Figures 4.1 (a) and (c), where the vertical edges of the blocks are in very close vicinity of the sides of the embankment, "block walk-out" is a concern particularly at relatively high levels of ground motion.

FLAC Model

An 8 by 20 m EPS embankment topped with 1-m thick pavement system with properties and boundary conditions similar to those discussed in the preceding chapters was modeled in FLAC. Horizontal interfaces were included at every layer, whereas vertical interfaces were applied 1 m from the side of the embankment and at every other layer as shown in the schematic presented in Figure 4.2. The horizontal interface stiffnesses are similar to those used in Chapter 3, however, for vertical interfaces the normal stiffness was assigned as 7.17 MPa (i.e., obtained by FLAC manual

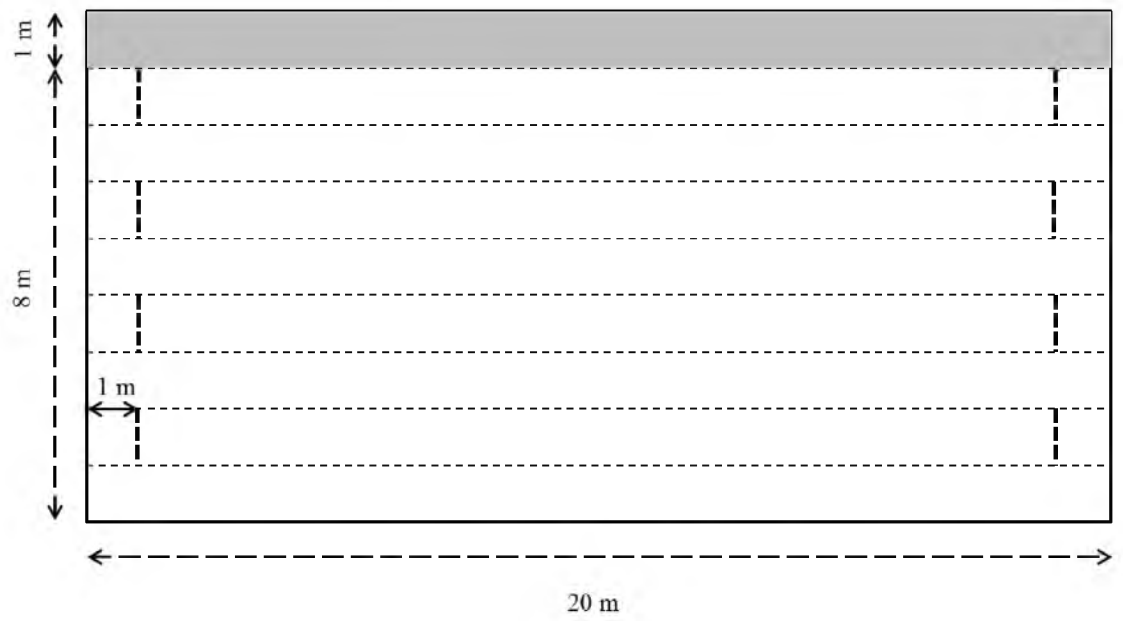

Figure 4.2. Schematic of the EPS geofoam embankment model consisting of horizontal and vertical interfaces

recommendations discussed in Chapter 3) and the shear stiffness was assigned as 1 MPa based on the experimental results conducted by Barrett (2008). This value is corresponding to the lowest normal stress (i.e., 9 kPa) used in the experimental study (see Figure 3.2). The location of the vertical interfaces in the model assumes a cross section dimension of 1 m by 1 m for the EPS geofoam blocks. This assumption appears to be reasonable as the EPS geofoam blocks used in the I-15 construction project were 0.8-m high and 1.2-m wide in cross section (Bartlett et al., 2012).

Two levels of harmonic motion were applied to the base of the embankment comprising both horizontal and vertical components. The two waves used in the analyses were of 0.6 g and 1 g horizontal acceleration amplitudes, and 0.24 g and 0.4 g vertical amplitudes (i.e., 40% of the horizontal amplitudes), respectively. The harmonic motions were applied at the fundamental period of the embankment.

For simplicity the wave associated with 0.6 g horizontal acceleration amplitude and 0.24 g vertical acceleration amplitude is referred to as wave 1 and the wave characterized with 1 g horizontal acceleration amplitude and 0.4 g vertical acceleration amplitude is referred to as wave 2. Two percent Rayleigh damping was also applied to the EPS geofoam embankment.

Figure 4.3 shows a slight separation of the blocks at the edges of the embankment after wave 1 was applied. However, when the embankment was excited with wave 2 as shown in Figure 4.4 the great extent of sliding that took place in the embankment caused the blocks on the sides to be pushed out and therefore the integrity of the block assemblage in the embankment was compromised. In order to study the potential to "block walk-out" in the EPS geofoam embankment when sliding prevention strategies such as use of adhesive or shear keys are applied in the middle of the embankment, neglecting the blocks on the edges, another scenario was exercised. In this scenario all horizontal interfaces were glued (i.e., prohibited from sliding) except the ones corresponding to the EPS blocks on the vertical edges of the embankment. This was done for two reasons: first, to exercise a more intense condition where most of the seismic energy is focused on the blocks with walk-out potential (i.e., since sliding and yielding is prevented within the embankment) and secondly, to study the consequences of applying sliding remedies disregarding the "block walk-out" potential. Figures 4.5 and 4.6 illustrate the behavior of the EPS blocks placed at the edges of the embankment when waves 1 and 2 were applied, respectively. Blocks appear to walk out from the sides of the embankment mostly at the top layer when wave 1 is imposed, as shown in Figure 4.5. This behavior is similarly observed when the embankment is excited with wave 2.

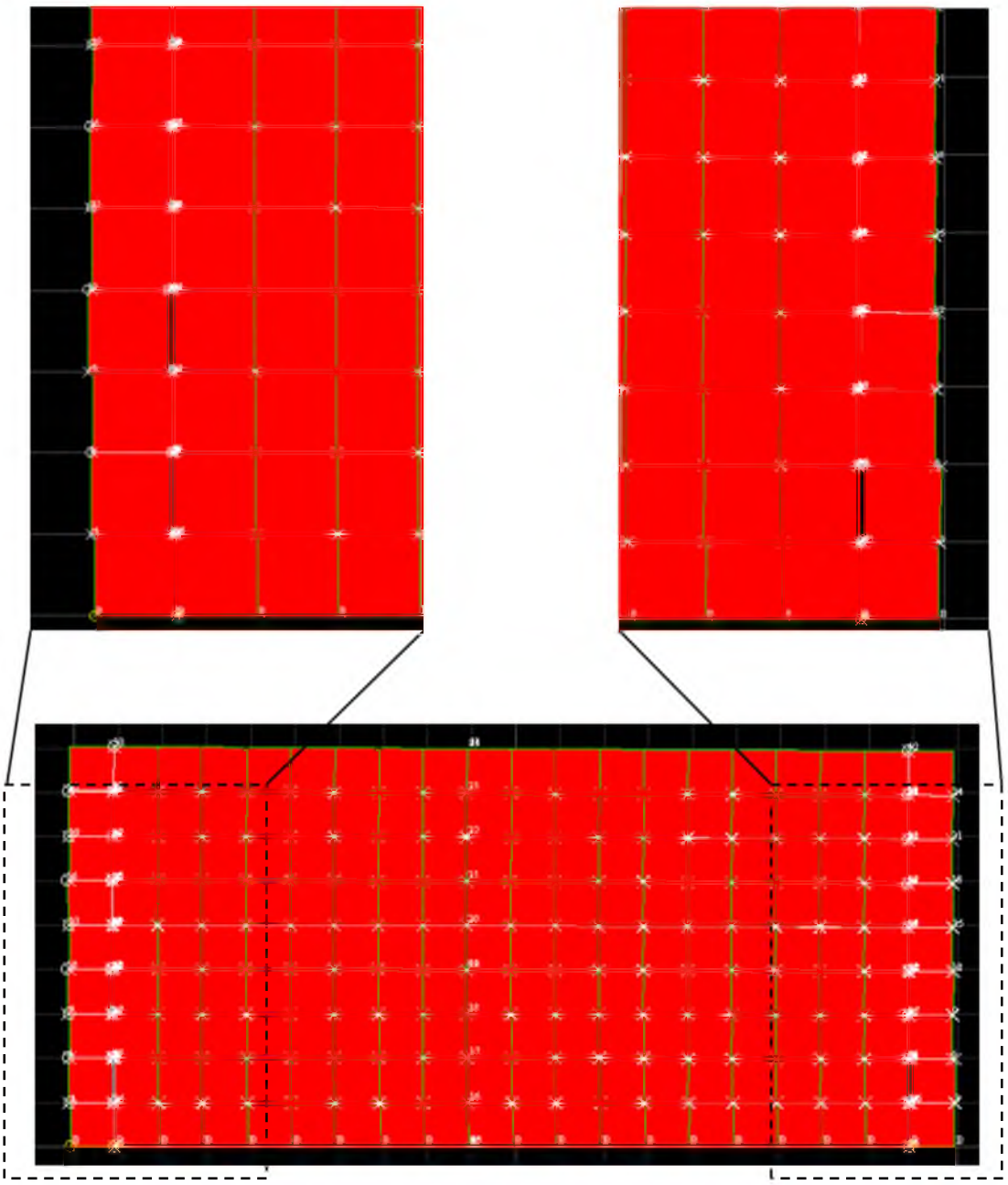

Figure 4.3. Block separation due to application of wave 1

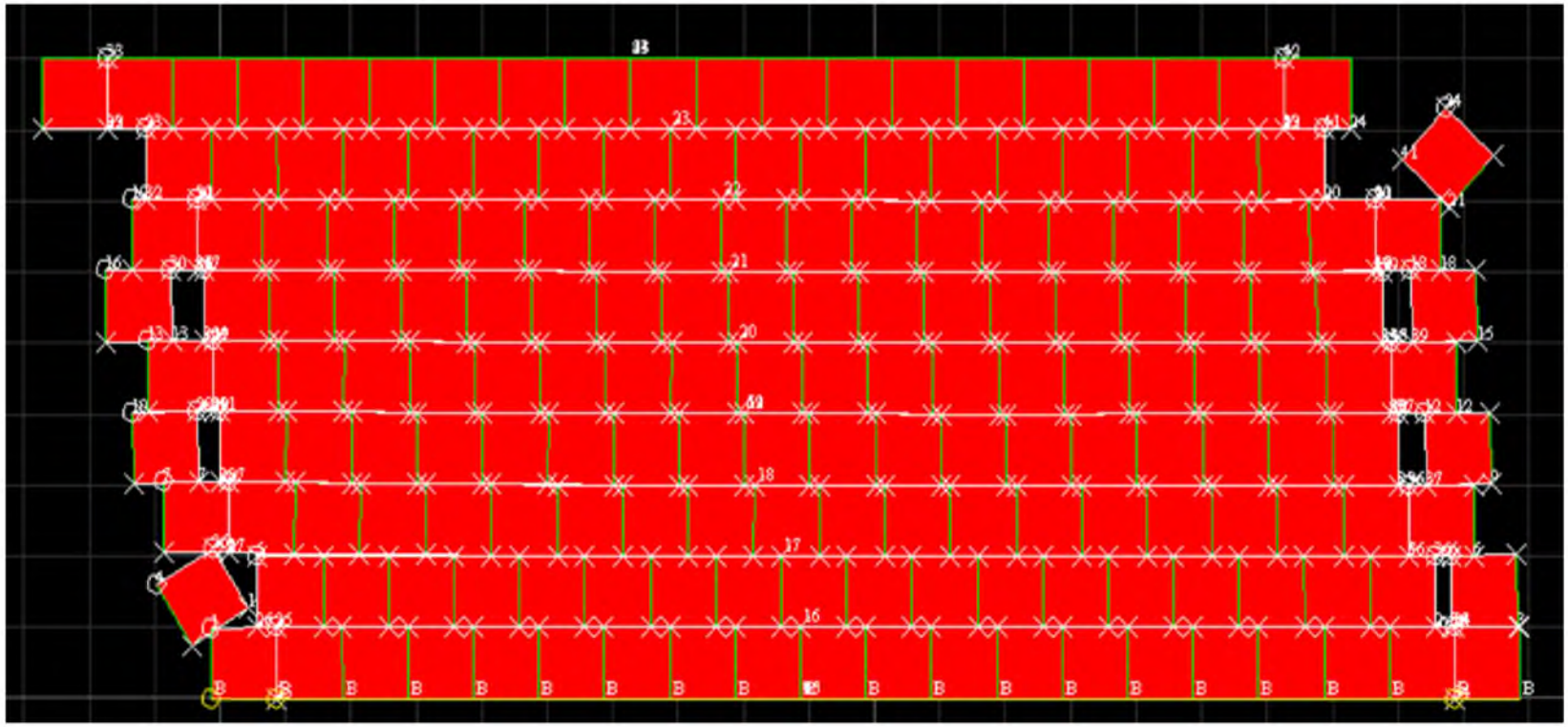

Figure 4.4. Block walk-out due to application of wave 2

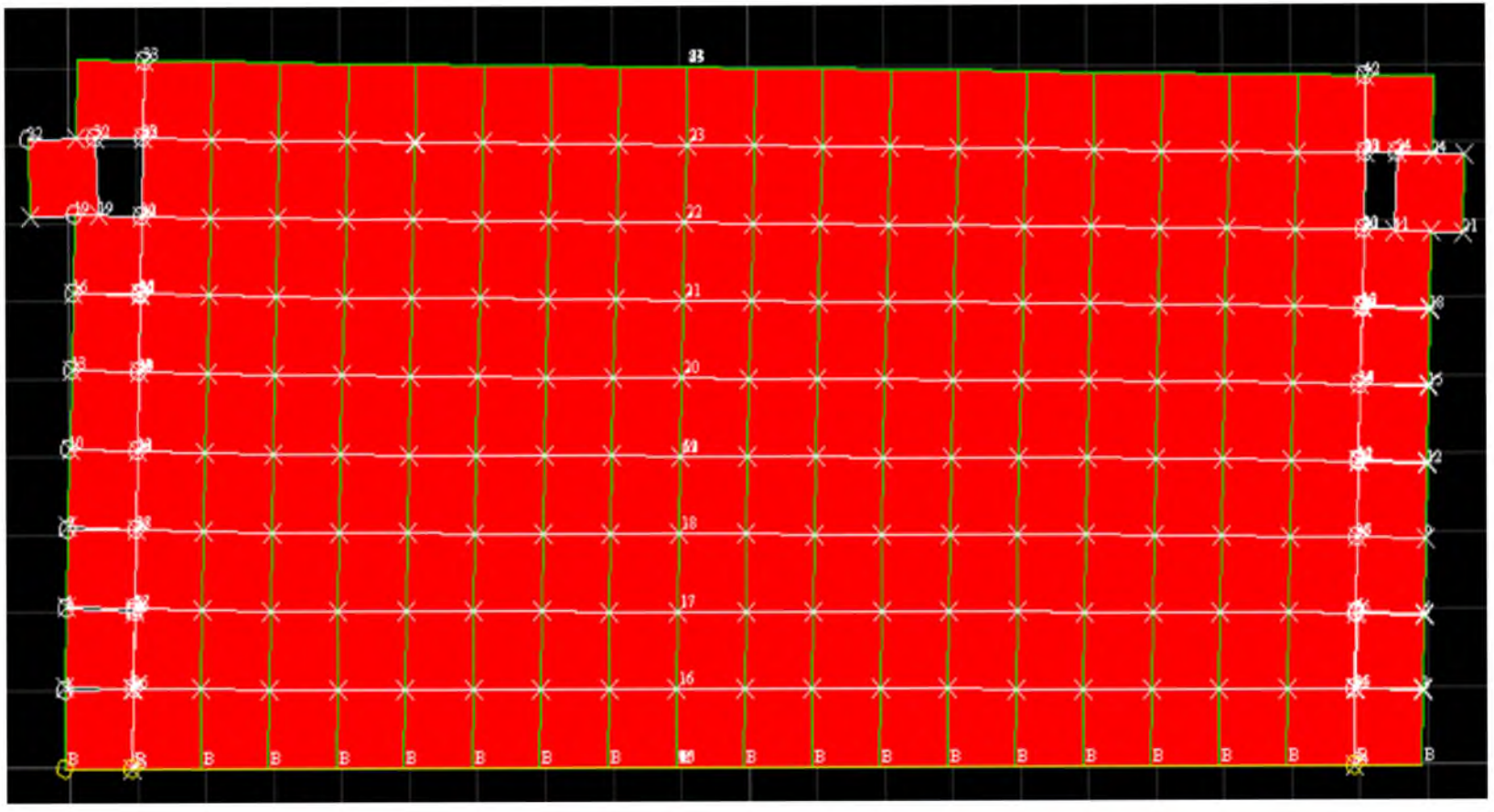

Figure 4.5. Block walk-out due to application of wave 1 when sliding is prevented

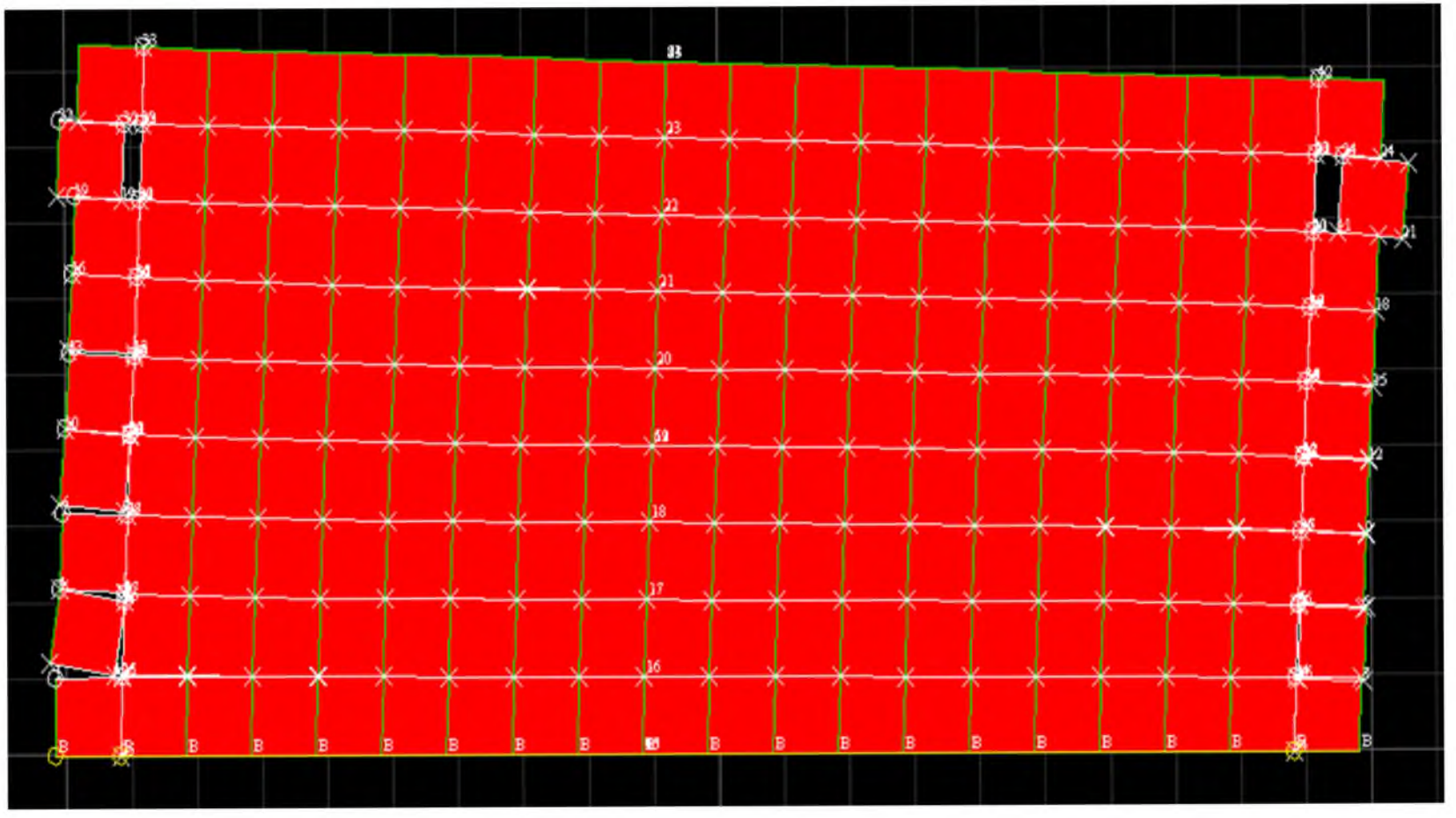

Figure 4.6. Block walk-out due to application of wave 2 when sliding is prevented

However, in this case block separation at the edges of lower layers is also evident as seen in Figure 4.6.

Conclusions

EPS geofoam blocks placed at the edges of the embankment may be subject to a phenomenon herein referred to as "block walk-out." When EPS blocks are placed in a manner where the longest dimension of the block is parallel to the side of the embankment, the close vicinity of the vertical edge of such blocks to the edge of the embankment can result in their partial or complete separation from the embankment body. This phenomenon (block walk-out) can vary in severity depending on the level of seismic forces imposed on the embankment and whether or not interlayer sliding in the embankment is prohibited.

Numerical analyses using FLAC show that for input acceleration amplitudes of 0.6 g and lower, block walk-out may not be a major concern when the embankment layers are free to move atop each other; however, if sliding remedies are deemed necessary they must be applied to the EPS blocks placed at the edges of the embankment as well securing these blocks from being pushed outwards. At higher amplitudes of input motion blocks located at the edge of the embankment can be pushed out and integrity of the EPS block assemblage of the embankment may be lost.

It is noteworthy that in cases where the EPS layers are prohibited from sliding in the middle of the embankment, the block walk-out is more evident at the upper layers. Such a pattern is an indication of energy concentration at the top of the embankment once the embankment is modeled as a semicoherent mass rather than in the form of individual

layers that are free to move. This is consistent with the basis of EPS geofoam embankment seismic stability design guidelines published by NCHRP where the embankment is assumed to be a coherent mass. Nevertheless, block walk-out must be prevented at relatively high levels of ground motion and at all times, disregarding the ground motion level, if other parts of the embankment are subject to sliding remedies.

CHAPTER 5

INTERLAYER SLIDING PREVENTION STRATEGIES

Shear keys and adhesive can be used in order to prevent interlayer sliding in EPS geofoam embankments. Shear keys have been used in various EPS embankment construction projects to interlock the EPS blocks together. Commercially available adhesive such as that used in the experiments conducted in this study (Chapter 2) may also be another efficient solution to EPS geofoam embankment interlayer sliding. The use of proper adhesive prevents the EPS blocks from sliding atop each other by mobilizing the cohesive shear strength of the EPS geofoam through redirecting the shear plane form the boundary of the two blocks of geofoam into the EPS geofoam block.

However, in order to efficiently apply such strategies guidelines are required regarding the extent and location of application within the embankment. As concluded in the previous chapter, interlayer sliding is an efficient energy dissipating mechanism. Hence once sliding is prevented, dynamic response of the embankment will differ from that of when sliding is allowed. While the seismic energy is not significantly dissipated through interlayer horizontal movement, dynamic behavior of the EPS geofoam may be more similar to an embankment of coherent mass potentially experiencing sway and rocking modes.

This chapter sheds more light on the effectiveness of sliding prevention strategies discussed and provides answers as to where, when and to what extent should these methods be used. Dynamic behavior of the EPS geofoam embankment after application of sliding preventive methods is also investigated in this chapter.

Model Development

To address the efficiency of the sliding preventive strategies, explore optimum application approaches and to investigate dynamic behavior of the EPS geofoam embankment postapplication of sliding preventive methods, the modeling procedure was conducted in two stages. The first stage focused on efficient application of sliding preventive methods and the second stage emphasized consequent dynamic response of the EPS geofoam embankment due to precluding interlayer sliding.

Application of Sliding Preventive Methods

Whether adhesive, shear key or a combination of both is the method chosen to prevent interlayer sliding, the numerical modeling implementation in FLAC is similar. This can be achieved by gluing the interface between the EPS geofoam layers in the embankment. Gluing the interfaces prohibits slip and separation of the two zones on the sides of the interface. As discussed in the previous chapter, in order not to affect the dynamic of the of the model the interface shear and normal stiffnesses are set to 50 times their real values while the interface is glued by “glue” command in FLAC.

The process of attaching the EPS geofoam layers efficiently involves two main

provisions: 1) the proportion of the attached area to the contact area is large enough to prevent interlayer sliding; and 2) the attached area is small enough to prevent yielding of a significant portion of the embankment. To find the minimum area required to be attached in order to prevent sliding the horizontal interfaces between the EPS geofoam layers were divided into three segments where the midsegment was glued at all layers and therefore prohibited from sliding while the two remaining segments on the sides were left free to slip and separate. Figure 5.1 shows a schematic of the model.

Consequently the model is exposed to horizontal and vertical harmonic motions as discussed in Chapter 3 with 2% Rayleigh damping. While the horizontal relative movement was monitored at the gridpoints closest to the vertical boundary of the model at each interface, the area covered by the glued midsegment of the interfaces was gradually increased. This was carried on until the relative horizontal movement did not exceed 1 inch (2.5 cm). Since the sliding preventive methods may be required for embankments susceptible to interlayer sliding, this part of the analysis was performed on

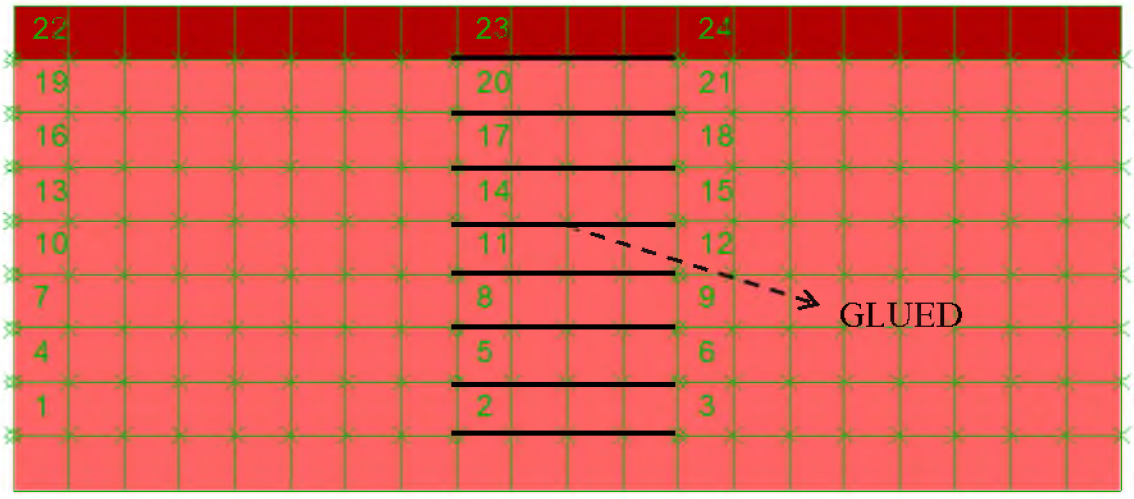

Figure 5.1. Implementation of sliding preventive methods in FLAC

embankments exposed to 0.6, 0.8 and 1 g input acceleration amplitudes. According to Figure 3.24, relative horizontal movements induced by 0.5 g amplitude accelerations are below 1 inch.

Postsliding Remediation

Once sliding is prevented, high levels of seismic forces within the embankment push the embankment system out of the elastic mode and nonlinearity will become significant in the model. Hence application of solely a constant damping ratio will no longer be appropriate. FLAC can capture this nonlinearity by allowing the use of hysteretic damping to model the strain-dependent modulus and damping in the geofoam.

Shear modulus degradation and damping curves developed for equivalent linear method can be used in the nonlinear formulation in FLAC. Elastic or Mohr Coulomb material properties may be used with hysteretic damping in FLAC that prohibit and allow yielding of the material, respectively. To avoid any excessive loss of energy through yielding and thus introducing high extents of damping to the system, elastic material properties were used in the model. However, compressive and shear stresses were monitored throughout the embankment model to identify any potential yielding of the EPS geofoam blocks.

Shear modulus degradation and damping curves appropriate for geofoam were obtained by Athanasopoulos et al. (1999) for densities of 12.5 and 17.1 kg/m^3. Using these results shear modulus degradation curve was developed for EPS 19 by extrapolation. Various fitting functions are available to reproduce the shear modulus degradation curve obtained from experimental study in FLAC. For this purpose a three-

parameter sigmoidal model (sig3) (Itasca, 2005) was chosen. Within a defined range sigmoidal curves are monotonic with appropriate asymptotic behavior. Thus the functions are well-suited for the purpose of representing modulus degradation curves. The three-parameter sigmoidal model (sig3) is defined as follows.

$$M_s = \frac{a}{1+\exp(-(L-x_0)/b)} \tag{5.1}$$

where M_s is the normalized secant modulus, L is logarithmic strain, and a, x_0, and b are fitting parameters.

Figure 5.2 shows the shear modulus degradation curves obtained from extrapolation of the experimental results and that attained from the sigmoidal model using $a = 1$, $b = -0.38$ and $x_0 = 0.5$.

Results

According to the results obtained in Chapter 3 if the EPS geofoam embankment is exposed to acceleration amplitudes equal to or higher than 0.6 g, sliding is a potential concern. Therefore a parametric study was performed on embankment models exposed to such input accelerations to obtain the minimum area requiring adhesive or shear key treatment. This was done by incrementally increasing the glued segment of the interfaces in the middle of the embankment while monitoring the relative horizontal movement of each interface at gridpoints in the vicinity of the vertical boundaries of the model.

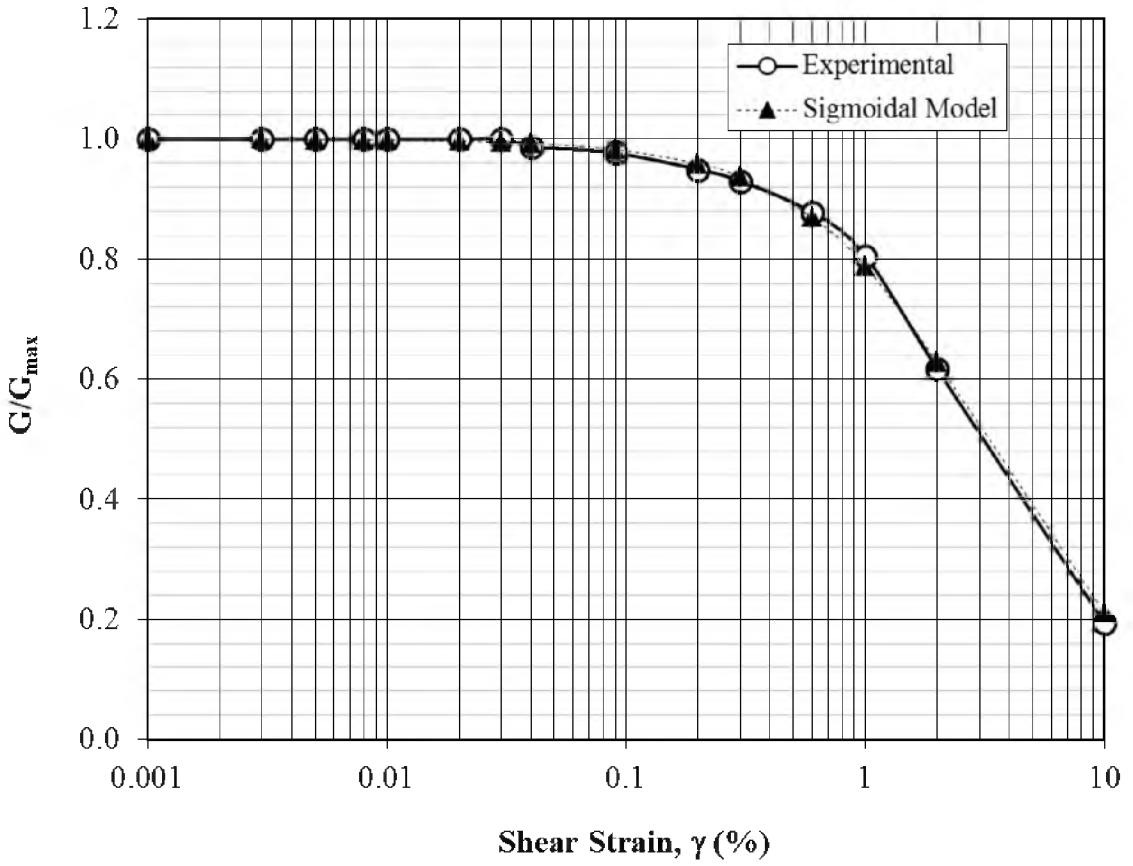

Figure 5.2. Shear modulus degradation curve used in *FLAC's* hysteretic damping option

The minimum glued segment corresponding to relative horizontal movement values below 1 inch (2.5 cm) was identified as the area requiring sliding remedies such as shear keys and adhesive. The results of FLAC analysis show that this minimum area is about 10% for embankments exposed to acceleration amplitudes of 0.6 g and 20% for those excited with 0.8 g and 1 g acceleration amplitudes. Figures 5.3, 5.4 and 5.5 show the relative horizontal movement time histories for input acceleration amplitudes of 0.6, 0.8 and 1 g, respectively. The legend in the figures is in ascending order (from bottom to top of the embankment).

Once sliding is prevented, the seismic energy may introduce high levels of shear

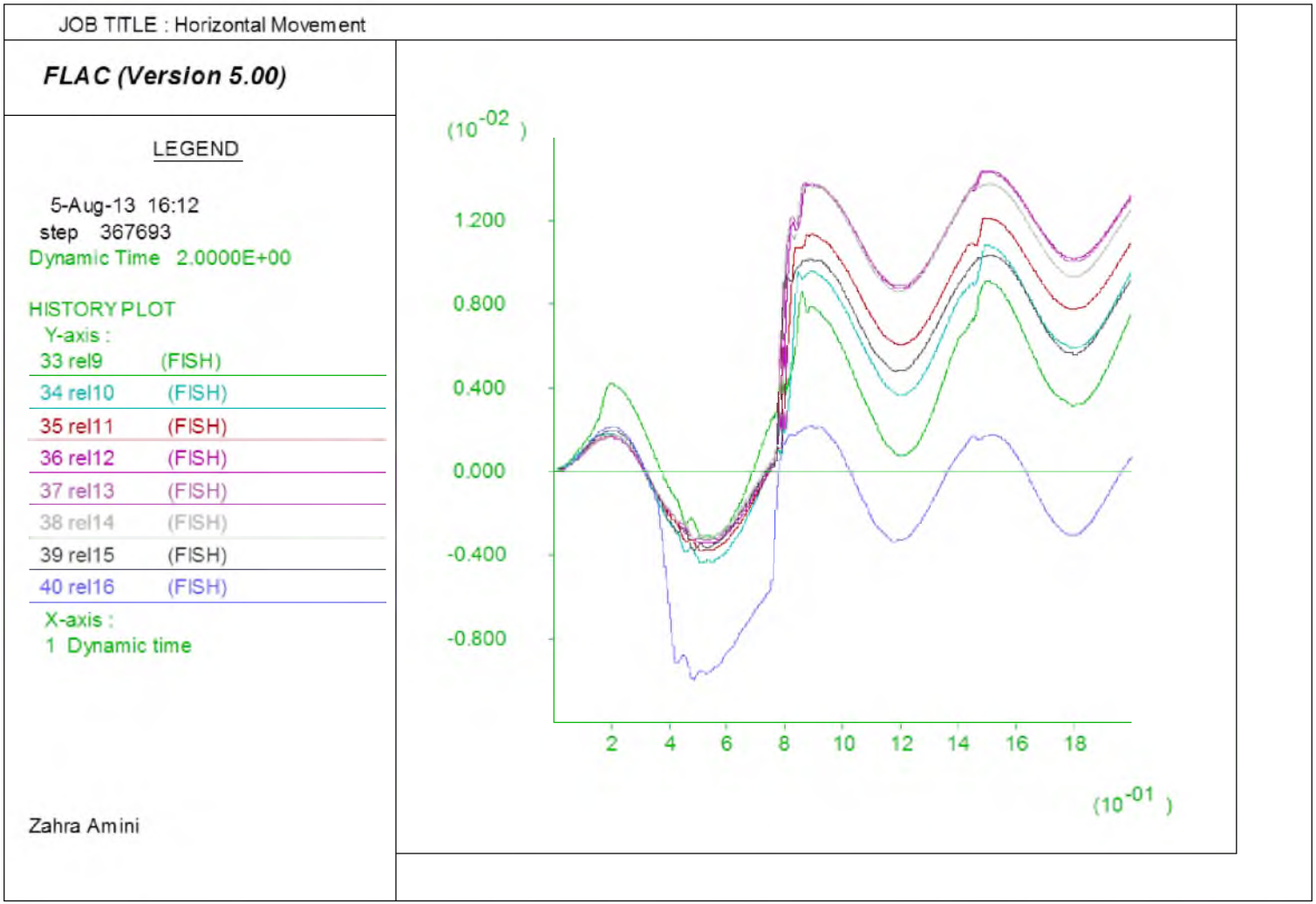

Figure 5.3. Relative horizontal movement at interfaces due to 0.6 and 0.24g horizontal and vertical amplitudes of input motion

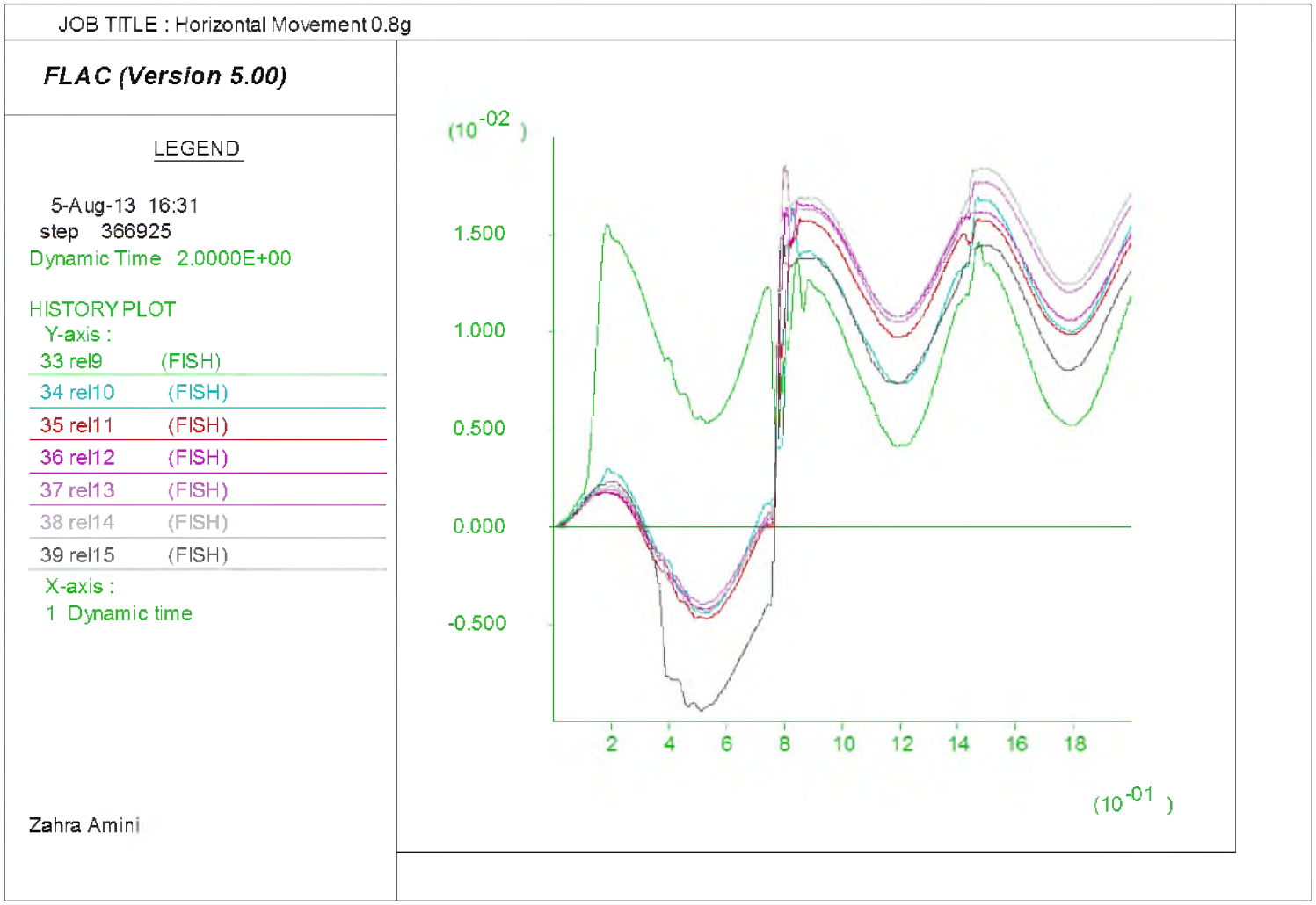

Figure 5.4. Relative horizontal movement at interfaces due to 0.8 and 0.32g horizontal and vertical amplitudes of input motion

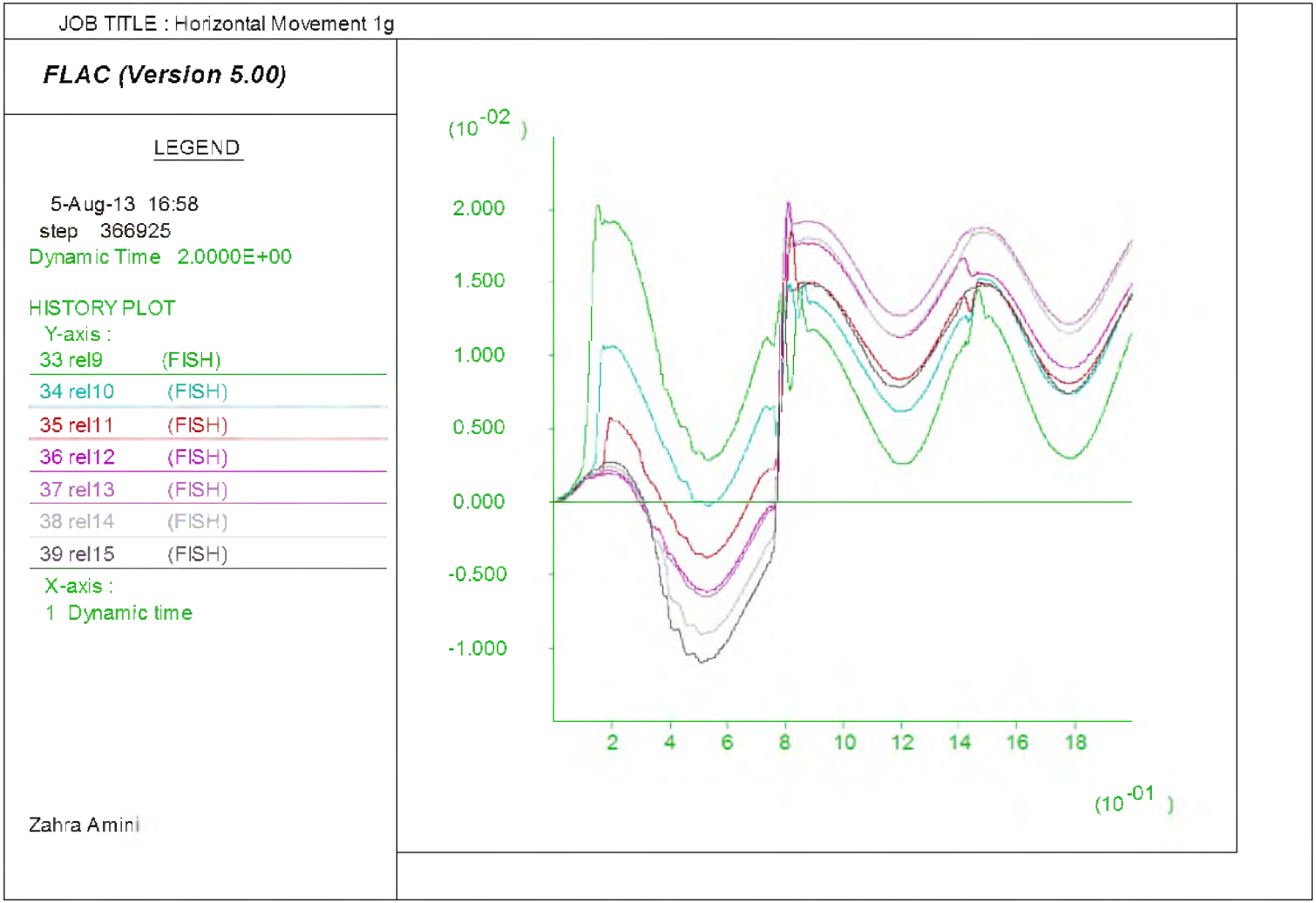

Figure 5.5. Relative horizontal movement at interfaces due to 1 and 0.4g horizontal and vertical amplitudes of input motion

or normal stresses, which may cause the system to behave nonlinearly and potential yielding of the EPS geofoam can occur. Figures 5.6, 5.7 and 5.8 show the potential locations of yielding of the EPS geofoam when the model is excited with 0.6, and 0.8 and 1 g acceleration amplitude input motions, respectively. It is shown that when exposed to 0.6 g acceleration amplitude motion the embankment system is more likely to experience high stresses at the lower corners (zones 1 and 2 in Figure 5.6). This can also be seen in the case of 0.8 g input acceleration (Figure 5.7). However, in this case a zone of stress concentration (zone 3) can also be expected immediately below the pavement system and at the boundary of the glued segment of the embankment shown in Figure 5.1. A more extreme case is when the embankment system is excited with 1 g acceleration amplitude input motion where the potential yielding zones are more extensive. As shown in Figure 5.8 broader areas at the corners of the embankment may experience high stresses compared to those associated with lower acceleration amplitudes. It is shown that stress concentration at the vertical boundaries of the glued segment is highly expected.

To identify the nature of the stresses potentially leading to yielding of the EPS geofoam material, shear and normal stresses at the zones diagnosed with potential yielding were monitored. Figure 5.9 and 5.10 illustrate the time histories of shear and normal stresses surrounding zone 1 in Figure 5.6 where the input motion has an acceleration amplitude of 0.6 g in horizontal direction. EPS 19 has shear strength of about 60 kPa and a maximum compressive strength of about 118 kPa. Figure 5.9 shows that value of shear stresses are well below 60 kPa, whereas the compressive stresses shown in Figure 5.10 exceed the compressive strength of the EPS geofoam at some time intervals. A similar trend was observed for Zone 2, however, the results are not plotted to avoid

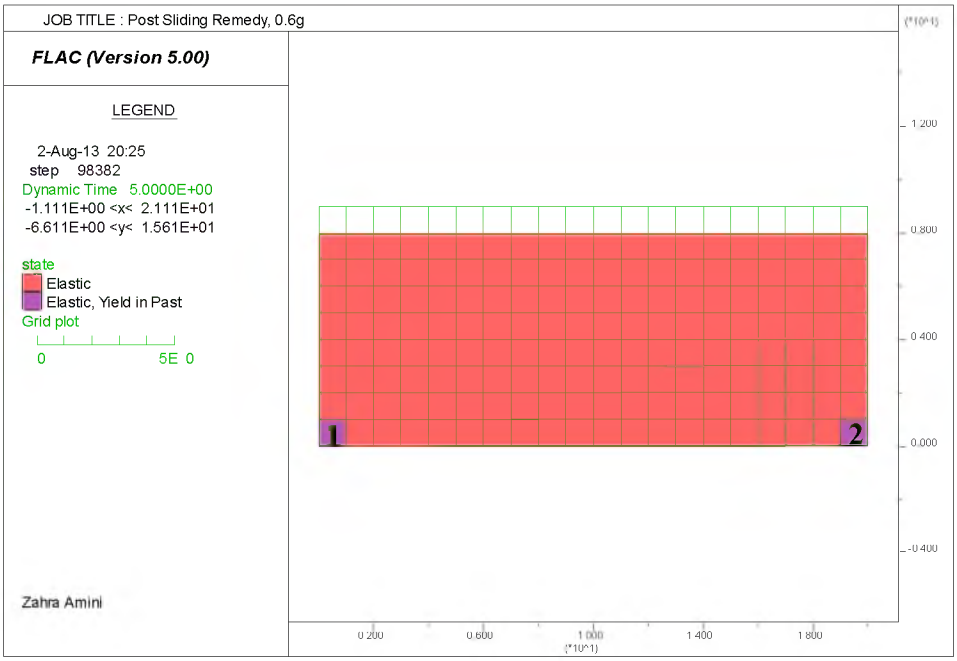

Figure 5.6. Potential yielding due to 0.6 g acceleration amplitude input motion

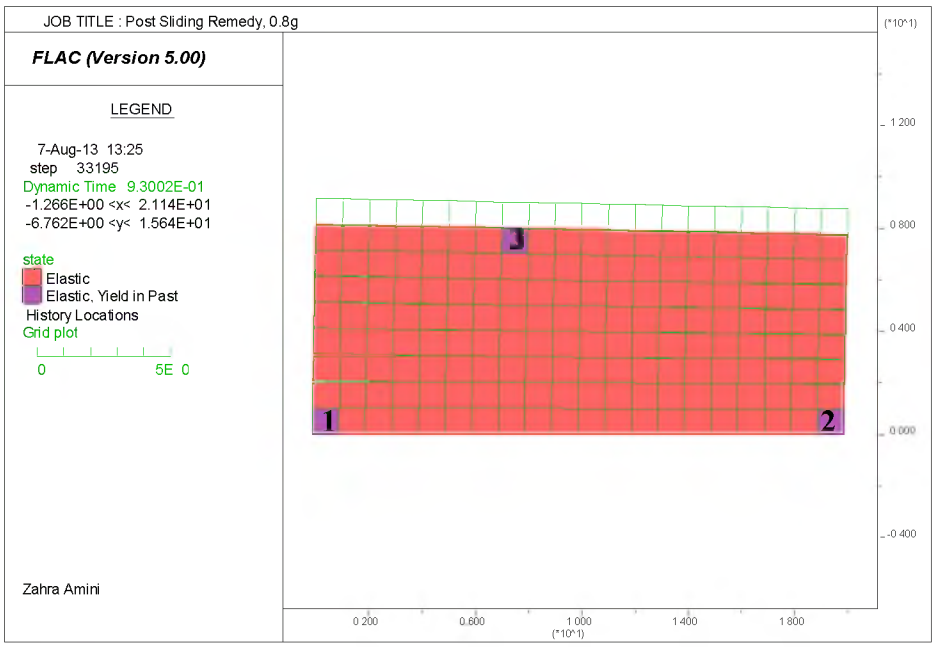

Figure 5.7. Potential yielding due to 0.8 g acceleration amplitude input motion

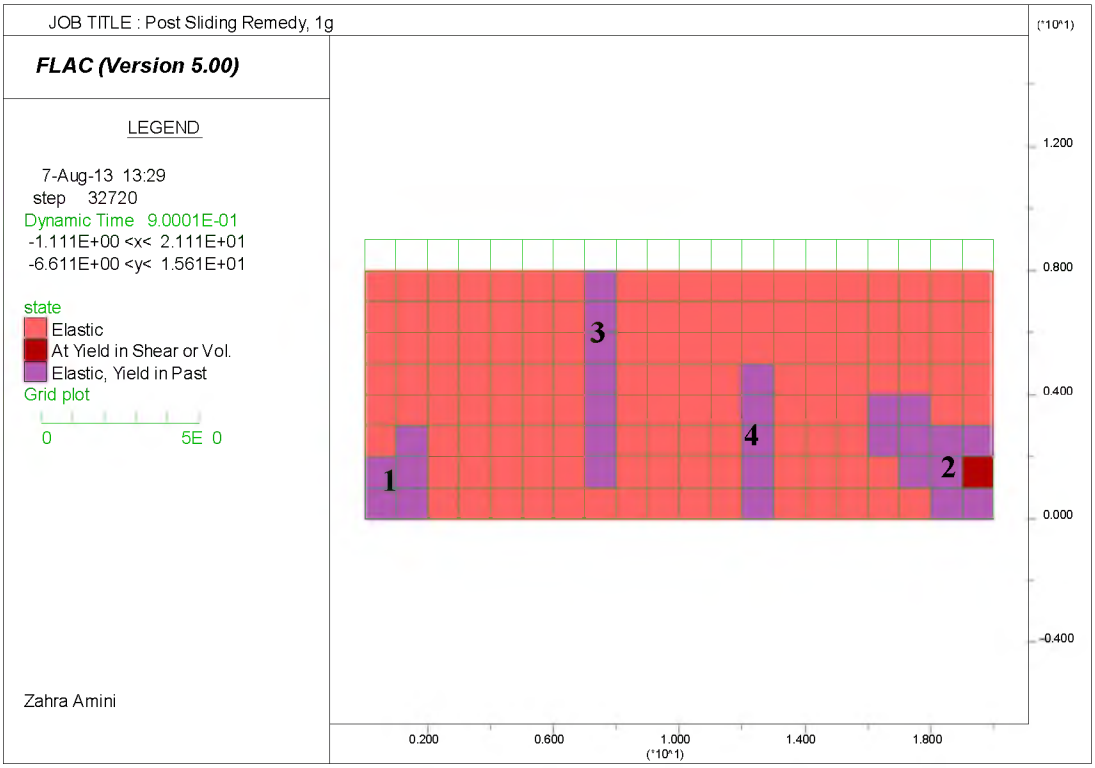

Figure 5.8. Potential yielding due to 1 g acceleration amplitude input motion

redundancy. Appendix D includes shear stress time histories through the embankment. Figures 5.11 and 5.12 show time histories of shear and normal stresses in zone 1 of Figure 5.7 where the input acceleration amplitude is 0.8 g. Shear stresses appear to remain below 60 kPa while normal stresses exceed EPS 19 compressive strength. Normal stress time history graphs illustrated in Figure 5.12 are characterized with a "flat-top" shape indicating constant normal stress over various time intervals. This occurs due to separation of the EPS geofoam blocks at the horizontal interfaces in the vertical direction when the layers are lifted due to rocking motion. This is discussed in more detail later on in this chapter.

Figures 5.13 and 5.14 show shear and normal stresses time histories in zone 3.

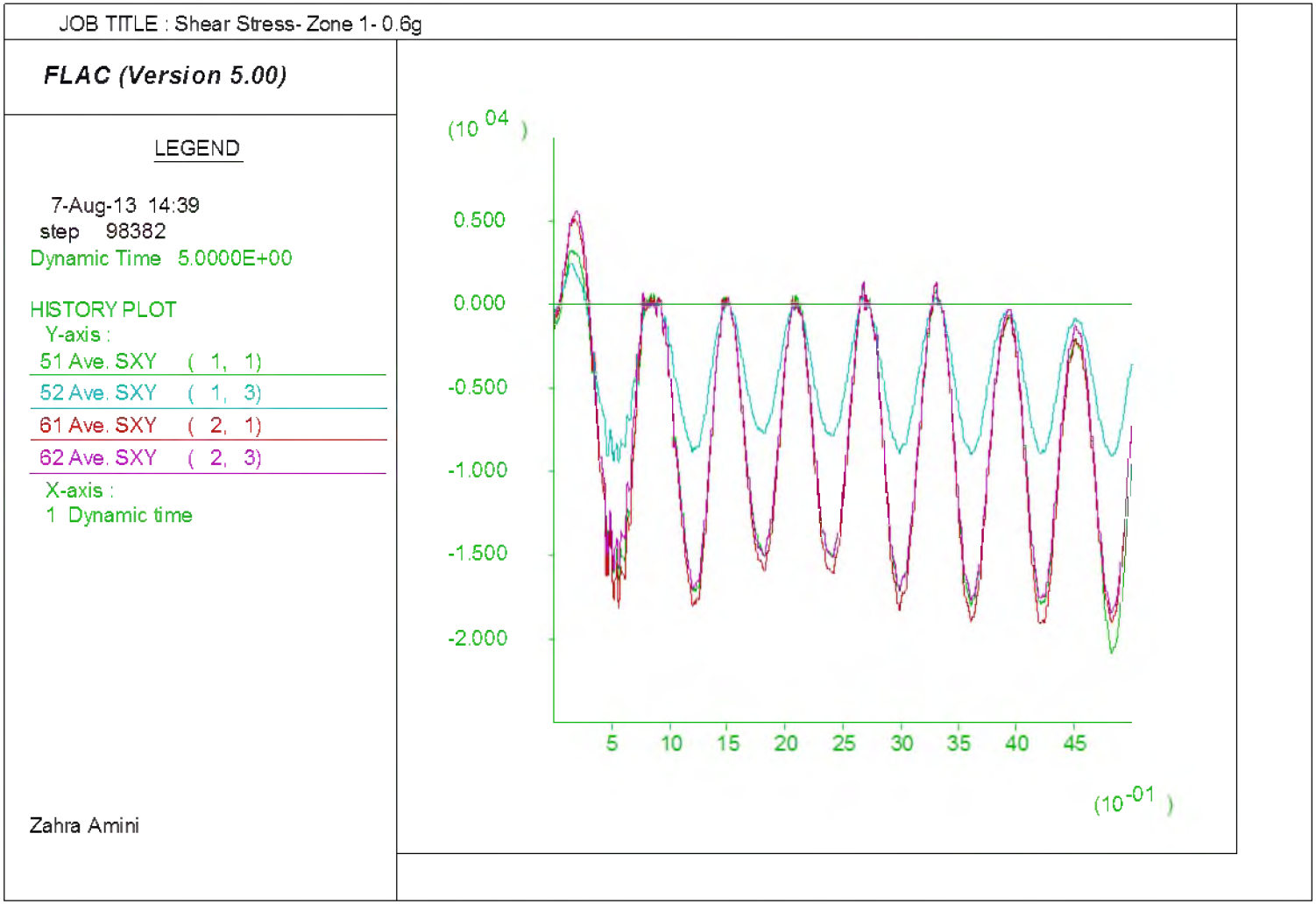

Figure 5.9. Shear stresses in zone 1 due to acceleration amplitude of 0.6g

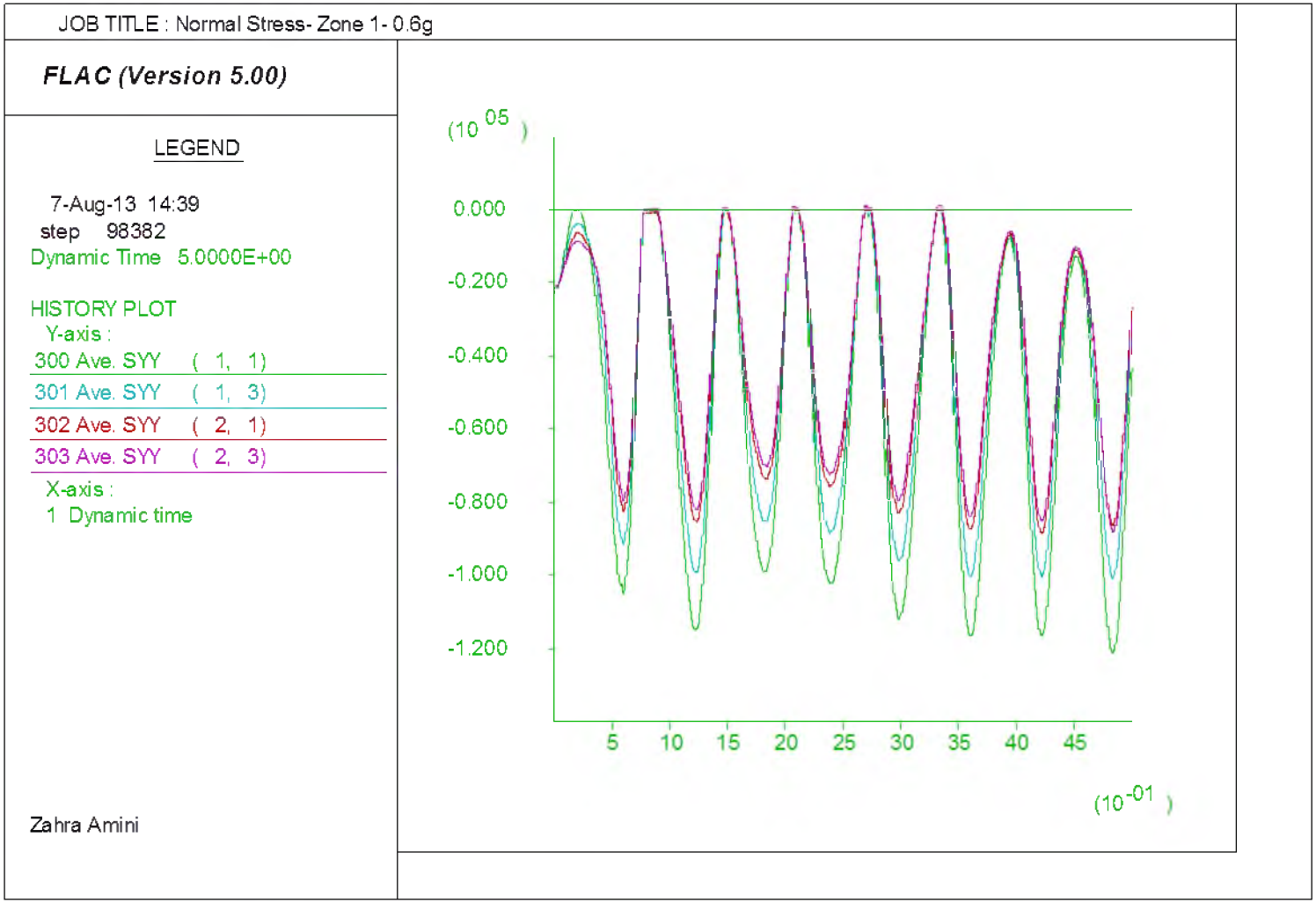

Figure 5.10. Normal stresses in zone 1 due to acceleration amplitude of 0.6g

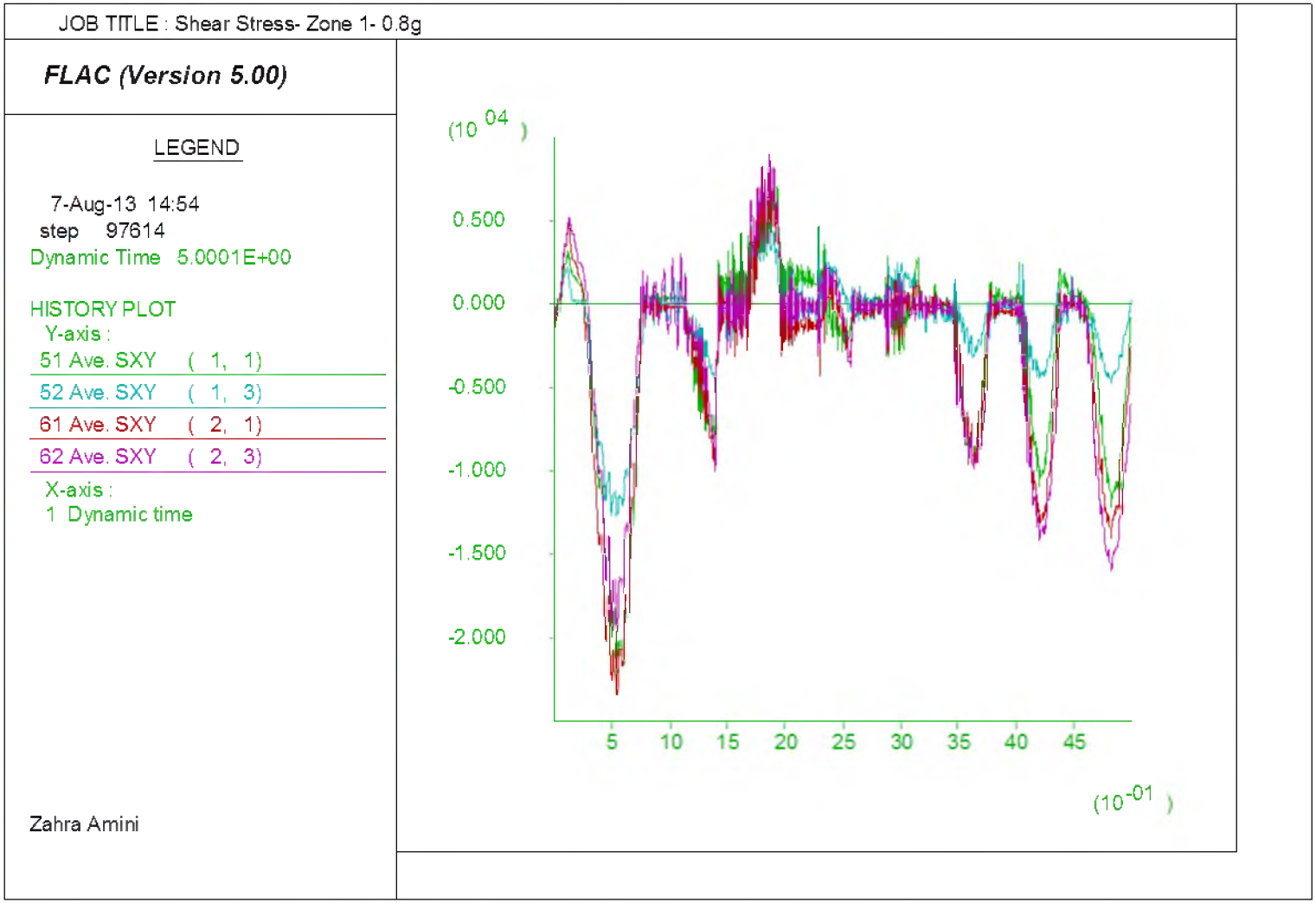

Figure 5.11. Shear stresses in zone 1 due to acceleration amplitude of 0.8g

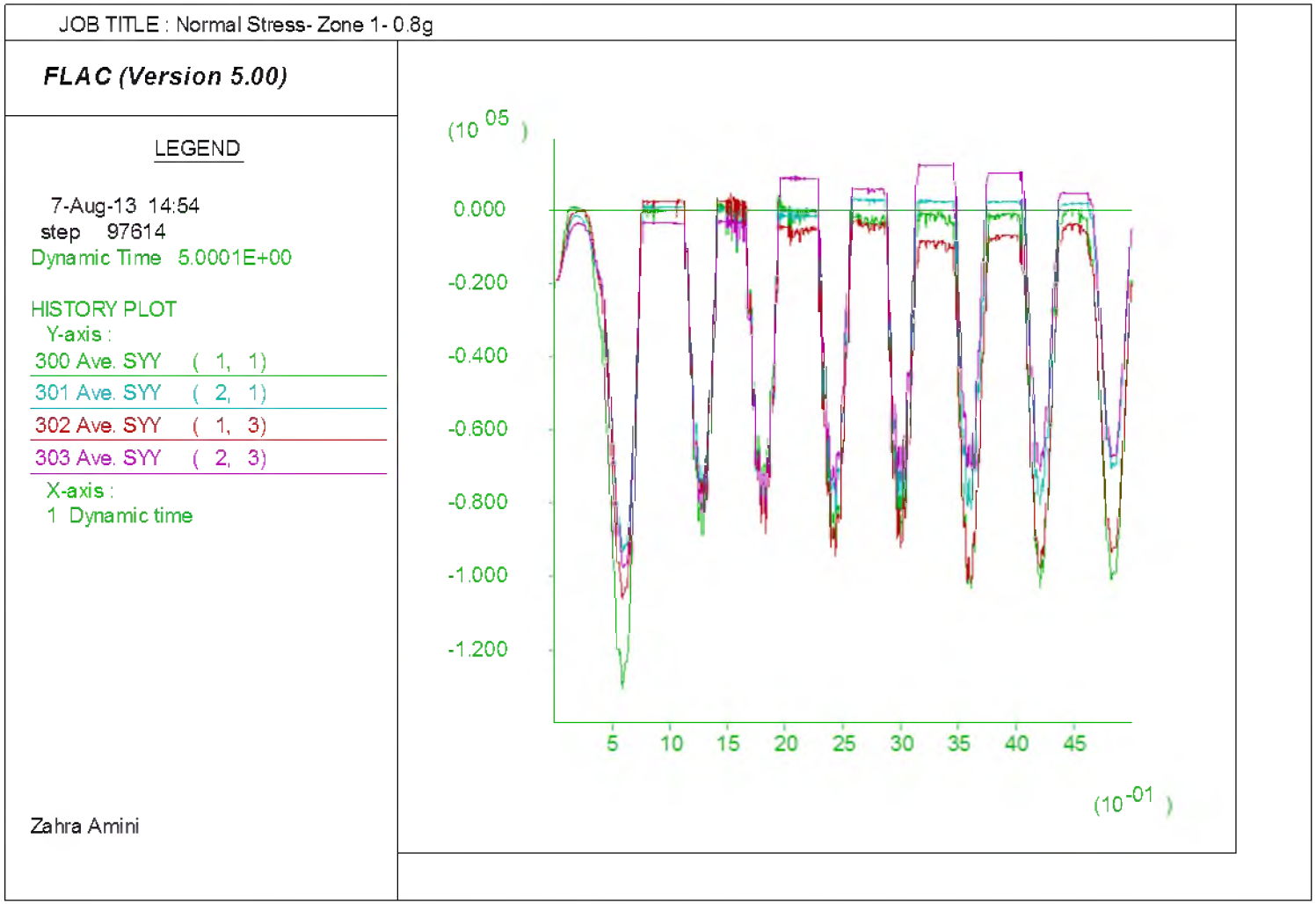

Figure 5.12. Normal stresses in zone 1 due to acceleration amplitude of 0.8g

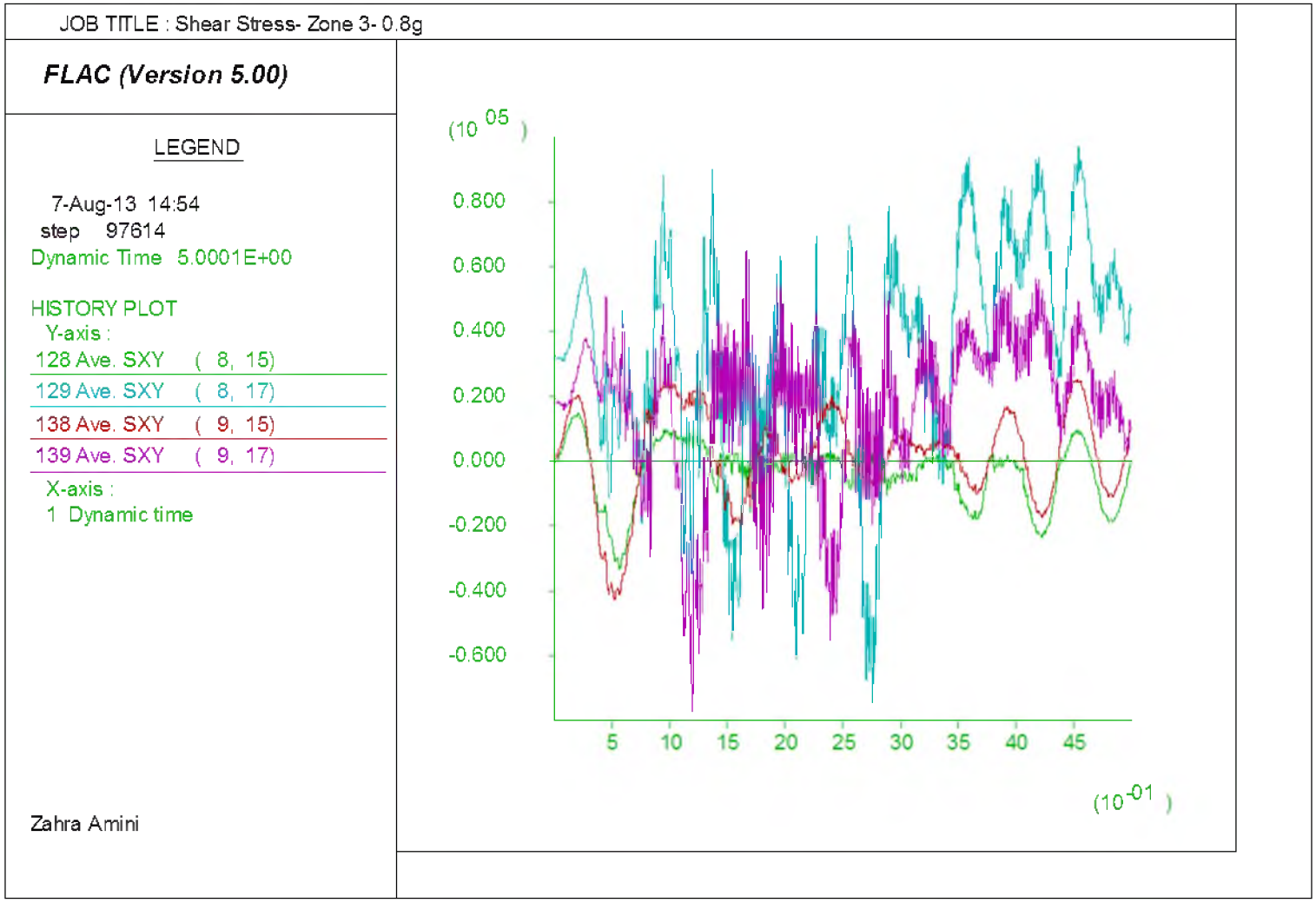

Figure 5.13. Shear stresses in zone 3 due to acceleration amplitude of 0.8g

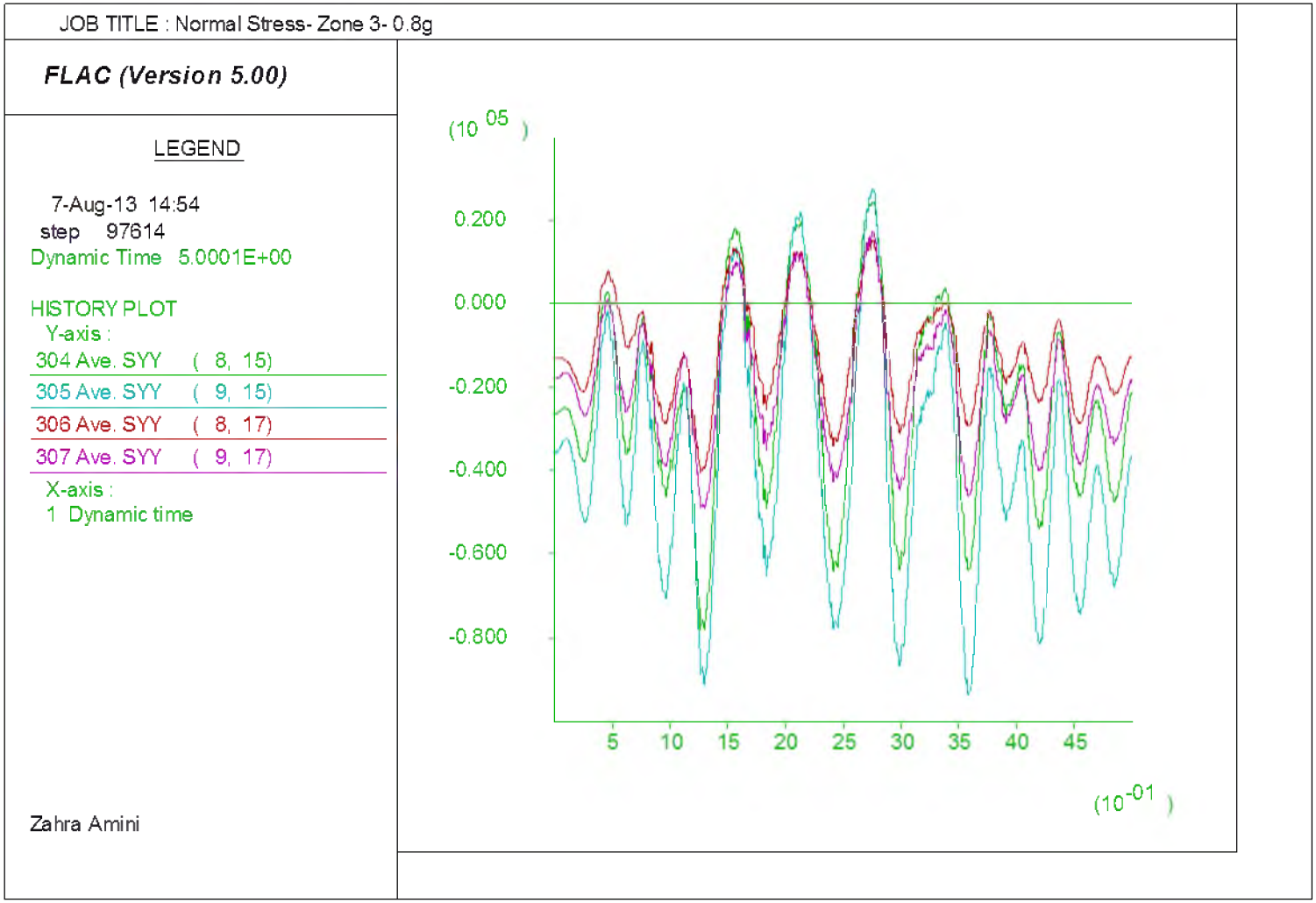

Figure 5.14. Normal stresses in zone 3 due to acceleration amplitude of 0.8g

Figure 5.13 indicates high shear stress concentration in this zone particularly at the boundary of the uppermost layer of EPS and the pavement system. According to Figure 5.14 stresses are not sufficiently large to cause any yielding in compression. Similar phenomena were observed in the model excited with 1 g acceleration where compressive stresses at the corners of the embankment exceed compressive strength of the EPS and significant concentrations of shear stresses occurred adjacent to the vertical boundaries of the glued segment of the embankment. However, the extent of potential yielding area in this case can be excessive and therefore EPS 19 may not be appropriate to be used at sites susceptible to such levels of ground motion. What leads to stress concentration patterns discussed here lies under the type of movement that the embankment experiences while exposed to seismic forces. Figure 5.15 shows the evolution of the embankment model movement when exposed to a horizontal acceleration amplitude of 0.6 g along with vertical acceleration amplitude of 0.24 g. The system experienced a sway-like movement in early stages of the excitation (Figure 5.15 (a) followed by rocking up and down (Figure 5.15 (b) and (c) as the motion carried on. As shown in Figure 5.15 (b) while one side of the embankment (the left side in this snap shot) is under compression the opposite side experiences tension. However, no tensile yielding of the EPS material was detected. This may be because once the side of the embankment is under tension, horizontal interfaces allow for slight separation of the blocks in the vertical direction when some energy dissipation takes place and thus tensile failures are prevented. Nevertheless, the side of the embankment under compression may experience compressive stresses exceeding EPS geofoam's compressive strength and hence local failure of the material is likely.

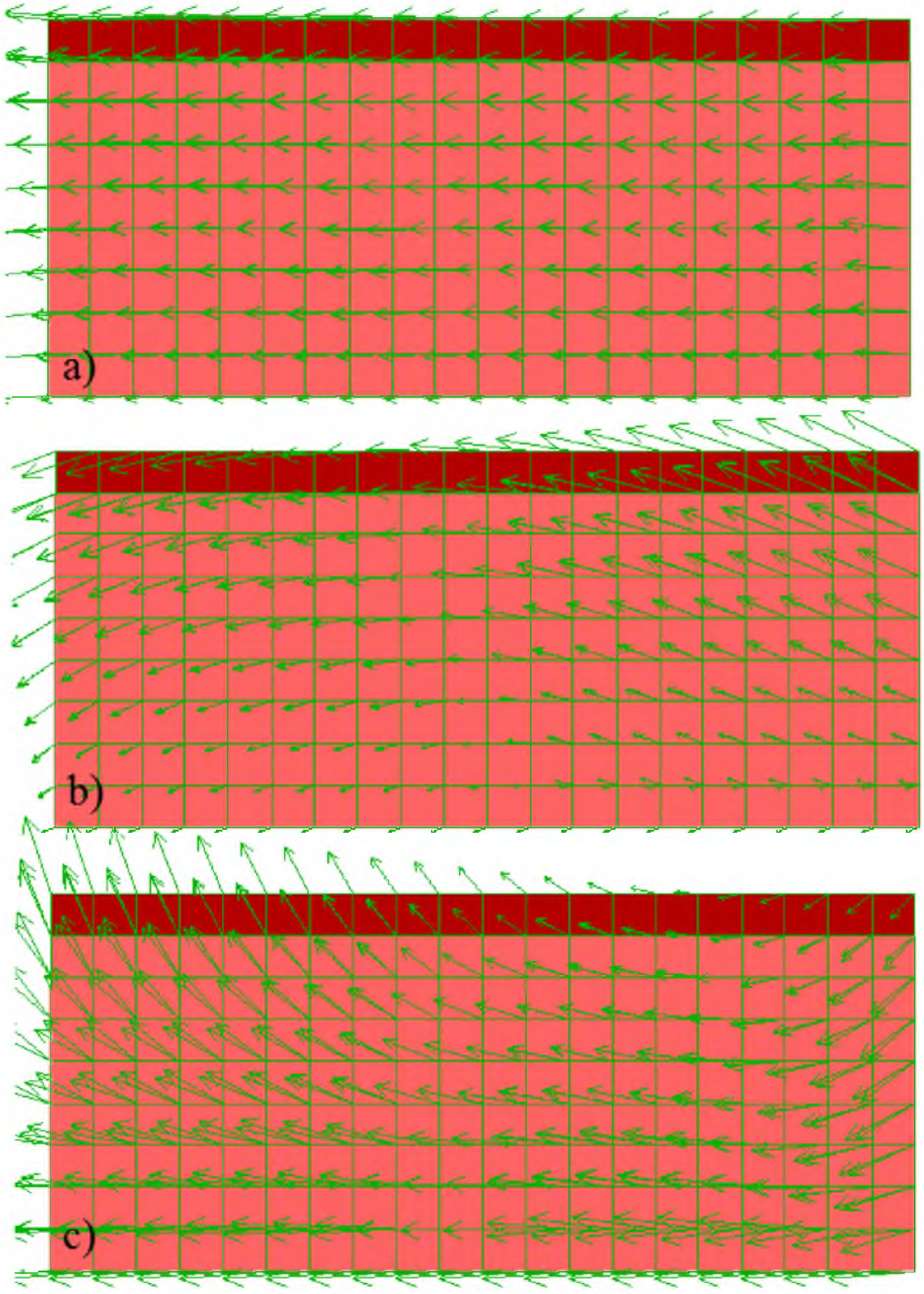

Figure 5.15. EPS geofoam embankment model: a) Sway, b) Rocking downward and c) Rocking upward motion

Conclusions

Interlayer sliding in EPS geofoam embankment can be prevented by the use of shear keys and proper adhesive. FLAC analysis results show that this is achievable by applying such sliding preventive methods between the EPS 19 geofoam layers covering 10% of the area where the embankment is susceptible to ground motion accelerations of 0.6 g, and 20% where the embankment is likely to experience acceleration amplitudes of 0.8 to 1 g.

Postsliding remedy FLAC analysis was performed by applying the hysteretic damping obtained from experimental studies to the embankment model. Models showed a sequence of sway and rocking type of movement.

When exposed to acceleration amplitudes of 0.6 to 0.8 g the EPS geofoam blocks placed in the lower corners of the embankment may experience local stress concentrations which can be accommodated by the use EPS geofoam of higher densities with higher compressive strength. Higher amplitudes of acceleration are likely to produce stresses that exceed the strength of the EPS 19 and consequently cause yielding of the material in significant number of zones particularly in the vicinity of the segment treated with adhesive or shear keys and in the corners of the embankment.

CHAPTER 6

CONCLUSIONS

Dynamic behavior and interlayer sliding of freestanding vertical EPS geofoam embankment has been investigated using laboratory testing and numerical modeling. The overall conclusion is that interlayer sliding may occur if the embankment is exposed to acceleration amplitudes of 0.6 g or higher. However, interlayer sliding can be prevented using shear keys and proper adhesive if applied over an appropriate extent of area. Use of EPS geofoam with a higher density and compressive strength compared to those of EPS 19 must be considered at the lower corners of the embankment and throughout the entire embankment at the sites susceptible to acceleration amplitudes greater than 0.8 g.

It was concluded that the Japanese Design Equation gives better estimates of the fundamental period for aspect ratios of 1.5, or lower; whereas the equation published in NCHRP reports (Stark et al., 2000) gives better results for wider EPS geofoam embankments (i.e., those with aspect ratios of 2 or higher). The experimental study showed that a commercially available adhesive designated for use on EPS geofoam is capable of withstanding forces that may potentially be imposed to the EPS/EPS boundary in a typical embankment. It was also observed that neither EPS nor the adhesive show any signs of degradation after treating with freeze-heat cycles.

It was concluded that in order to predict the full dynamic behavior of the EPS geofoam embankment it is essential to consider the layered structure of the embankment and once interlayer sliding is initiated, the EPS embankment ceases to behave as a coherent mass unlike what is assumed in the current NCHRP design guidelines.

This horizontal relative movement between layers is generally initiated at the lowermost interlayer and propagates upwards to the top of the embankment. Sliding is a very efficient energy dissipating mechanism therefore the extent of the movement decreases with time. It is concluded that disregarding the vertical component of the input motion does not appear to be conservative in predicting both the maximum extent of sliding and its location for high levels of input acceleration.

Interlayer sliding in EPS geofoam embankment can be prevented by the use of shear keys and proper adhesive. FLAC analysis results show that this is achievable by applying such sliding preventive methods between the EPS geofoam layers covering 10% of the area where the embankment is susceptible to ground motion accelerations of 0.6 g, and 20% where the embankment is likely to experience acceleration amplitudes of 0.8 to 1 g. It is recommended that the EPS blocks placed at the edges of the embankment and susceptible to block walk-out also be secured by application of adhesive.

When exposed to acceleration amplitudes of 0.6 to 0.8 g the EPS geofoam blocks placed in the lower corners of the embankment may experience local stress concentrations which can be accommodated by the use EPS geofoam of higher densities. Higher amplitudes of acceleration are likely to produce stresses that exceed the strength of the EPS 19 and cause yielding in a number of zones particularly in the vicinity of the segment treated with adhesive or shear keys and in the corners of the embankment.

APPENDIX A

EPS GEOFOAM EXPERIMENTAL DATA

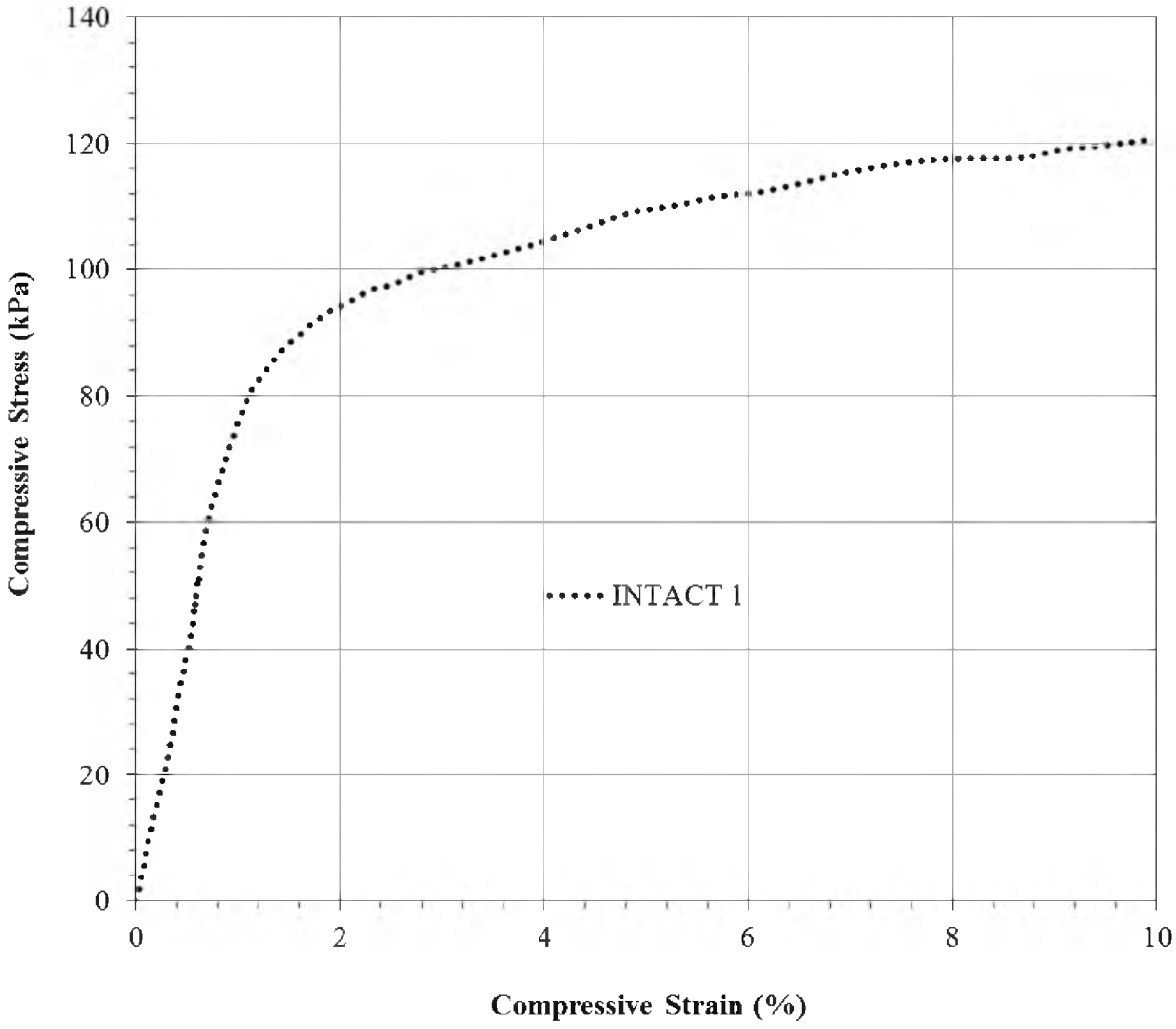

Figure A.I. Stress-strain behavior of an intact EPS with "INTACT 1" specimen ID in compression

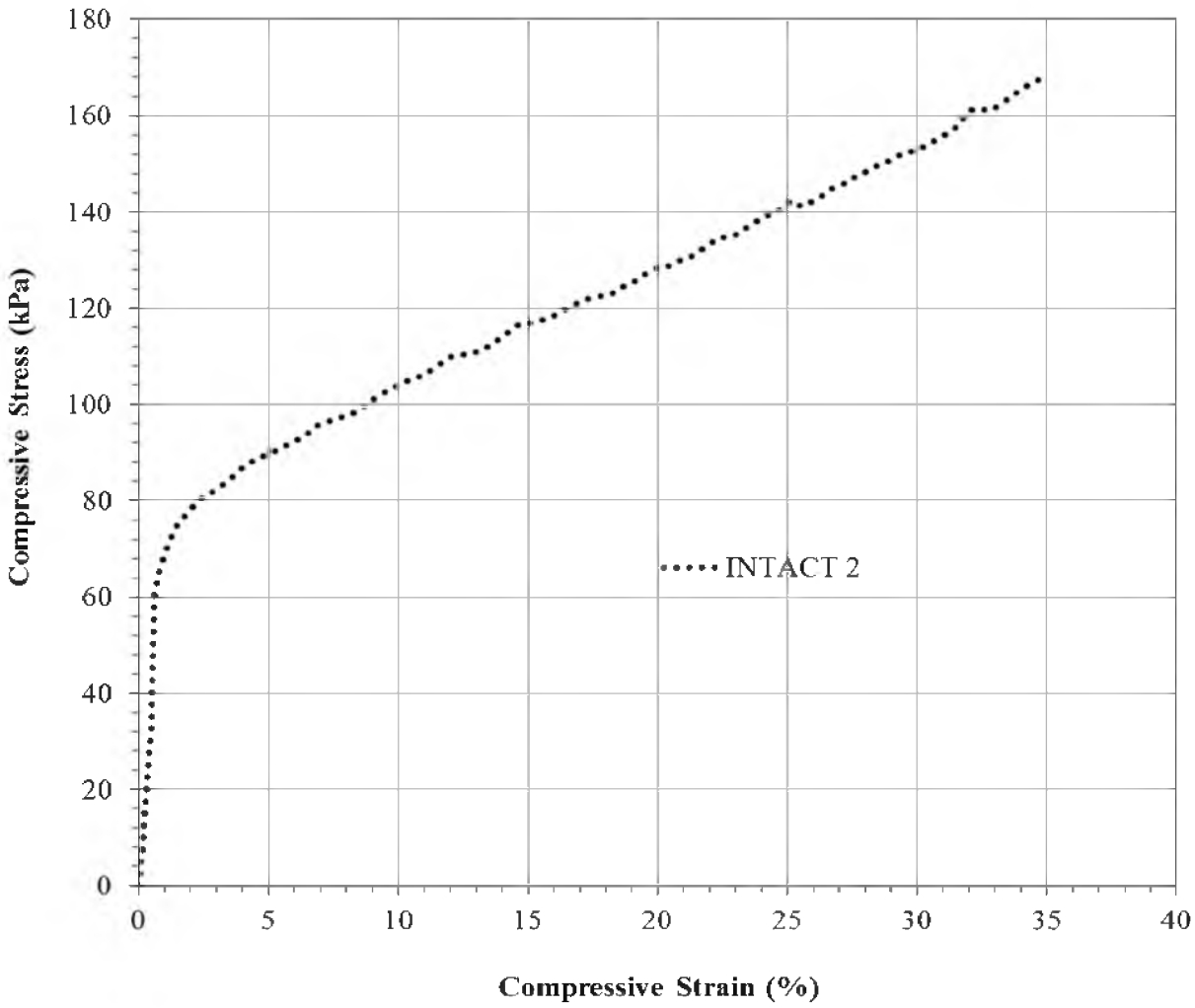

Figure A.2. Stress-strain behavior of an intact EPS with "INTACT 2" specimen ID in compression

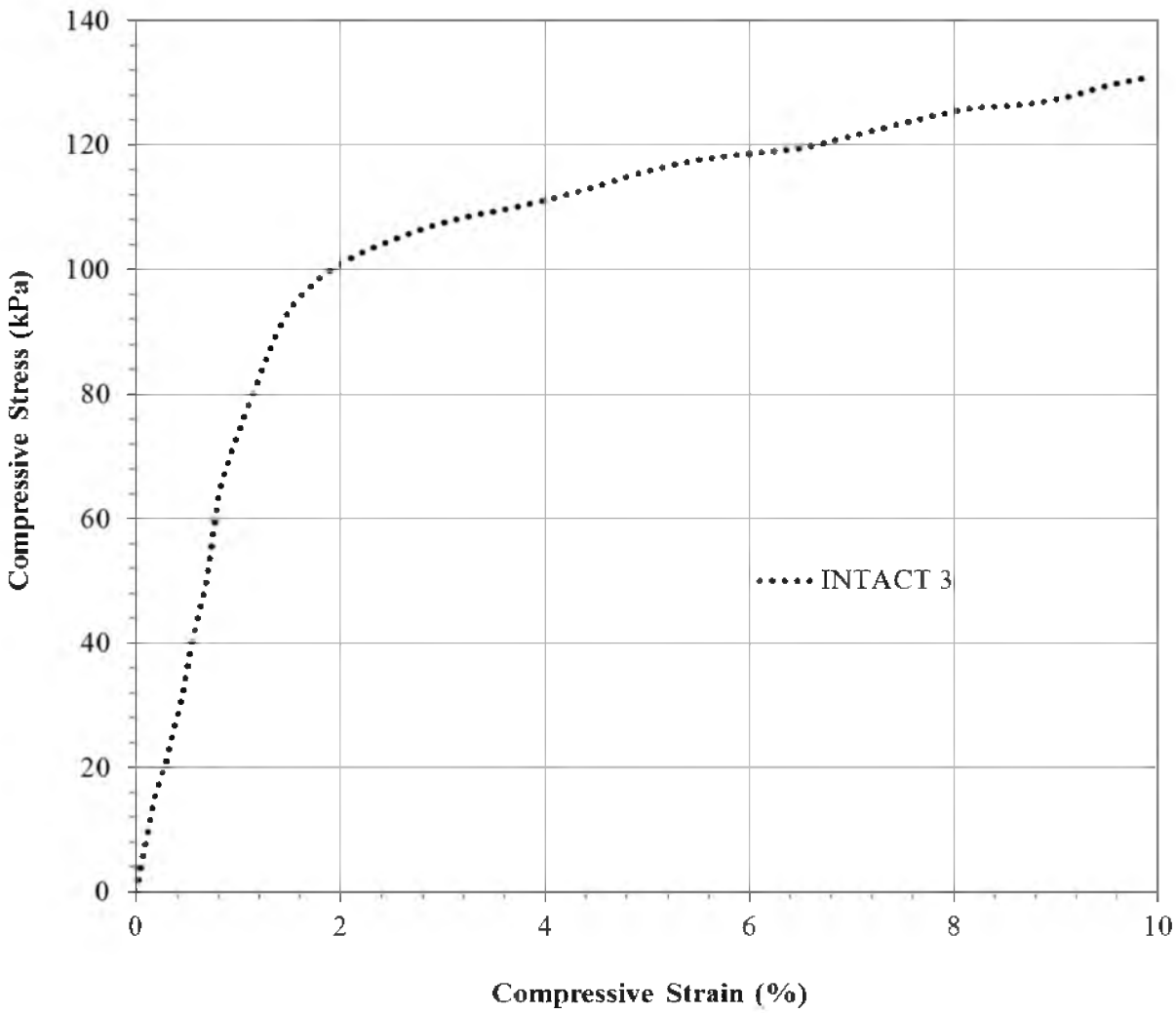

Figure A.3. Stress-strain behavior of an intact EPS with "INTACT 3" specimen ID in compression

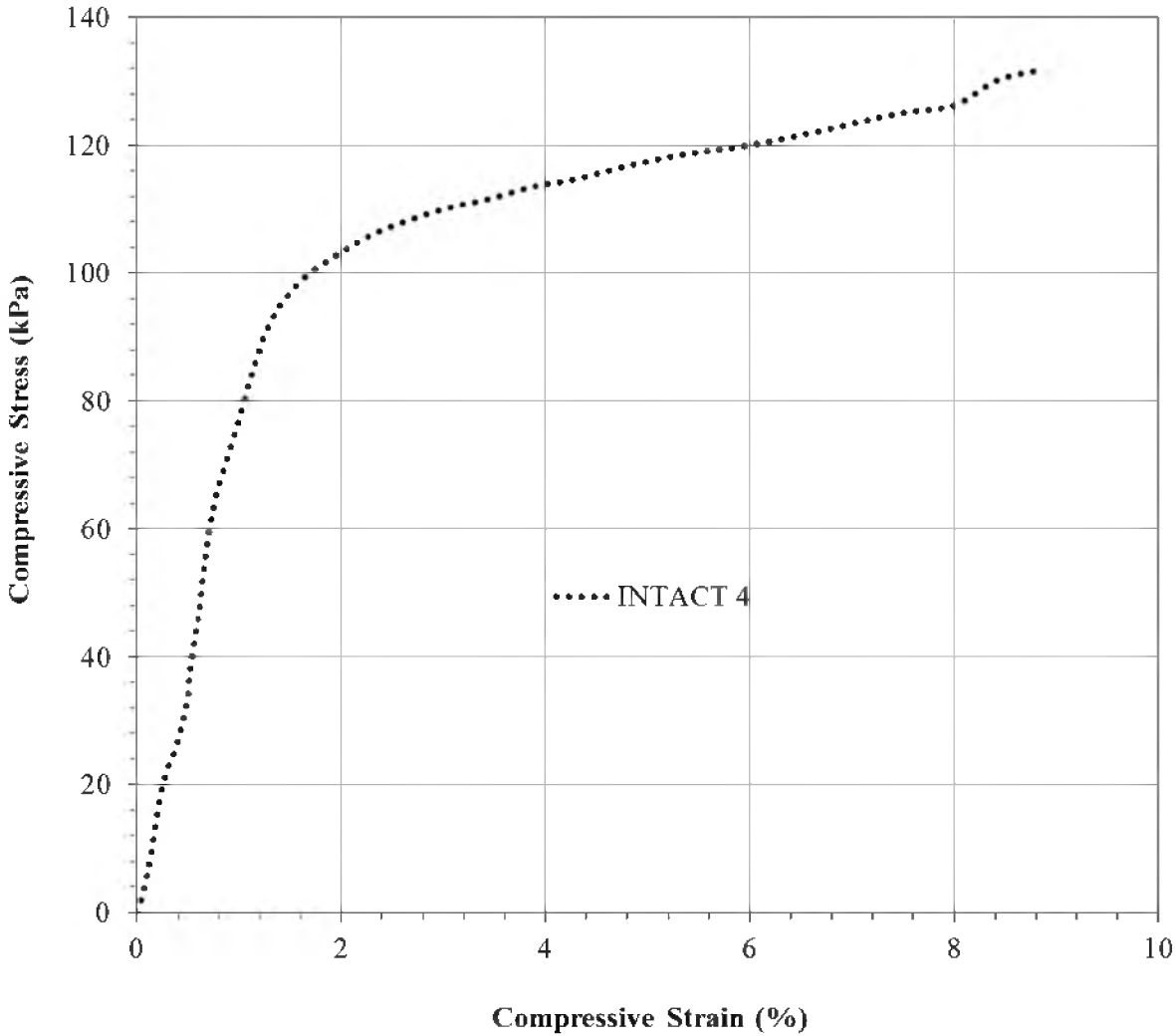

Figure A.4. Stress-strain behavior of an intact EPS with "INTACT 4" specimen ID in compression

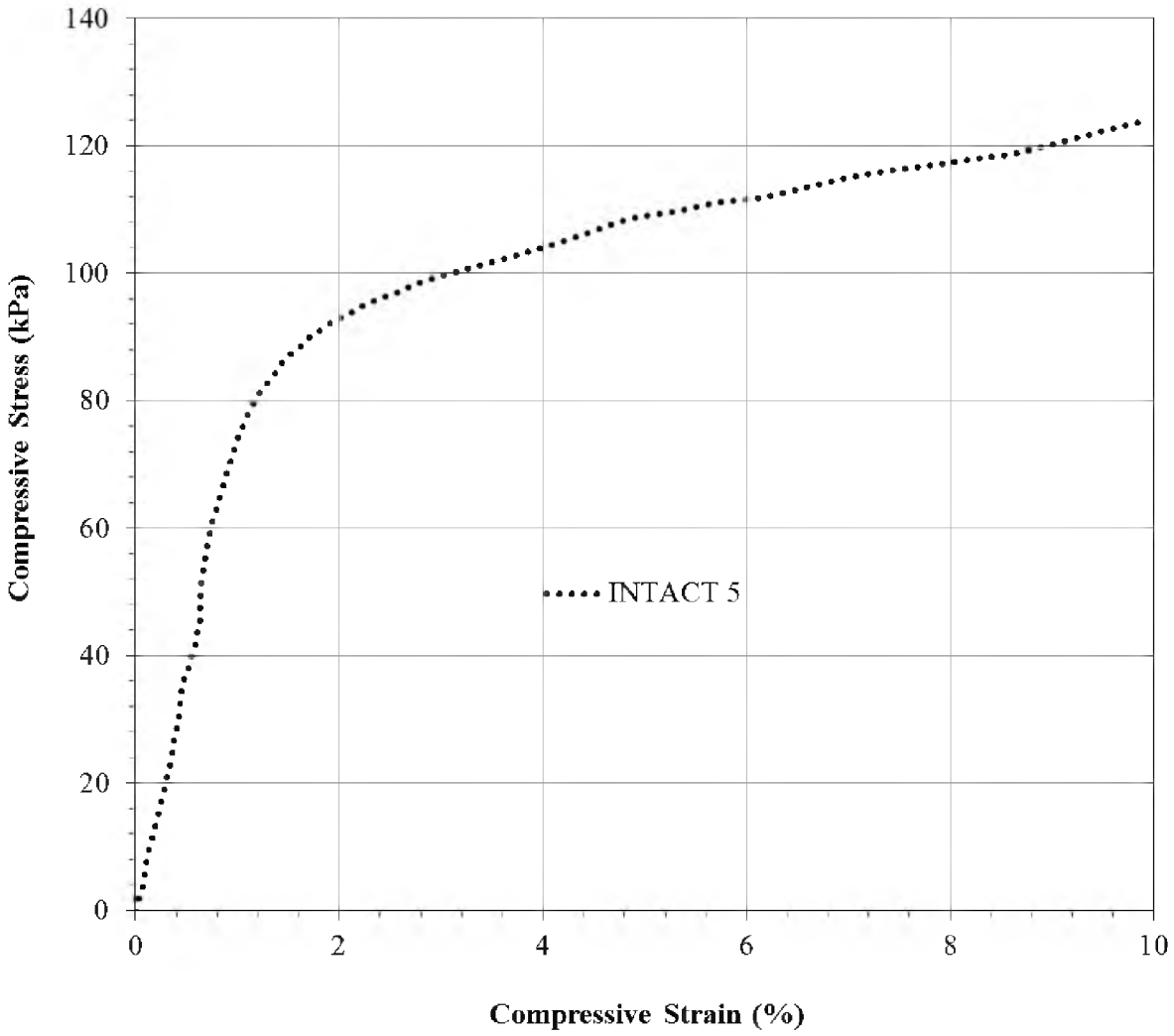

Figure A.5. Stress-strain behavior of an intact EPS with "INTACT 5" specimen ID in compression

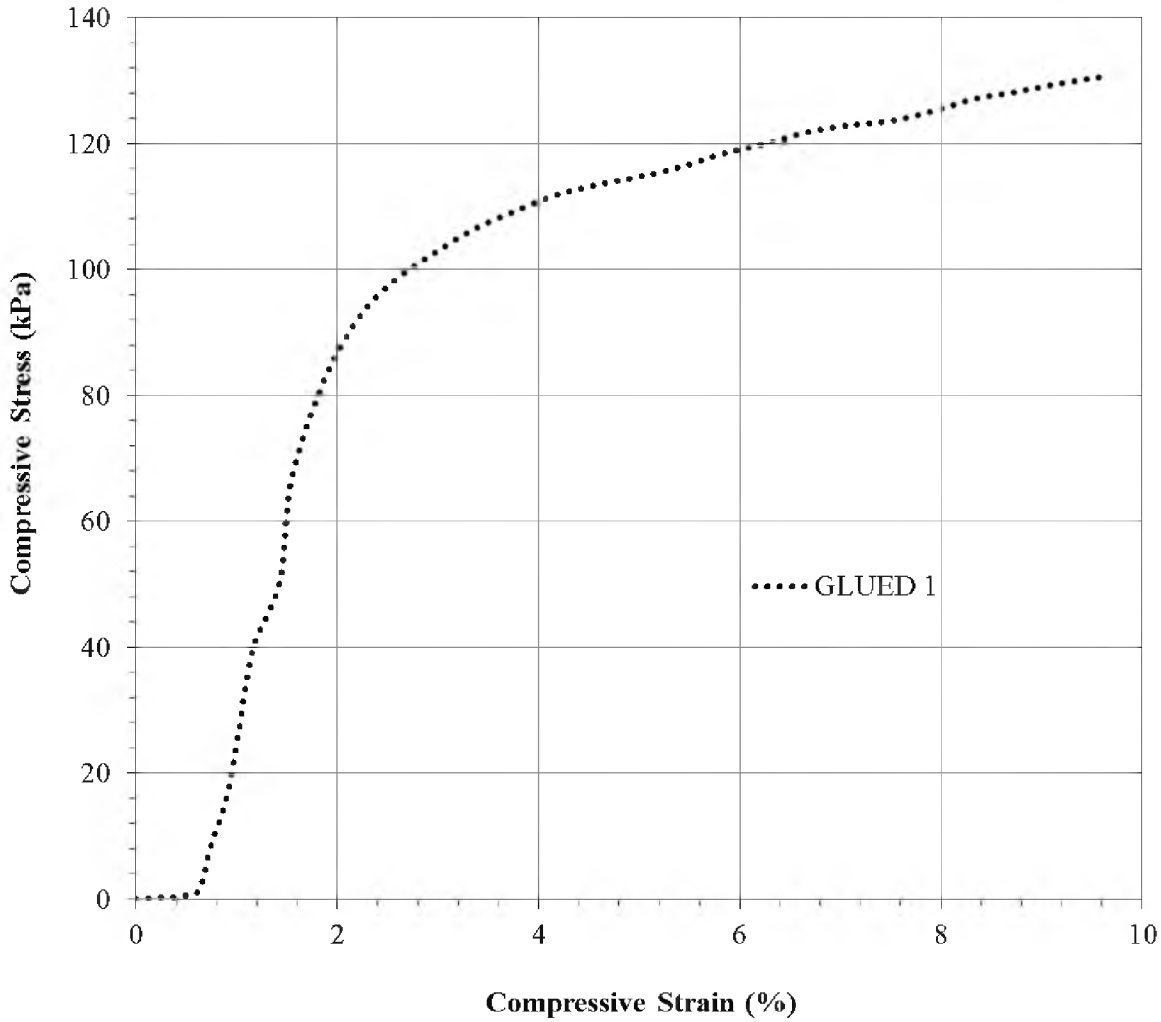

Figure A.6. Stress-strain behavior of a glued EPS with "GLUED 1" specimen ID in compression

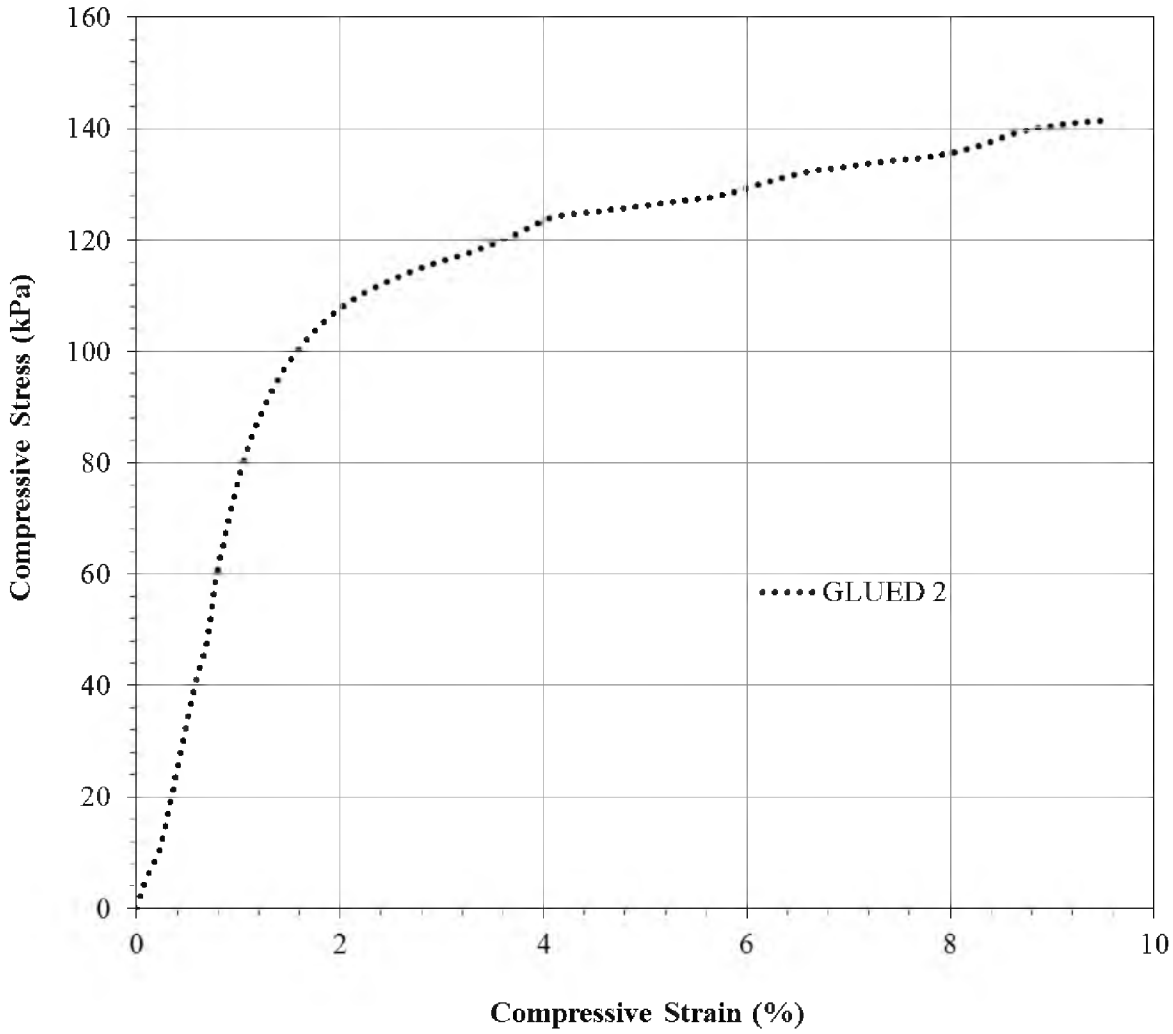

Figure A.7. Stress-strain behavior of a glued EPS with "GLUED 2" specimen ID in compression

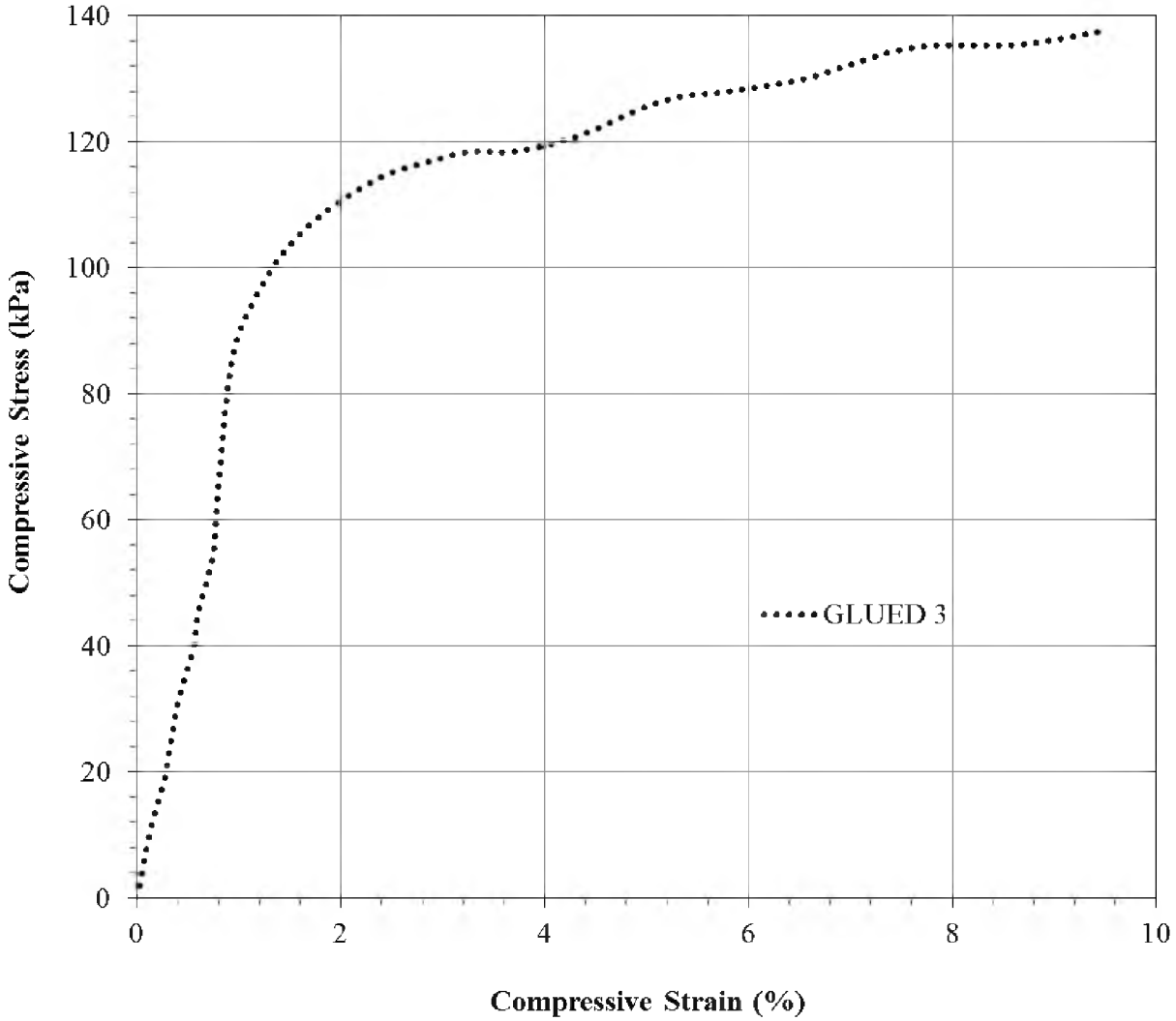

Figure A.8. Stress-strain behavior of a glued EPS with "GLUED 3" specimen ID in compression

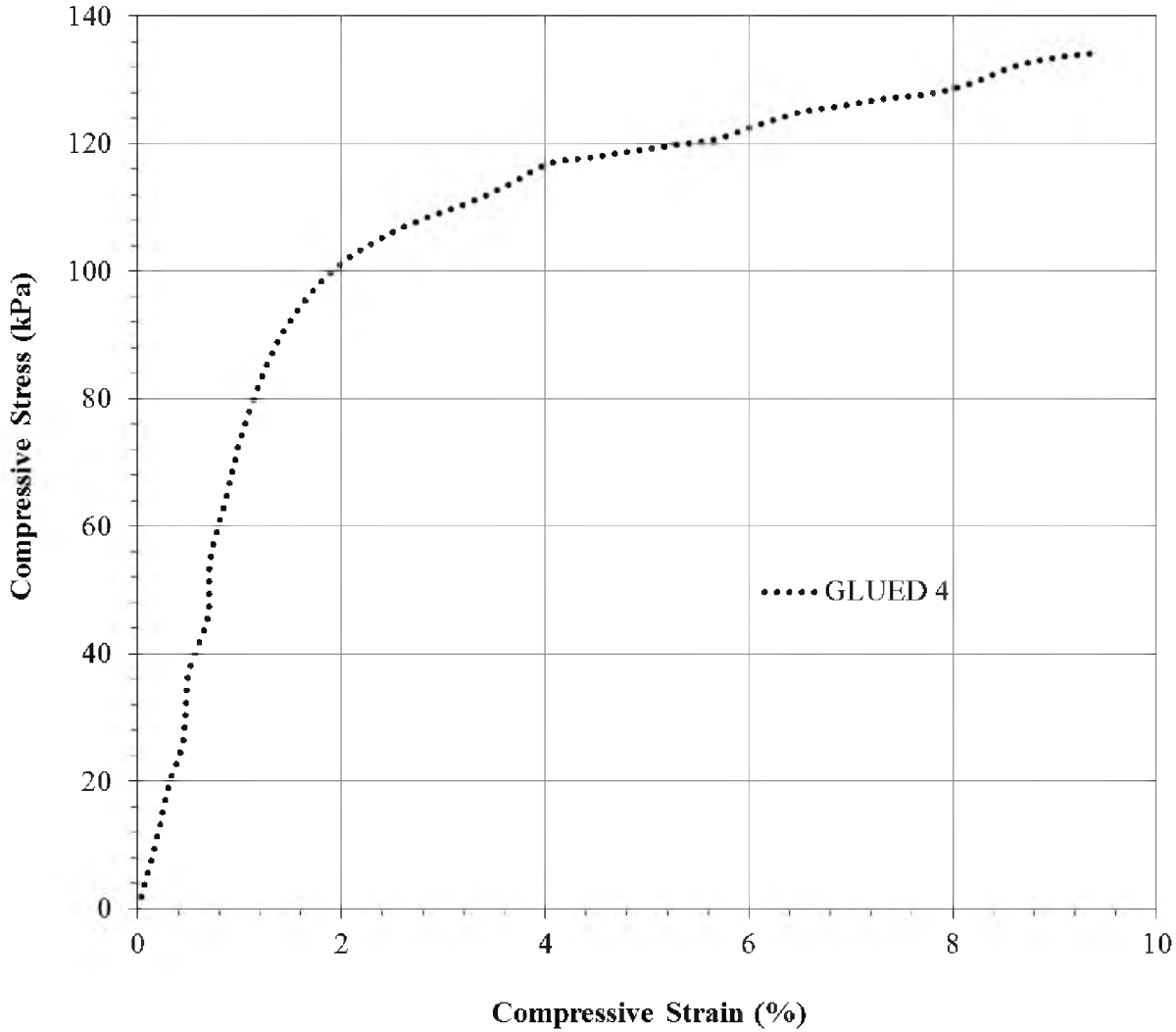

Figure A.9. Stress-strain behavior of a glued EPS with "GLUED 4" specimen ID in compression

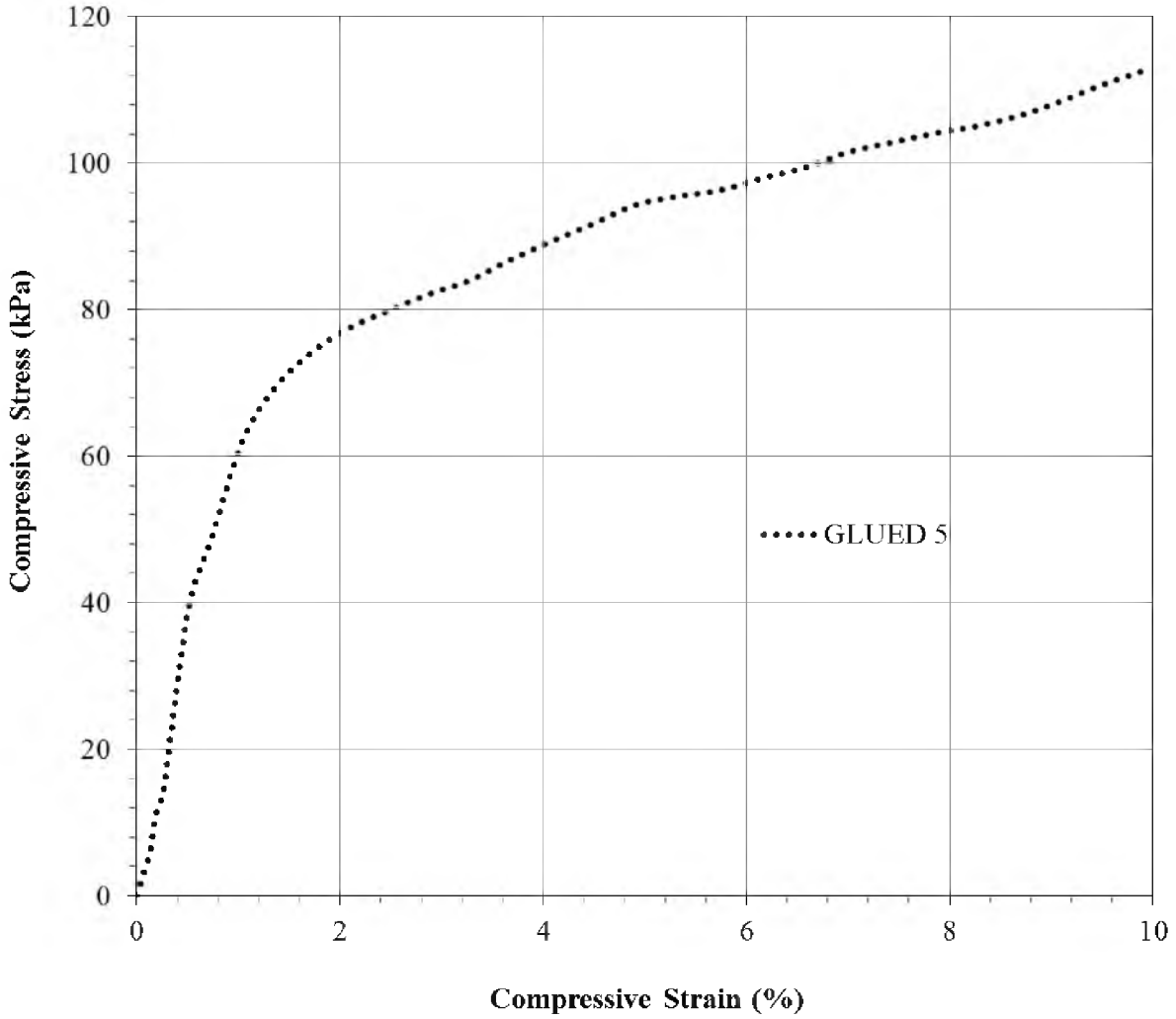

Figure A.10. Stress-strain behavior of a glued EPS with "GLUED 5" specimen ID in compression

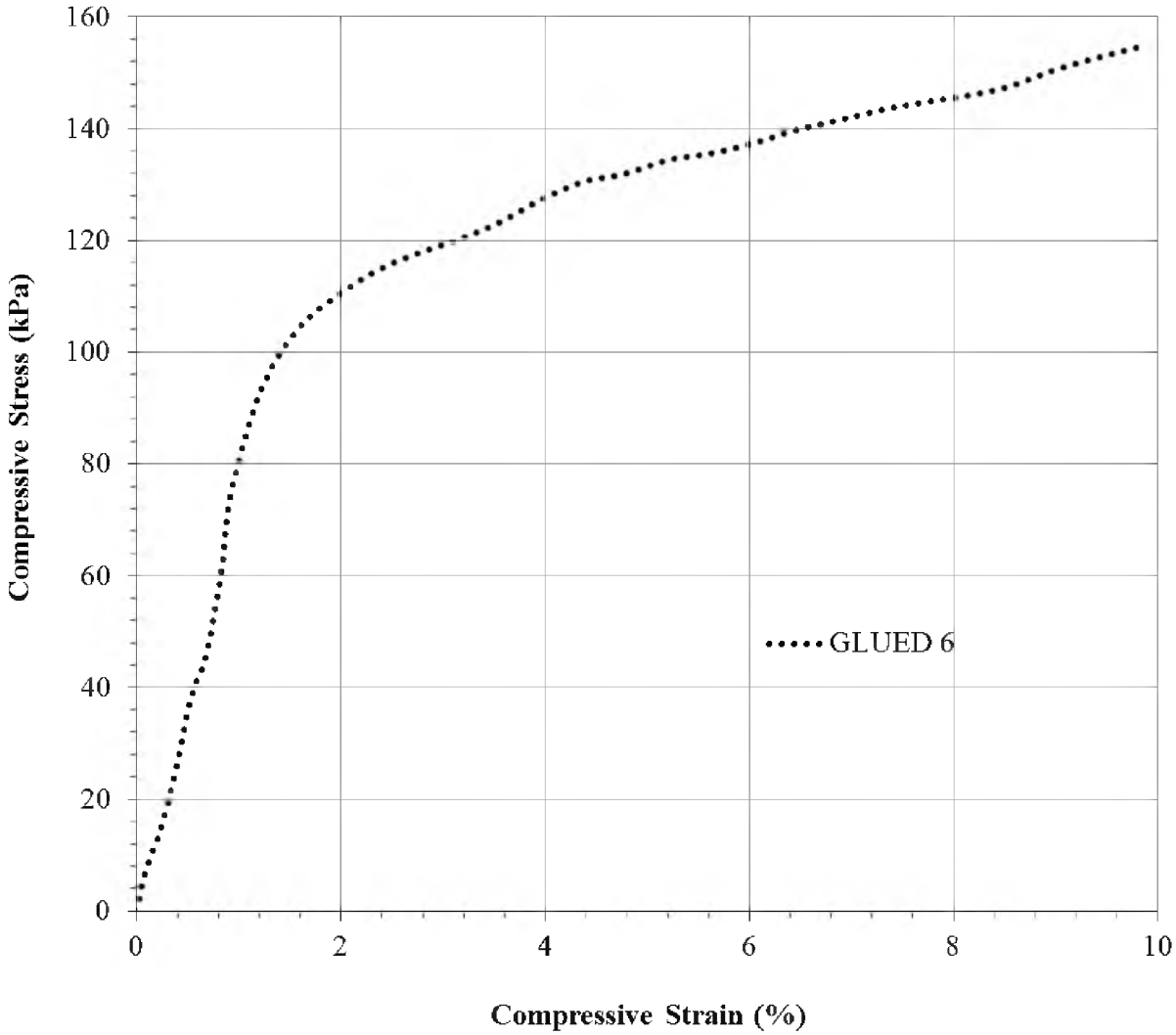

Figure A.11. Stress-strain behavior of a glued EPS with "GLUED 6" specimen ID in compression

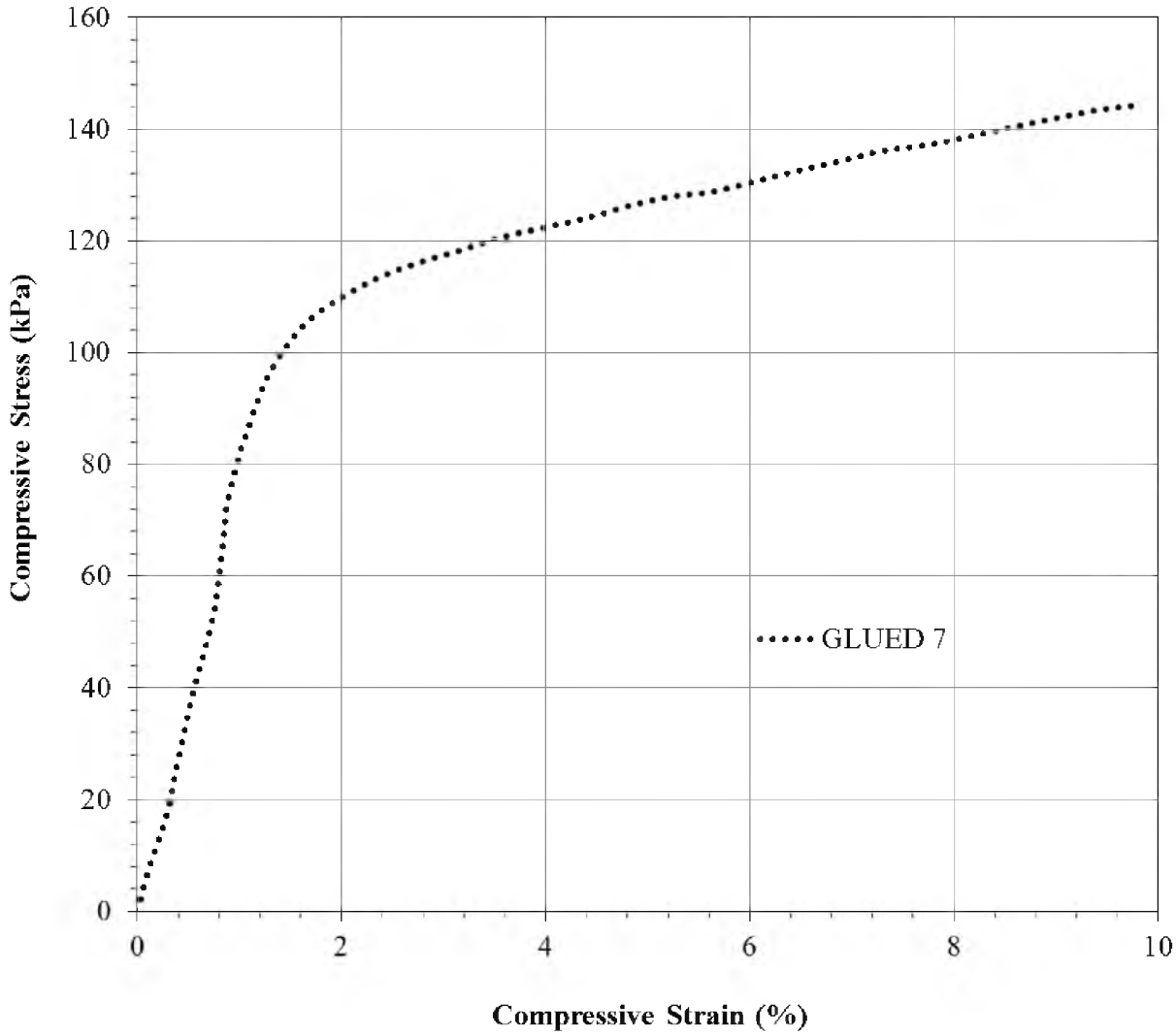

Figure A.12. Stress-strain behavior of a glued EPS with "GLUED 7" specimen ID in compression

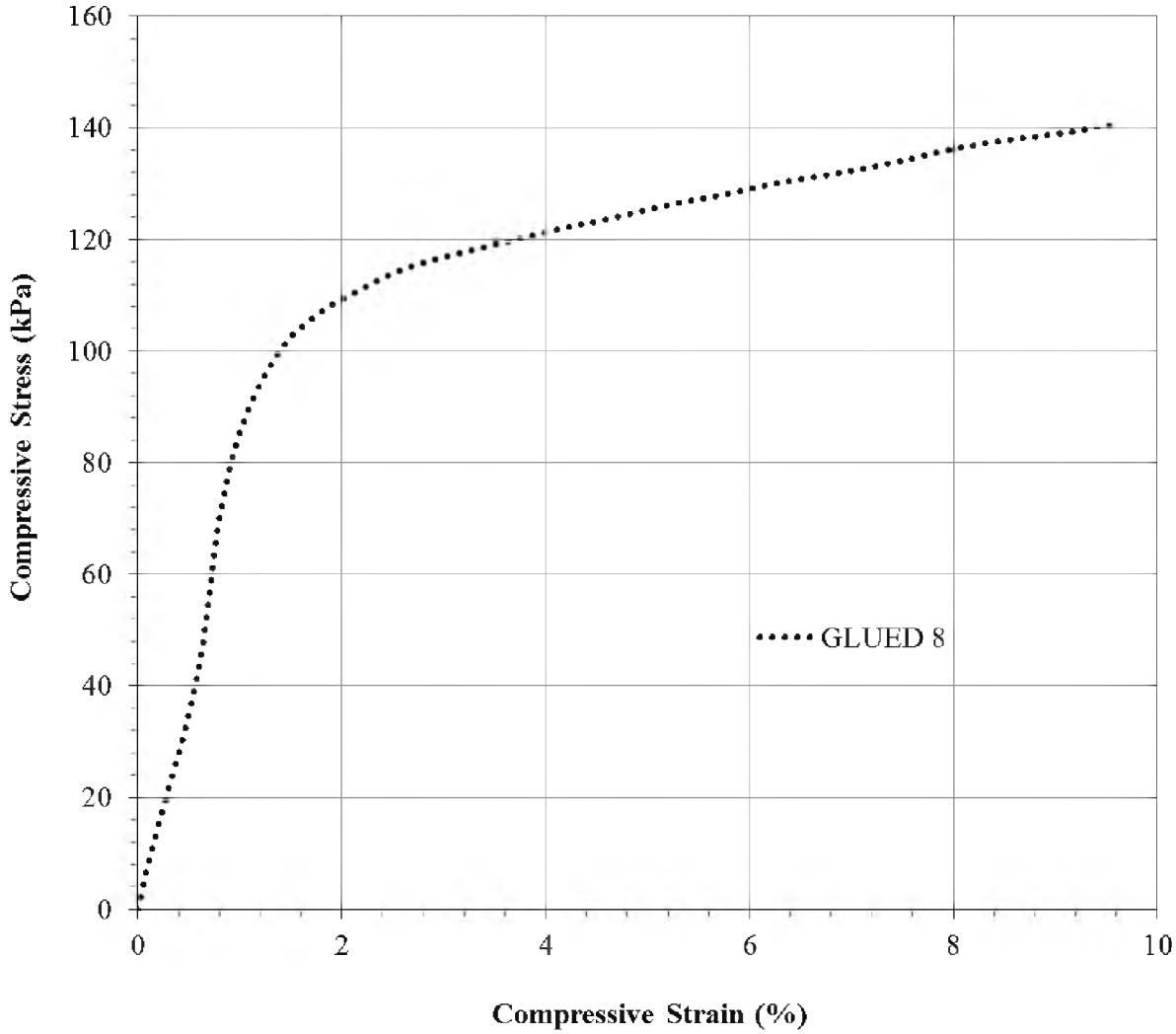

Figure A.13. Stress-strain behavior of a glued EPS with "GLUED 8" specimen ID in compression

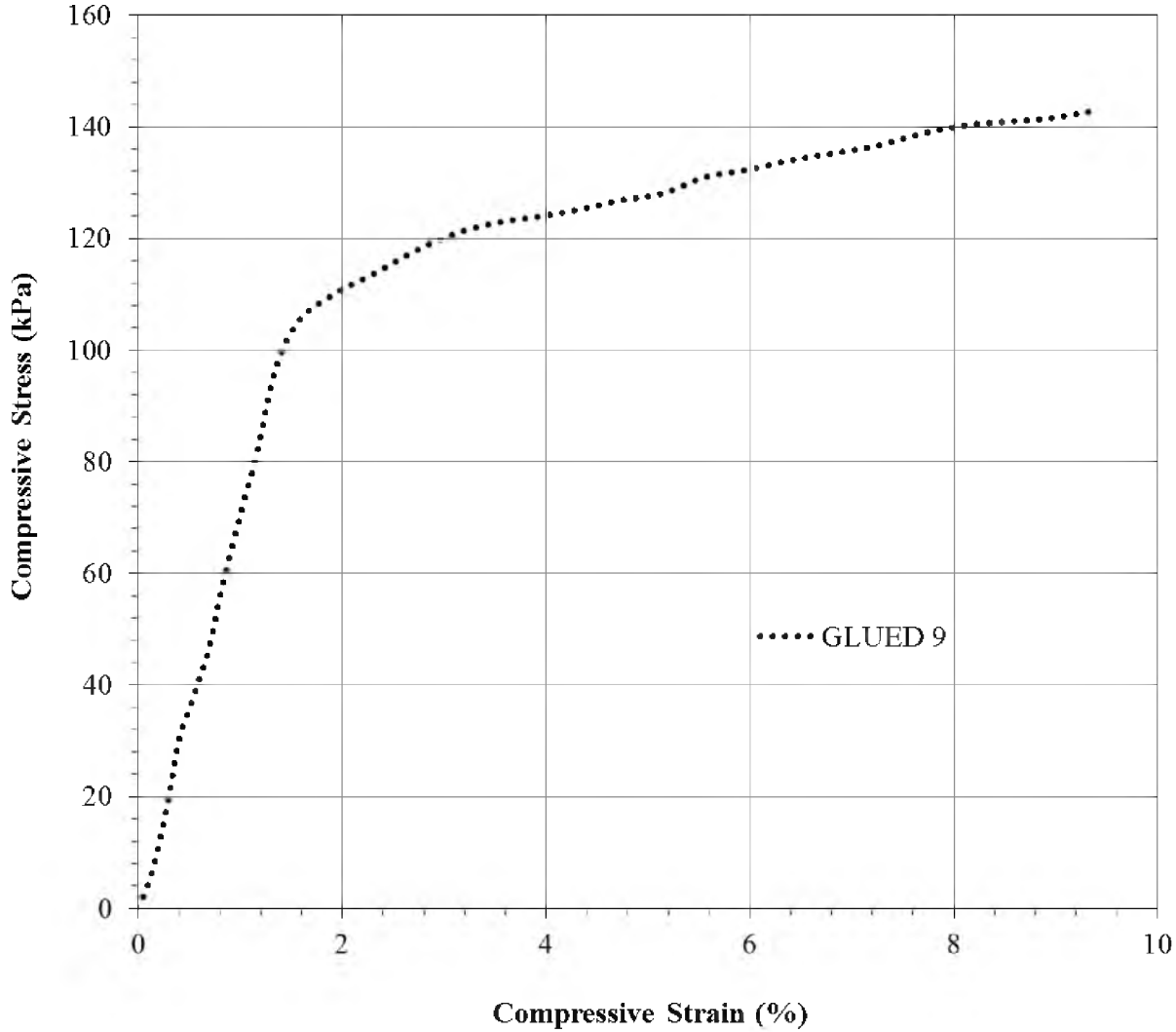

Figure A.14. Stress-strain behavior of a glued EPS with "GLUED 9" specimen ID in compression

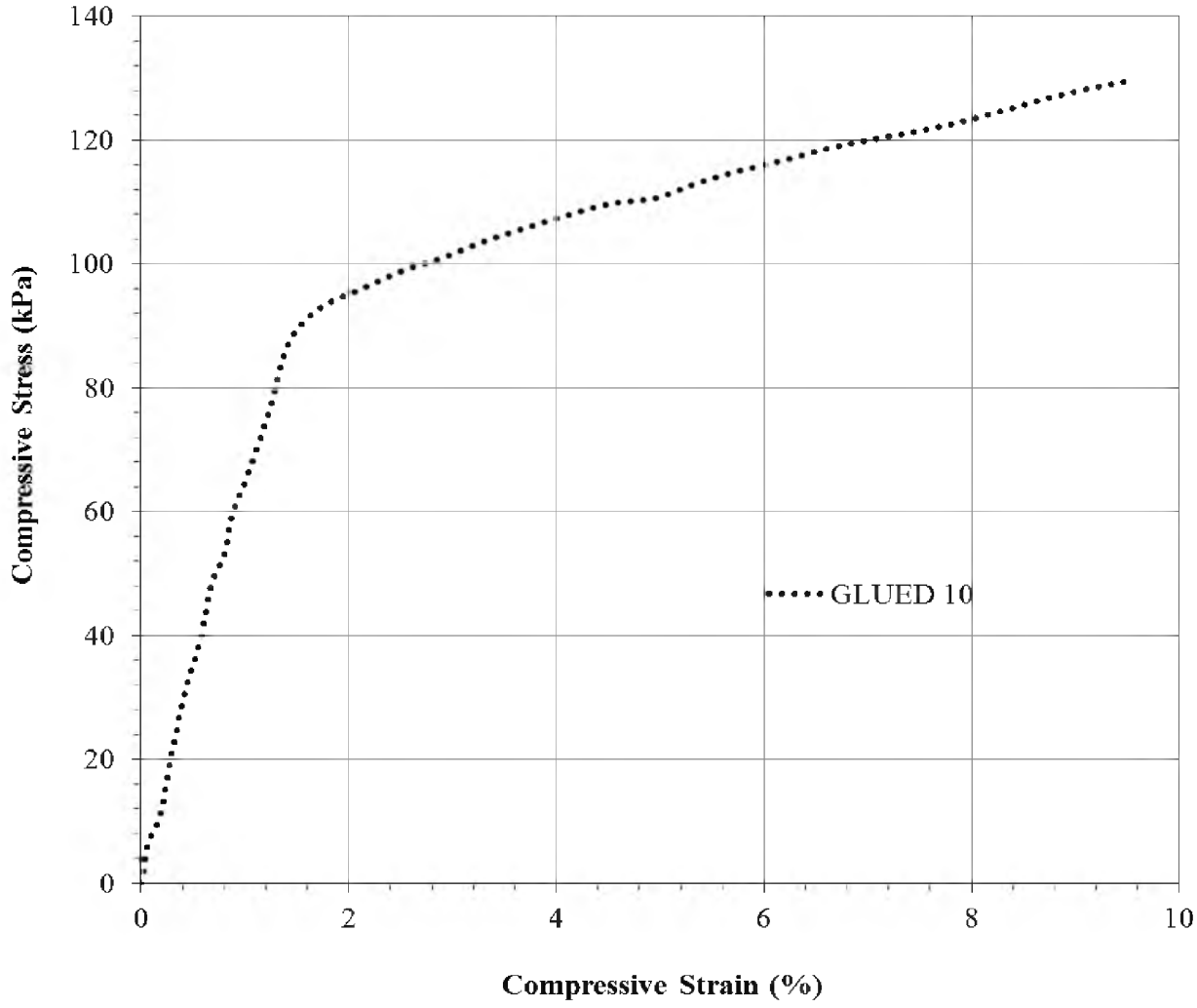

Figure A.15. Stress-strain behavior of a glued EPS with "GLUED 10" specimen ID in compression

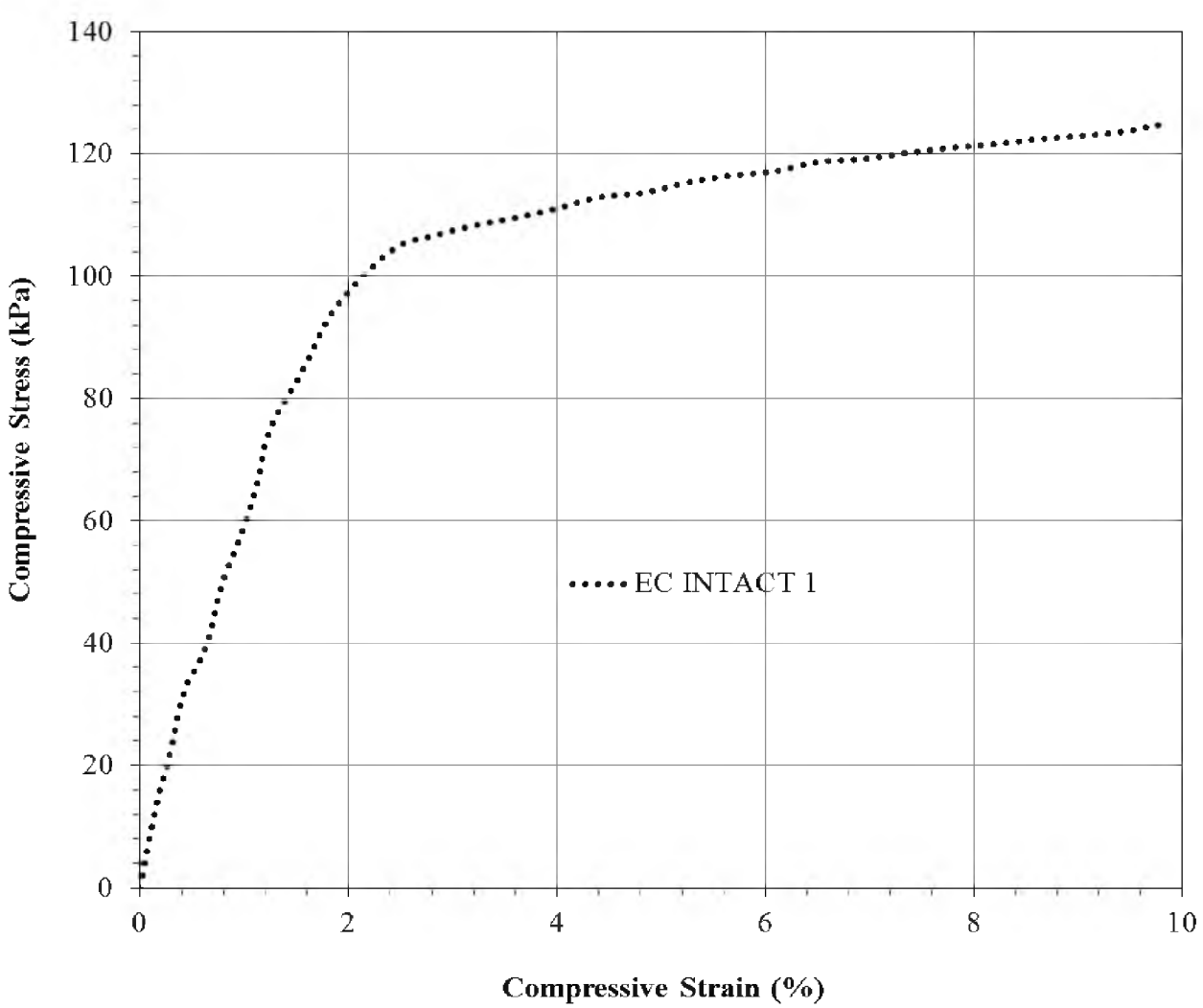

Figure A.16. Stress-strain behavior of a conditioned intact EPS with "EC INTACT 1" specimen ID in compression

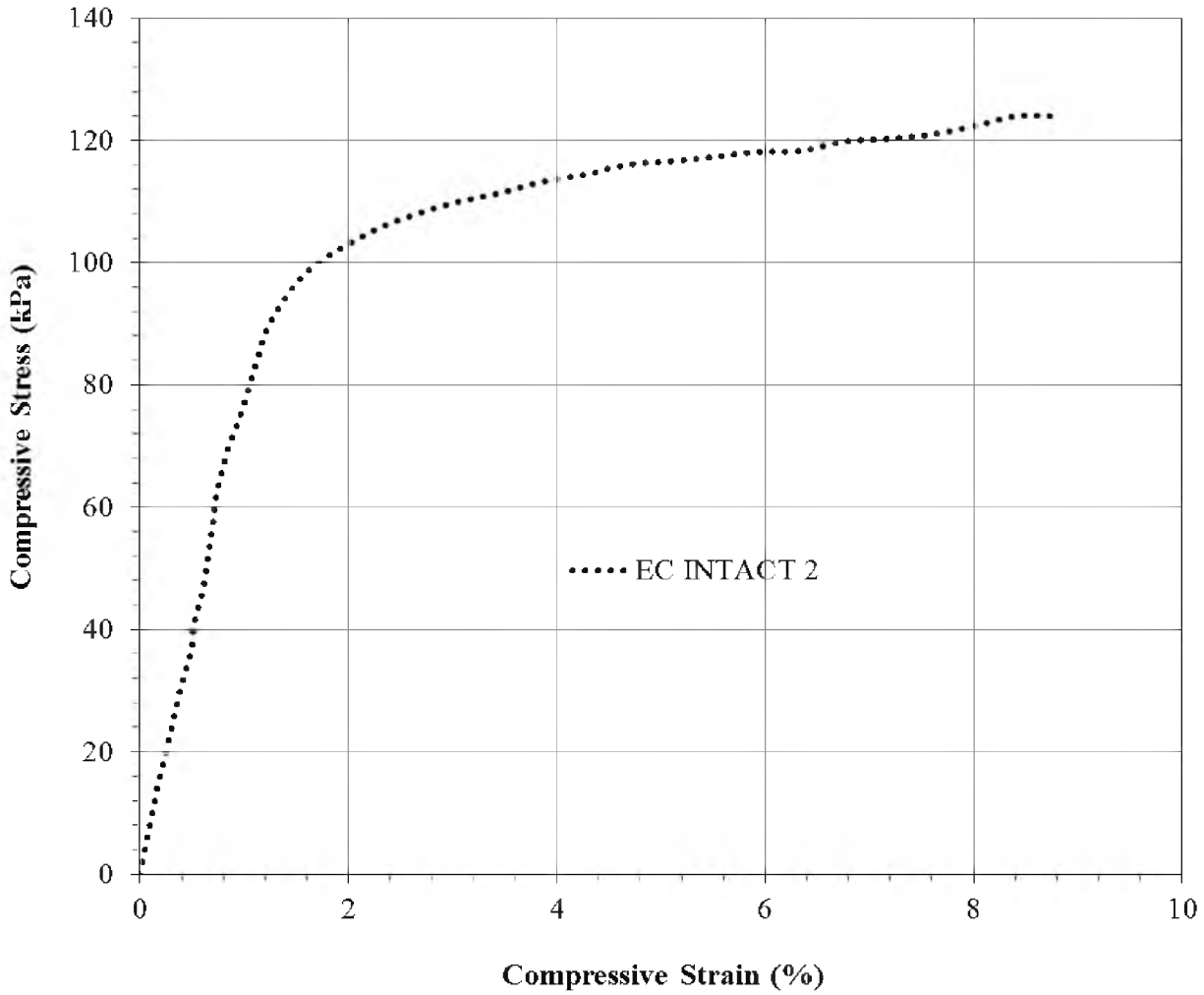

Figure A.17. Stress-strain behavior of a conditioned intact EPS with "EC INTACT 2" specimen ID in compression

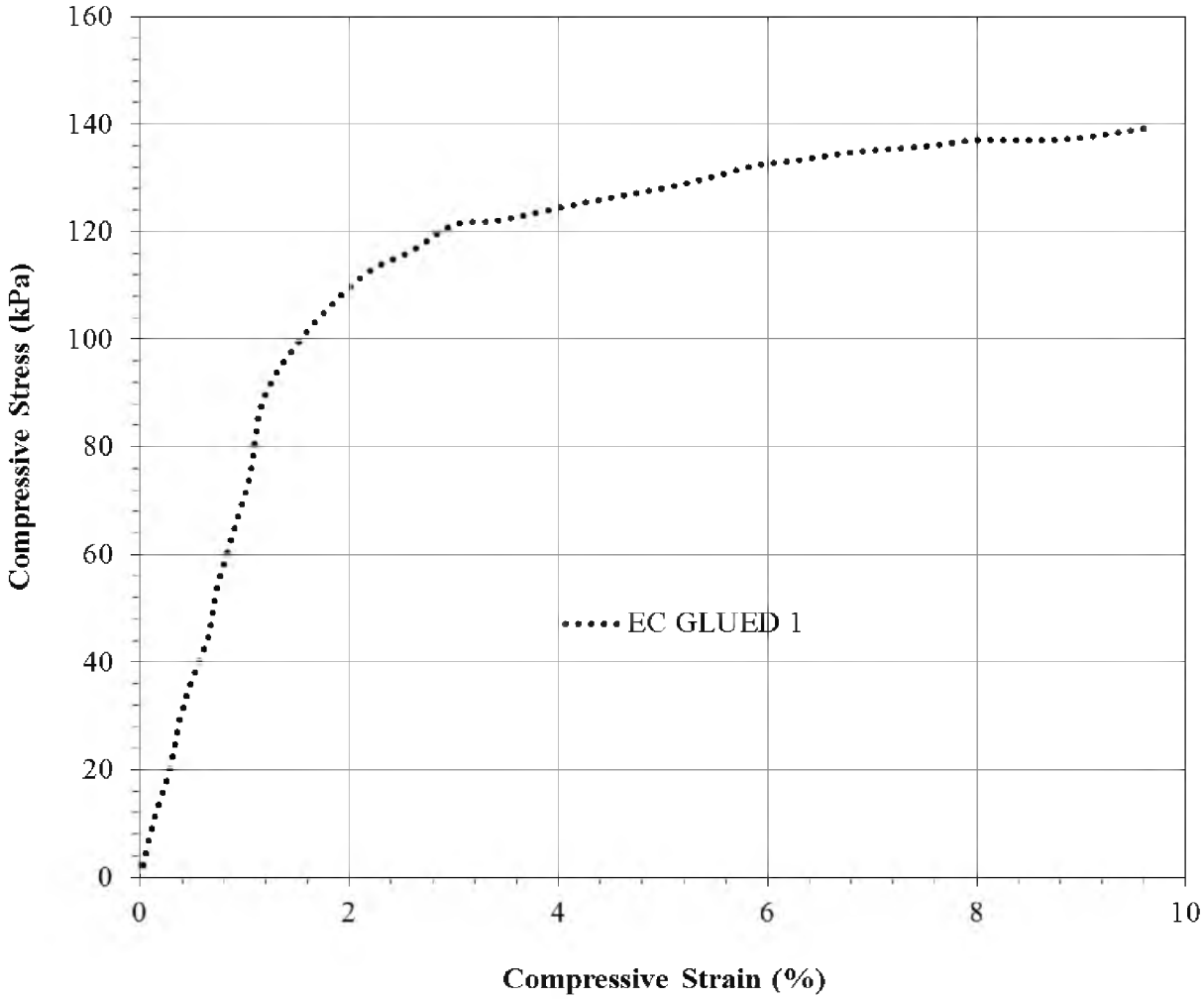

Figure A.18. Stress-strain behavior of a conditioned glued EPS with "EC GLUED 1" specimen ID in compression

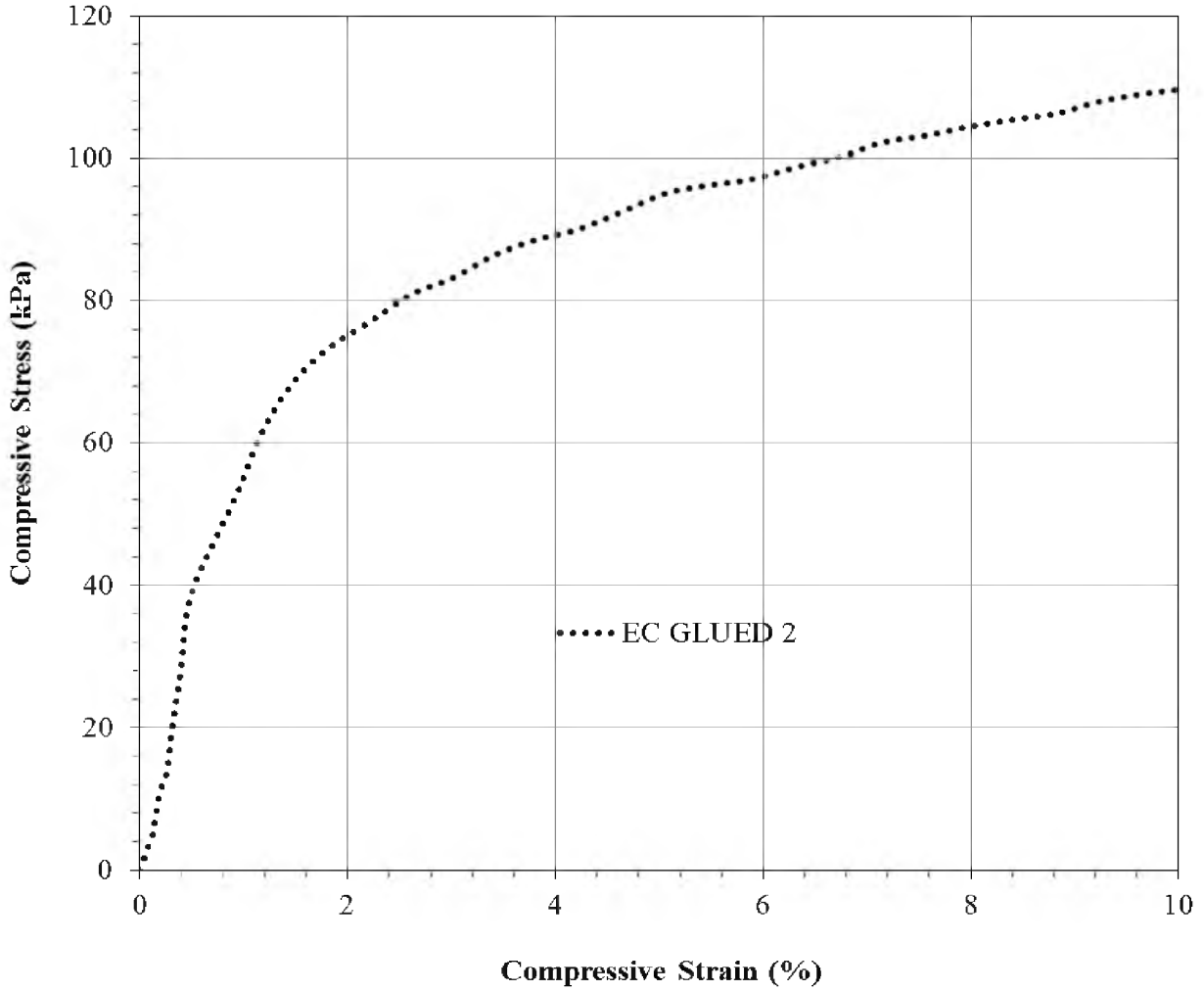

Figure A.19. Stress-strain behavior of a conditioned glued EPS with "EC GLUED 2" specimen ID in compression

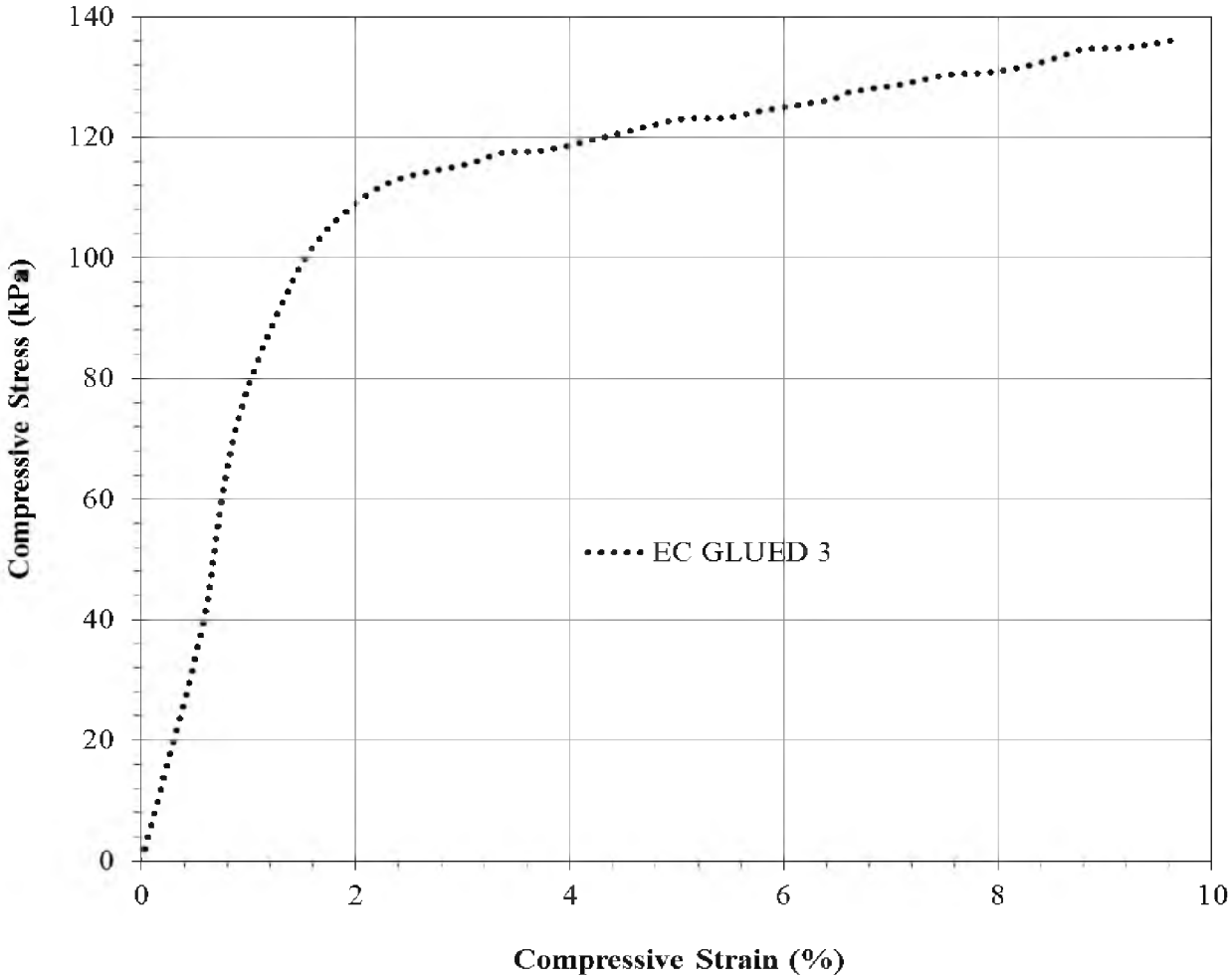

Figure A.20. Stress-strain behavior of a conditioned glued EPS with "EC GLUED 3" specimen ID in compression

Table A.1. Uniaxial compression test results of EPS specimens

Specimen ID	ε_e (%)	σ_e (kPa)	E_{ti} (MPa)	σ_c (kPa)
INTACT 1	0.55	42.5	7.6	109.4
INTACT 2	0.48	33.1	7.0	89.8
INTACT 3	0.68	49.6	7.3	115.7
INTACT 4	0.60	46.5	7.3	117.5
INTACT 5	0.42	30.0	6.9	108.9
GLUED 1[1]	------	------	------	114.7
GLUED 2	0.69	47.9	6.7	126.2
GLUED 3	0.74	54.4	7.4	125.5
GLUED 4	0.45	26.6	6.0	119.2
GLUED 5	0.73	48.5	6.8	94.6
GLUED 6	0.83	60.5	7.0	133.2
GLUED 7	0.74	52.5	7.0	127.0
GLUED 8	0.69	55.0	7.5	125.4
GLUED 9	0.84	58.7	6.9	127.7
GLUED 10	0.87	58.9	6.9	110.9
EC INTACT 1	0.44	32.9	7.7	114.3
EC INTACT 2	0.66	52.7	7.8	116.5
EC GLUED 1	0.95	68.1	7.2	128.1
EC GLUED 2	0.69	45.3	6.9	94.7
EC GLUED 3	0.61	42.4	6.8	122.9

[1] This specimen was associated with seating error

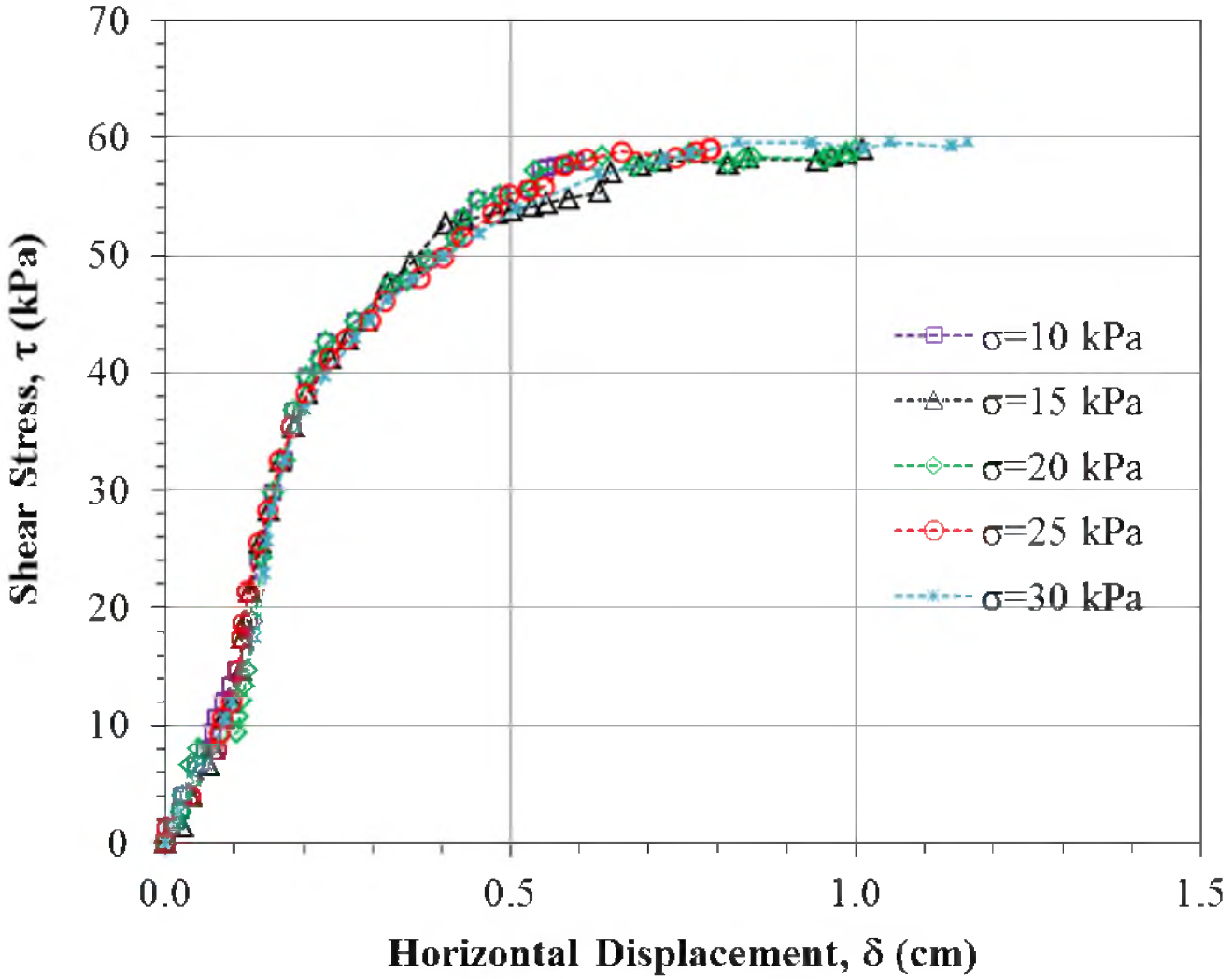

Figure A.21. Shear stress vs. displacement of intact EPS specimens under various normal stresses

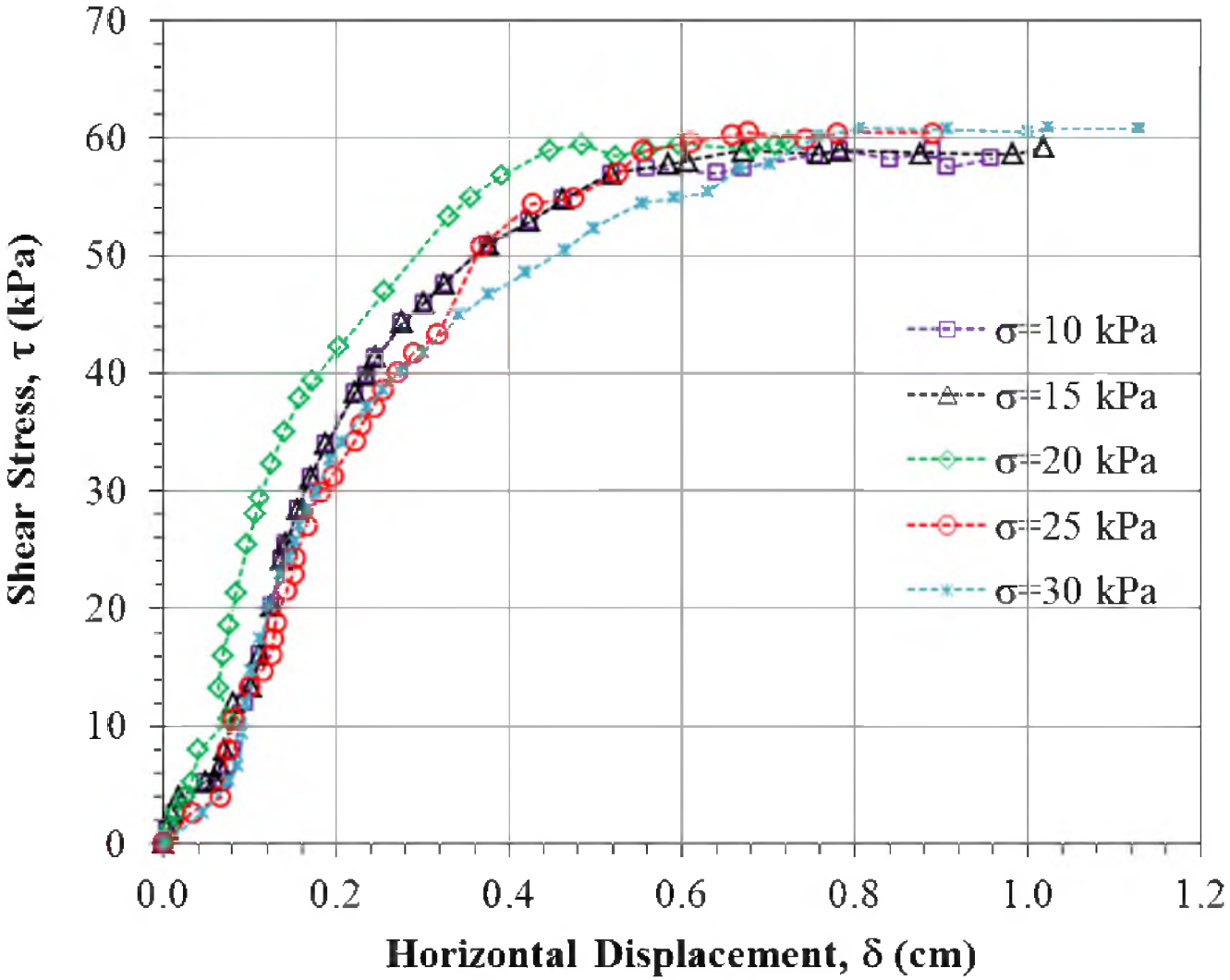

Figure A.22. Shear stress vs. displacement of glued EPS specimens under various normal stresses

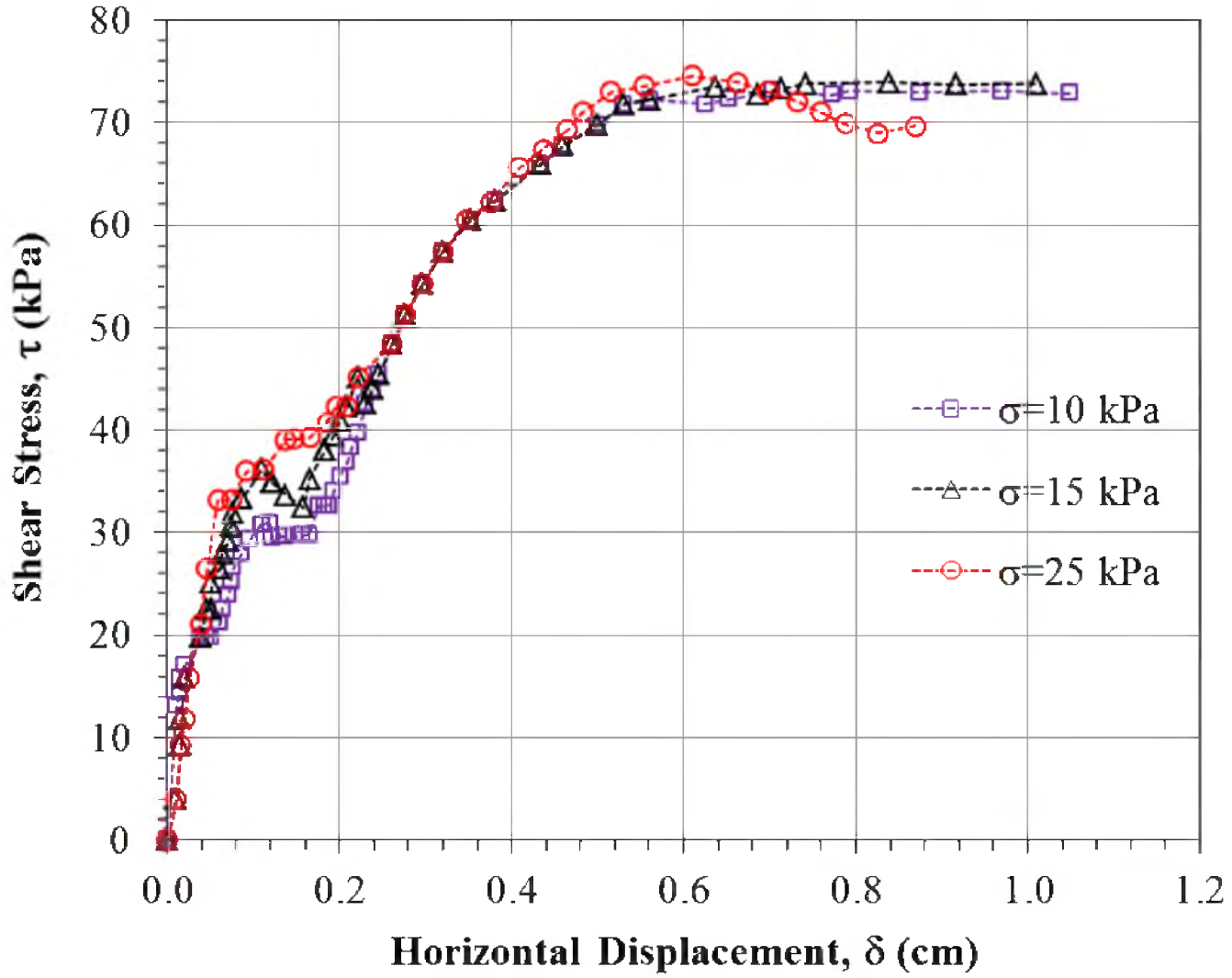

Figure A.23. Shear stress vs. displacement of environmentally conditioned intact EPS specimens under different normal stresses

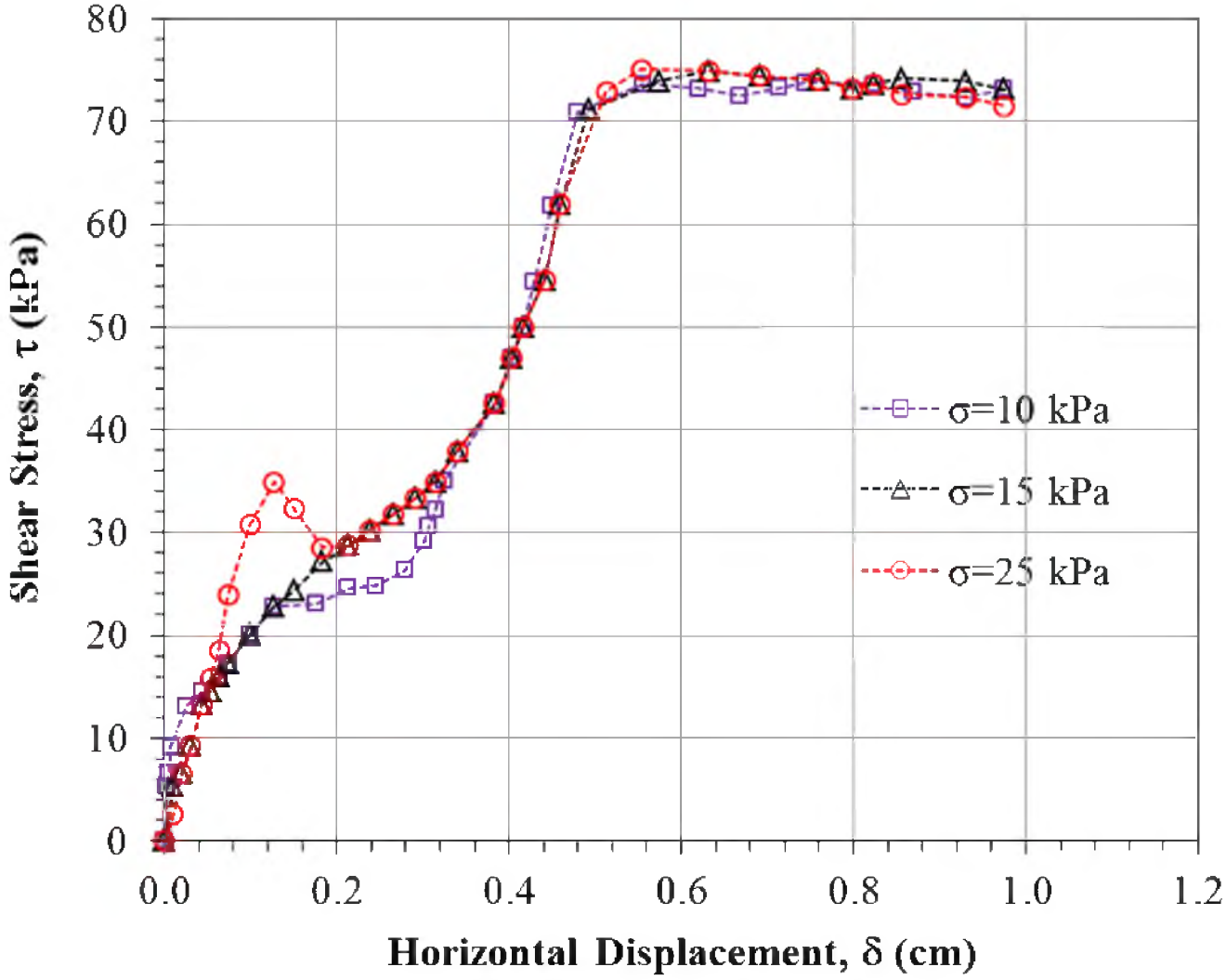

Figure A.24. Shear stress vs. displacement of environmentally conditioned glued EPS specimens under different normal stresses

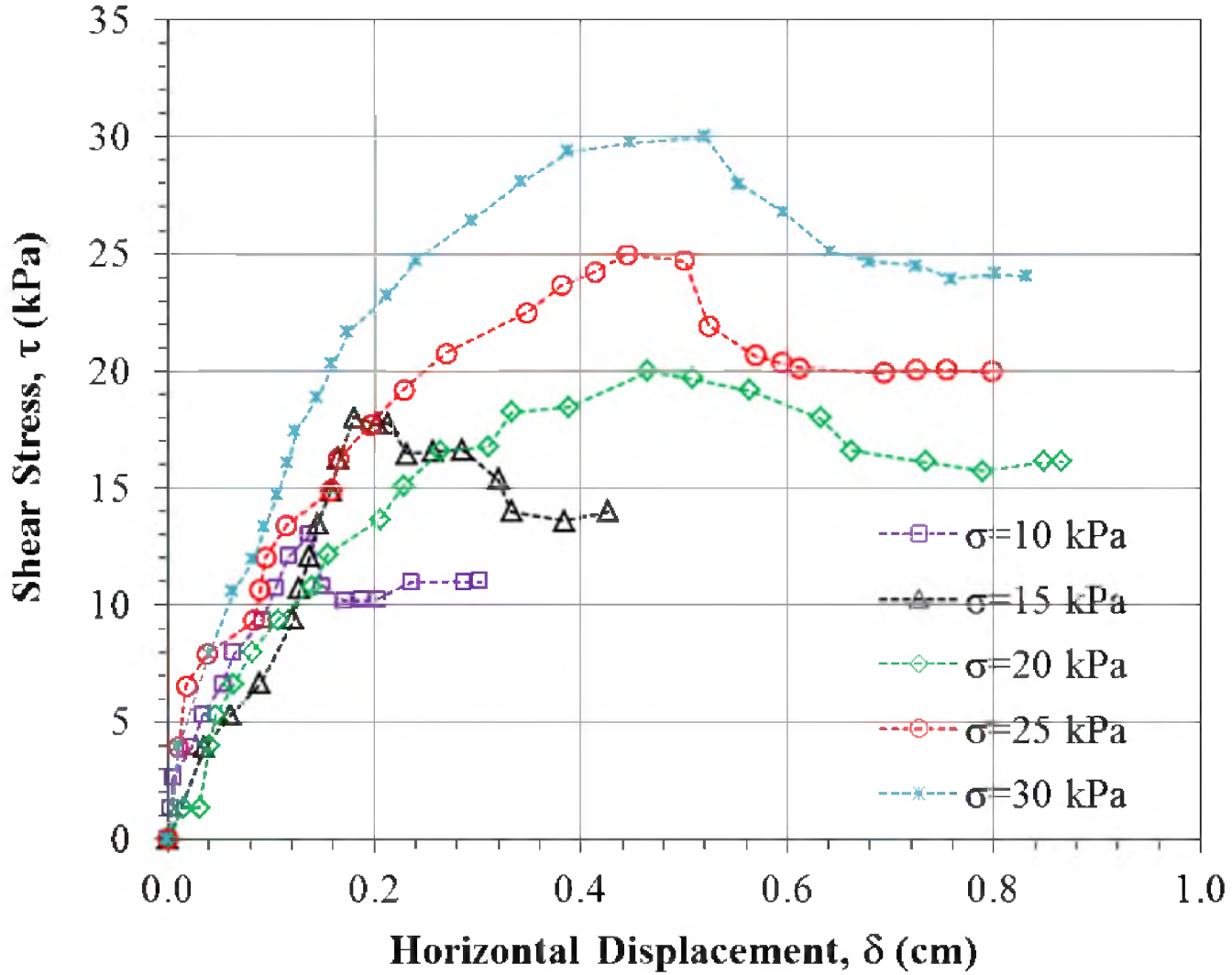

Figure A.25. Shear stress vs. displacement of intact EPS specimens under different normal stresses

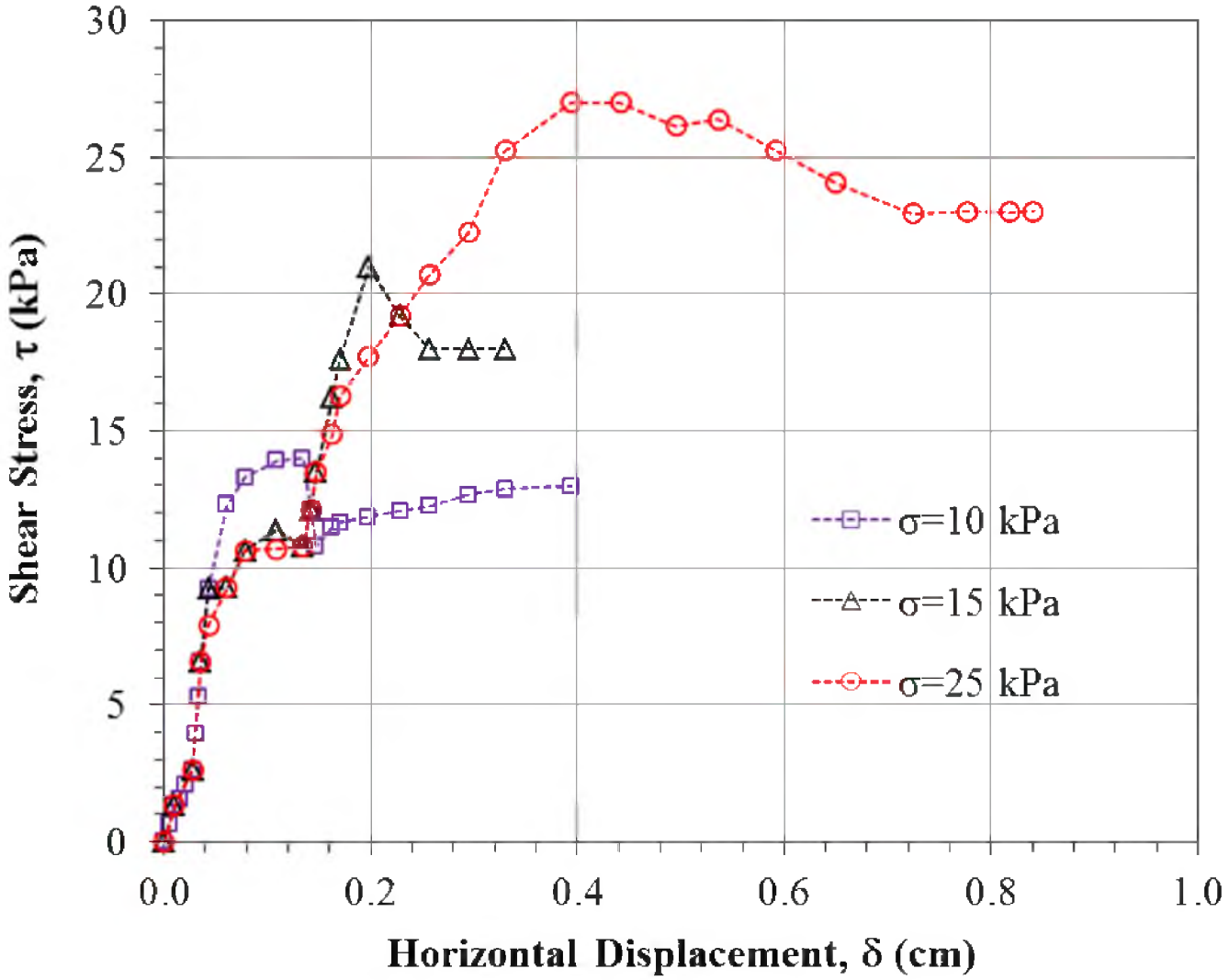

Figure A.26. Shear stress vs. displacement of environmentally conditioned intact EPS specimens under different normal stresses

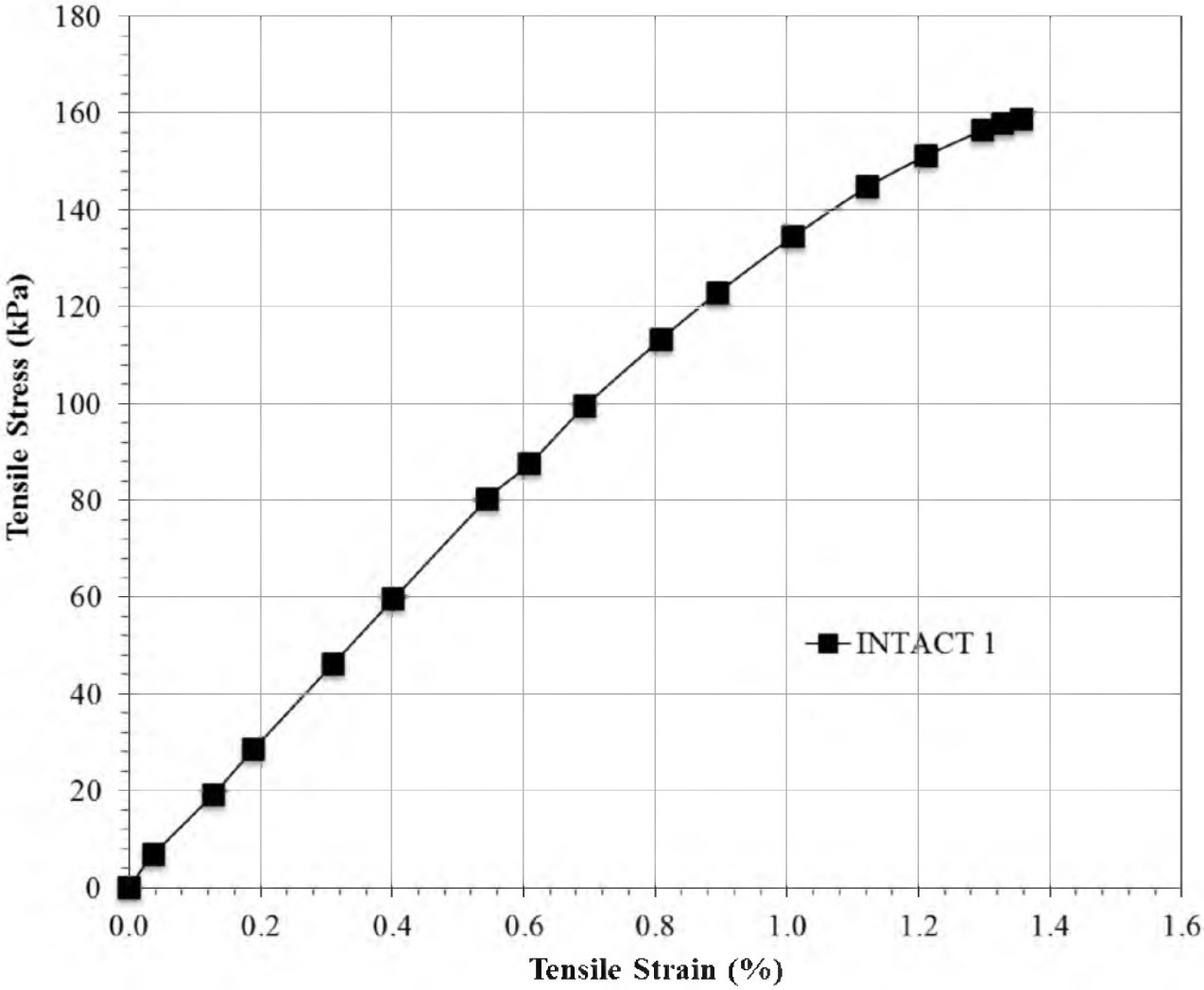

Figure A.27. Tensile stress-strain behavior of intact EPS specimen with "INTACT" specimen ID

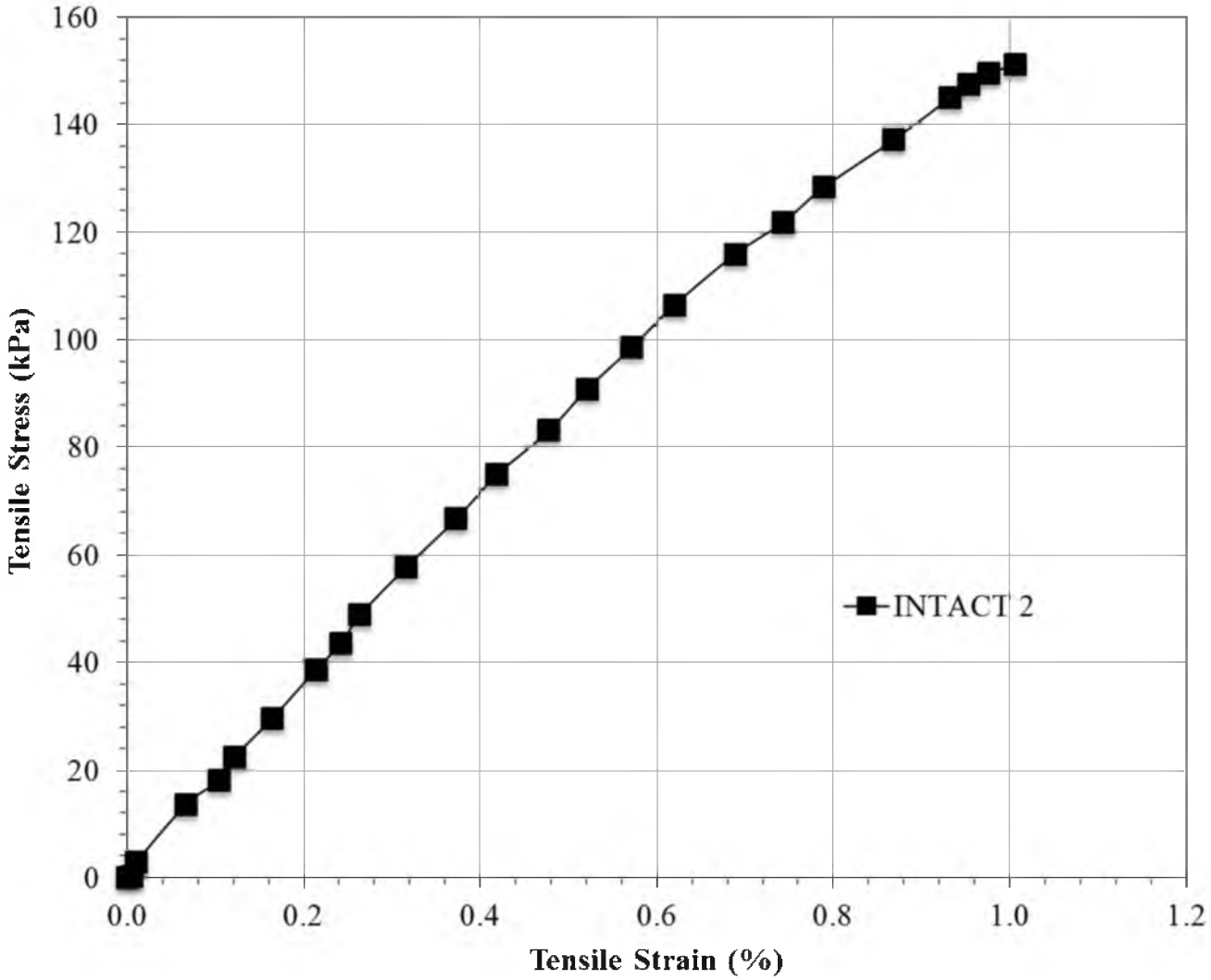

Figure A.28. Tensile stress-strain behavior of intact EPS specimen with "INTACT 2" specimen ID

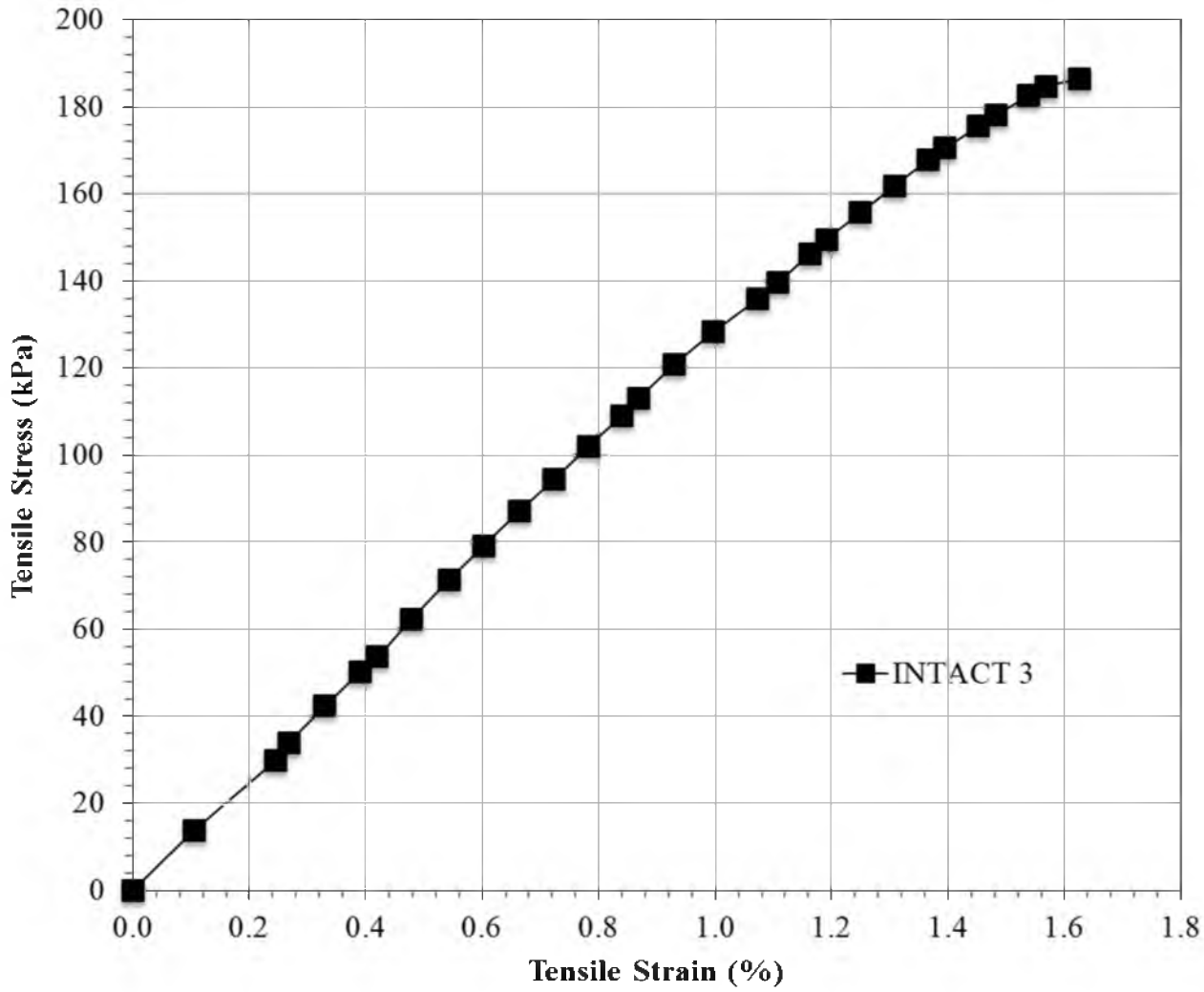

Figure A.29. Tensile stress-strain behavior of intact EPS specimen with "INTACT 3" specimen ID

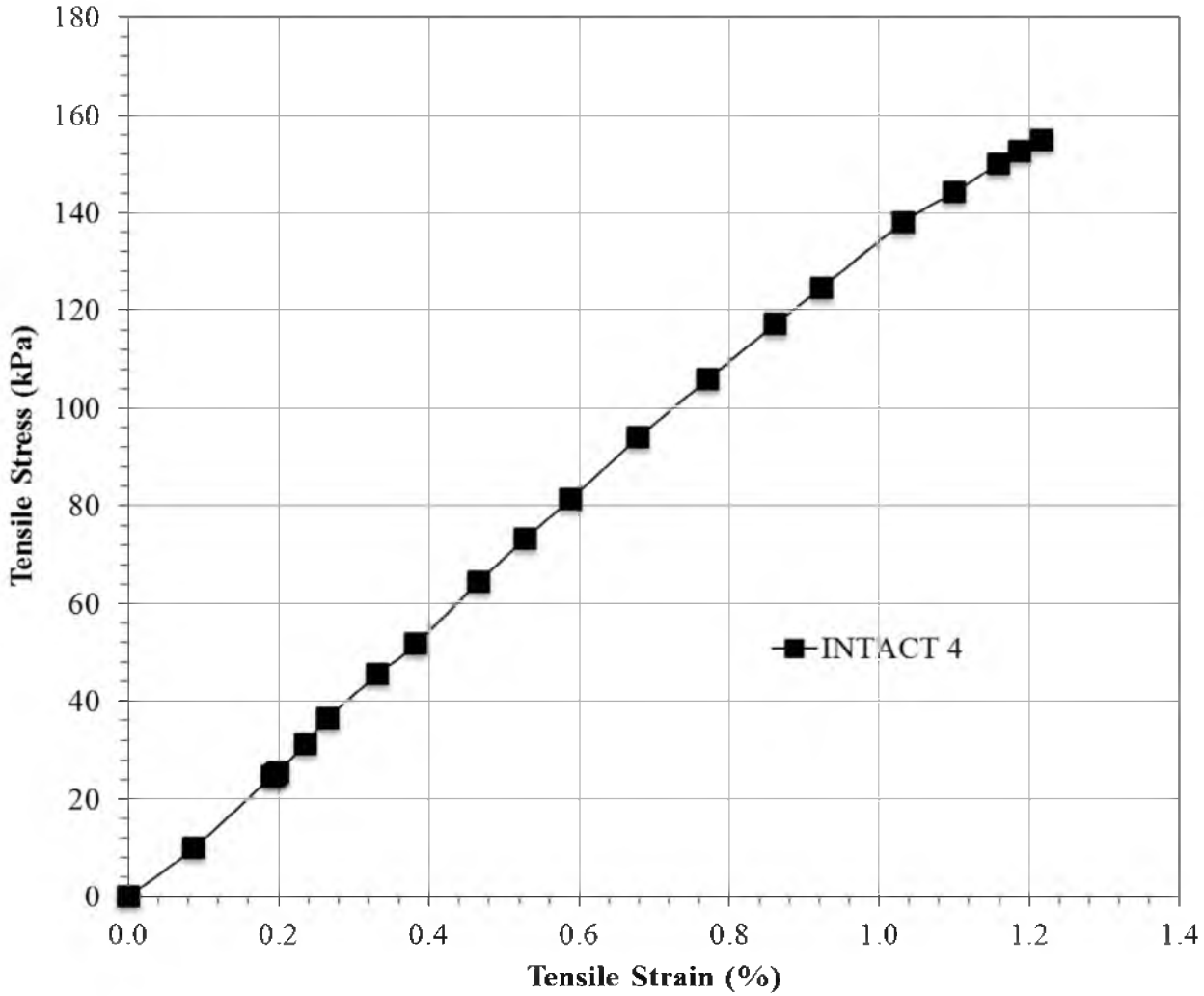

Figure A.30. Tensile stress-strain behavior of intact EPS specimen with "INTACT 4" specimen ID

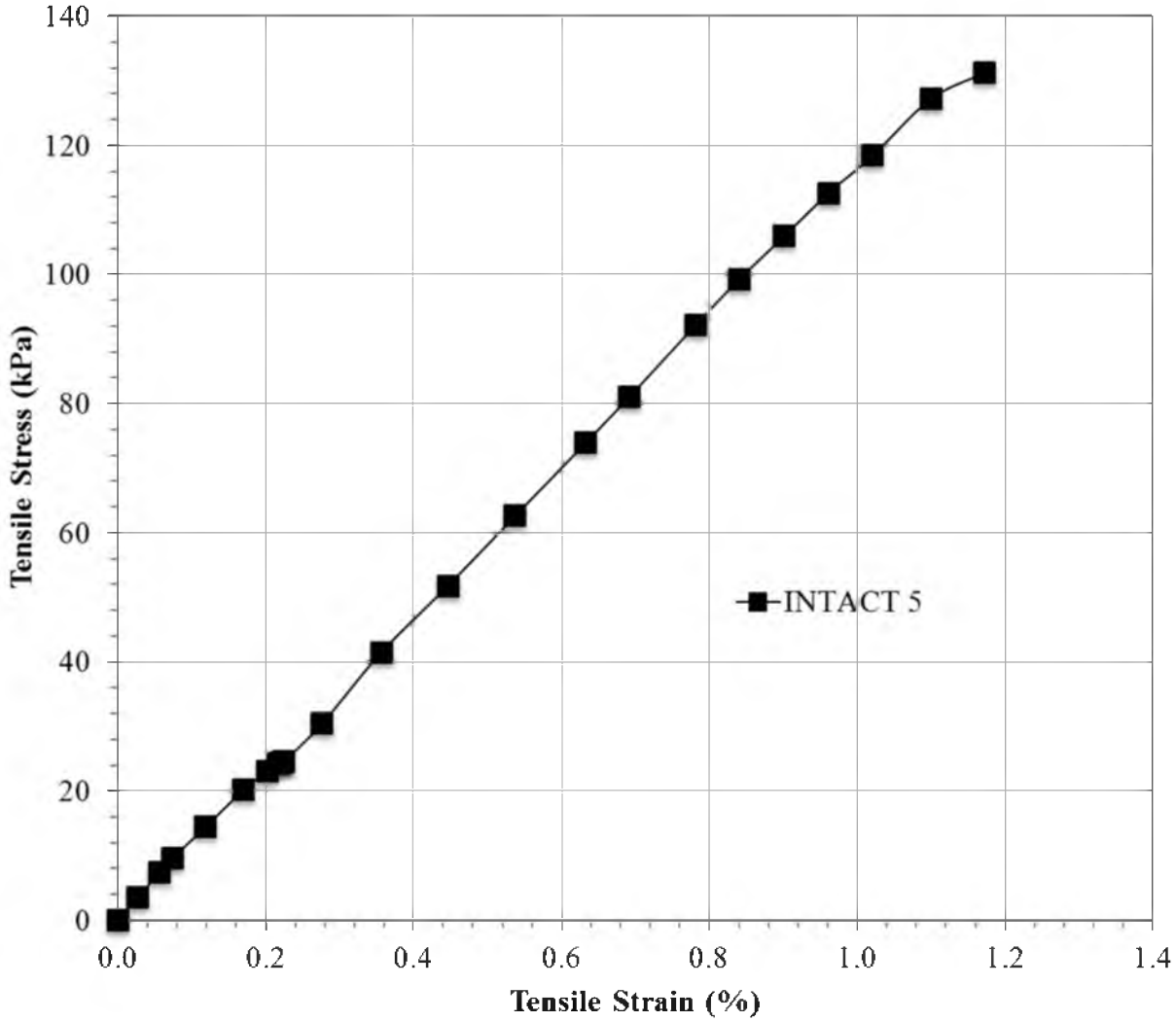

Figure A.31. Tensile stress-strain behavior of intact EPS specimen with "INTACT 5" specimen ID

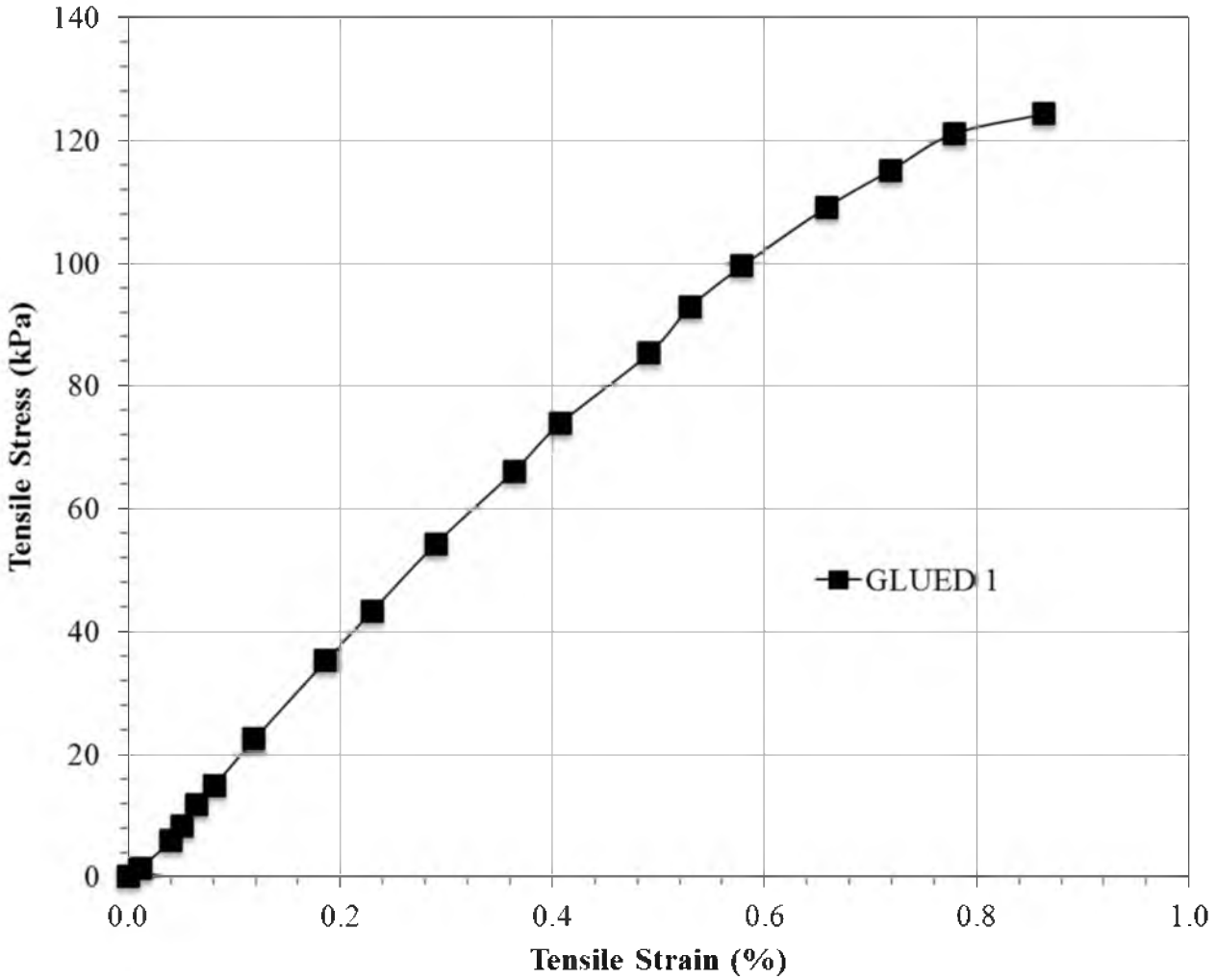

Figure A.32. Tensile stress-strain behavior of glued EPS specimen with "GLUED 1" specimen ID

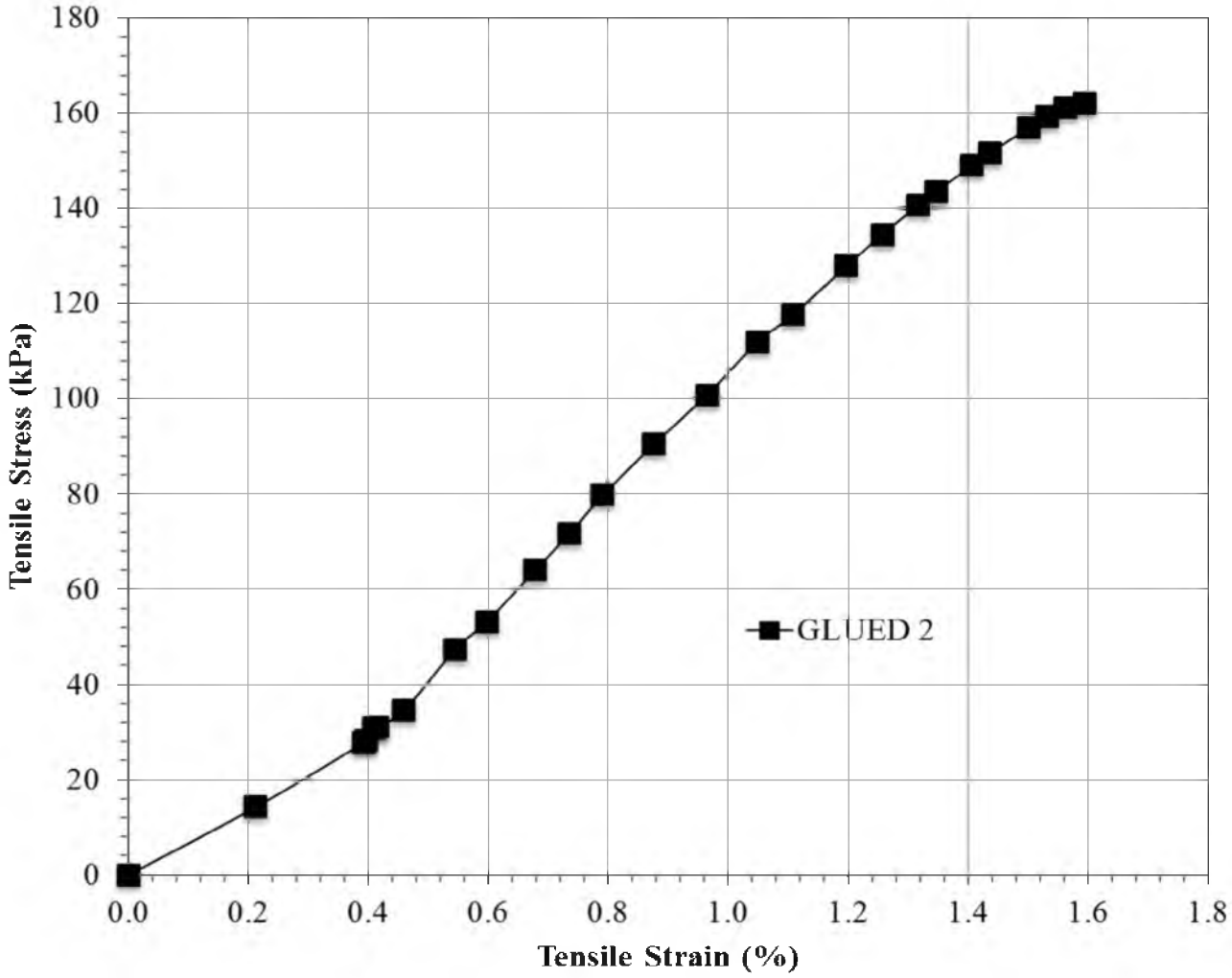

Figure A.33. Tensile stress-strain behavior of glued EPS specimen with "GLUED 2" specimen ID

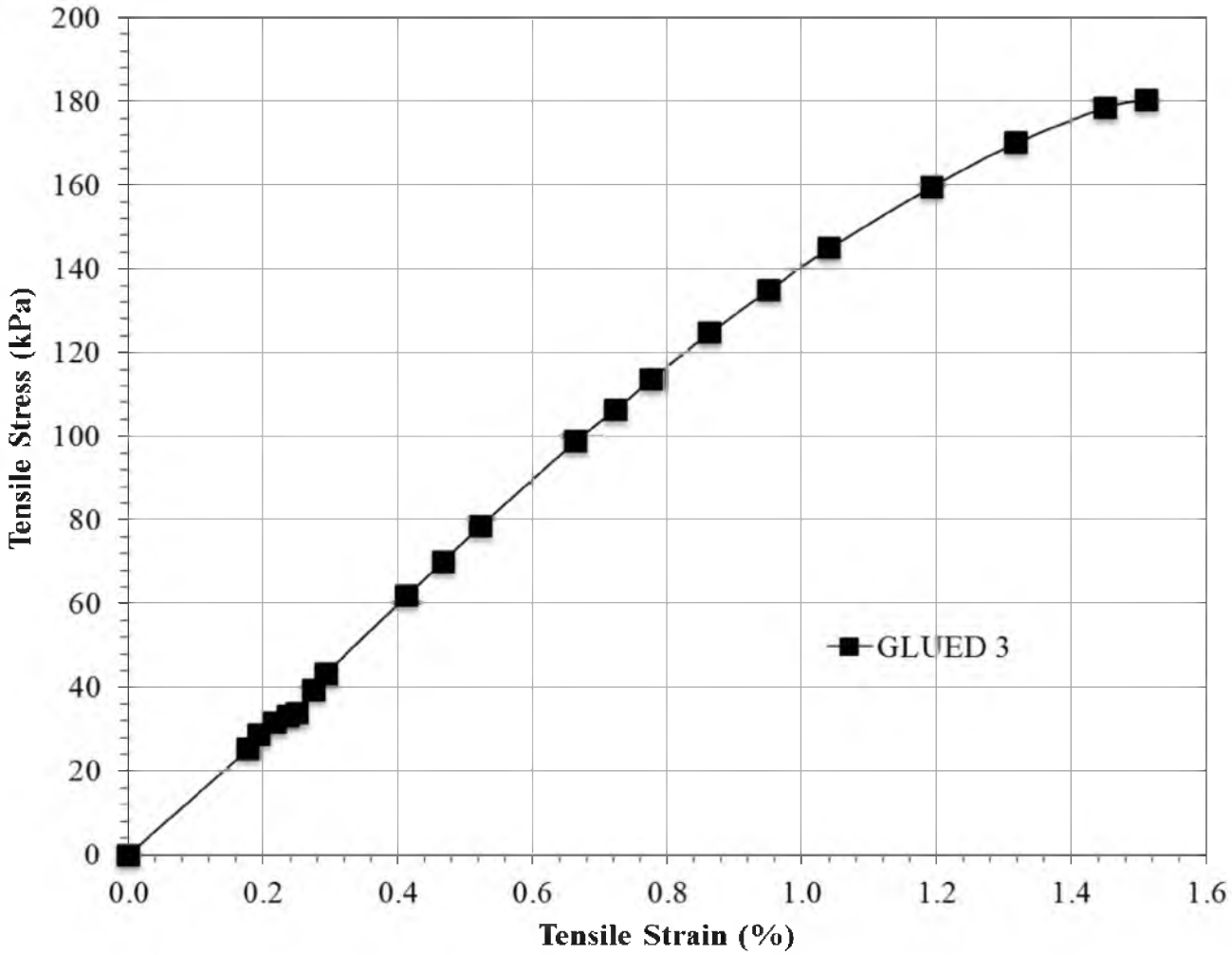

Figure A.34. Tensile stress-strain behavior of glued EPS specimen with "GLUED 3" specimen ID

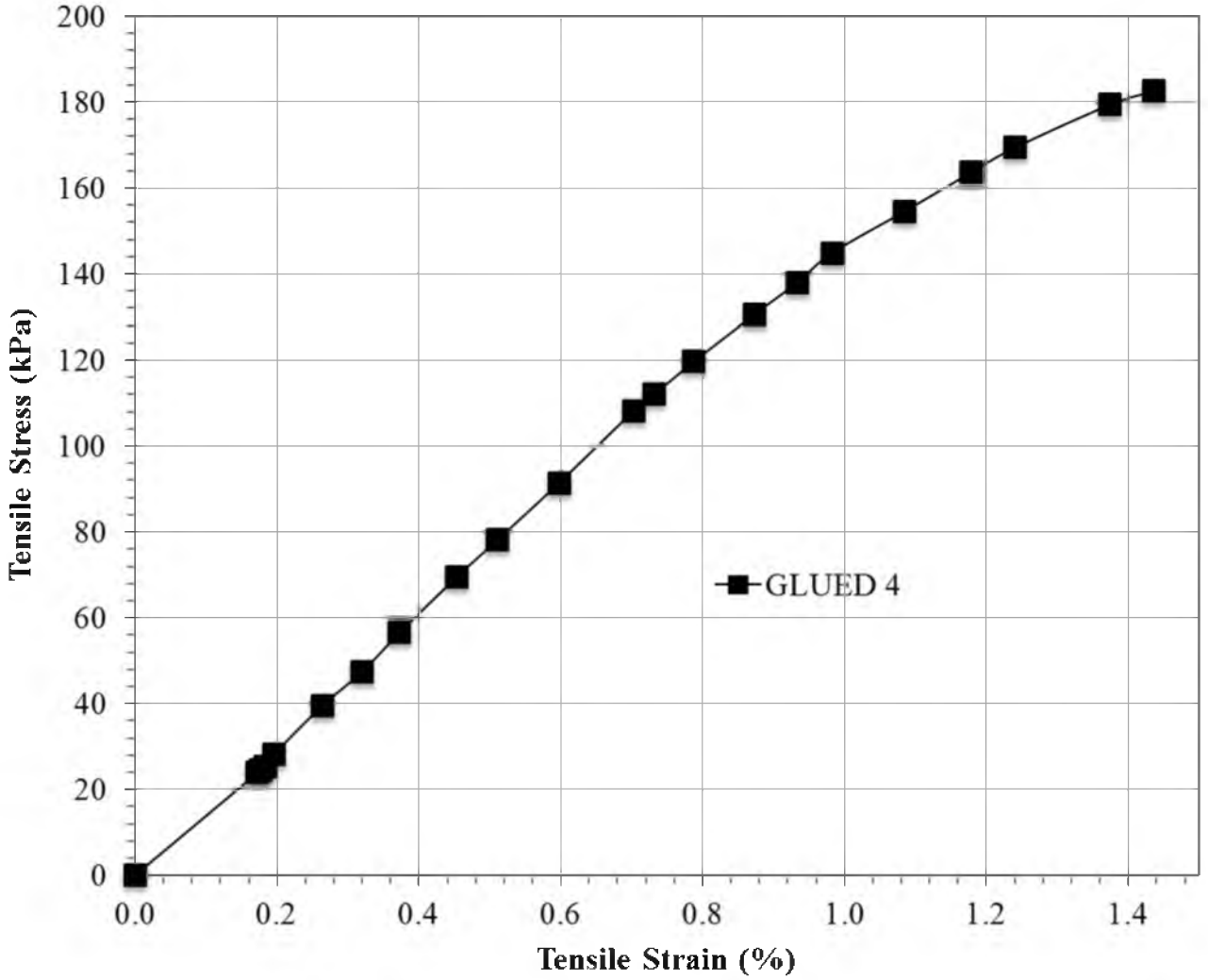

Figure A.35. Tensile stress-strain behavior of glued EPS specimen with "GLUED 4" specimen ID

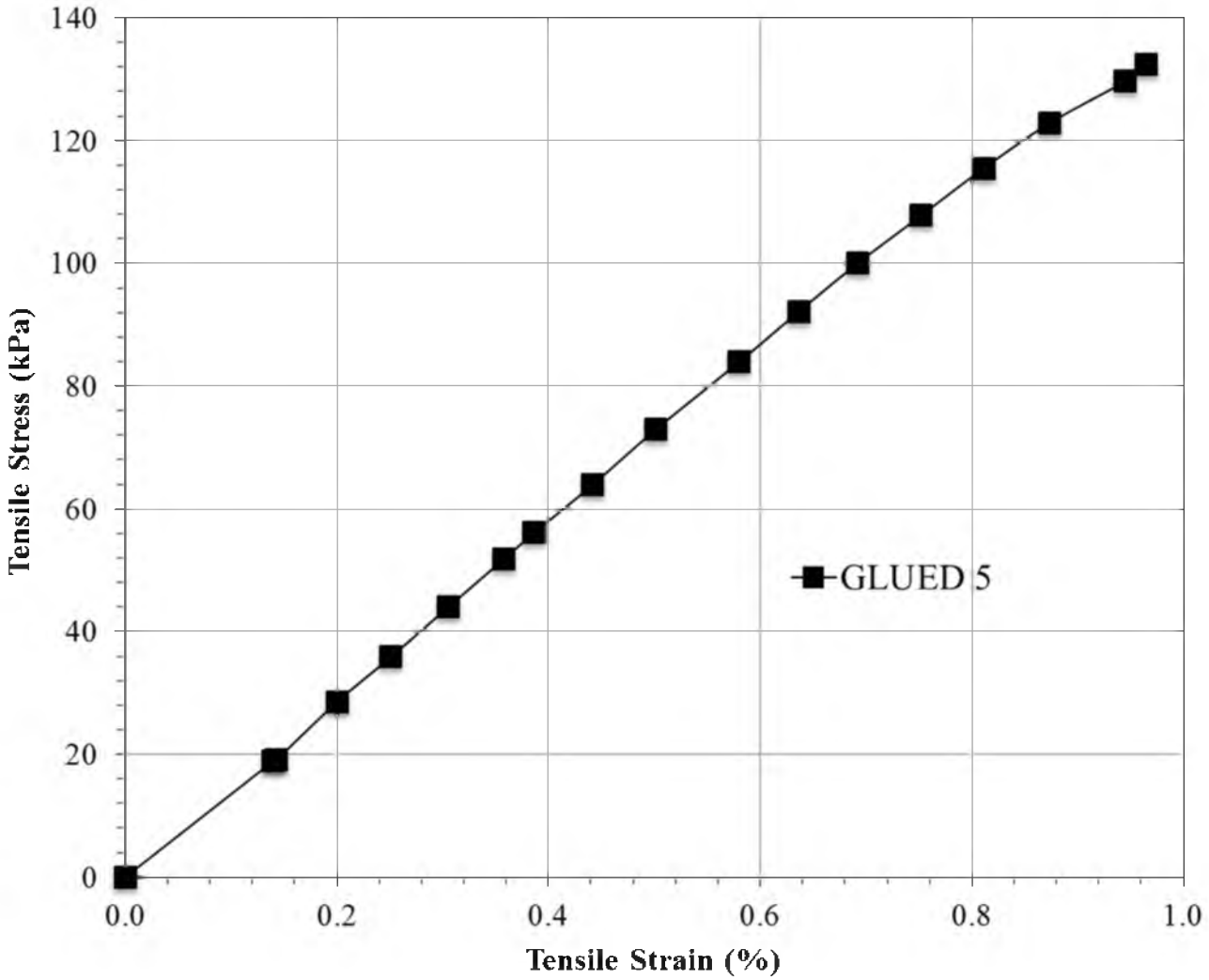

Figure A.36. Tensile stress-strain behavior of glued EPS specimen with "GLUED 5" specimen ID

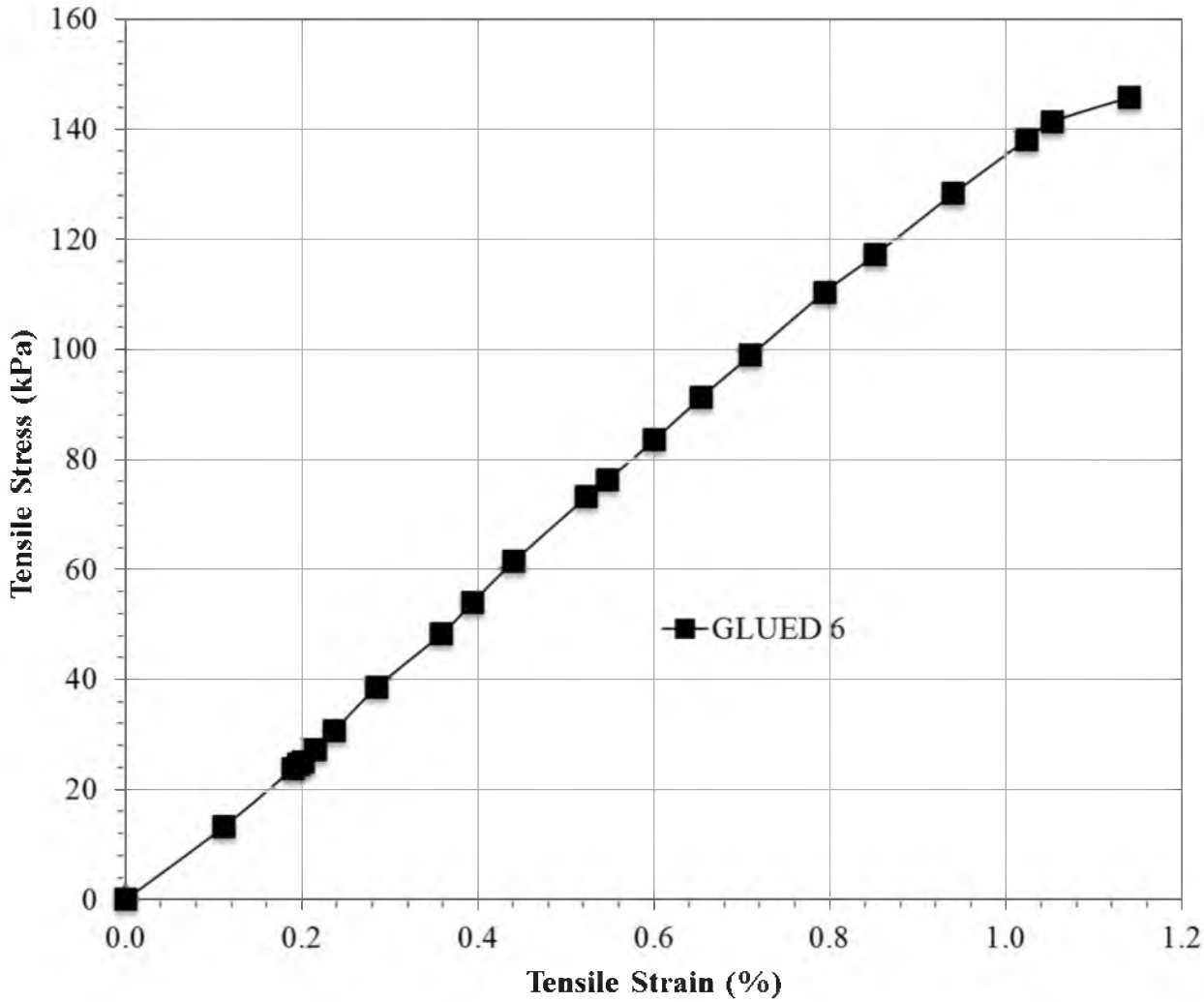

Figure A.37. Tensile stress-strain behavior of glued EPS specimen with "GLUED 6" specimen ID

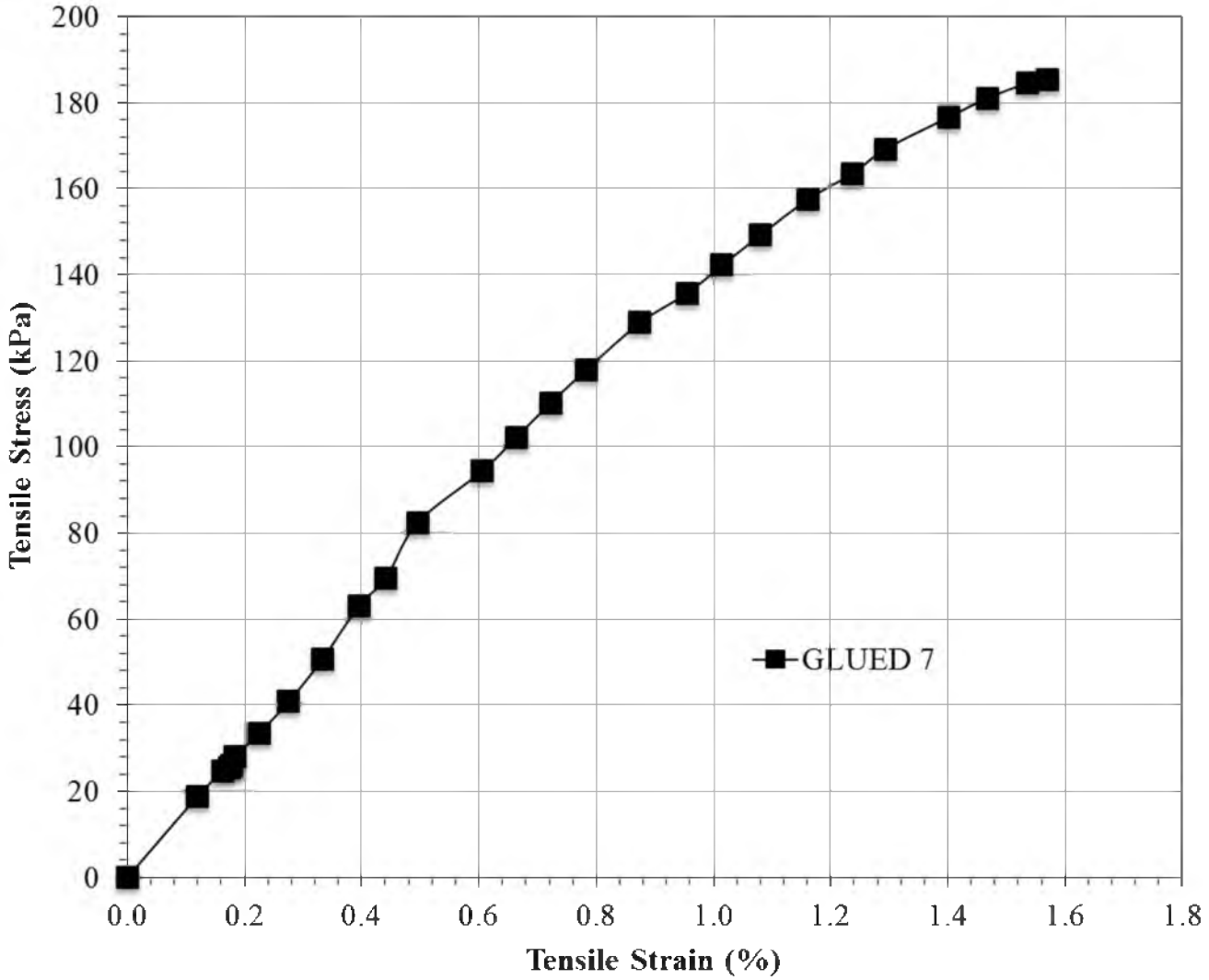

Figure A.38. Tensile stress-strain behavior of glued EPS specimen with "GLUED 7" specimen ID

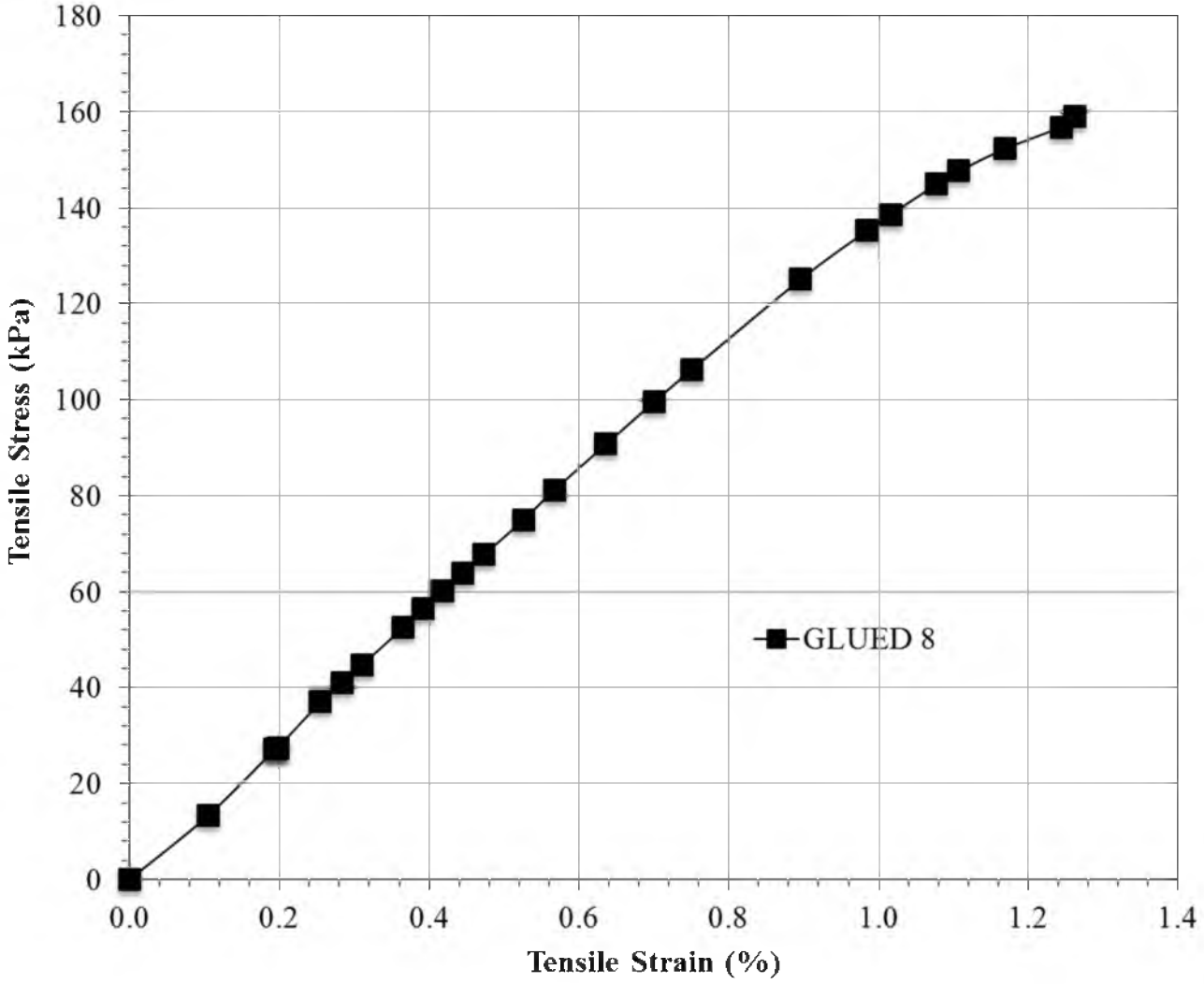

Figure A.39. Tensile stress-strain behavior of glued EPS specimen with "GLUED 8" specimen ID

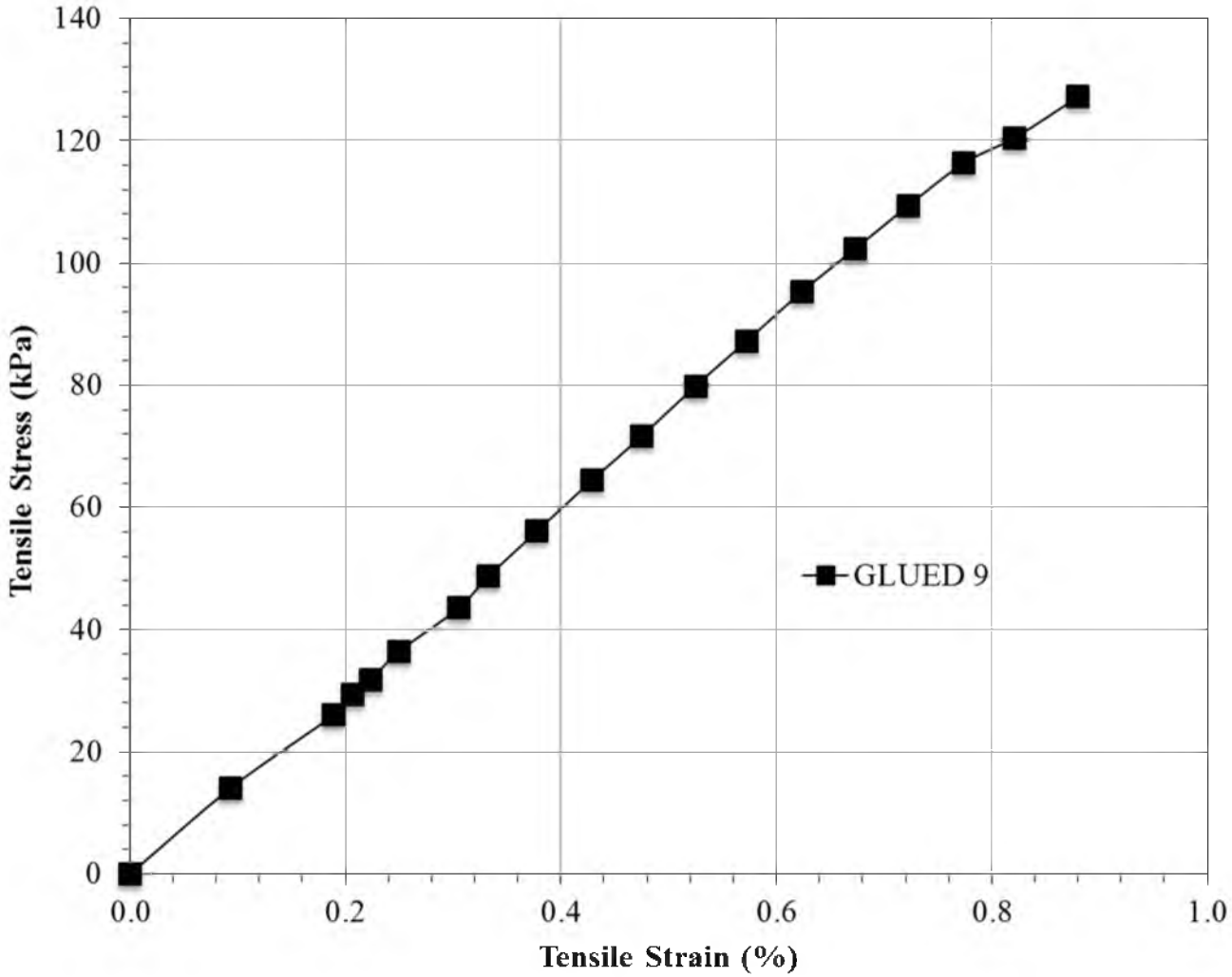

Figure A.40. Tensile stress-strain behavior of glued EPS specimen with "GLUED 9" specimen ID

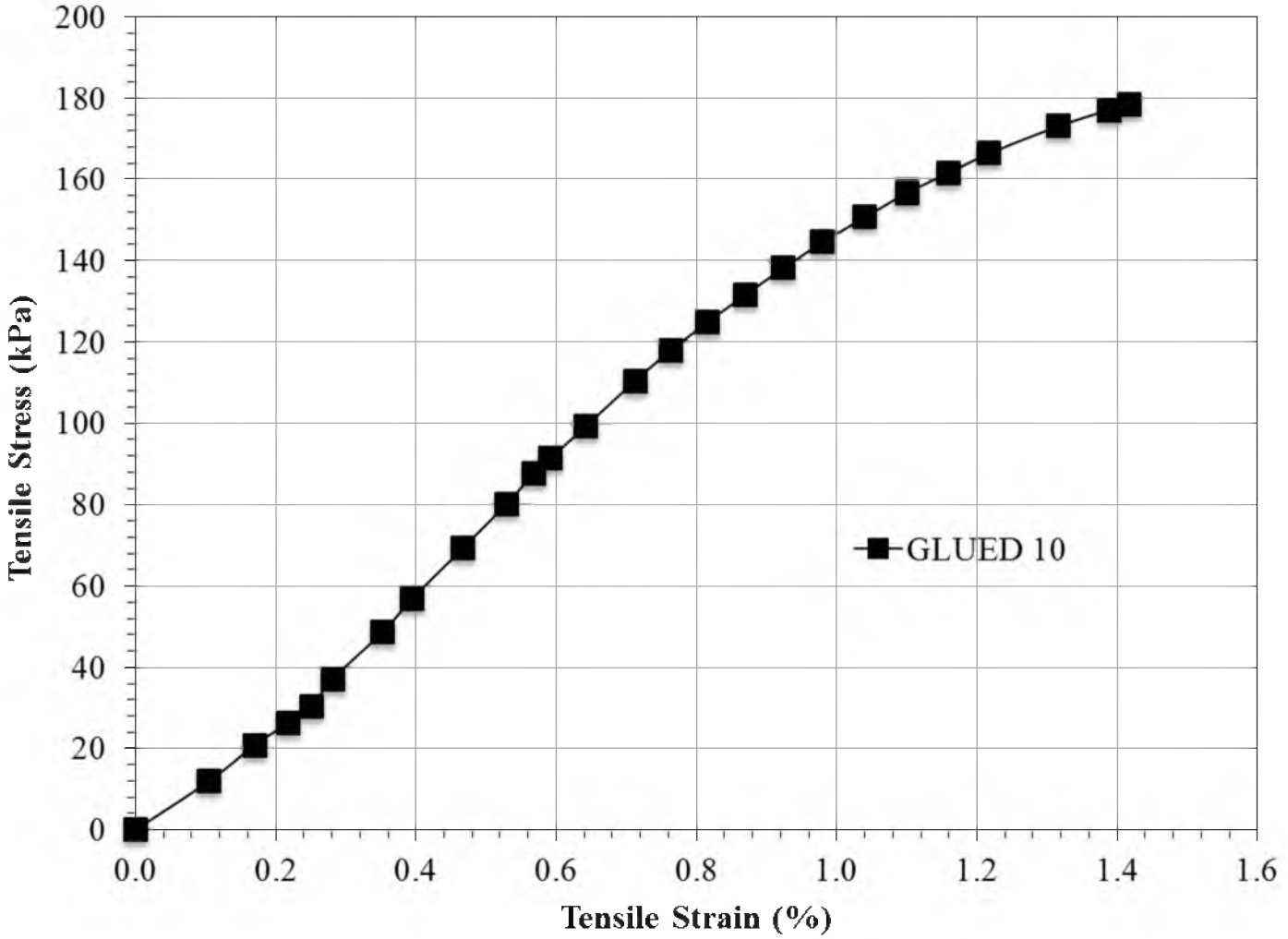

Figure A.41. Tensile stress-strain behavior of glued EPS specimen with "GLUED 10" specimen ID

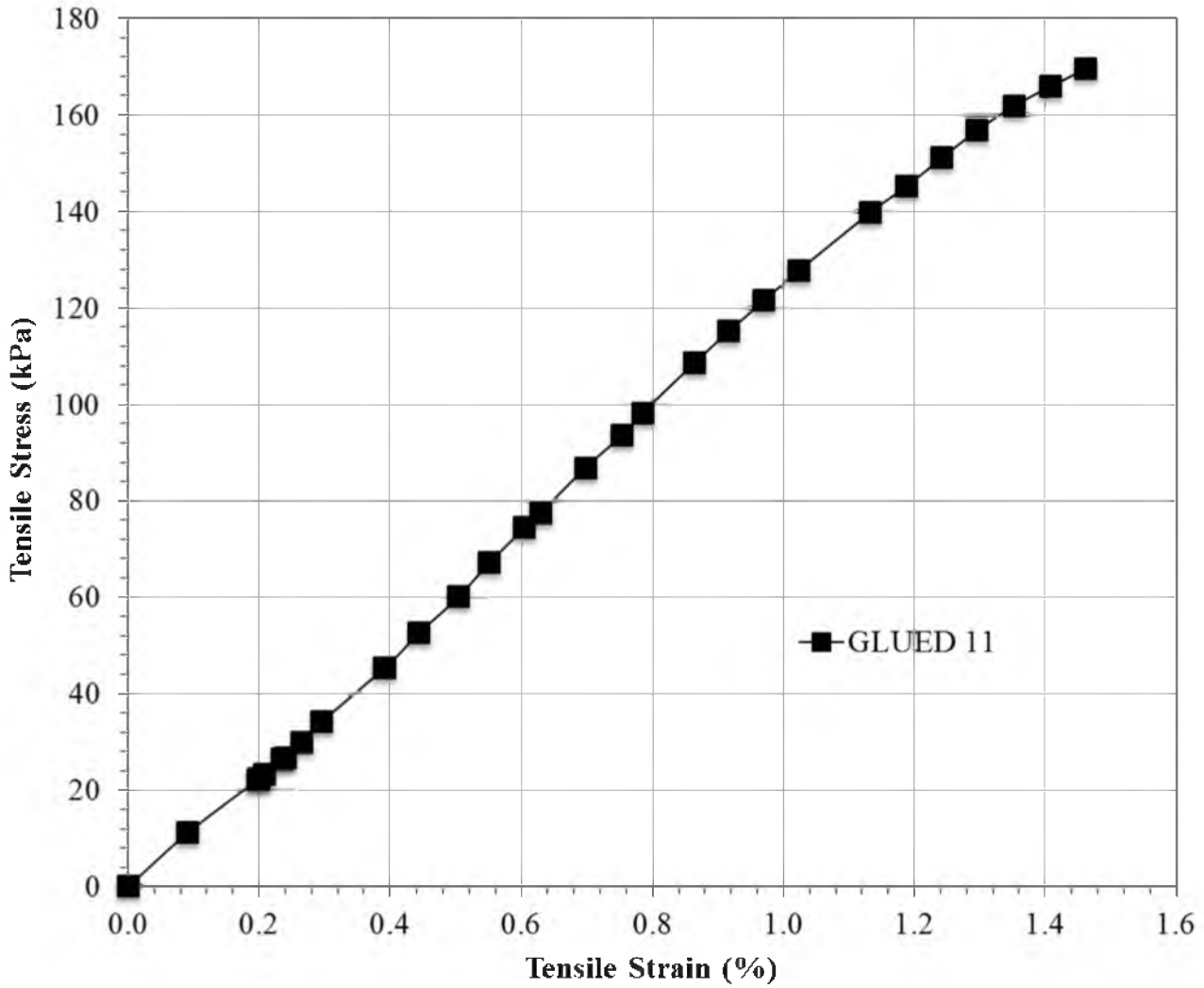

Figure A.42. Tensile stress-strain behavior of glued EPS specimen with "GLUED 11" specimen ID

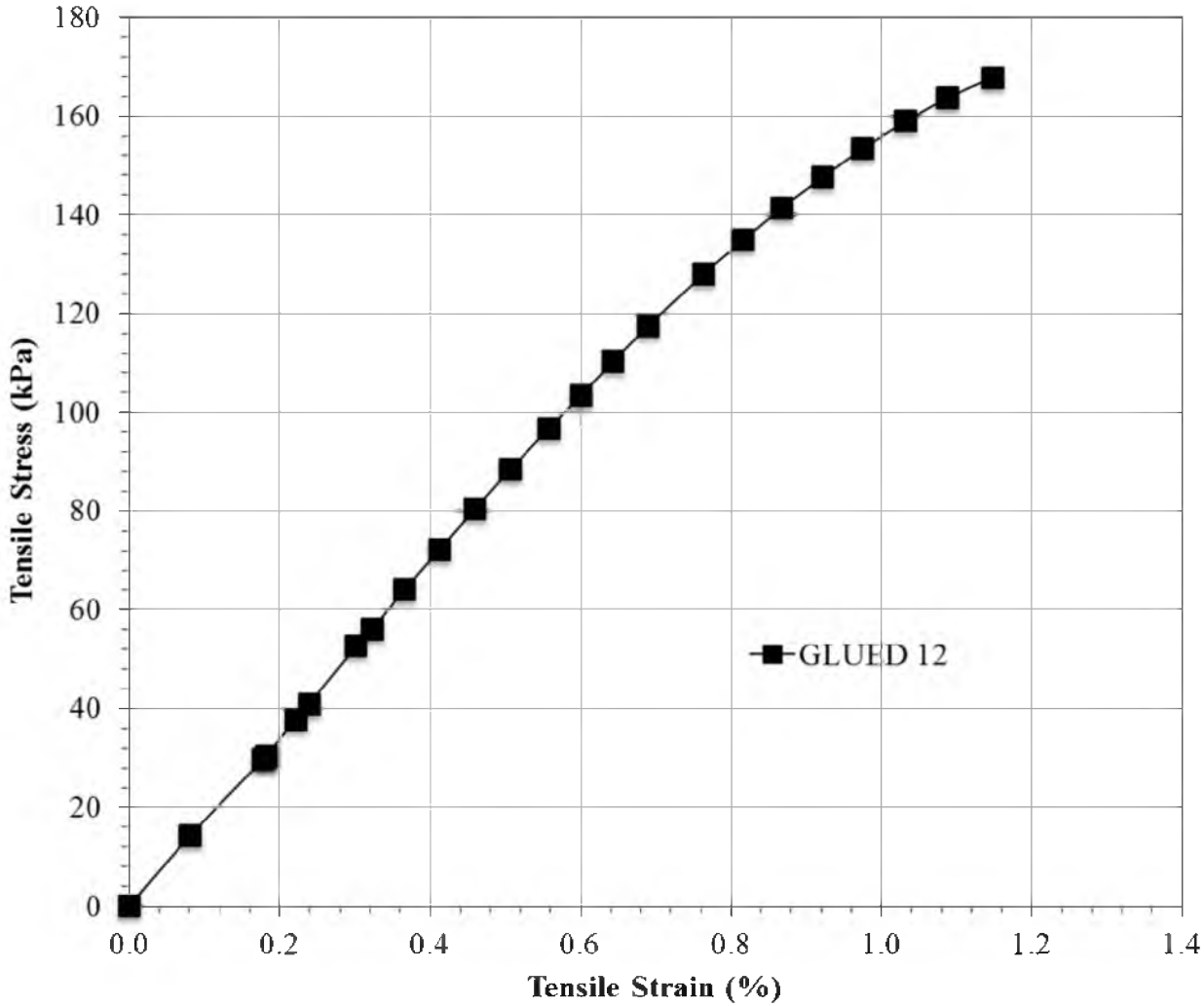

Figure A.43. Tensile stress-strain behavior of glued EPS specimen with "GLUED 12" specimen ID

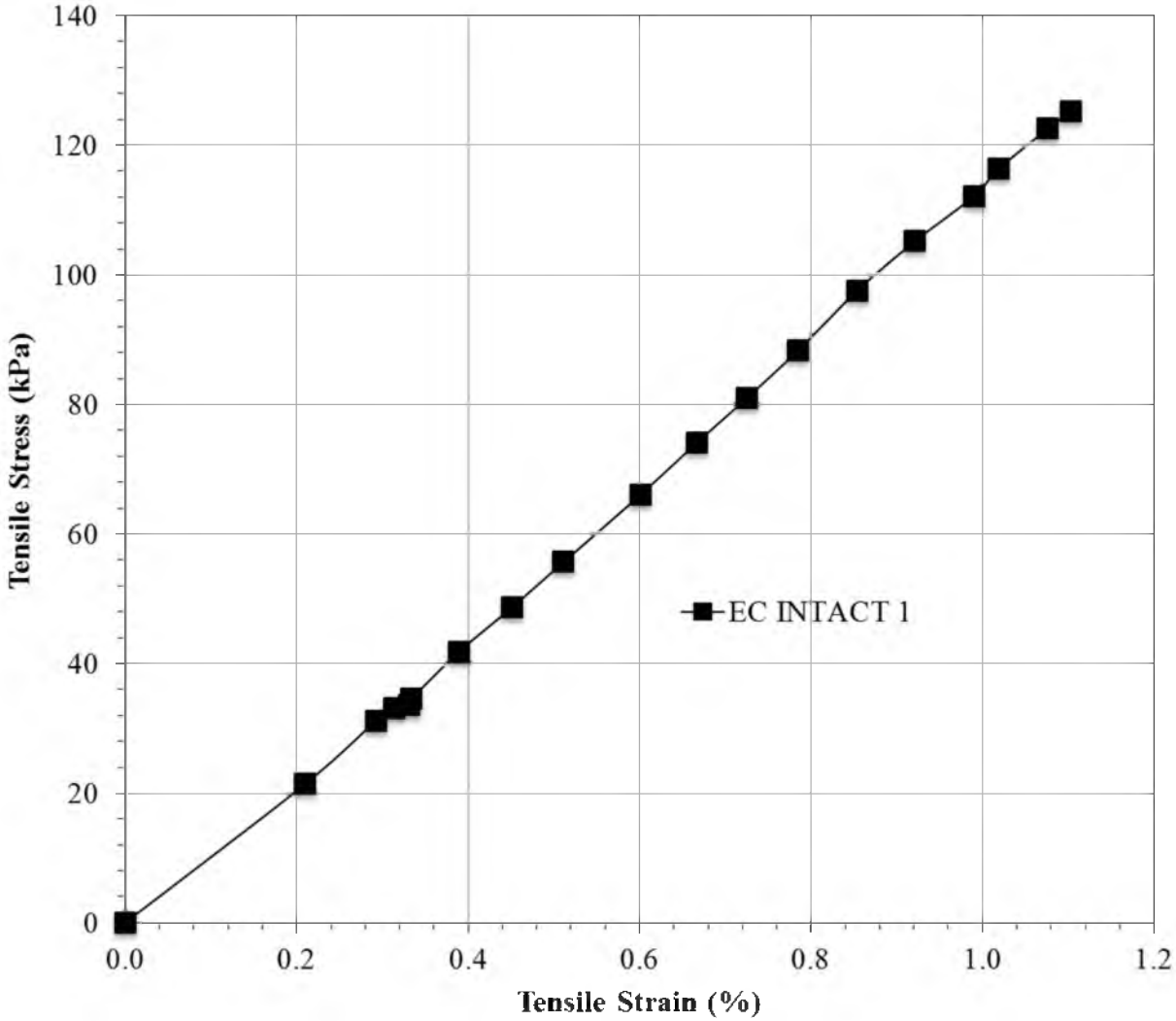

Figure A.44. Tensile stress-strain behavior of environmentally conditioned intact EPS specimen with "EC INTACT 1" specimen ID

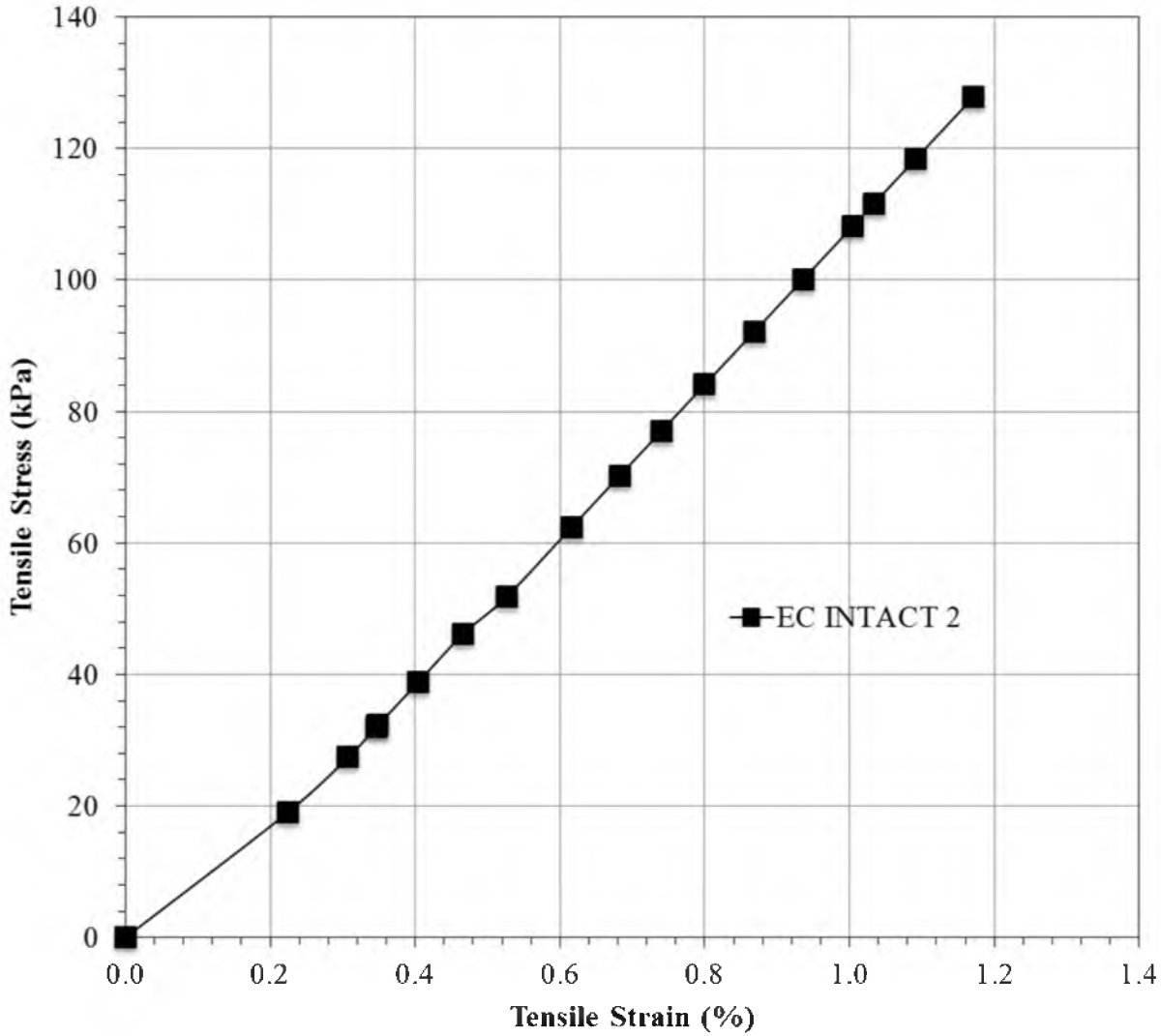

Figure A.45. Tensile stress-strain behavior of environmentally conditioned intact EPS specimen with "EC INTACT 2" specimen ID

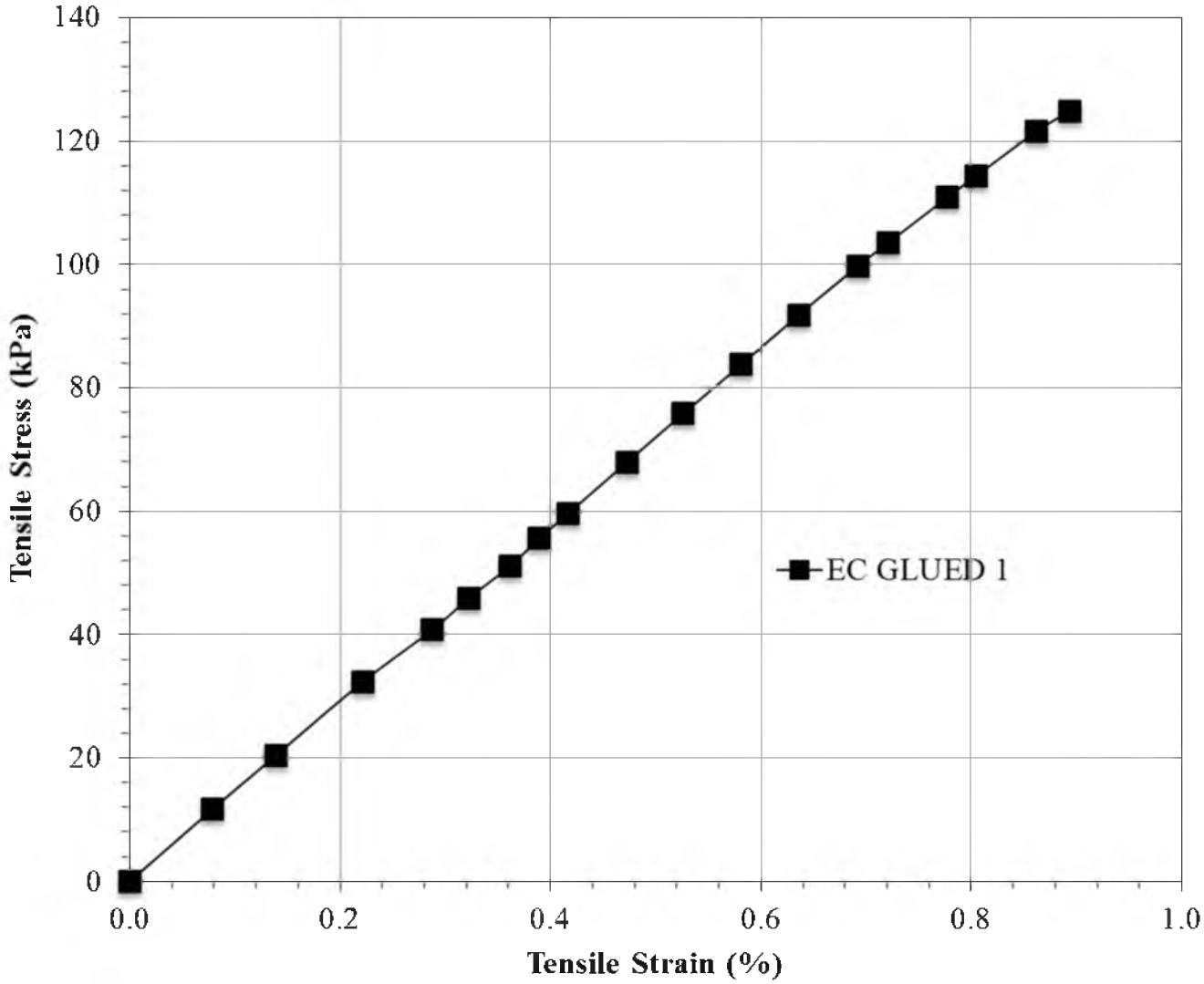

Figure A.46. Tensile stress-strain behavior of environmentally conditioned glued EPS specimen with "EC GLUED 1" specimen ID

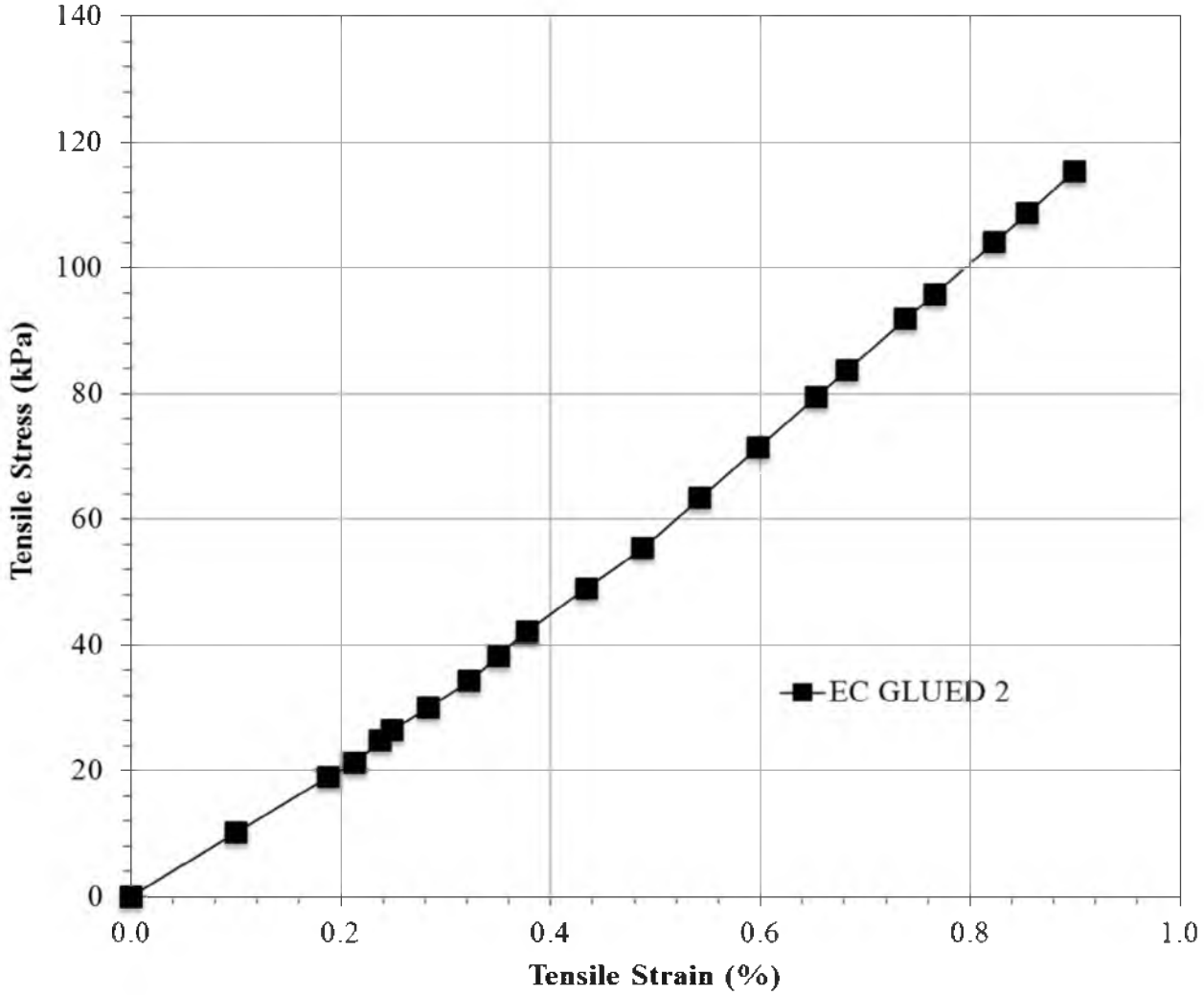

Figure A.47. Tensile stress-strain behavior of environmentally conditioned glued EPS specimen with "EC GLUED 2" specimen ID

Table A.2. Tensile test results of EPS specimens

Specimen ID	ε_e	σ_e	ε_t	σ_t
----------	*(%)*	*(kPa)*	*(%)*	*(kPa)*
INTACT 1	0.81	113.28	1.36	158.77
INTACT 2	0.62	106.65	1.01	151.26
INTACT 3	1.00	128.31	1.63	186.33
INTACT 4	0.92	124.54	1.22	154.88
INTACT 5	0.96	112.59	1.17	131.23
GLUED 1	0.41	73.88	0.86	124.26
GLUED 2	0.46	34.44	1.59	162.10
GLUED 3	0.86	124.70	1.51	180.36
GLUED 4	0.79	119.67	1.44	182.60
GLUED 5	0.87	122.89	0.97	132.48
GLUED 6	0.85	117.17	1.14	145.84
GLUED 7	0.40	63.04	1.57	185.22
GLUED 8	0.99	135.28	1.26	158.93
GLUED 9	0.77	116.33	0.88	127.19
GLUED 10	0.53	80.15	1.42	178.40
GLUED 11	0.97	121.48	1.46	169.49
GLUED 12	0.69	117.44	1.15	167.82
EC INTACT 1	0.92	105.20	1.10	125.25
EC INTACT 2	1.00	108.24	1.17	127.84
EC GLUED 1	0.86	121.62	0.89	124.83
EC GLUED 2	0.90	115.41	0.90	115.41

APPENDIX B

DYNAMIC CHARACTERISTICS OF EPS EMBANKMENT

Soil-Structure Interaction

Because the design ground motion is usually specified as a free-field motion at the ground surface, throughout the study the input motion in the numerical model was applied at the ground surface (i.e., base of the EPS embankment). This approach assumes that there is minimal soil-structure interaction between the EPS embankment and the underlying soil and that it is conservative to disregard such effects.

Two primary causes of soil-structure interaction are: the incapability of the structure base to match the free-field displacement and the effect of the dynamic response of the structure on the movement of the foundation soil. The former cause is associated with stiff structures embedded in a soil deposit where the relatively high stiffness of the structure leads in kinematic interaction. The latter cause, however, corresponds to the mass of the structure which can transmit forces to the compliant foundation soil and produce movement that would not take place in a fixed-based structure. In this case the effects of soil compliance on the resulting response are due to inertial interaction (Kramer, 1996). In an EPS geofoam embankment the shallow embedment of the basal blocks and rather low stiffness of the EPS minimizes kinematic interaction while low mass of the EPS embankment system minimizes inertial interaction. Nonetheless, regardless of the magnitude of the soil-structure interaction effects it is expected that disregarding such effects is on the conservative side.

In order to verify the validity of neglecting the soil-structure effects in an EPS geofoam embankment a FLAC model was developed. The model is capable of capturing the free-field accelerations and comparing them with those at the base of an embedded EPS embankment.

An 8 m high and 20 m wide EPS embankment topped with a 1 m thick lumped mass was modeled in FLAC where the embankment was embedded (i.e., with an embedment depth of 0.5 m) in a 52 m wide and 16 m high soft clay deposit. The embankment and soil deposit were modeled elastically with 5% Rayleigh damping assigned to the soil. Table B.1 shows the material properties used in the model. Harmonic waves in both horizontal and vertical directions were imposed to the base of the soil. Horizontal wave was applied with acceleration amplitude of 0.2 g at the fundamental period of the embankment (i.e., 0.6 s) and the vertical wave had an amplitude equivalent to 40% of the horizontal amplitude and was applied at the period of 0.3 s. The bottom of the soil deposit was fixed in the y direction and free-field condition was assigned to the sides of the soil deposit. Figure B.1 illustrates the mesh, material assignment and the boundary conditions.

To investigate the soil-structure effects the accelerations at a gridpoint located on the far left of the model (on the soil surface) characterized by the free-field condition (point 1 in Figure B.1) was compared with that of the EPS geofoam embankment base (point 2 in Figure B.1). Figure B.2 shows the free-field acceleration at the soil surface in green and the embankment basal acceleration in blue. It is shown that for the most part the acceleration time histories show a similar trend and magnitude. However, the peak acceleration values corresponding to the base of the embankment are up to 30% smaller compared to those of the free-field. Therefore, one would only be conservative in applying the seismic input motion at the base of the embankment rather than the base of the soil without altering the dynamics of the system significantly.

Table B.1. EPS geofoam embankment system material properties

Material	ρ	E	υ	G	K
----------	kg/m^3	MPa	----------	MPa	MPa
EPS	19	7	0.1	3.2	2.9
Lumped Mass	2321	30000	0.2	12712	15625
Foundation Soil	1900	6	0.4	2.1	10

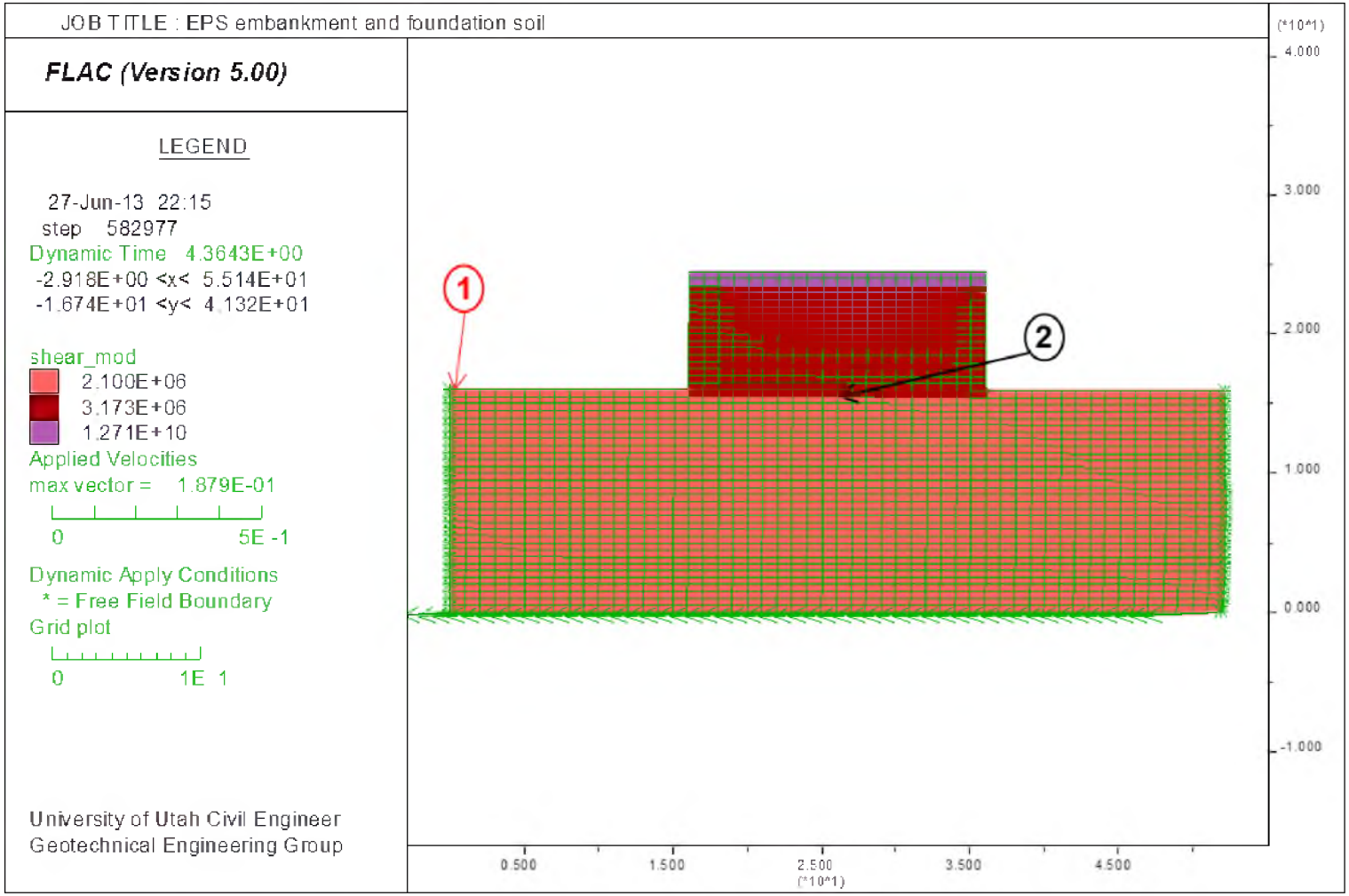

Figure B.1. EPS geofoam embankment and the foundation soil FLAC model

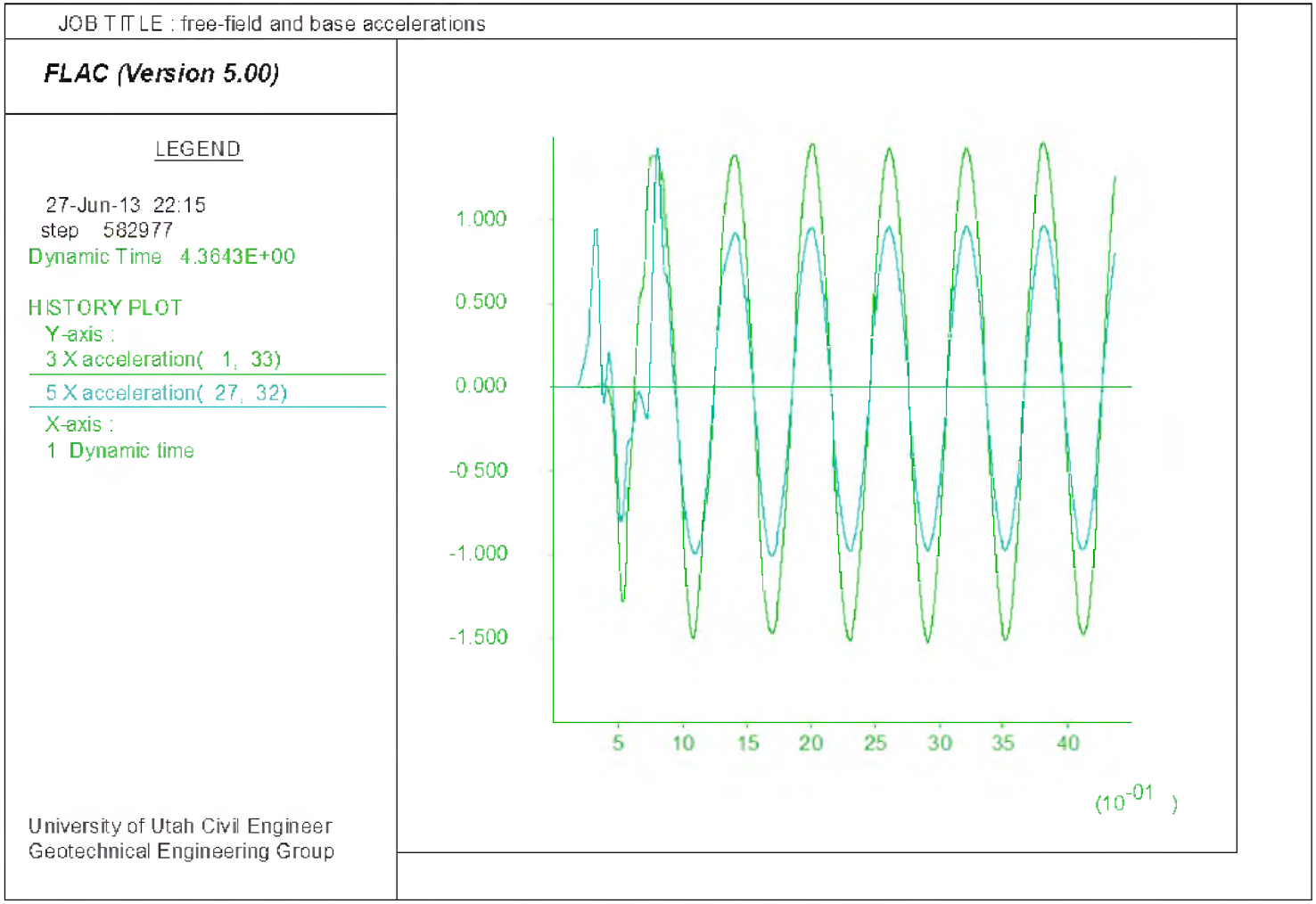

Figure B.2. Response accelerations at the free-field boundary and base of the EPS embankment

APPENDIX C

SLIDING ANALYSIS

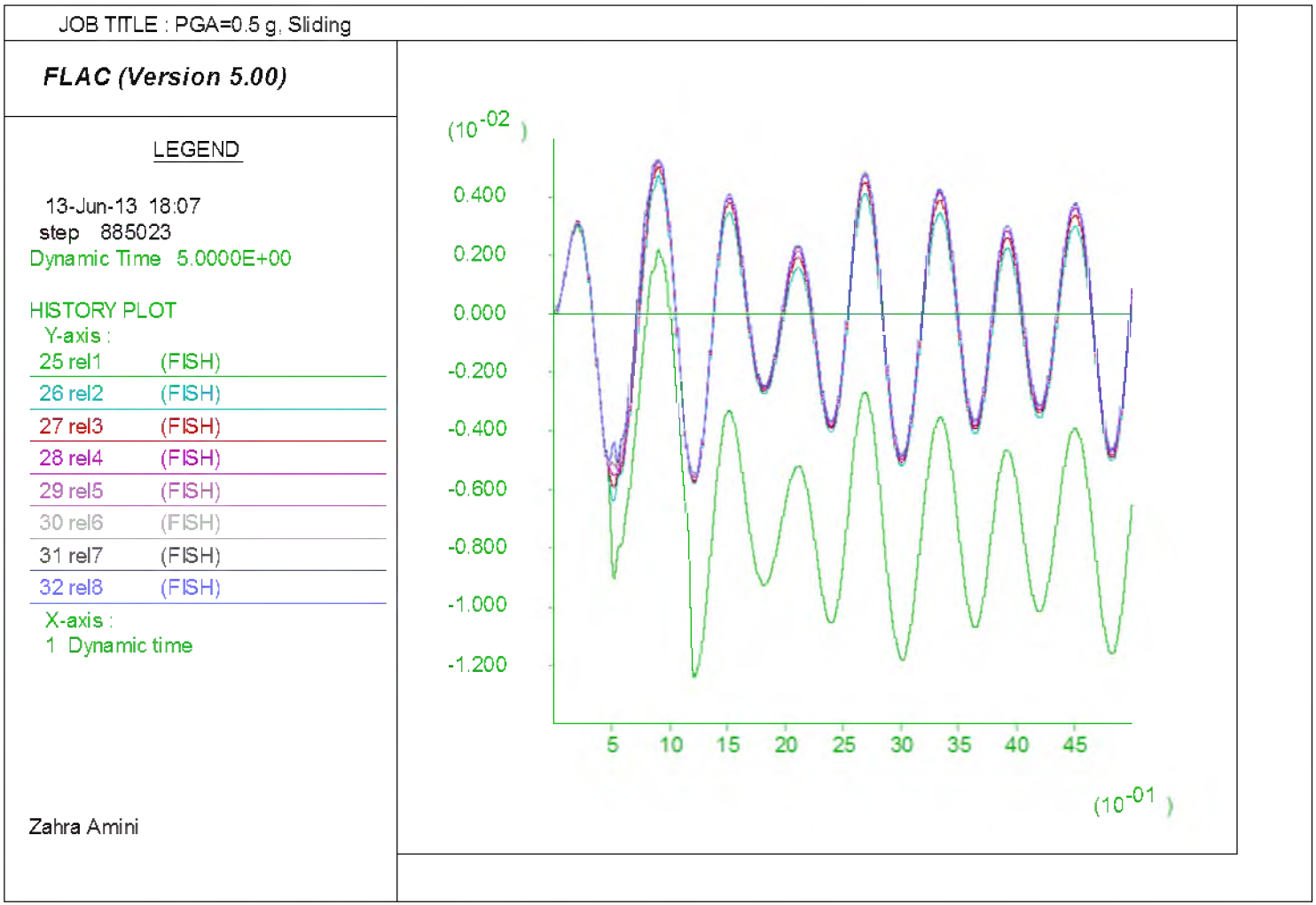

Figure C.1. Interlayer sliding within the EPS embankment due to 0.5g amplitude horizontal input motion

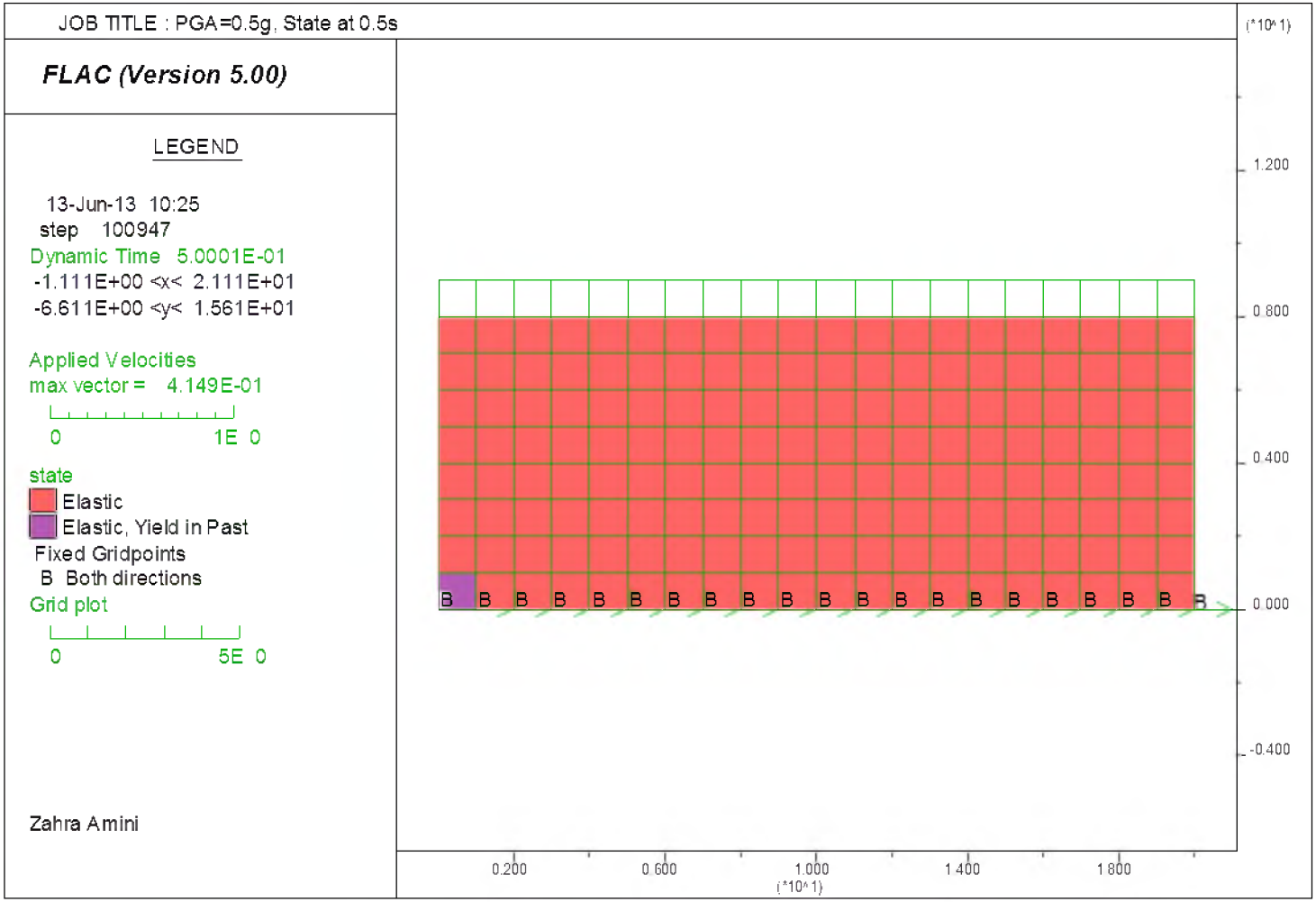

Figure C.2. State of the EPS embankment after one cycle of 0.5g amplitude horizontal input motion

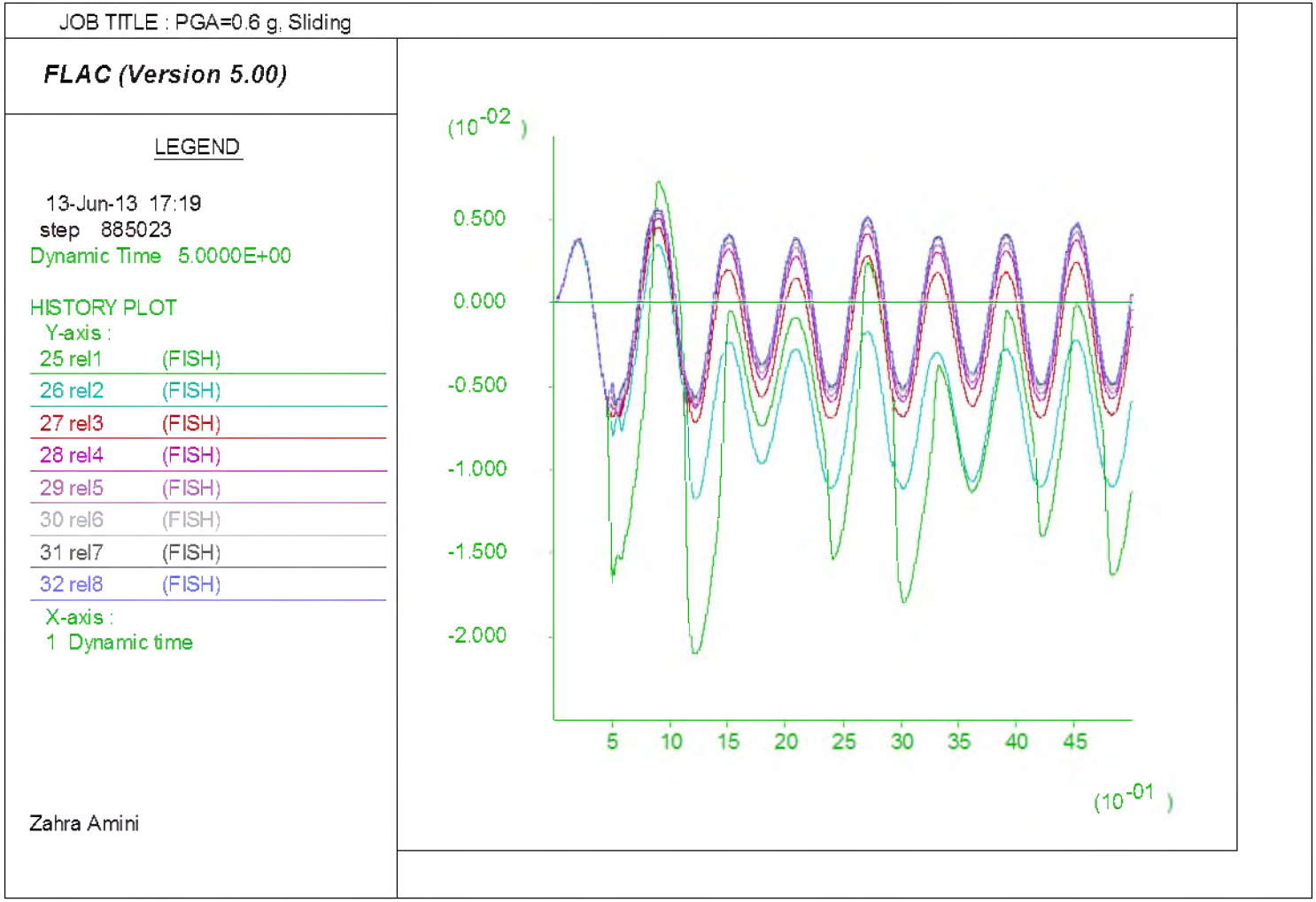

Figure C.3. Interlayer sliding within the EPS embankment due to 0.6g amplitude horizontal input motion

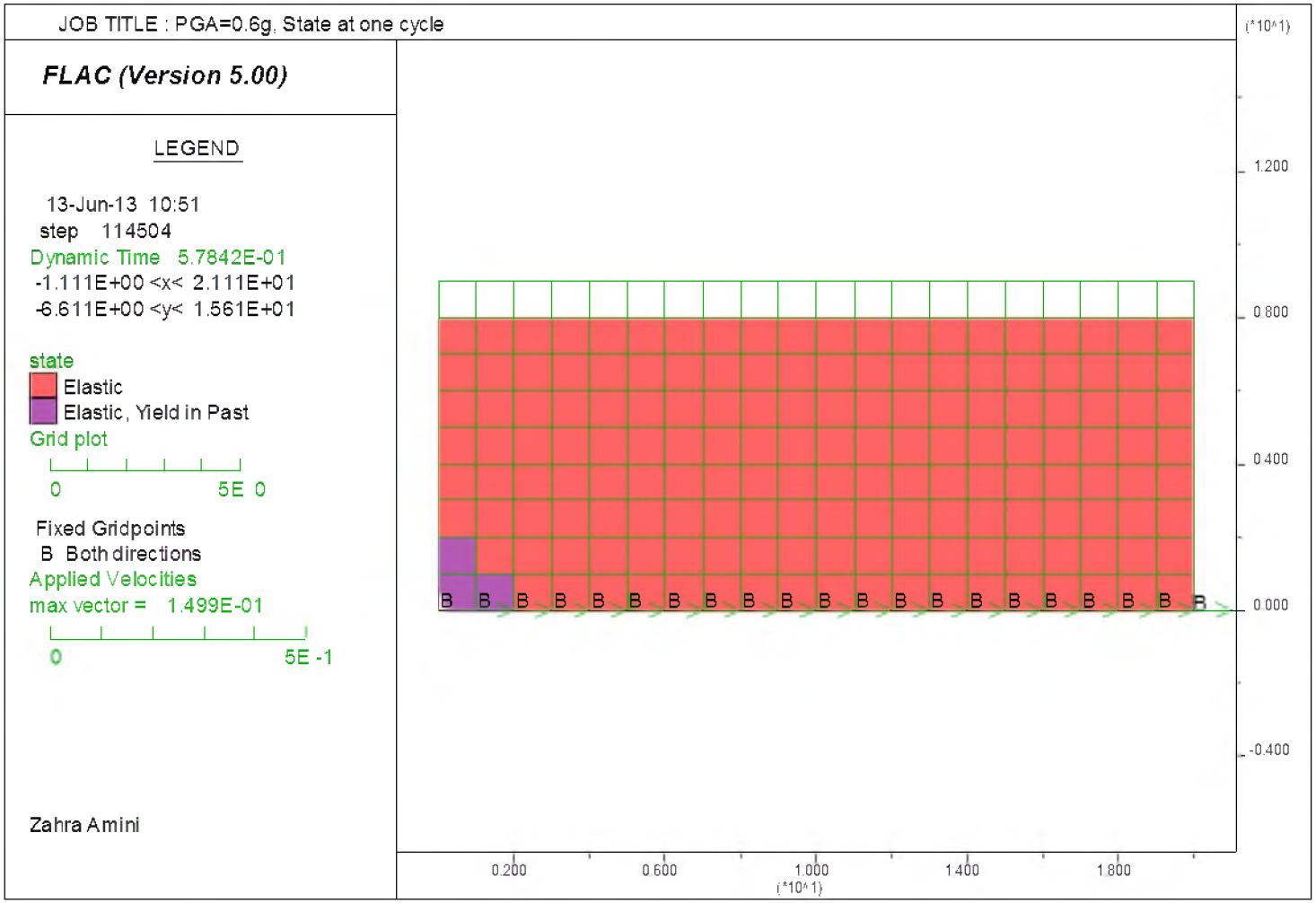

Figure C.4. State of the EPS embankment after one cycle of 0.6g amplitude horizontal input motion

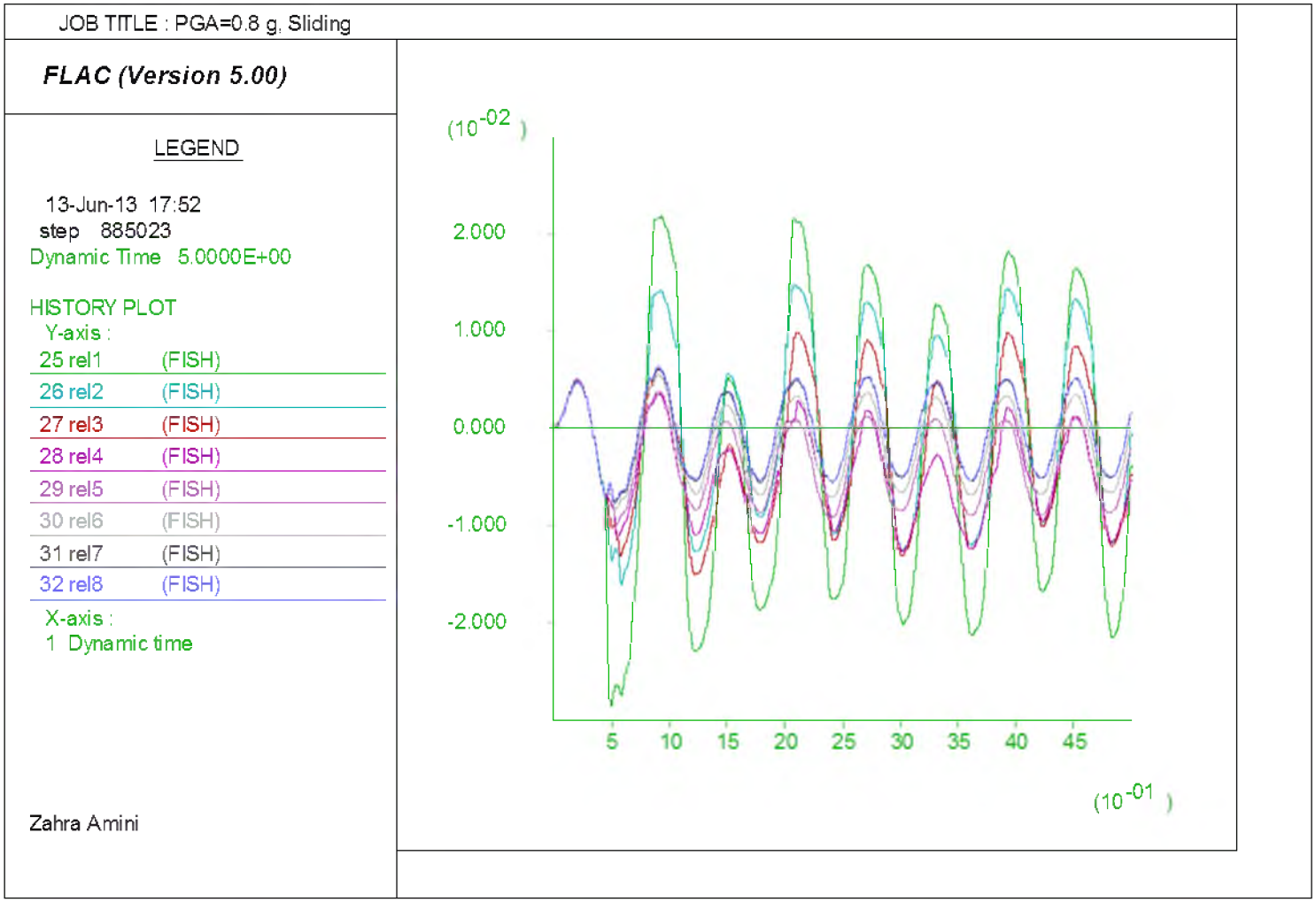

Figure C.5. Interlayer sliding within the EPS embankment due to 0.8g amplitude horizontal input motion

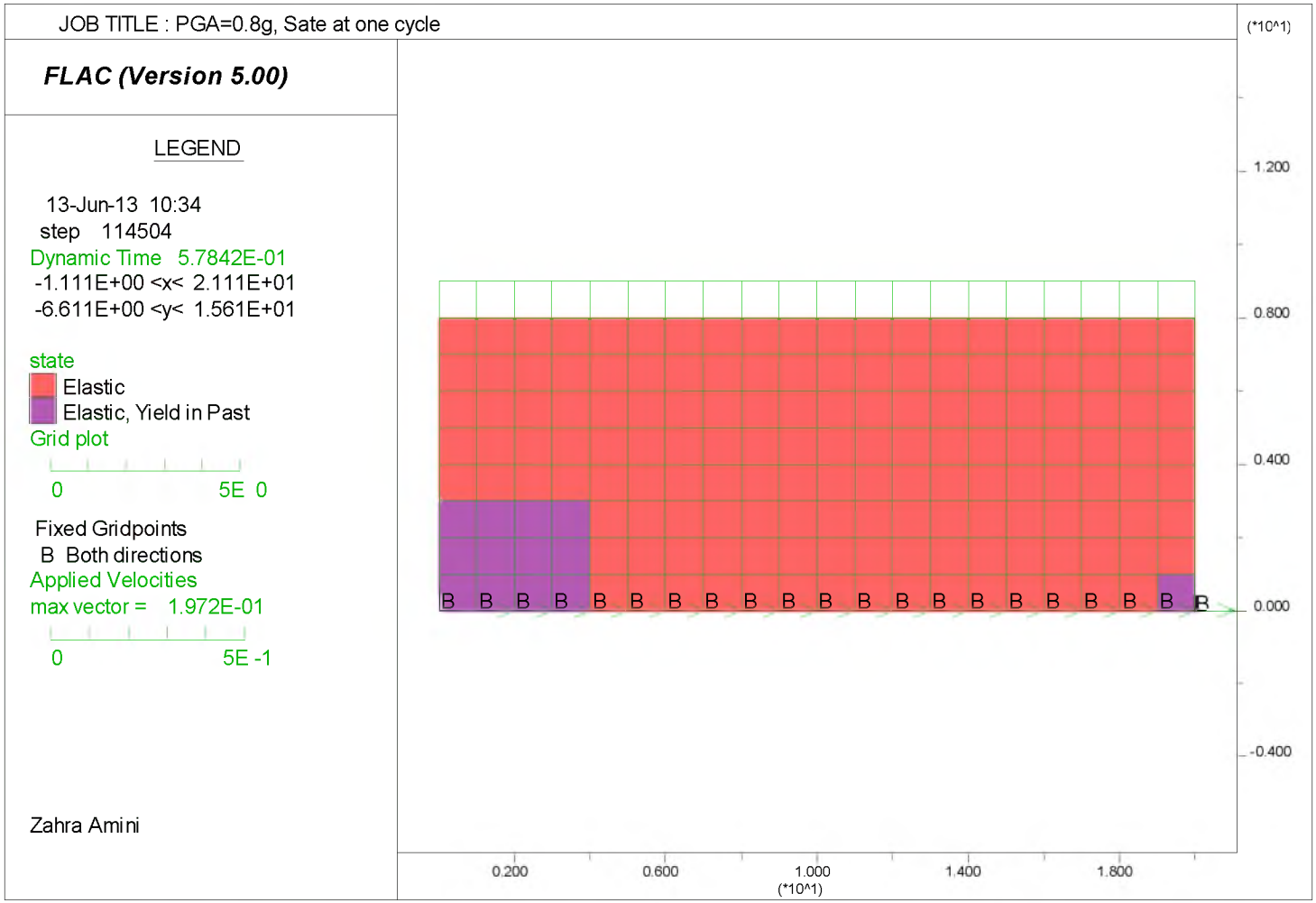

Figure C.6. State of the EPS embankment after one cycle of 0.8g amplitude horizontal input motion

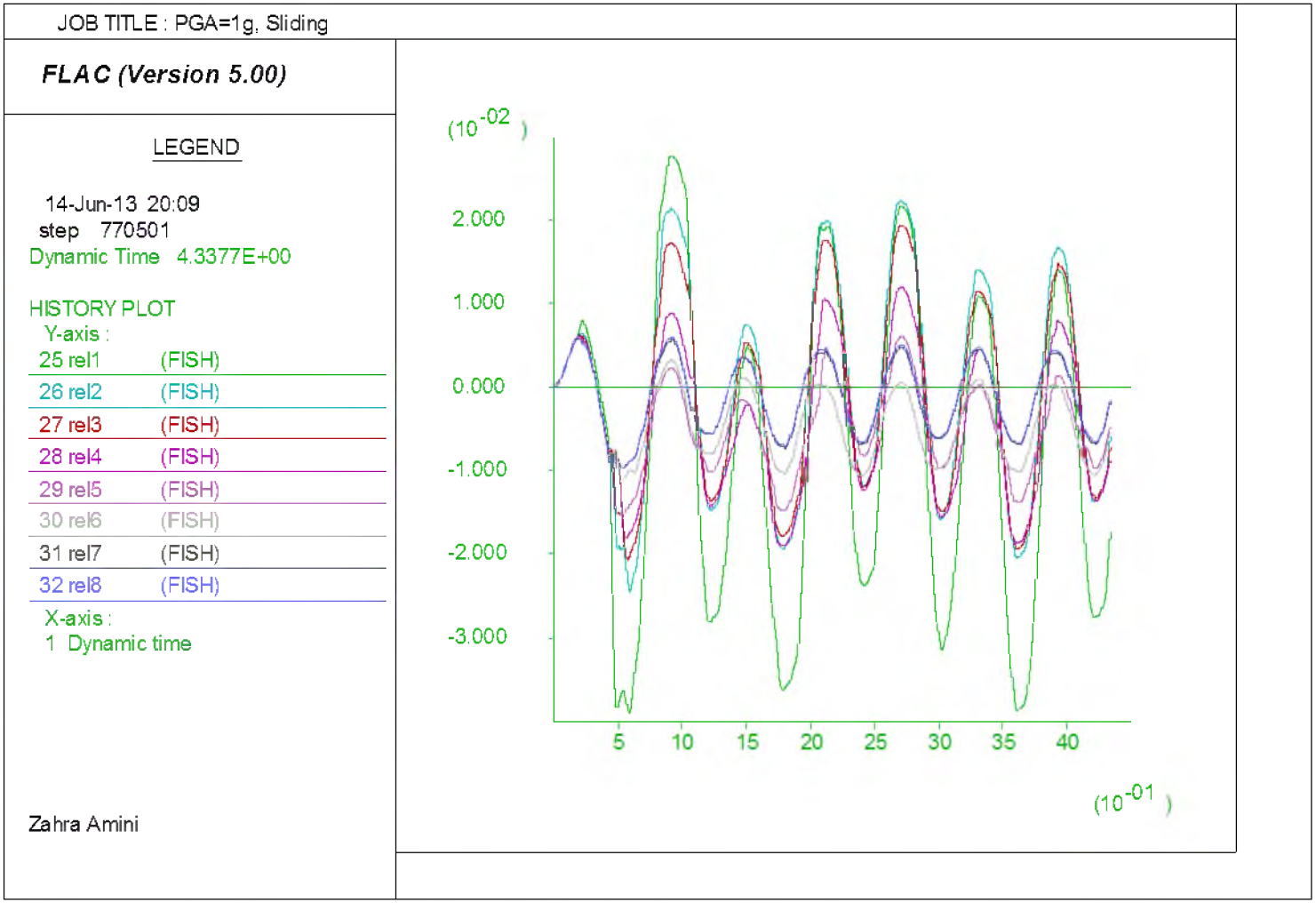

Figure C.7. Interlayer sliding within the EPS embankment due to 1g amplitude horizontal input motion

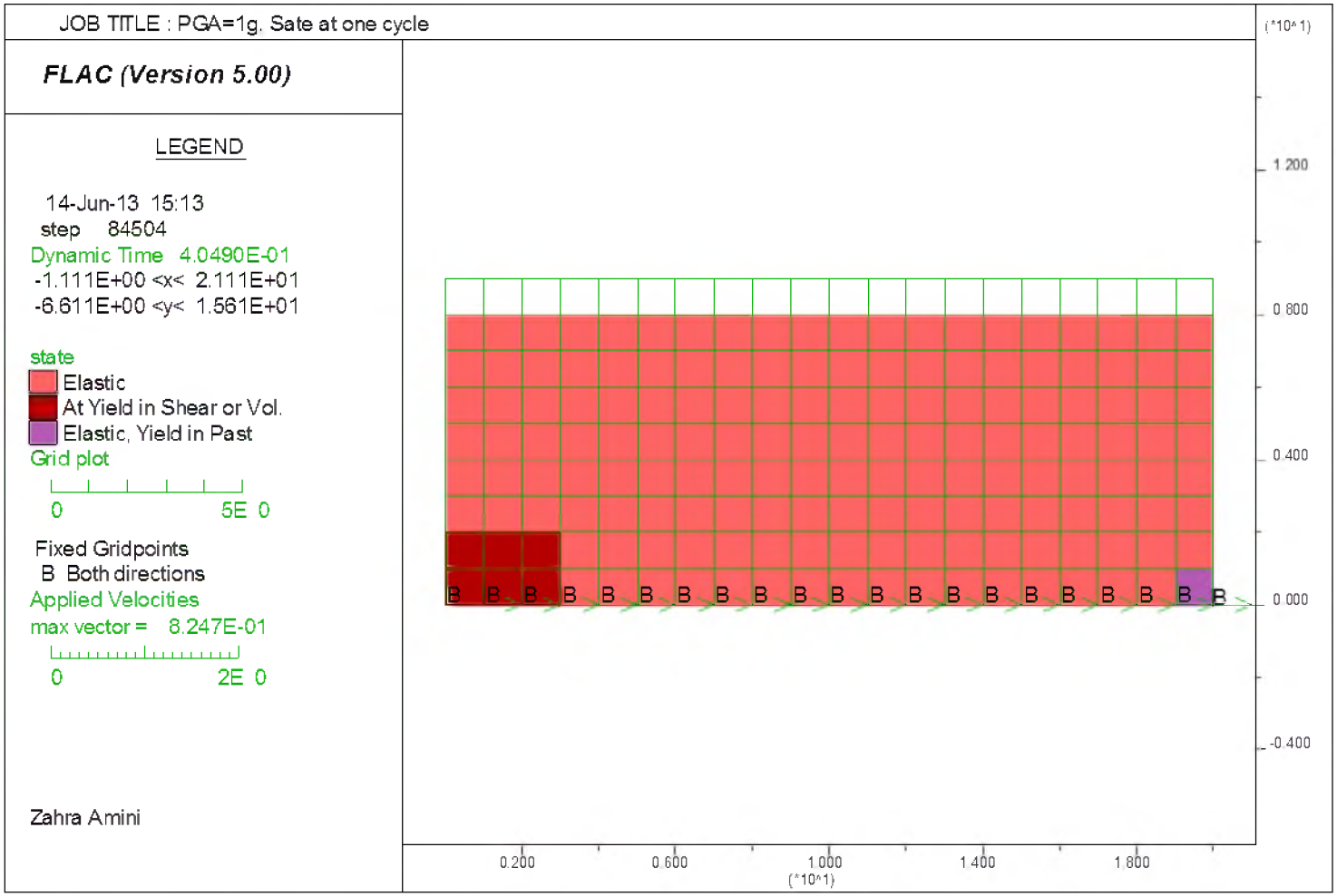

Figure C.8. State of the EPS embankment after one cycle of 1g amplitude horizontal input motion

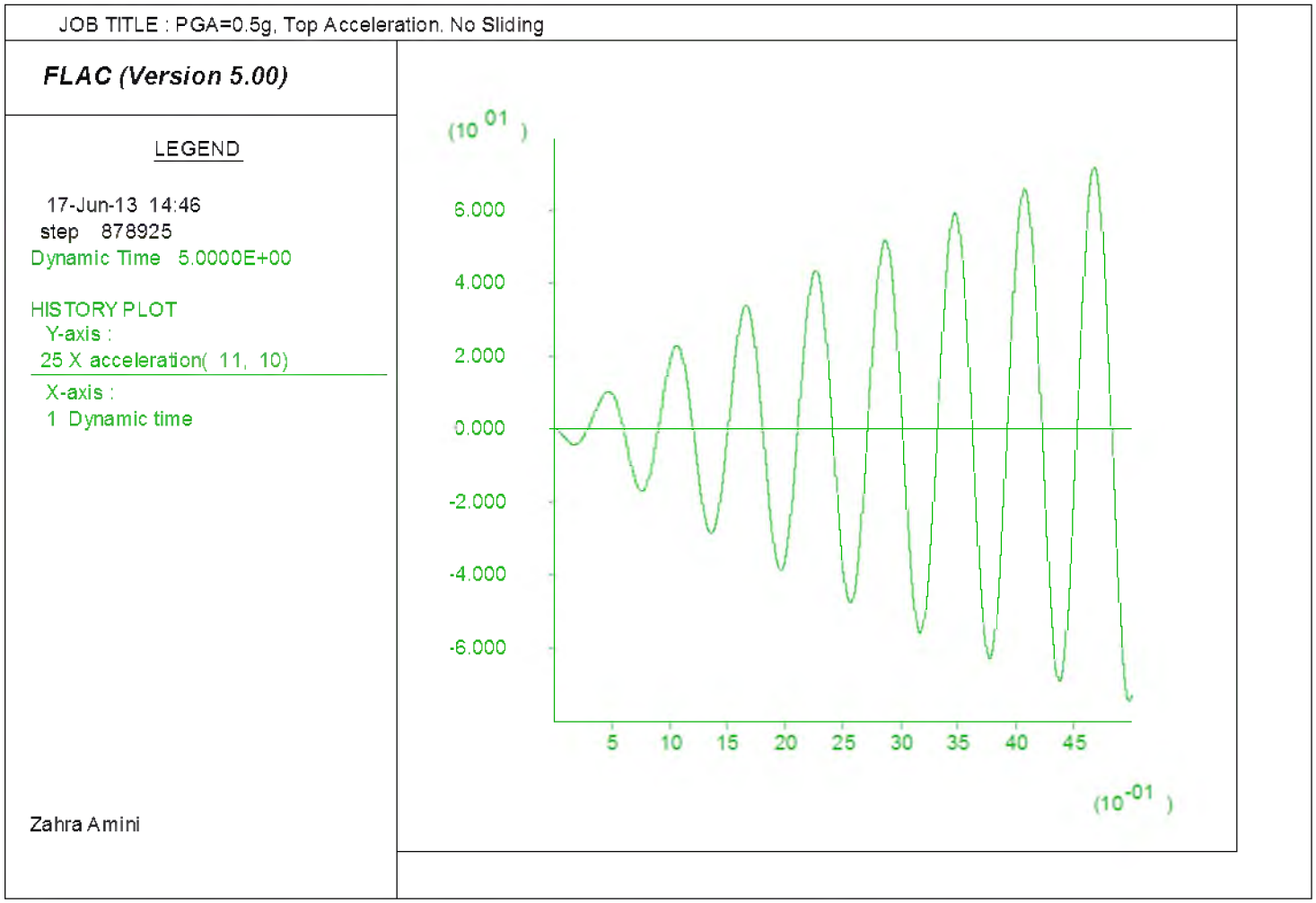

Figure C.9. Response acceleration at the top of the EPS embankment without interfaces due to amplitude 0.5g input motion

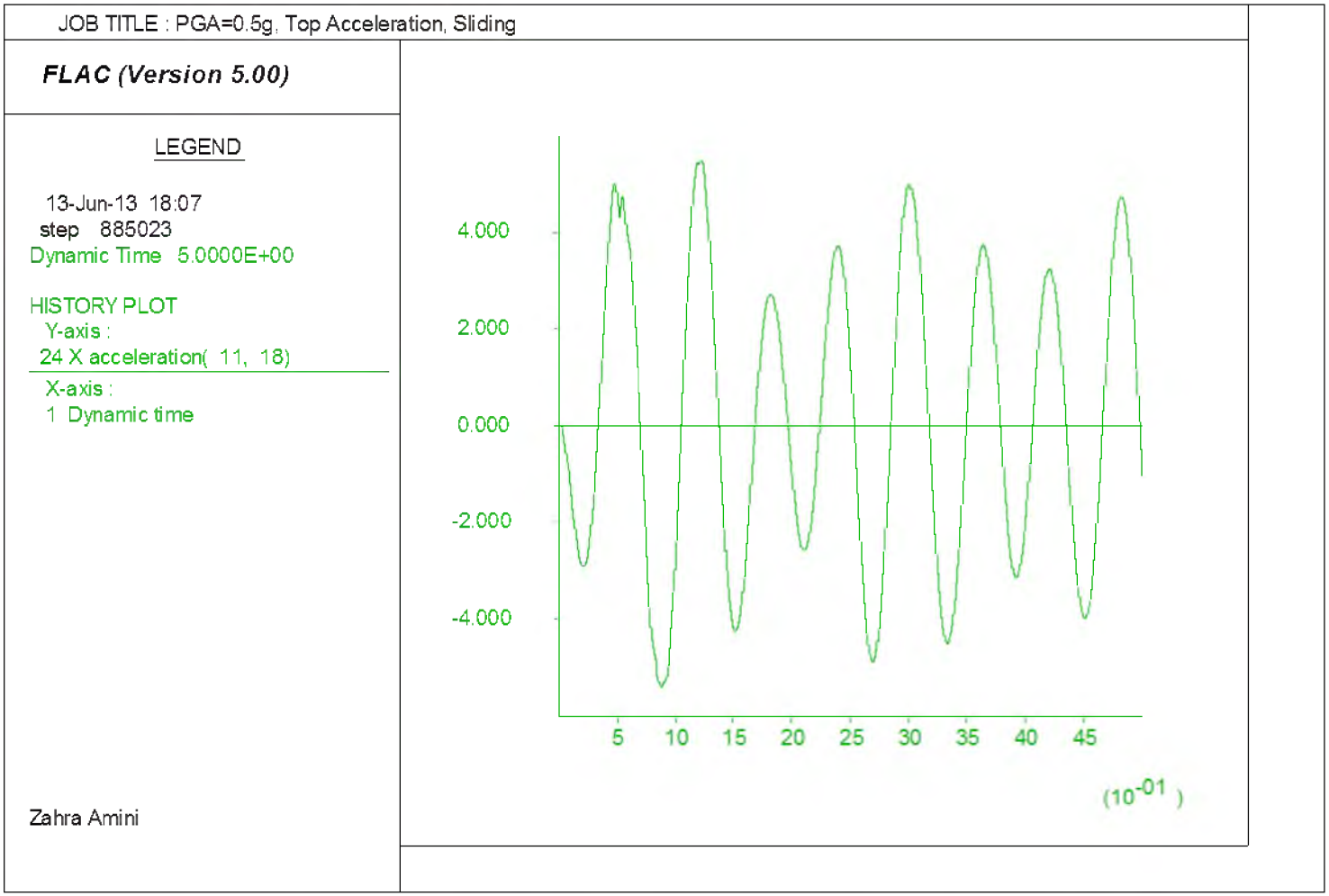

Figure C.10. Response acceleration at the top of the EPS embankment with interfaces due to amplitude 0.5g input motion

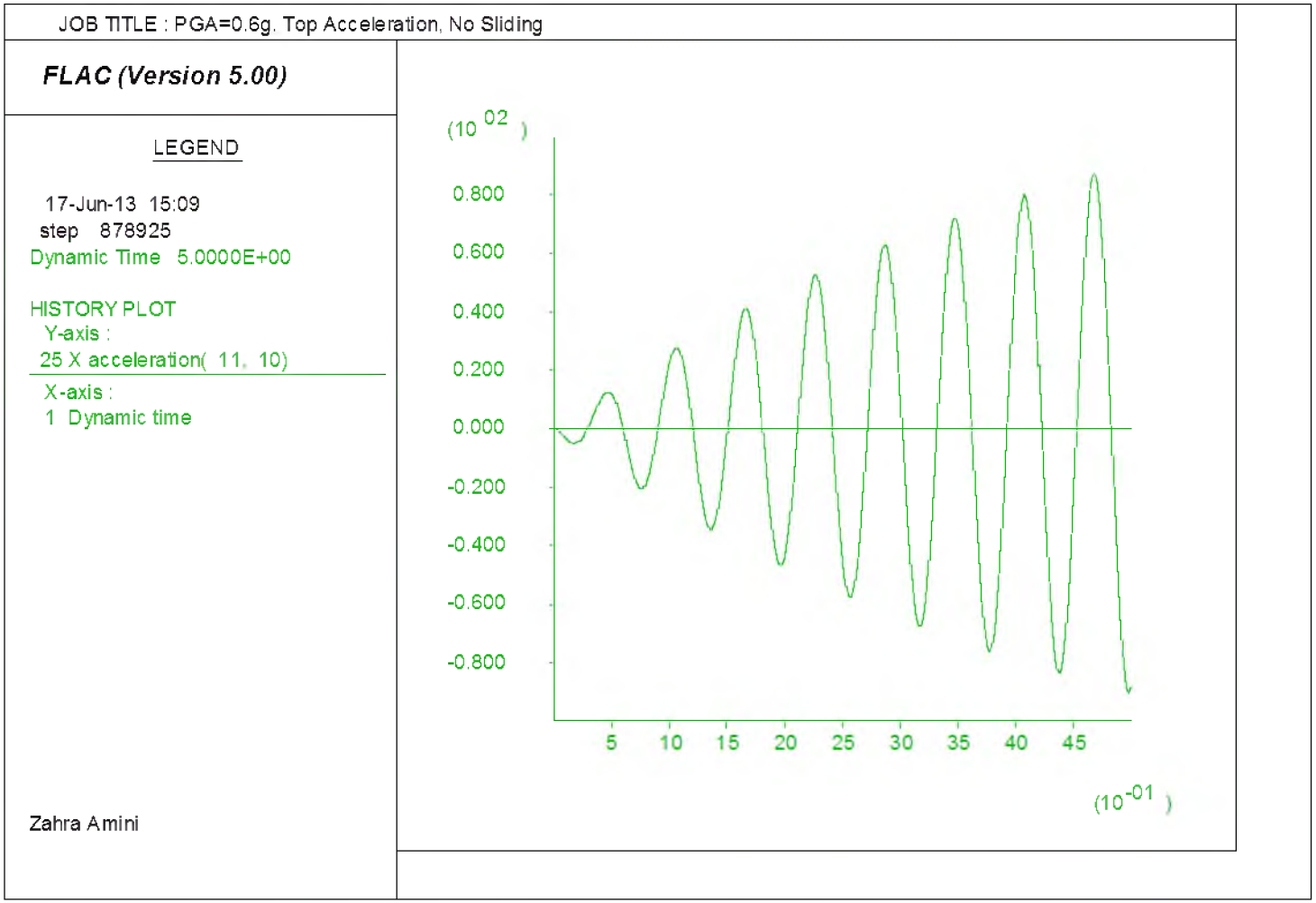

Figure C.11. Response acceleration at the top of the EPS embankment without interfaces due to amplitude 0.6g input motion

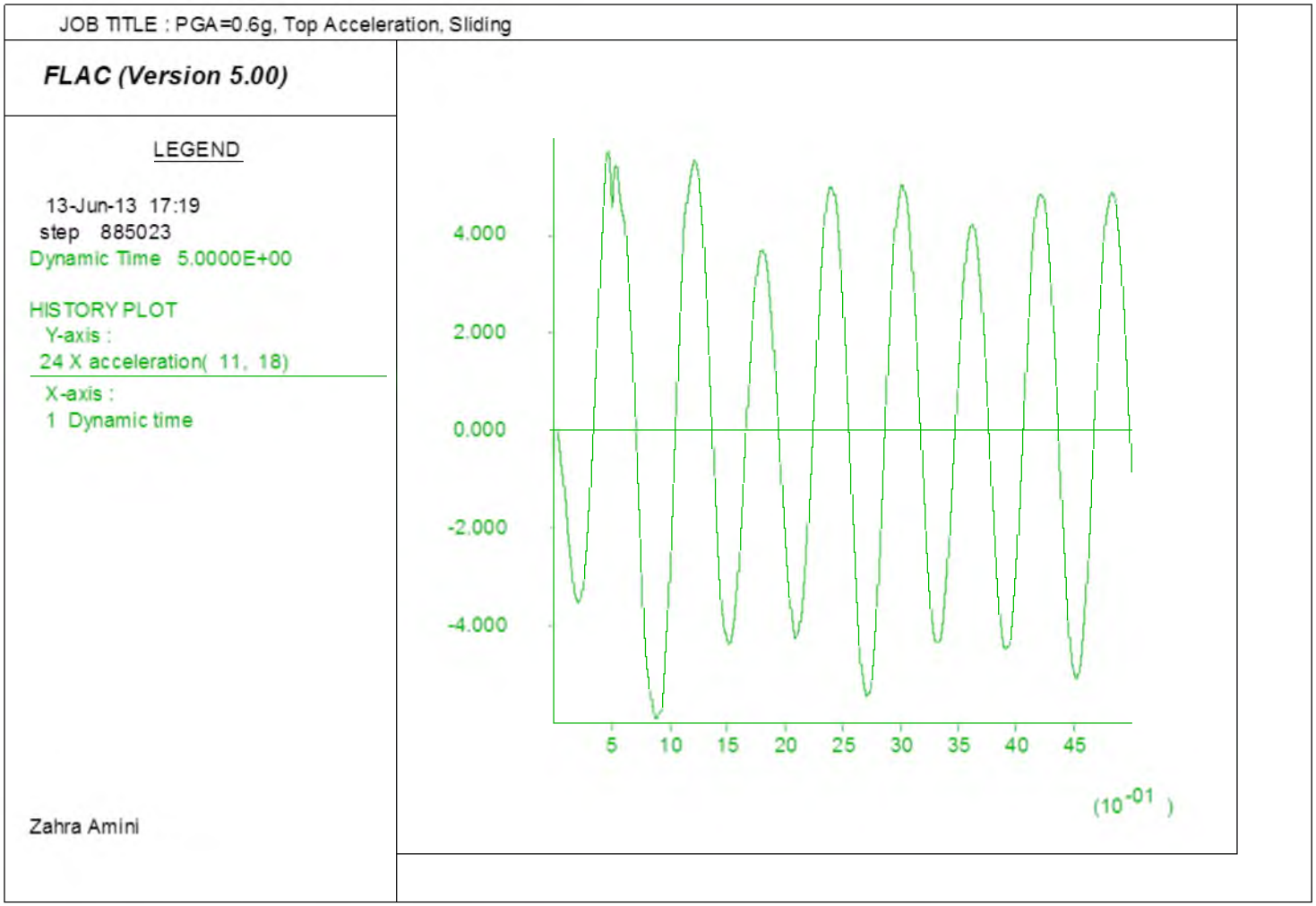

Figure C.12. Response acceleration at the top of the EPS embankment with interfaces due to amplitude 0.6g input motion

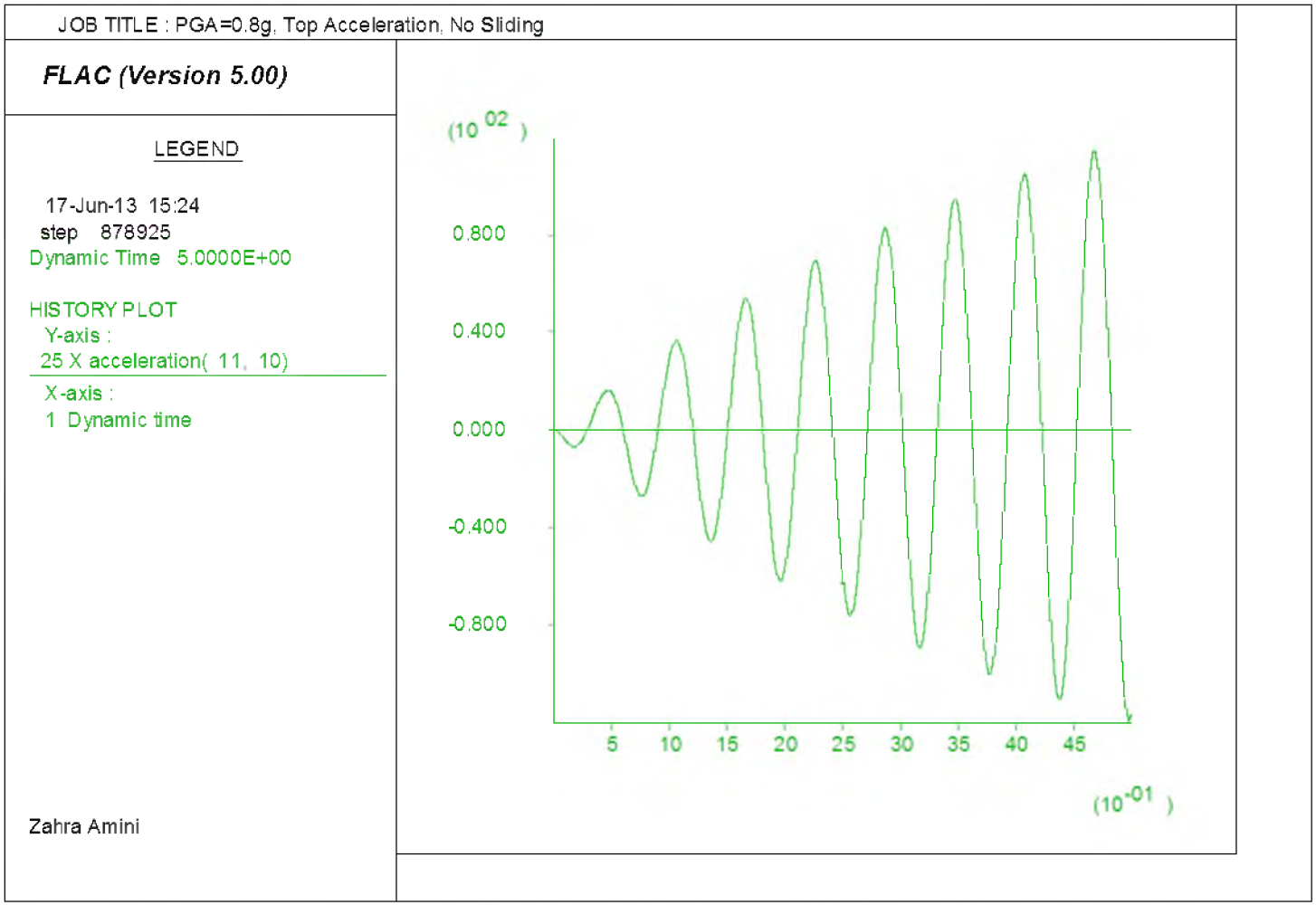

Figure C.13. Response acceleration at the top of the EPS embankment without interfaces due to amplitude 0.8g input motion

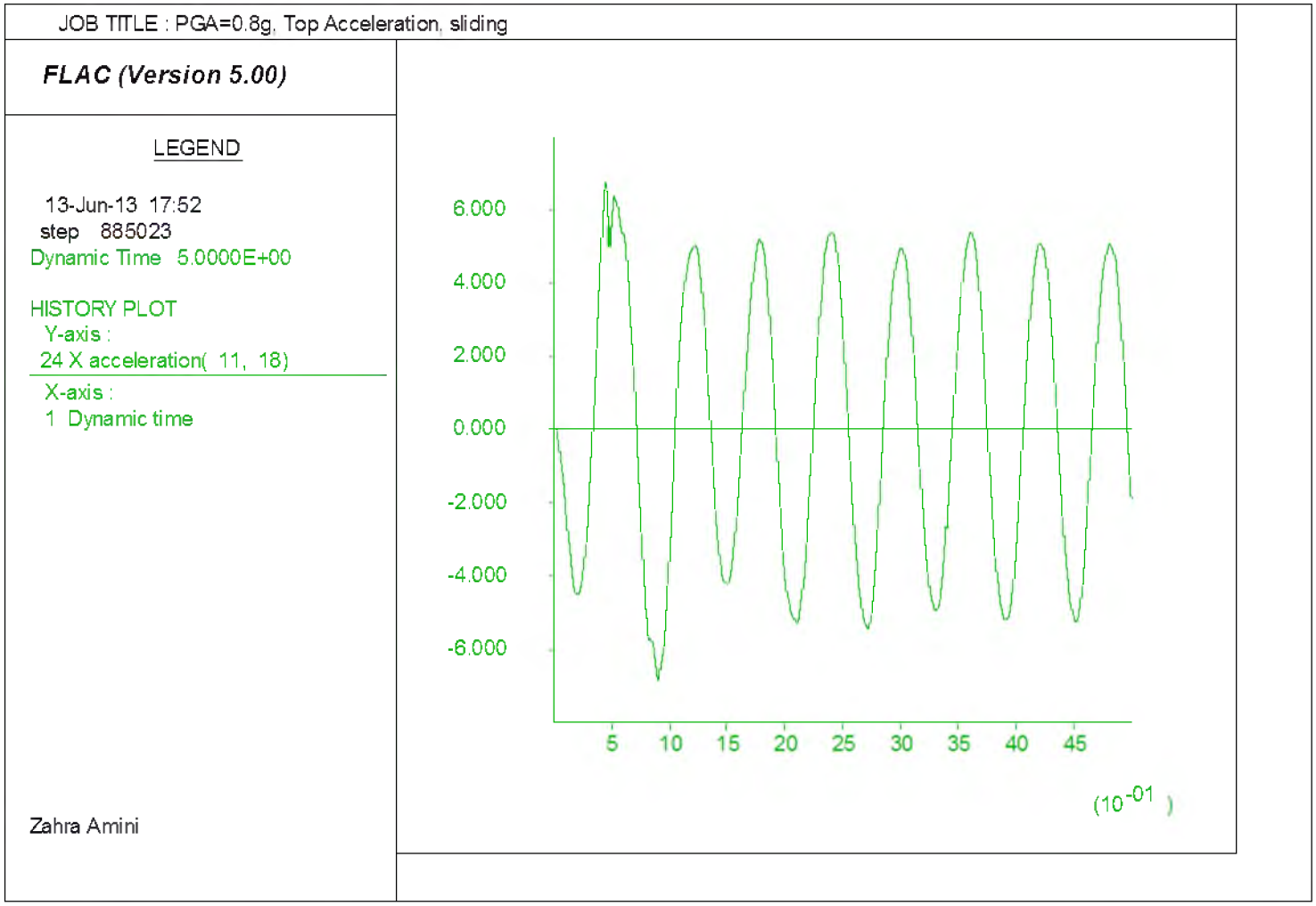

Figure C.14. Response acceleration at the top of the EPS embankment with interfaces due to amplitude 0.8g input motion

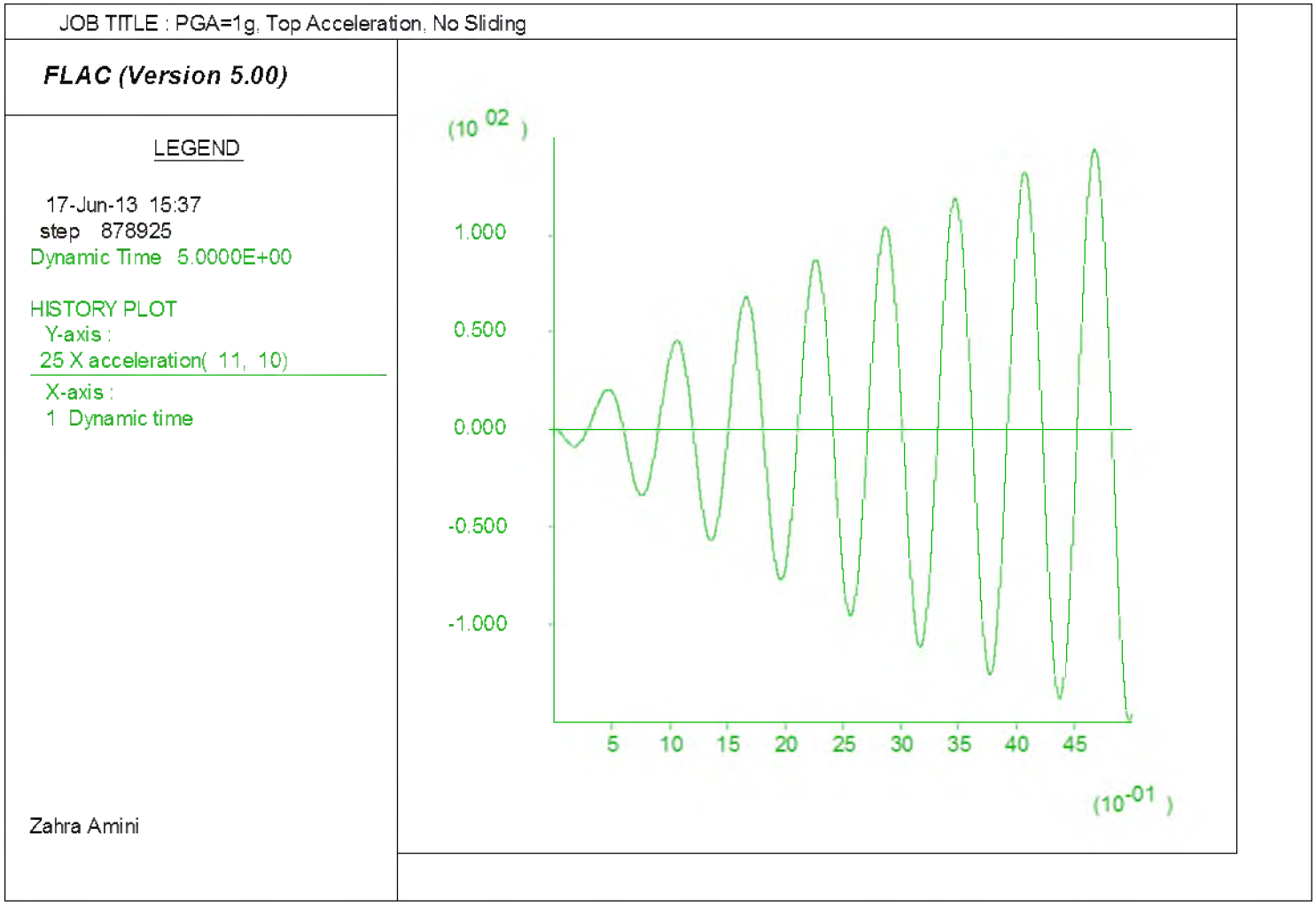

Figure C.15. Response acceleration at the top of the EPS embankment without interfaces due to amplitude 1g input motion

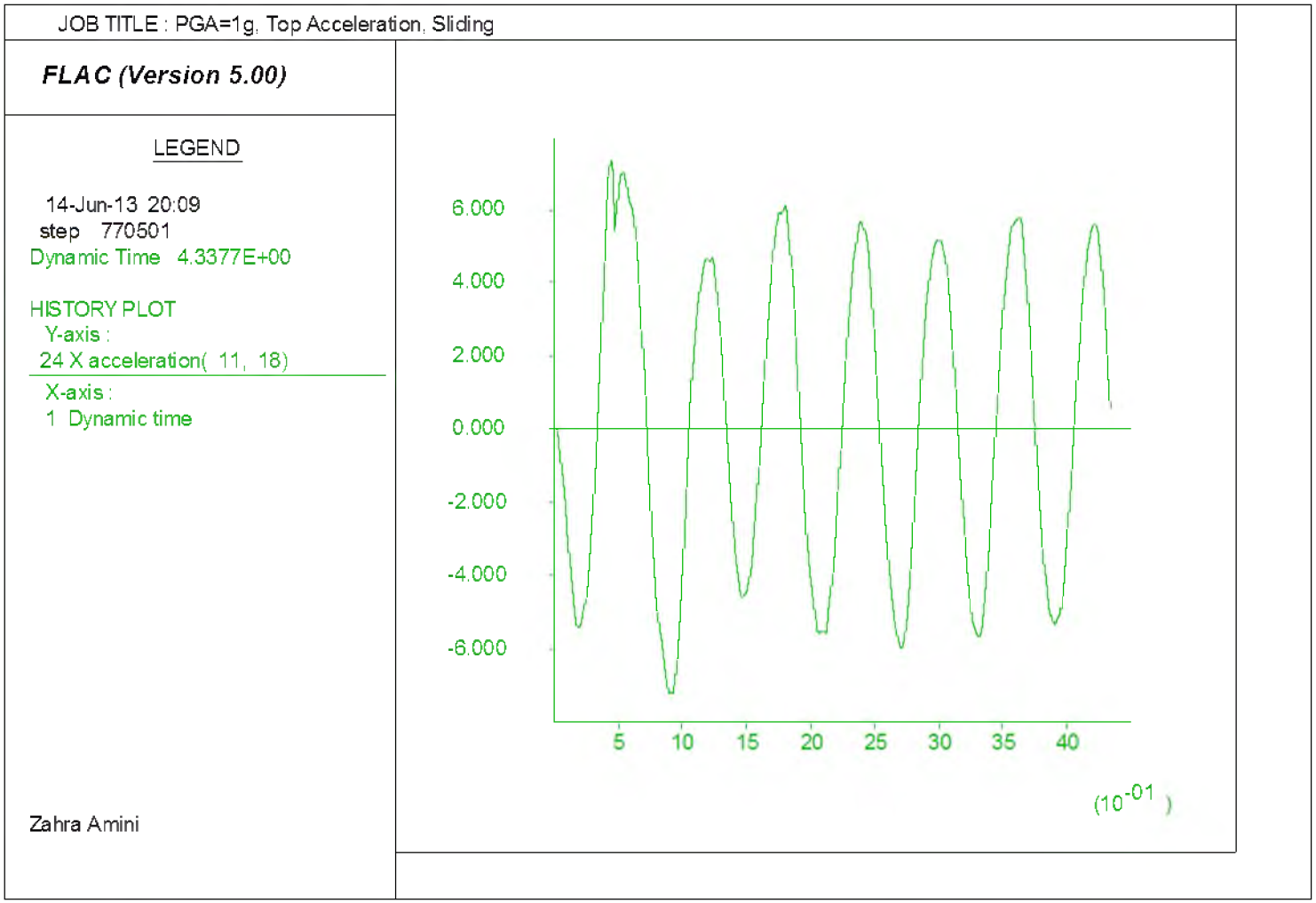

Figure C.16. Response acceleration at the top of the EPS embankment with interfaces due to amplitude 1g input motion

FLAC code for direct shear test

```
;Barrett direct shear test simulation
;normal stress: 18.1 kPa
config
g 12 13
model elas
gen 0,0 0,1.3 1.2,1.3 1.2,0
model null j 7
;model null i 1,4 j 12,21
;model null i 17,20 j 12,21
;ini x add .05 j 8 13
ini y add -.1 j 8 14
int 1 Aside from 1,7 to 13,7 Bside from 1,8 to 13,8
int 1 kn 42e6 ks 1.667e6 fric 41 dil 0
prop dens 30 bu 1.72e6 sh 1.86e6
fix x y j=1
fix x i=1 j 1,7
fix x i=13 j=1,7
;
;apply normal stress
apply p=18.1e3 i=1,13 j=14
;
his unb
solve
;
; functions to calculate average joint stresses and displacements
call int.fin
```

```
;
def ini_jdisp
njdisp0 = 0.0
sjdisp0 = 0.0
pnt = int_pnt
loop while pnt # 0
pa = imem(pnt+$kicapt)
loop while pa # 0
sjdisp0 = sjdisp0 + fmem(pa+$kidasd)
njdisp0 = njdisp0 + fmem(pa+$kidand)
pa = imem(pa)
end_loop
pa = imem(pnt+$kicbpt)
loop while pa # 0
sjdisp0 = sjdisp0 + fmem(pa+$kidasd)
njdisp0 = njdisp0 + fmem(pa+$kidand)
pa = imem(pa)
end_loop
pnt = imem(pnt)
end_loop
end
ini_jdisp
;
def av_str
whilestepping
sstav = 0.0
nstav = 0.0
```

```
njdisp = 0.0
sjdisp = 0.0
ncon = 0
jlen = 0.0
pnt = int_pnt
loop while pnt # 0
pa = imem(pnt+$kicapt)
loop while pa # 0
sstav = sstav + fmem(pa+$kidfs)
nstav = nstav + fmem(pa+$kidfn)
jlen = jlen + fmem(pa+$kidlen)
sjdisp = sjdisp + fmem(pa+$kidasd)
njdisp = njdisp + fmem(pa+$kidand)
pa = imem(pa)
end_loop
pa = imem(pnt+$kicbpt)
loop while pa # 0
ncon = ncon + 1
sstav = sstav + fmem(pa+$kidfs)
nstav = nstav + fmem(pa+$kidfn)
jlen = jlen + fmem(pa+$kidlen)
sjdisp = sjdisp + fmem(pa+$kidasd)
njdisp = njdisp + fmem(pa+$kidand)
pa = imem(pa)
end_loop
pnt = imem(pnt)
end_loop
```

```
if ncon # 0
sstav = -sstav / jlen
nstav = nstav / jlen
sjdisp = (sjdisp-sjdisp0) / (2.0 * ncon)
njdisp = (njdisp-njdisp0) / (2.0 * ncon)
endif
end
hist sstav nstav sjdisp njdisp
;
ini xvel 1.667e-5 i= 1,13 j 8,14
fix x i= 1,13 j 8,14
;
hist ns 1
;
ini xdis 0.0 ydis 0.0
step 2000
save Barrett-LargeShear-18.sav 'last project state'
```

APPENDIX D

STRESS DISTRIBUTION AFTER APPLICATION OF SLIDING REMEDIES

Shear stress time histories were recorded throughout the embankment. Figure D.1 presents a reference to the location of stress time histories in the model. Figures D.2 to D.21 illustrate shear stress time histories recorded throughout the embankment at gridpoints shown in Figure D.1.

Figures D.22 to D.25 show the shear and normal stress time histories at the potentially yielding zones when the embankment model is excited with 1 g horizontal acceleration amplitude and 0.4 g vertical acceleration amplitude.

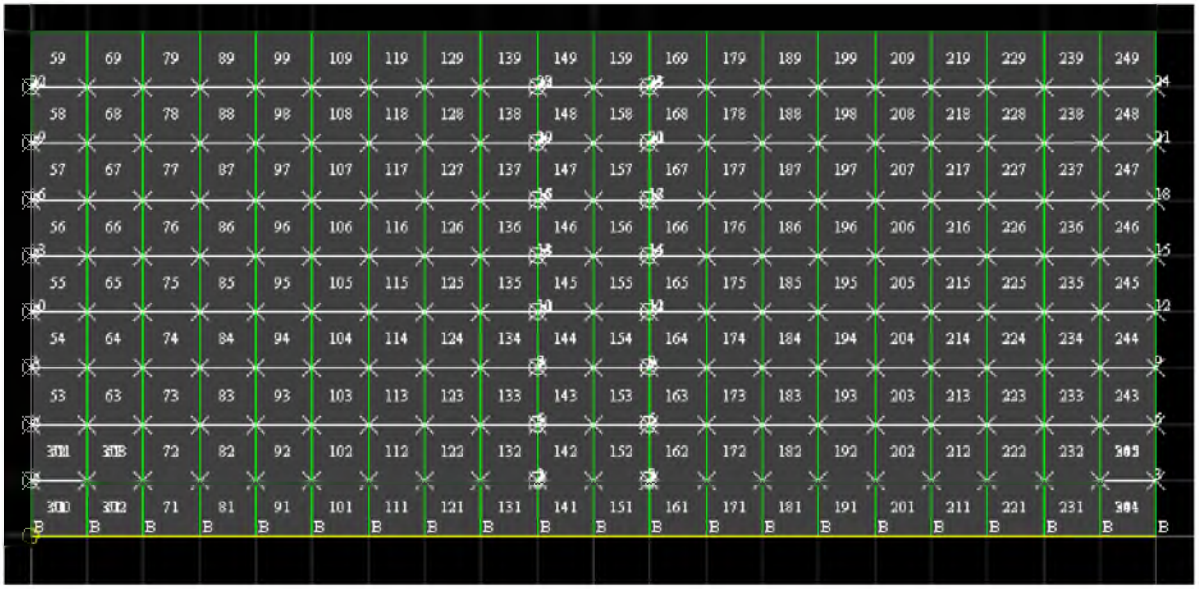

Figure D.1. Shear stress time history gridpoint reference

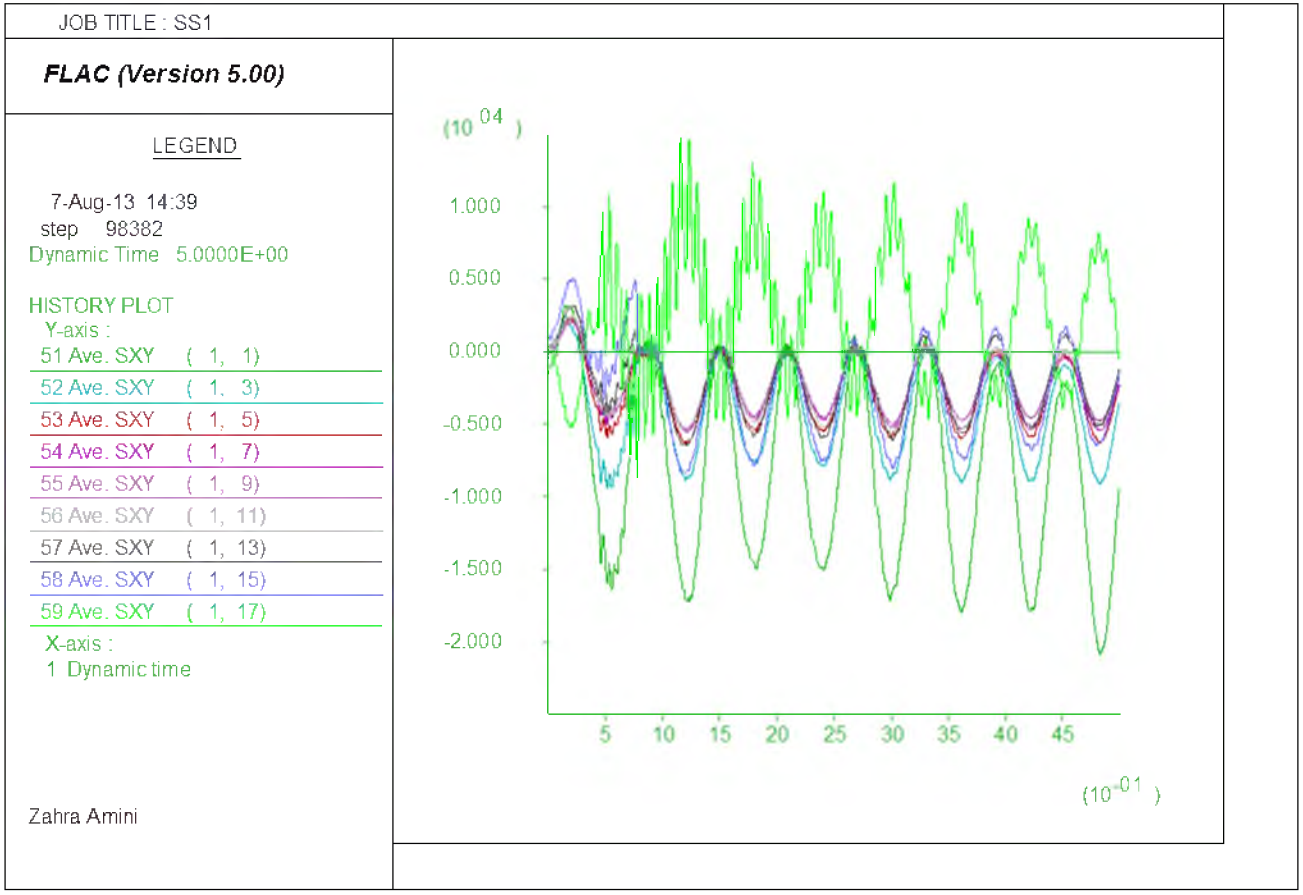

Figure D.2. Shear stress time histories at x=0 m due to horizontal acceleration amplitude of 0.6 g

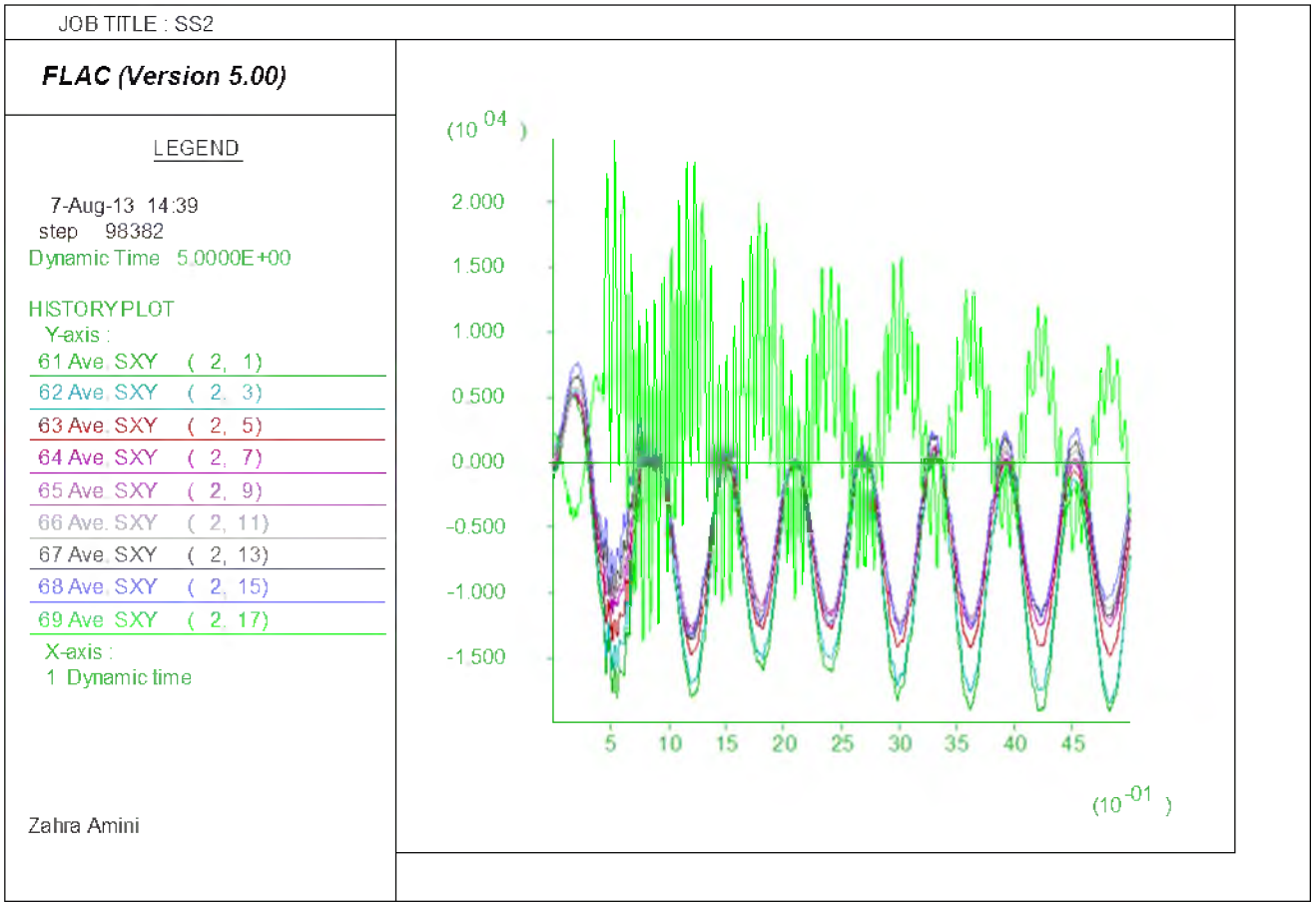

Figure D.3. Shear stress time histories at x=1 m due to horizontal acceleration amplitude of 0.6 g

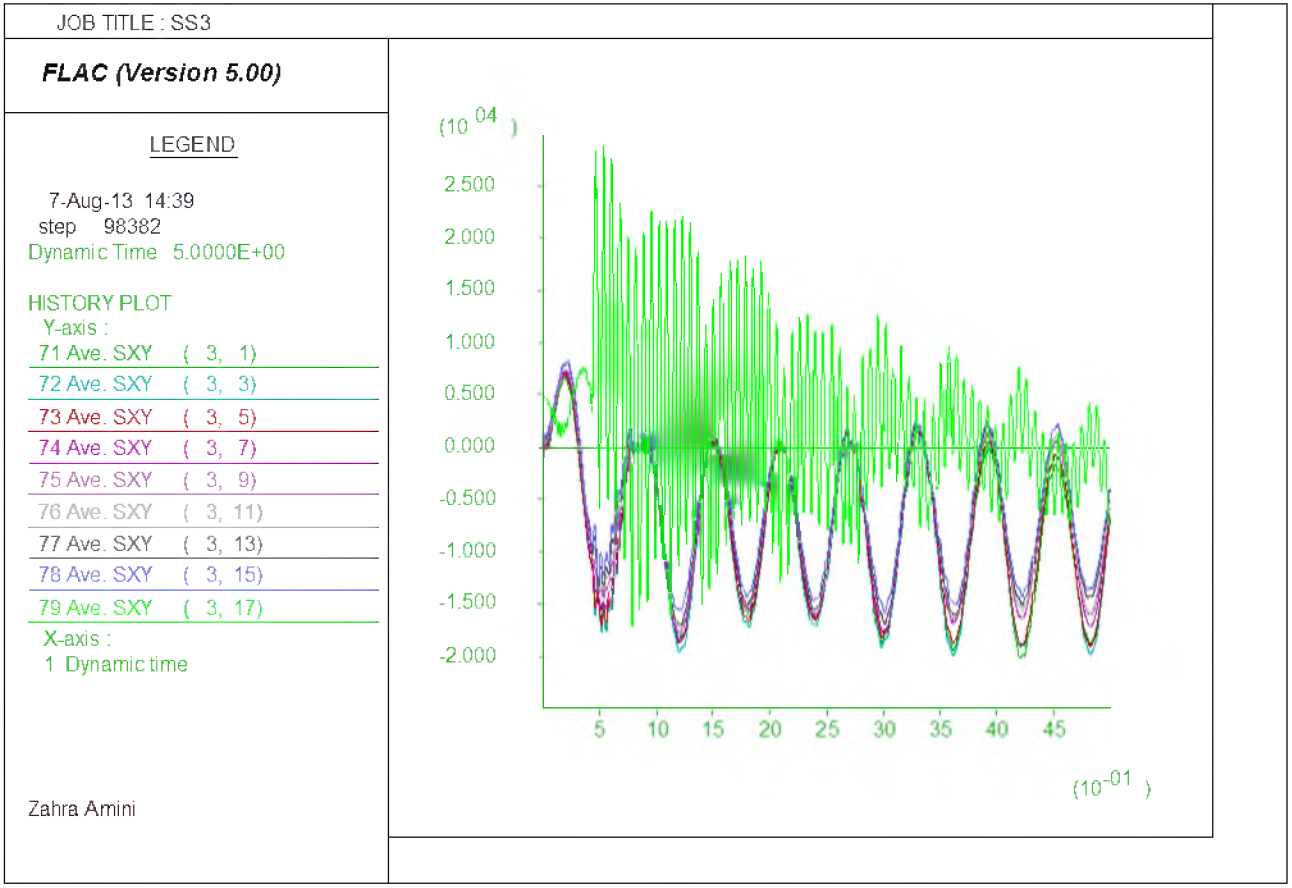

Figure D.4. Shear stress time histories at x=2 m due to horizontal acceleration amplitude of 0.6 g

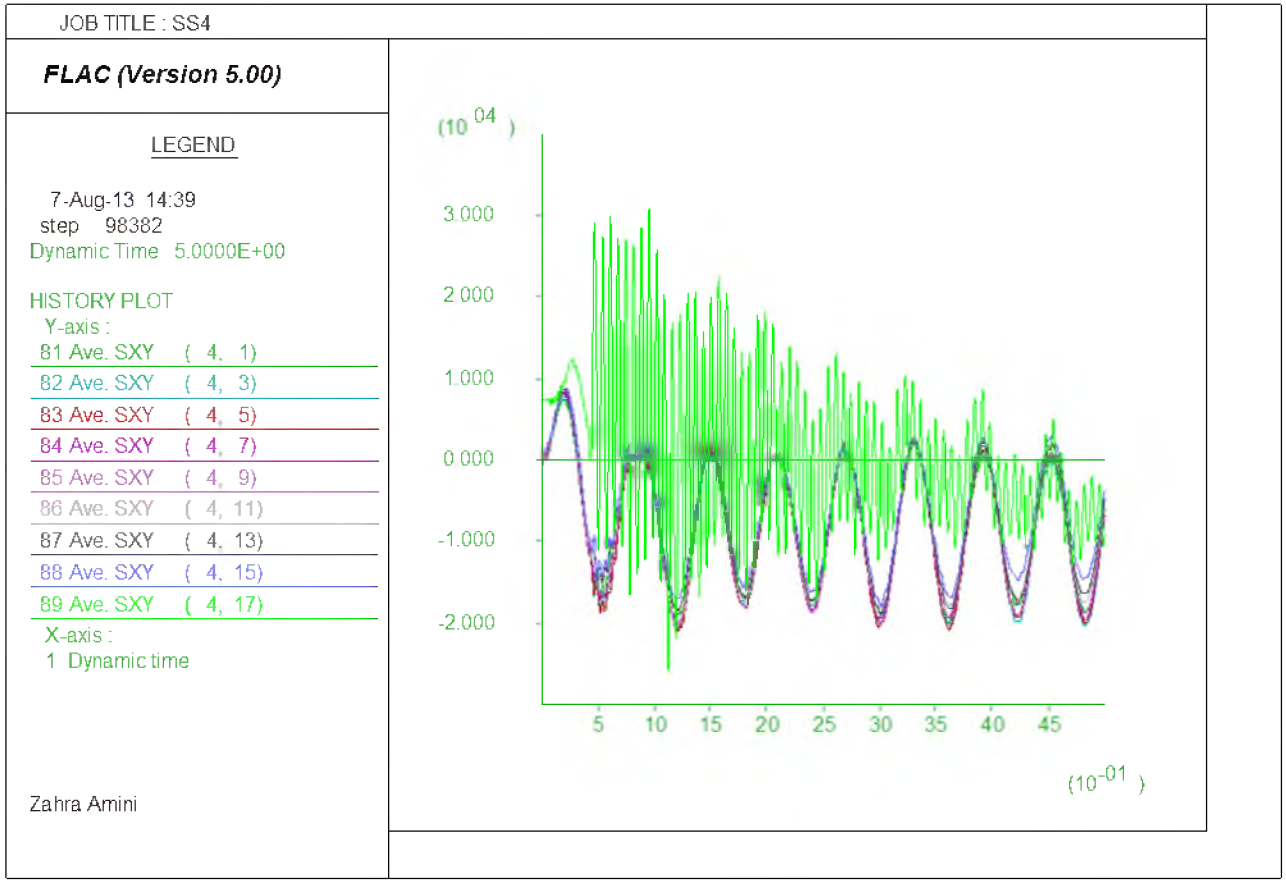

Figure D.5. Shear stress time histories at x=3 m due to horizontal acceleration amplitude of 0.6 g

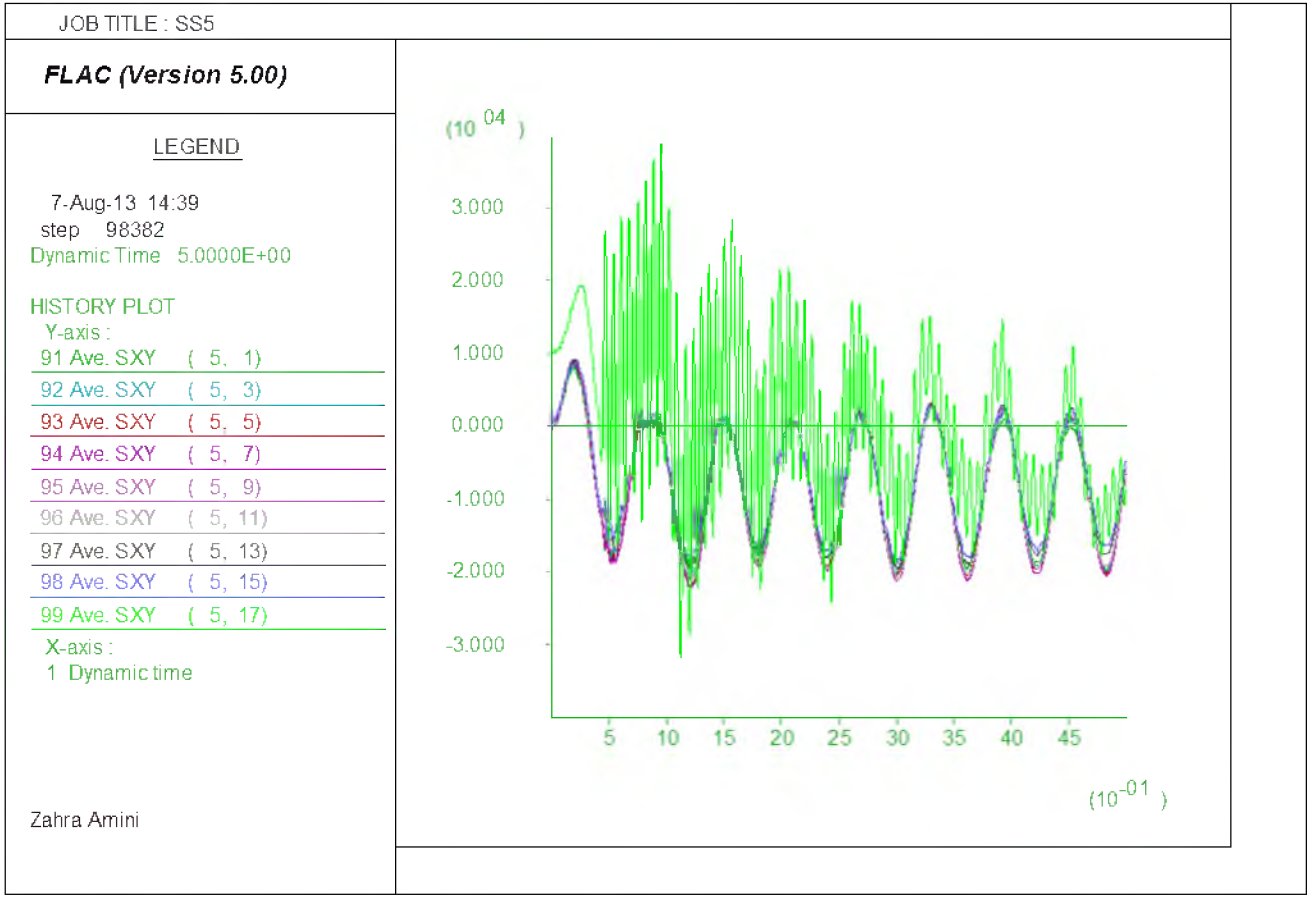

Figure D.6. Shear stress time histories at x=4 m due to horizontal acceleration amplitude of 0.6 g

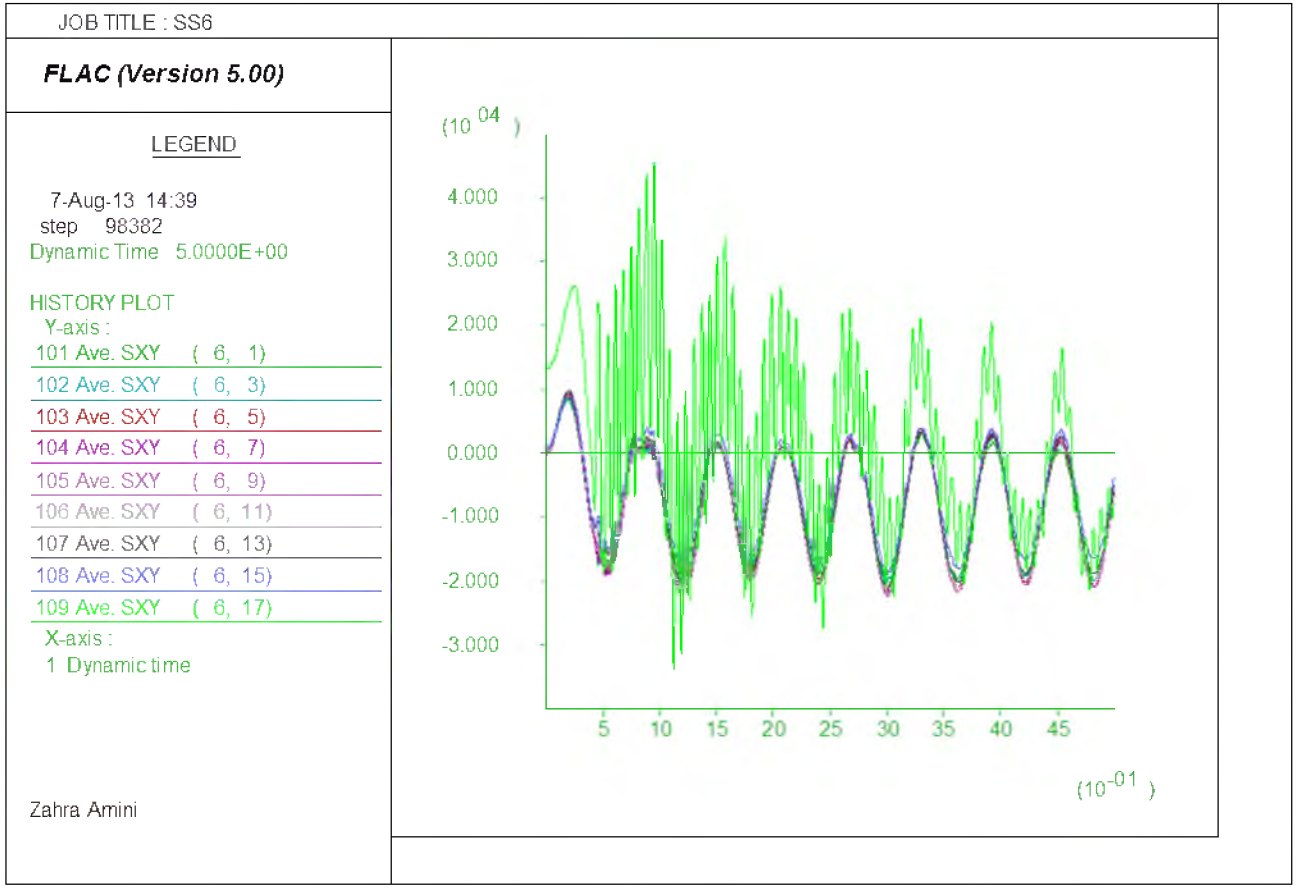

Figure D.7. Shear stress time histories at x=5 m due to horizontal acceleration amplitude of 0.6 g

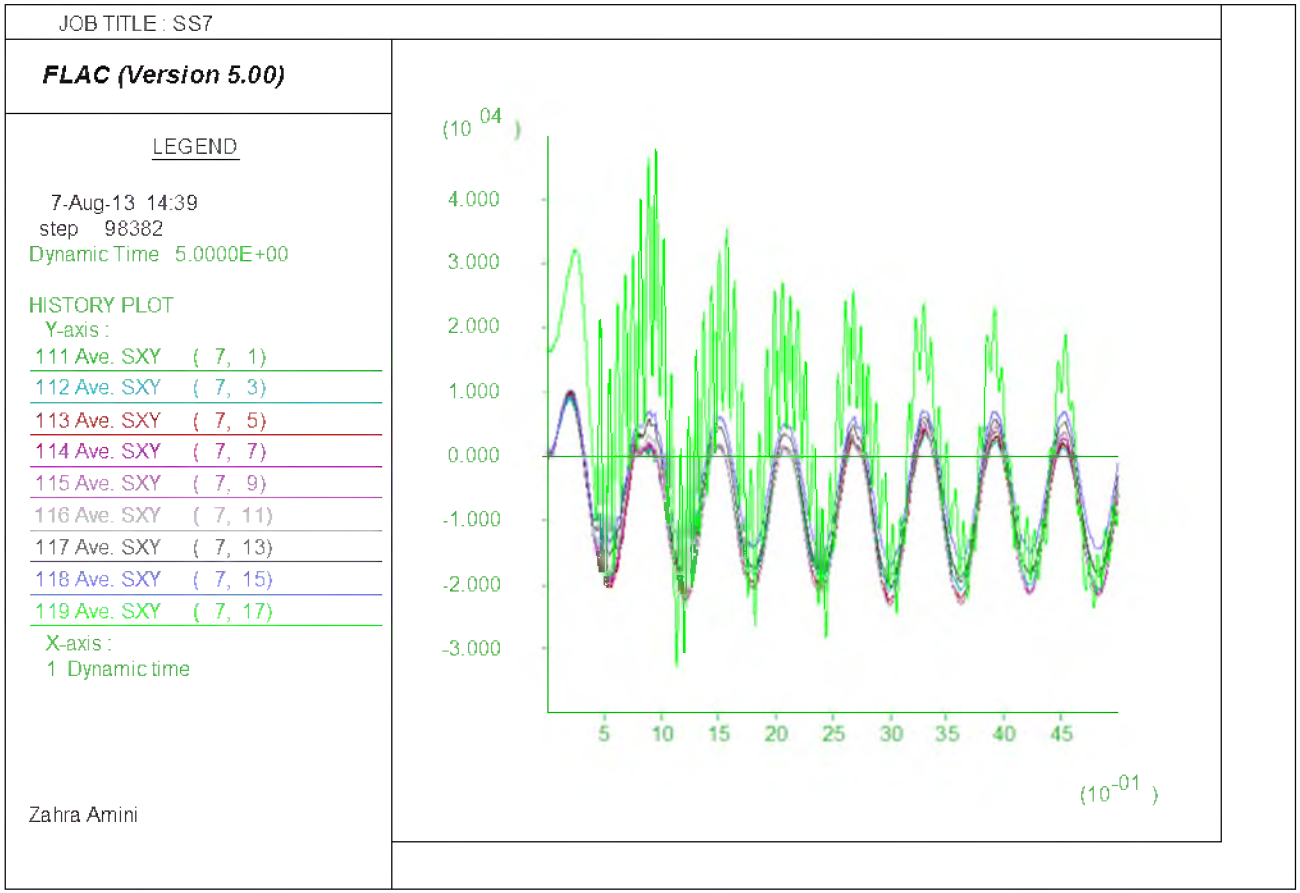

Figure D.8. Shear stress time histories at x=6 m due to horizontal acceleration amplitude of 0.6 g

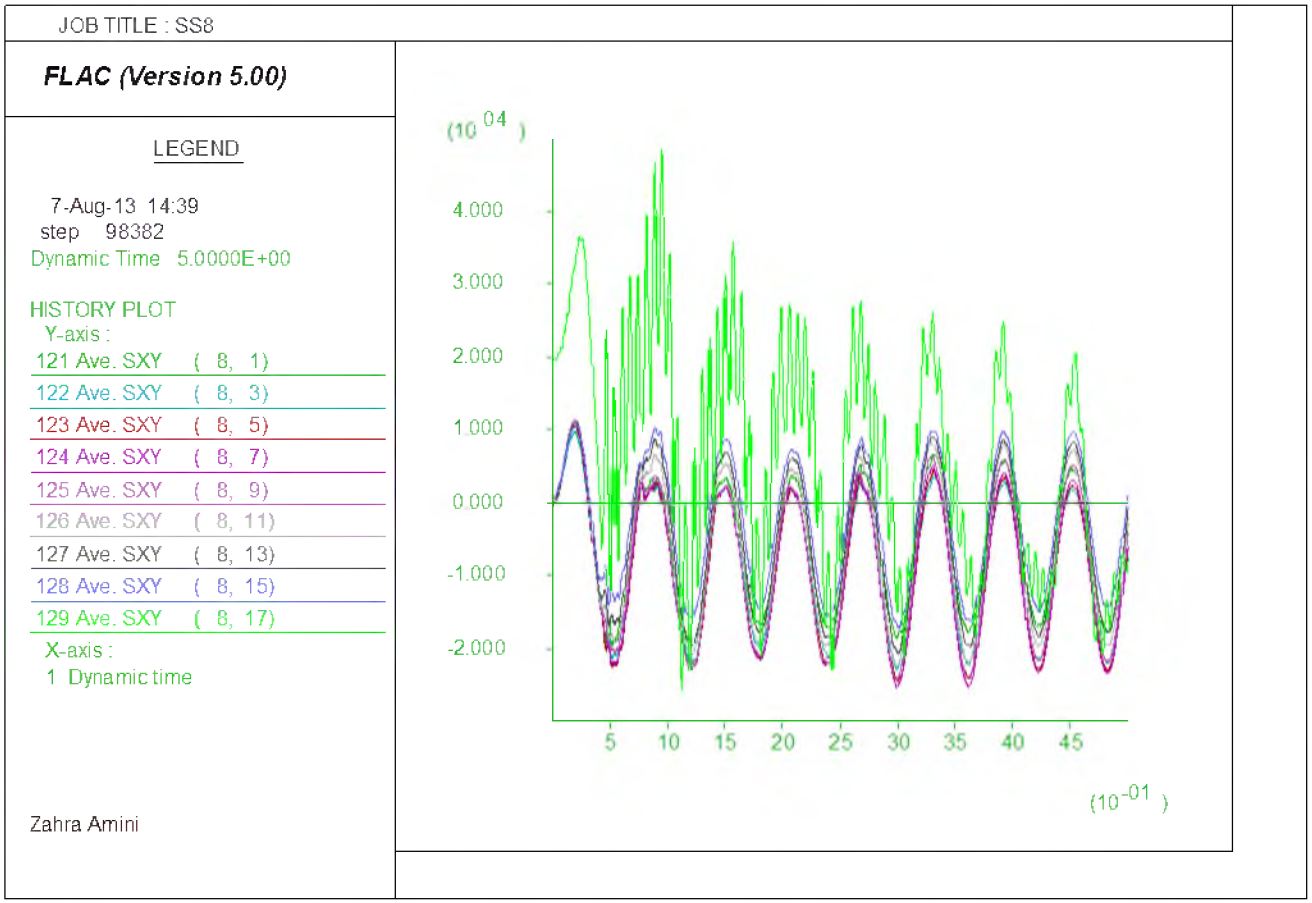

Figure D.9. Shear stress time histories at x=7 m due to horizontal acceleration amplitude of 0.6 g

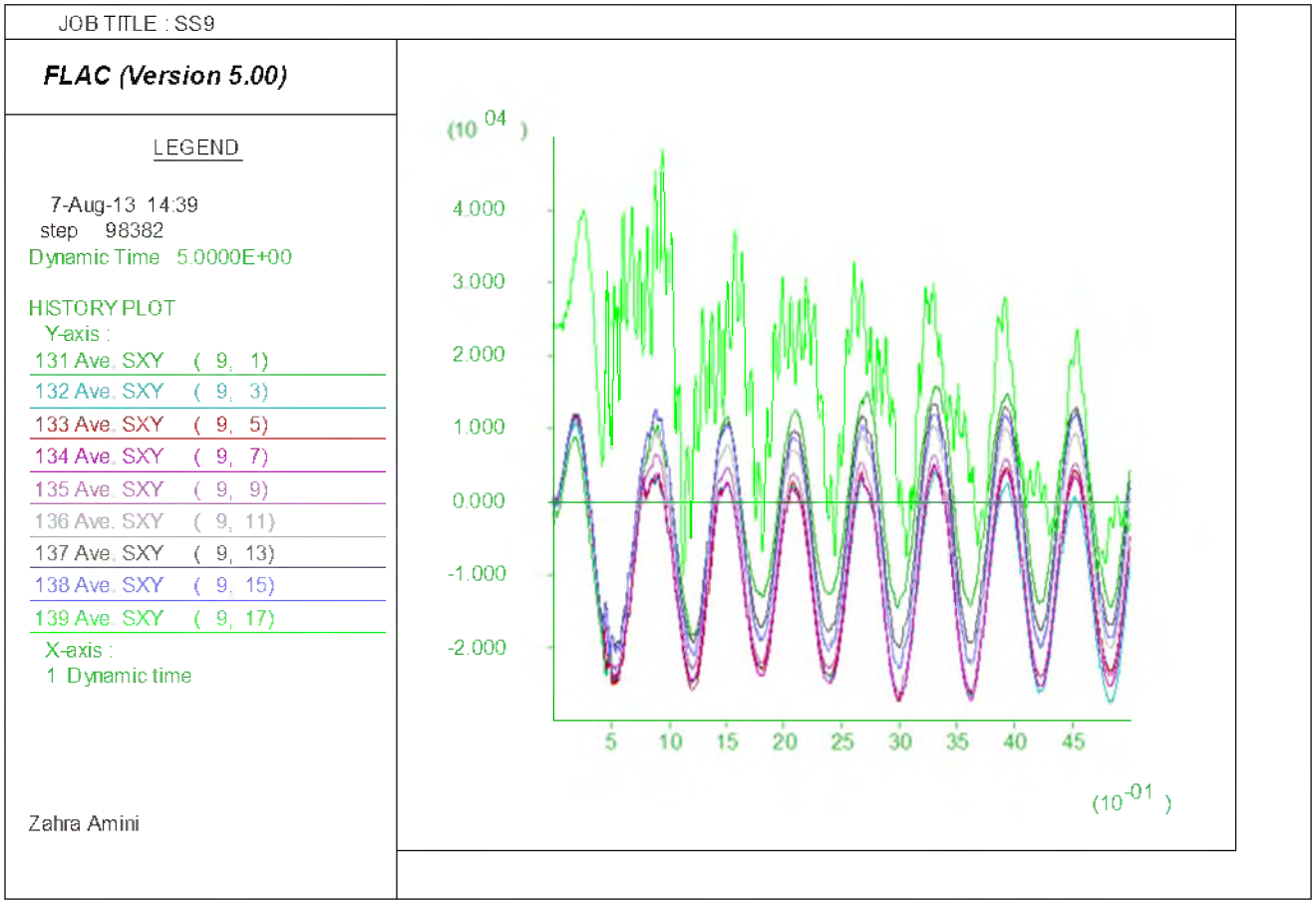

Figure D.10. Shear stress time histories at x=8 m due to horizontal acceleration amplitude of 0.6 g

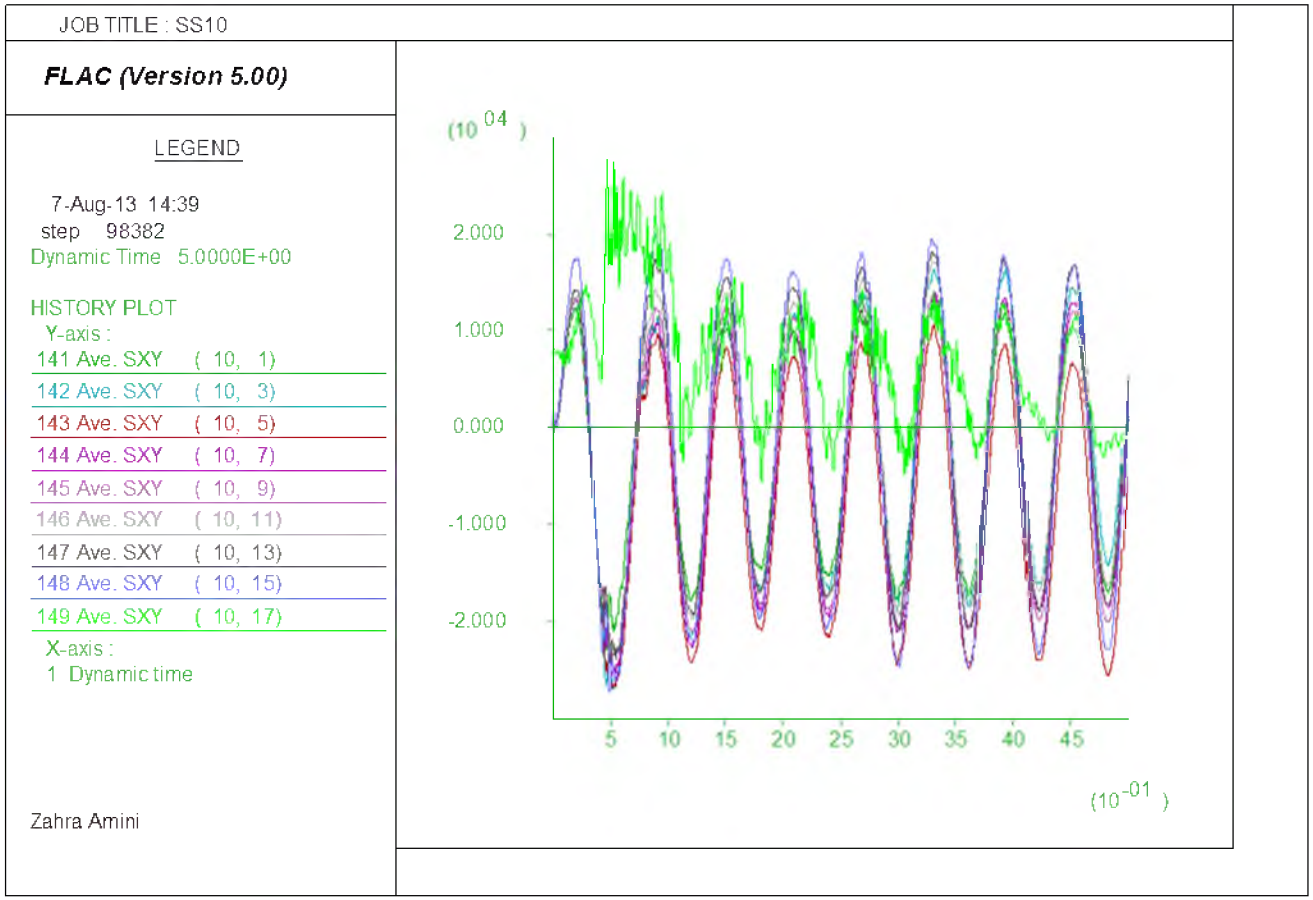

Figure D.11. Shear stress time histories at x=9 m due to horizontal acceleration amplitude of 0.6 g

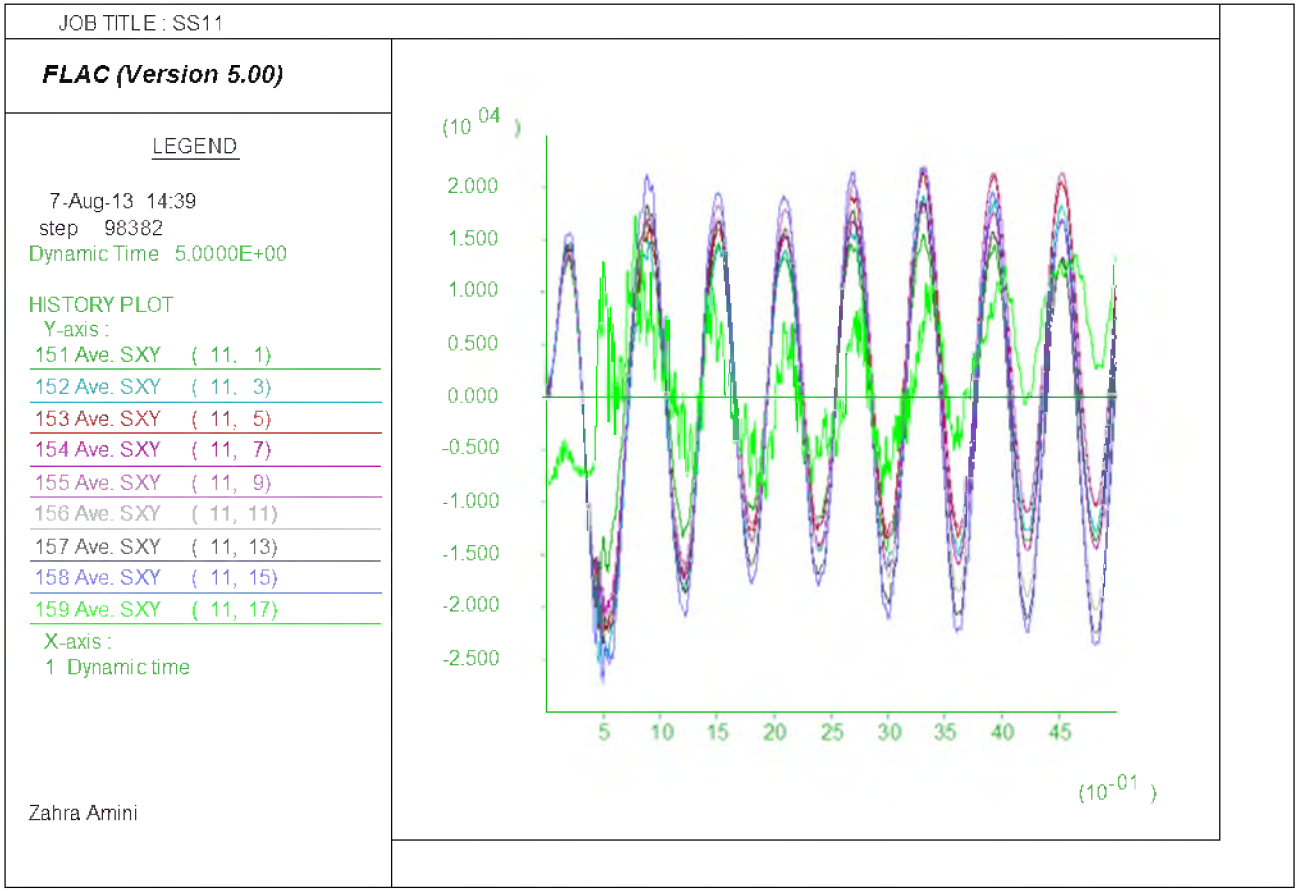

Figure D.12. Shear stress time histories at x=10 m due to horizontal acceleration amplitude of 0.6 g

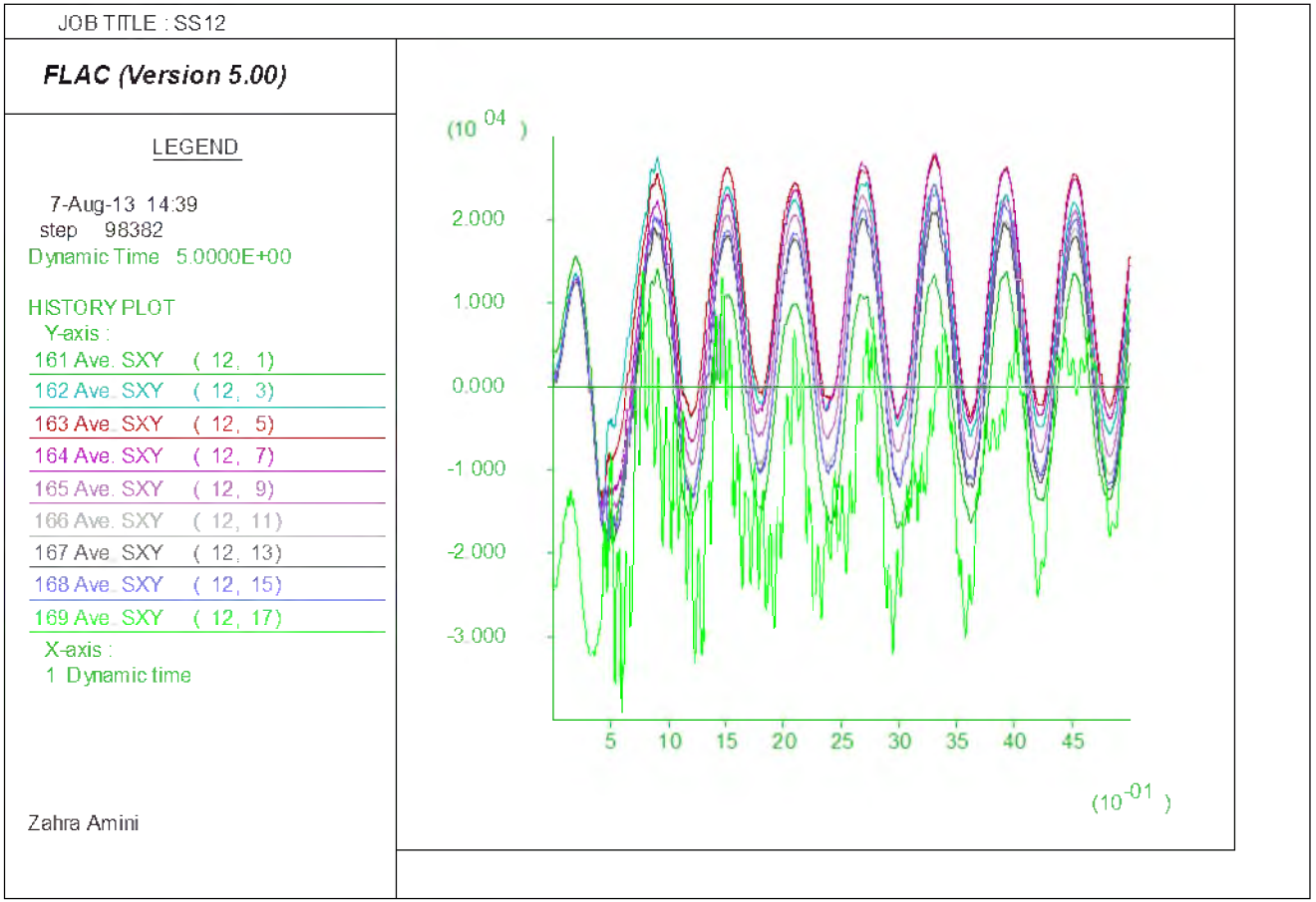

Figure D.13. Shear stress time histories at x=11 m due to horizontal acceleration amplitude of 0.6 g

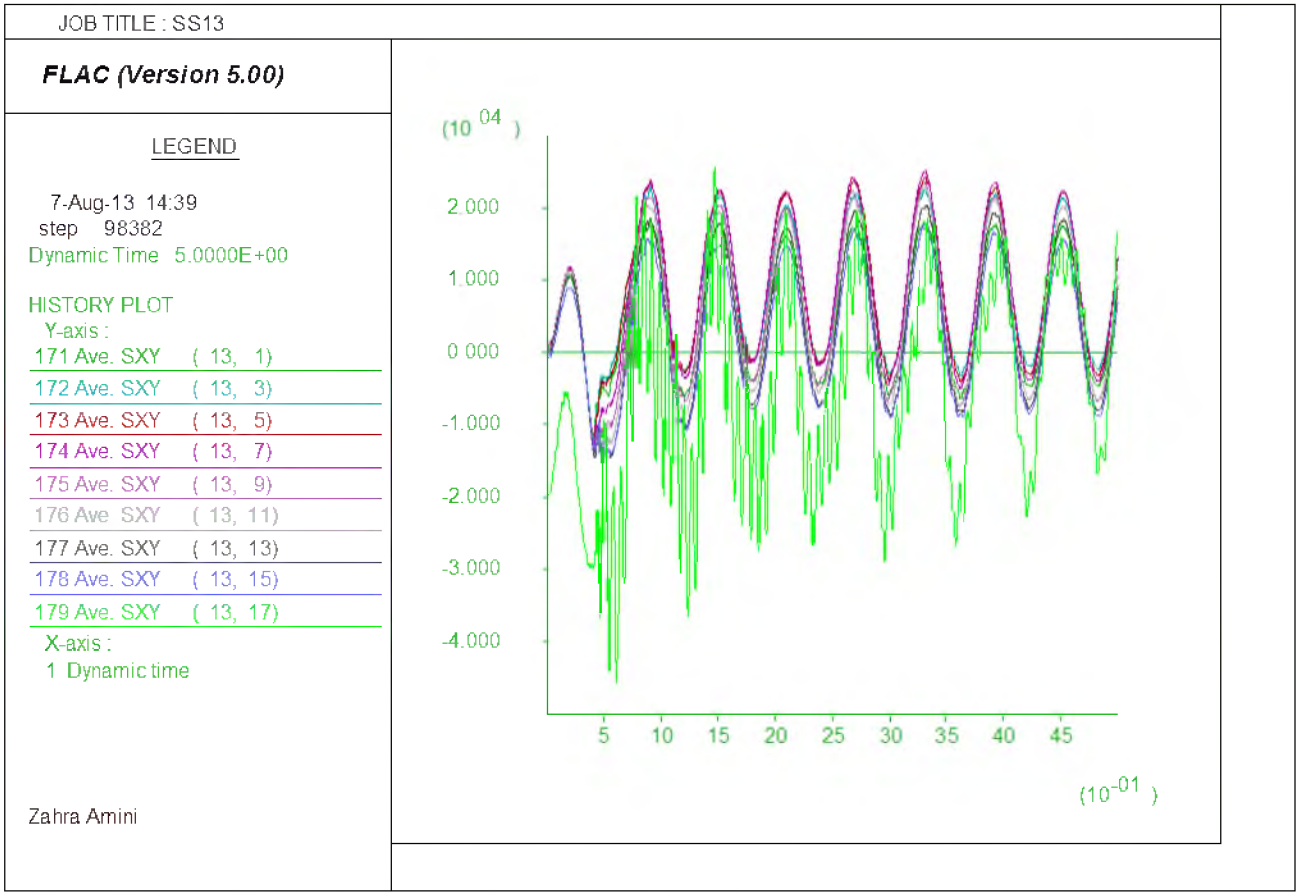

Figure D.14. Shear stress time histories at x=12 m due to horizontal acceleration amplitude of 0.6 g

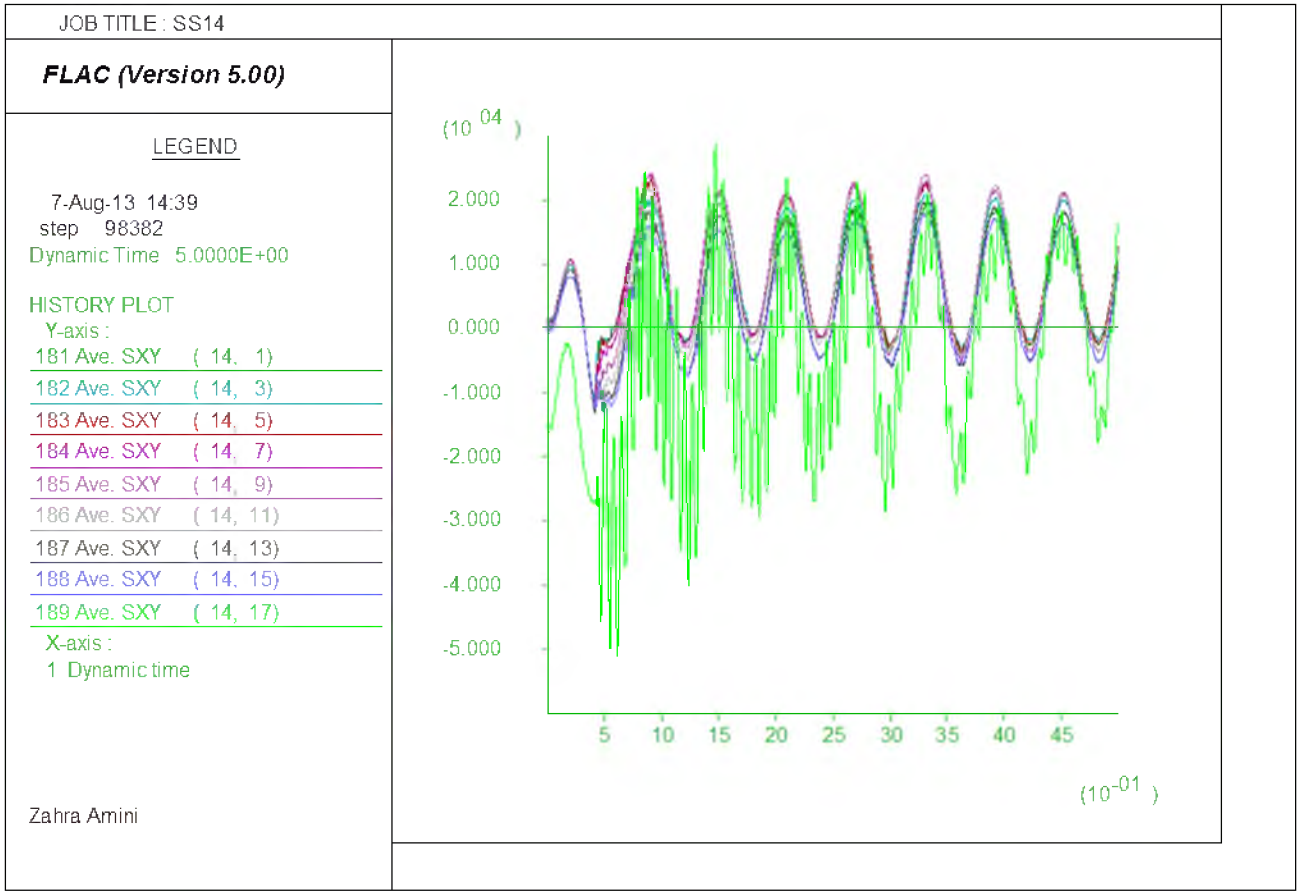

Figure D.15. Shear stress time histories at x=13 m due to horizontal acceleration amplitude of 0.6 g

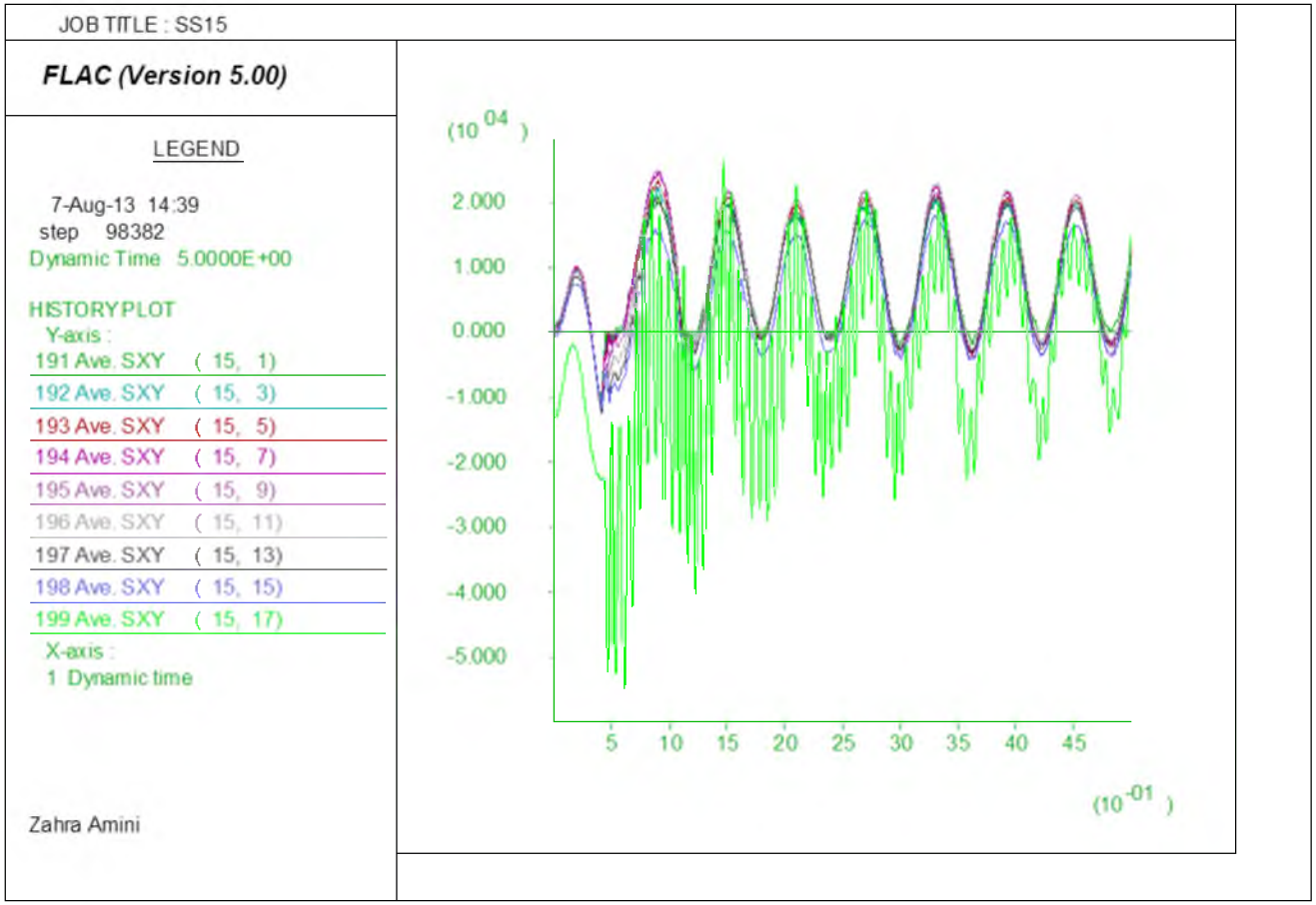

Figure D.16. Shear stress time histories at x=14 m due to horizontal acceleration amplitude of 0.6 g

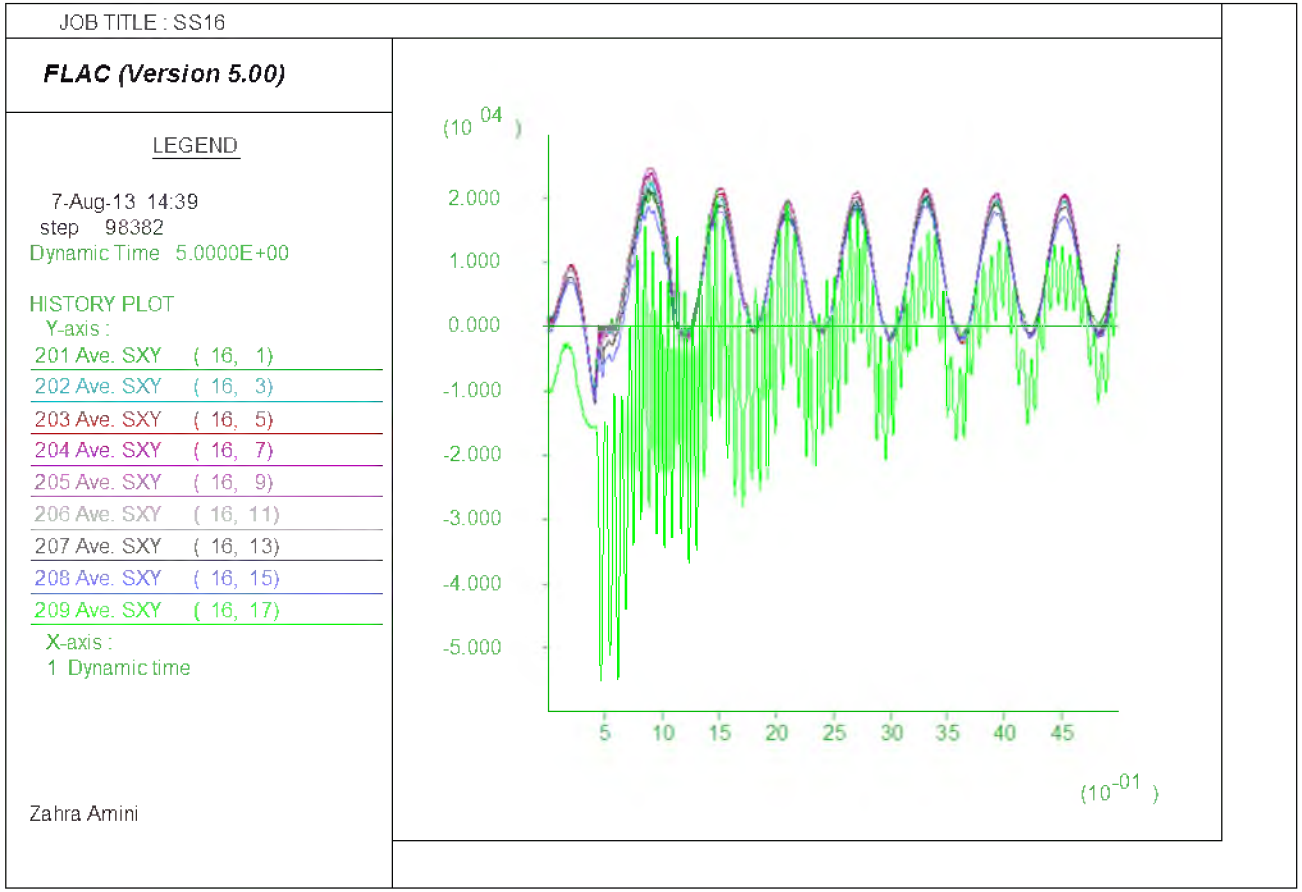

Figure D.17. Shear stress time histories at x=15 m due to horizontal acceleration amplitude of 0.6 g

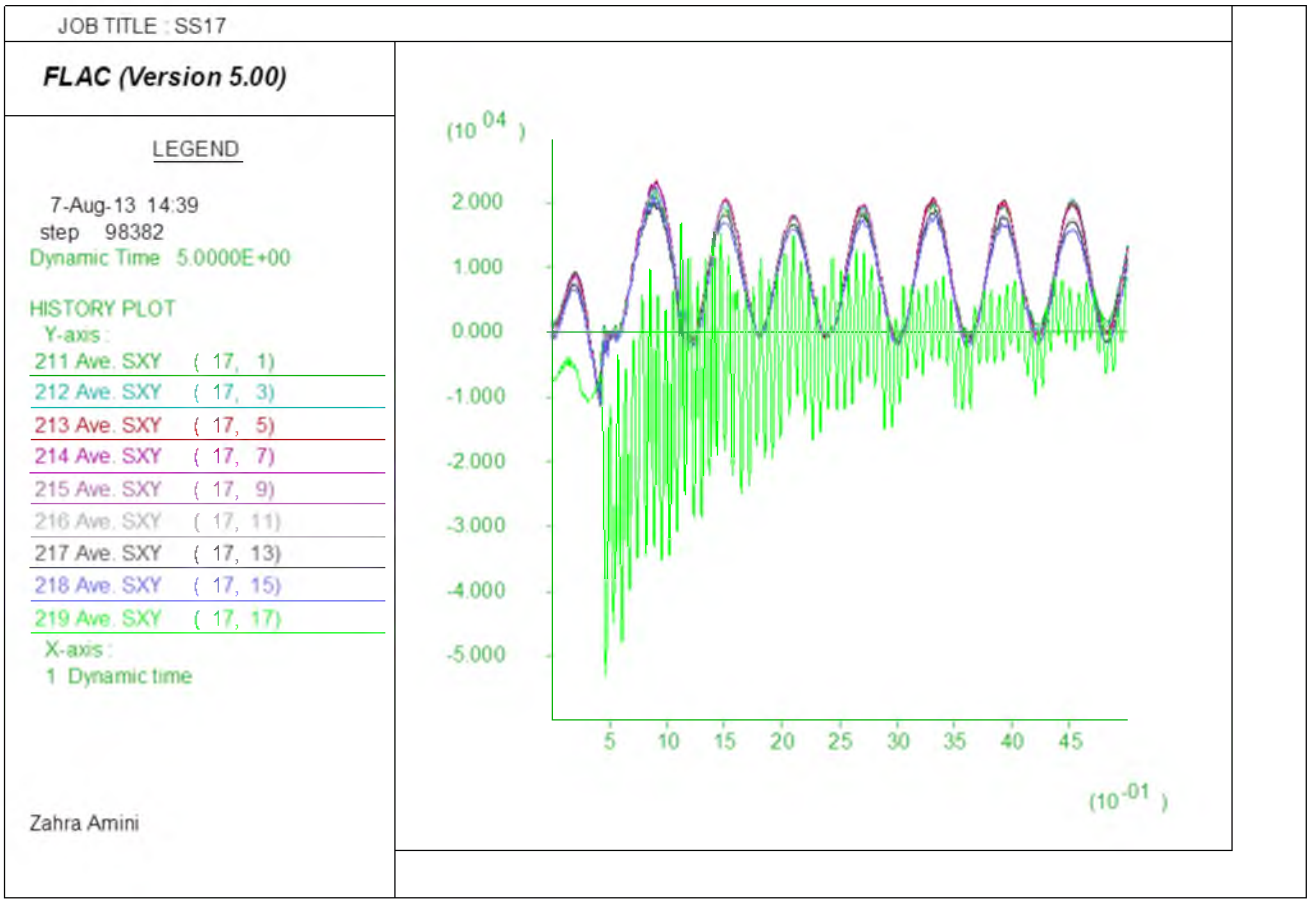

Figure D.18. Shear stress time histories at x=16 m due to horizontal acceleration amplitude of 0.6 g

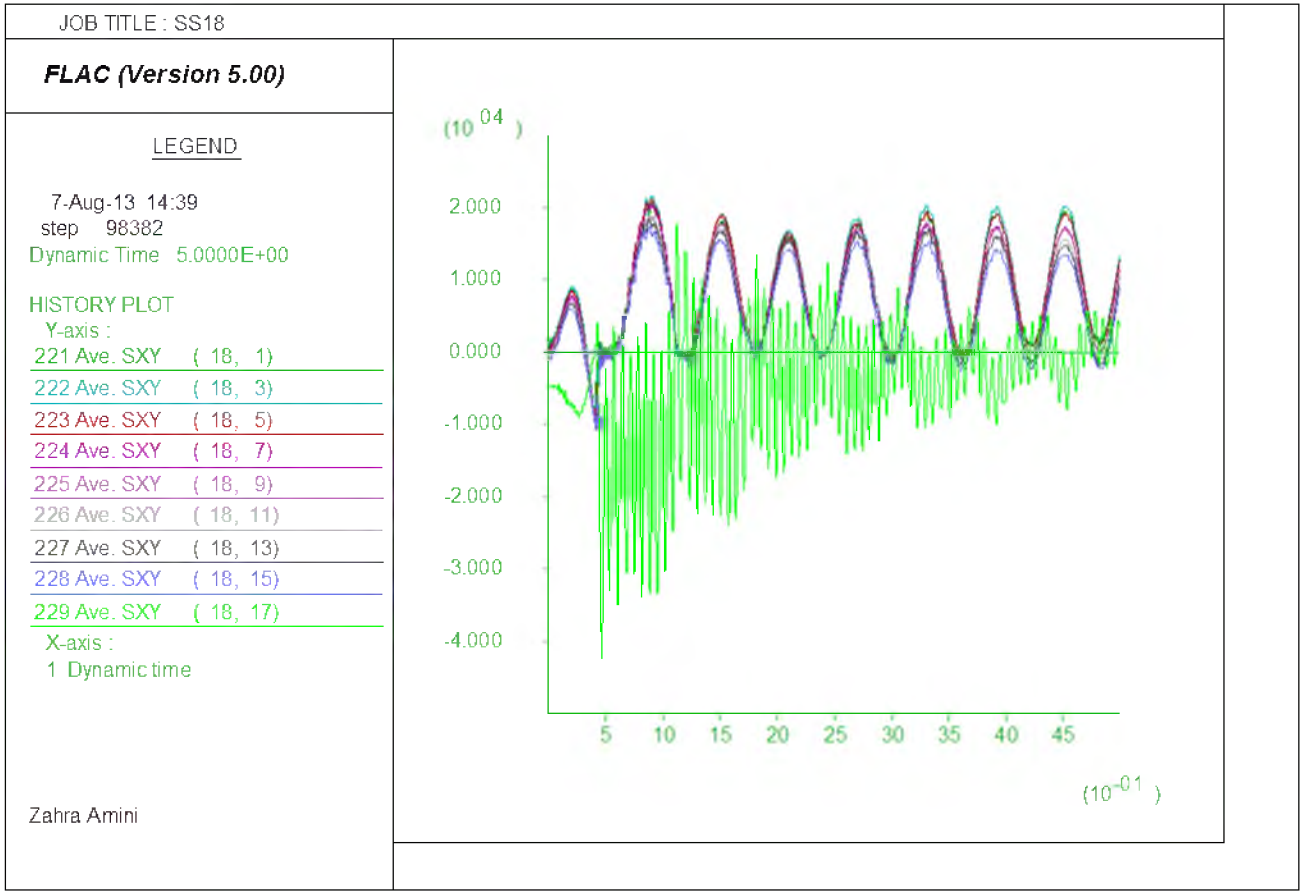

Figure D.19. Shear stress time histories at x=17 m due to horizontal acceleration amplitude of 0.6 g

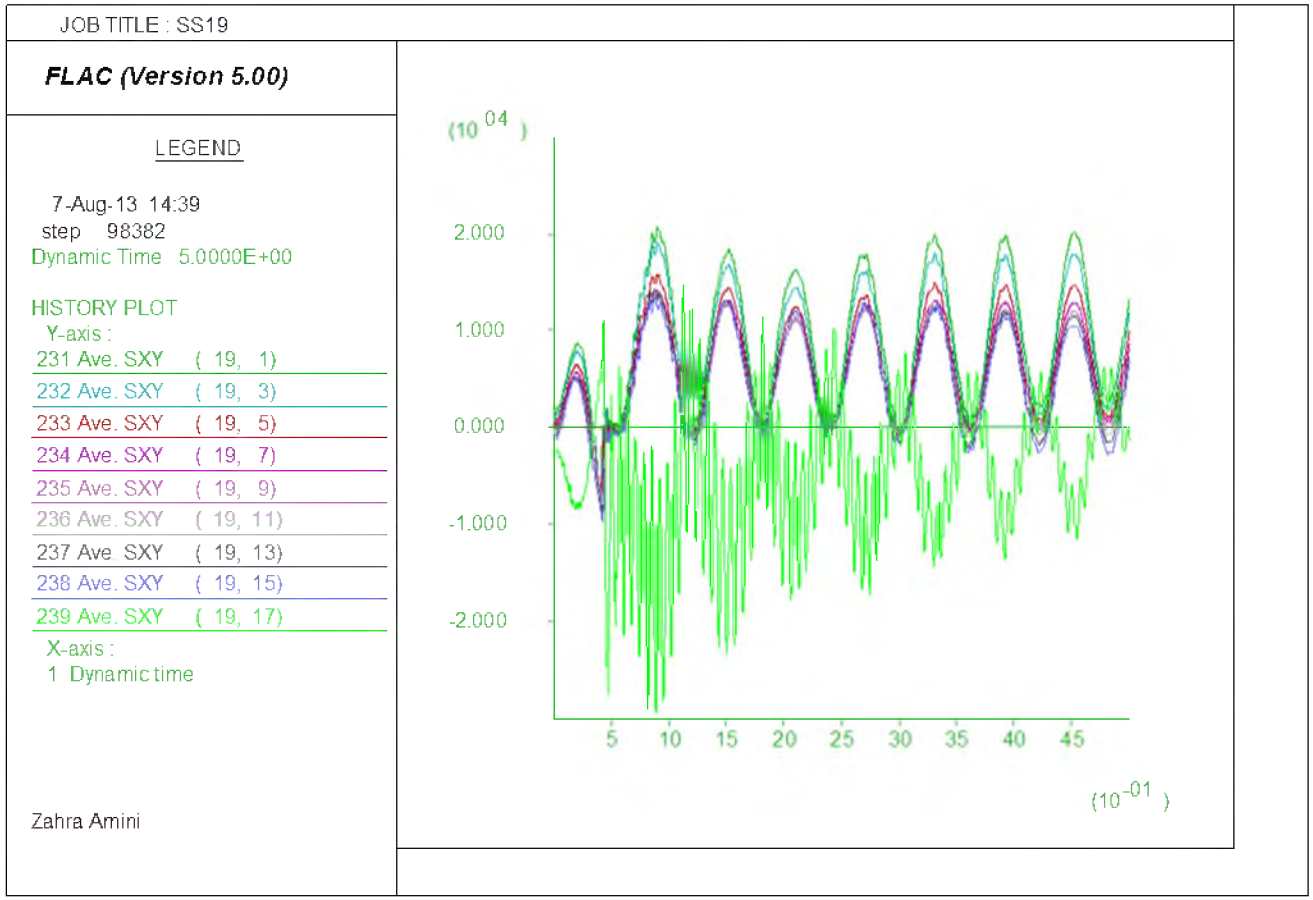

Figure D.20. Shear stress time histories at x=18 m due to horizontal acceleration amplitude of 0.6 g

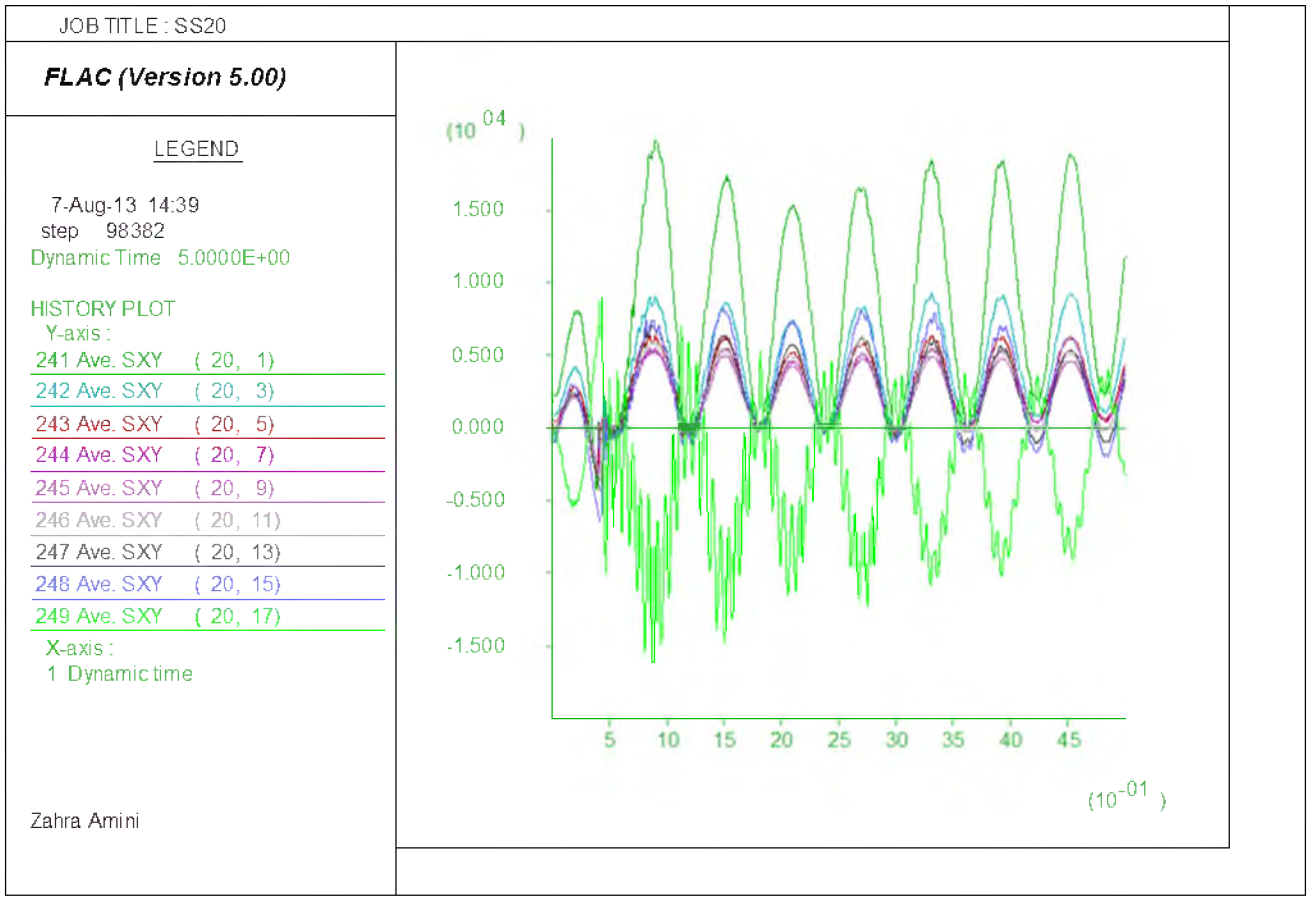

Figure D.21. Shear stress time histories at x=19 m due to horizontal acceleration amplitude of 0.6 g

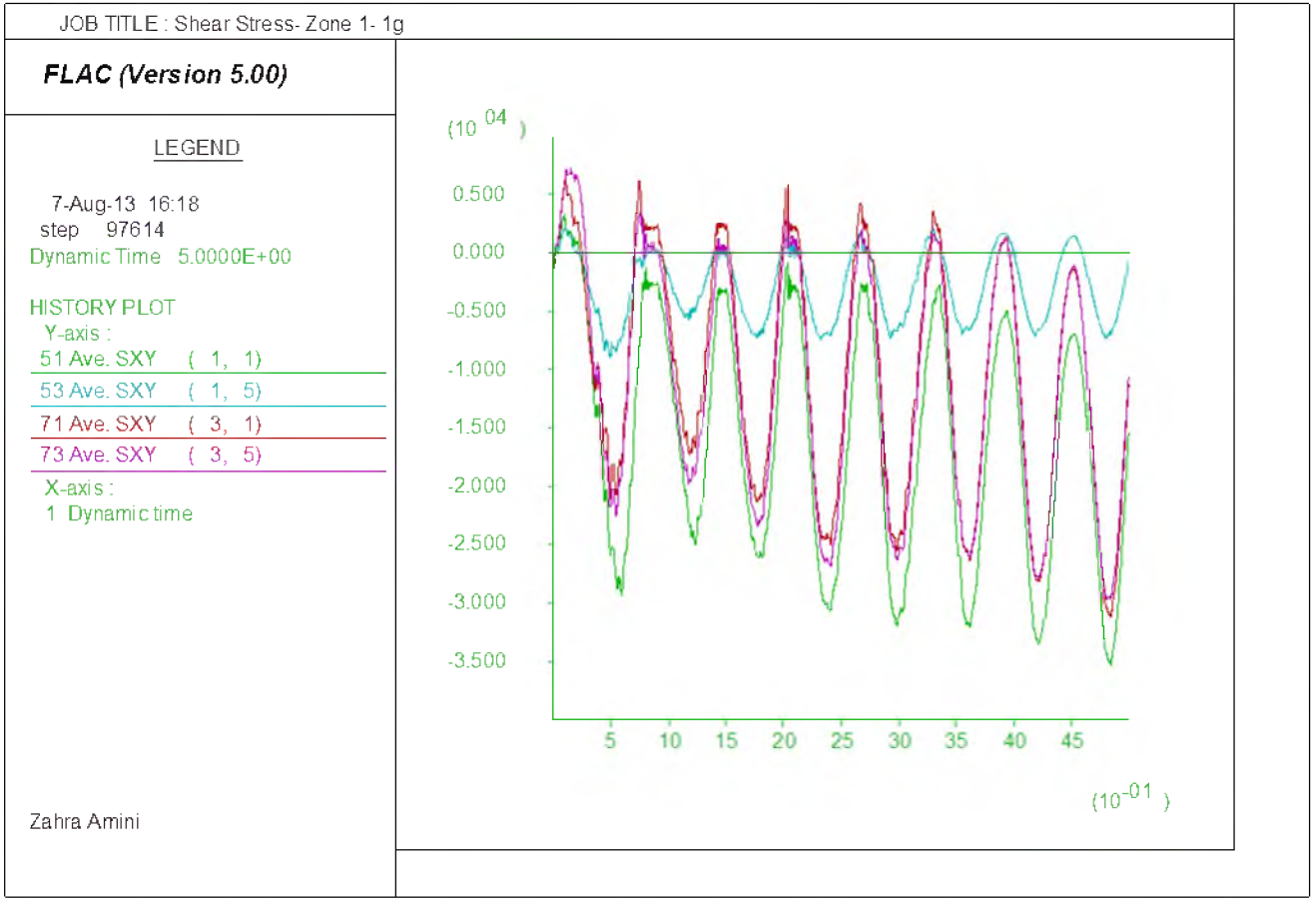

Figure D.22. Shear stress time histories at zone 1 due to horizontal acceleration amplitude of 1 g

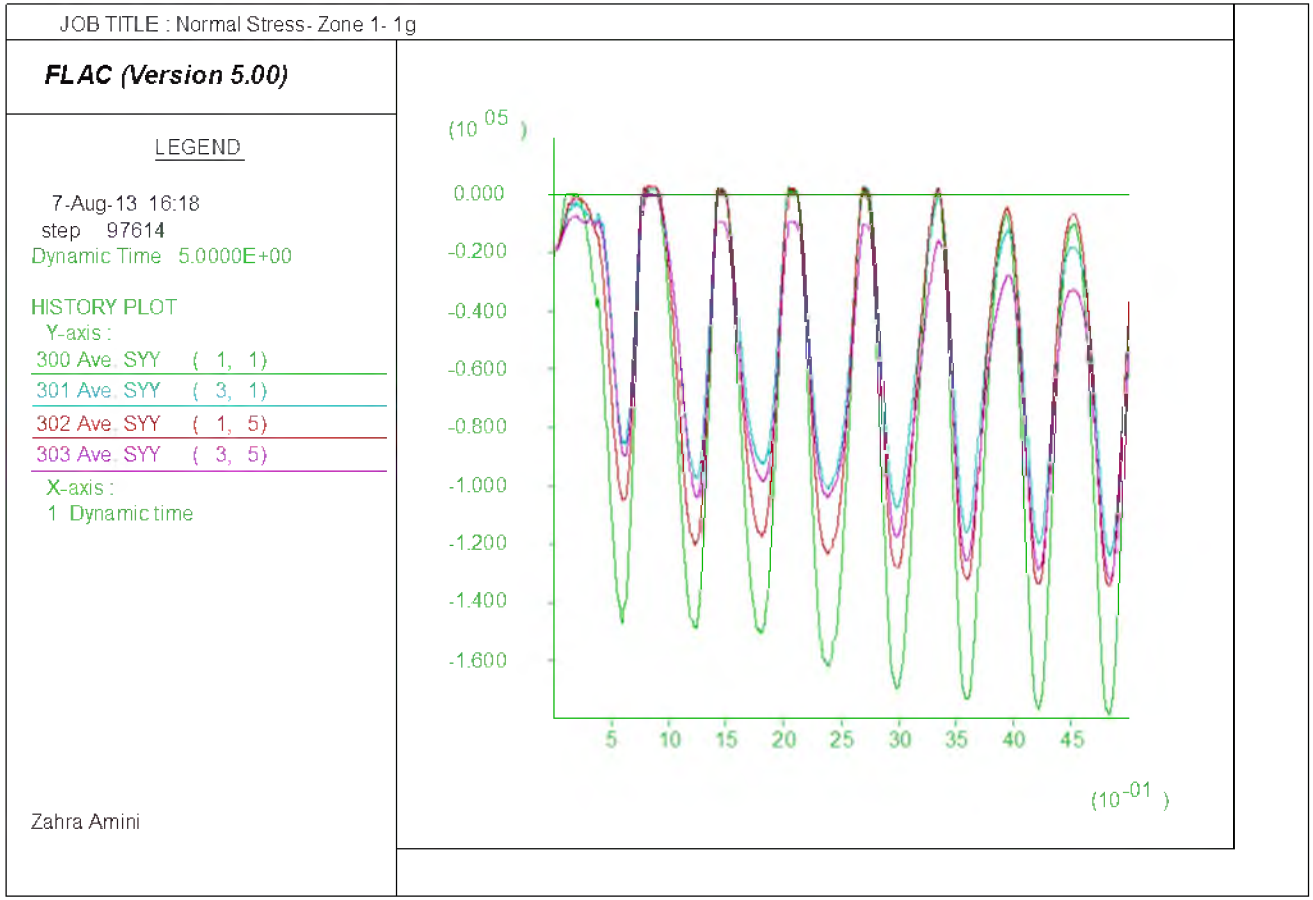

Figure D.23. Normal stress time histories at zone 1 due to horizontal acceleration amplitude of 1 g

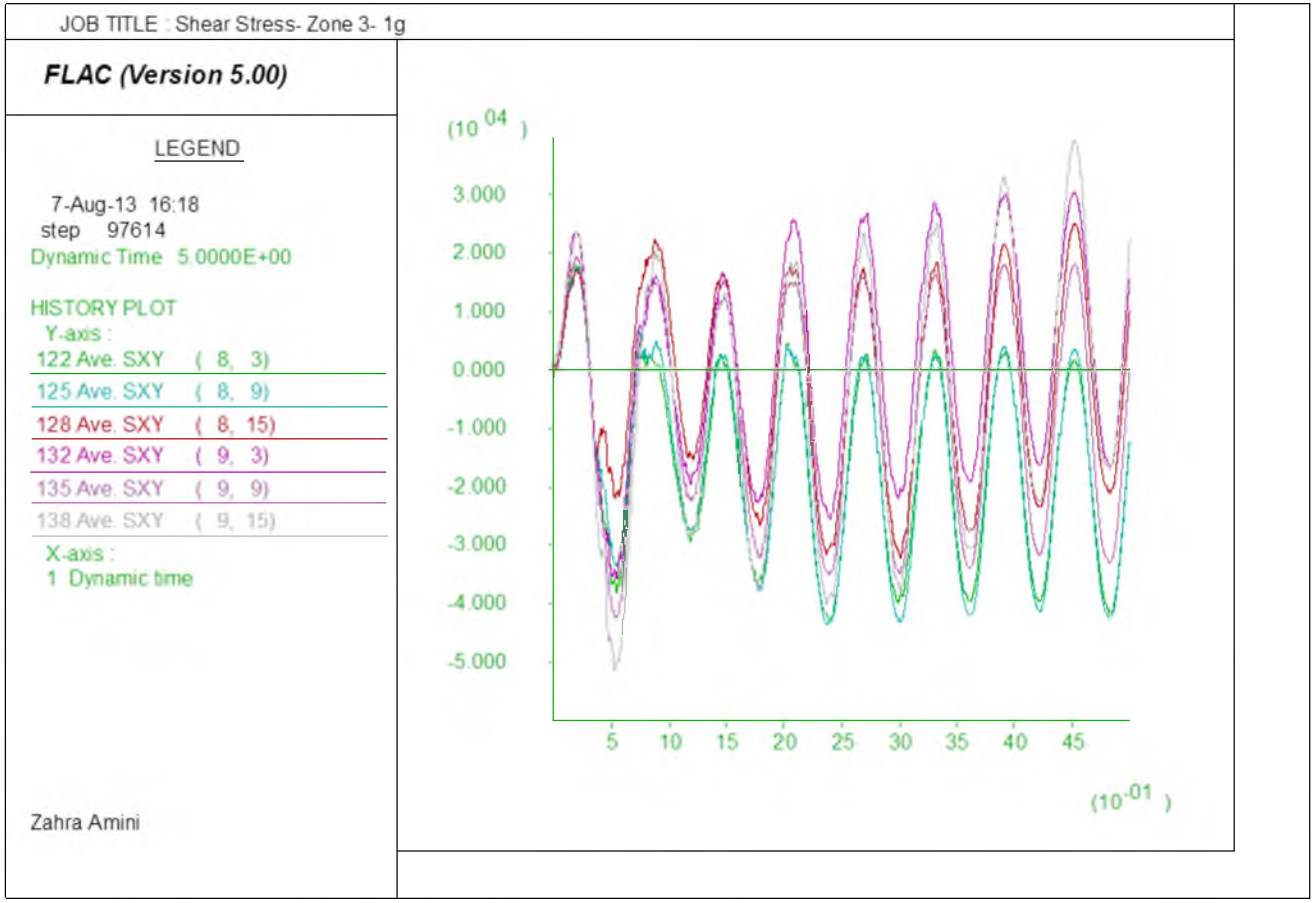

Figure D.24. Shear stress time histories at zone 3 due to horizontal acceleration amplitude of 1 g

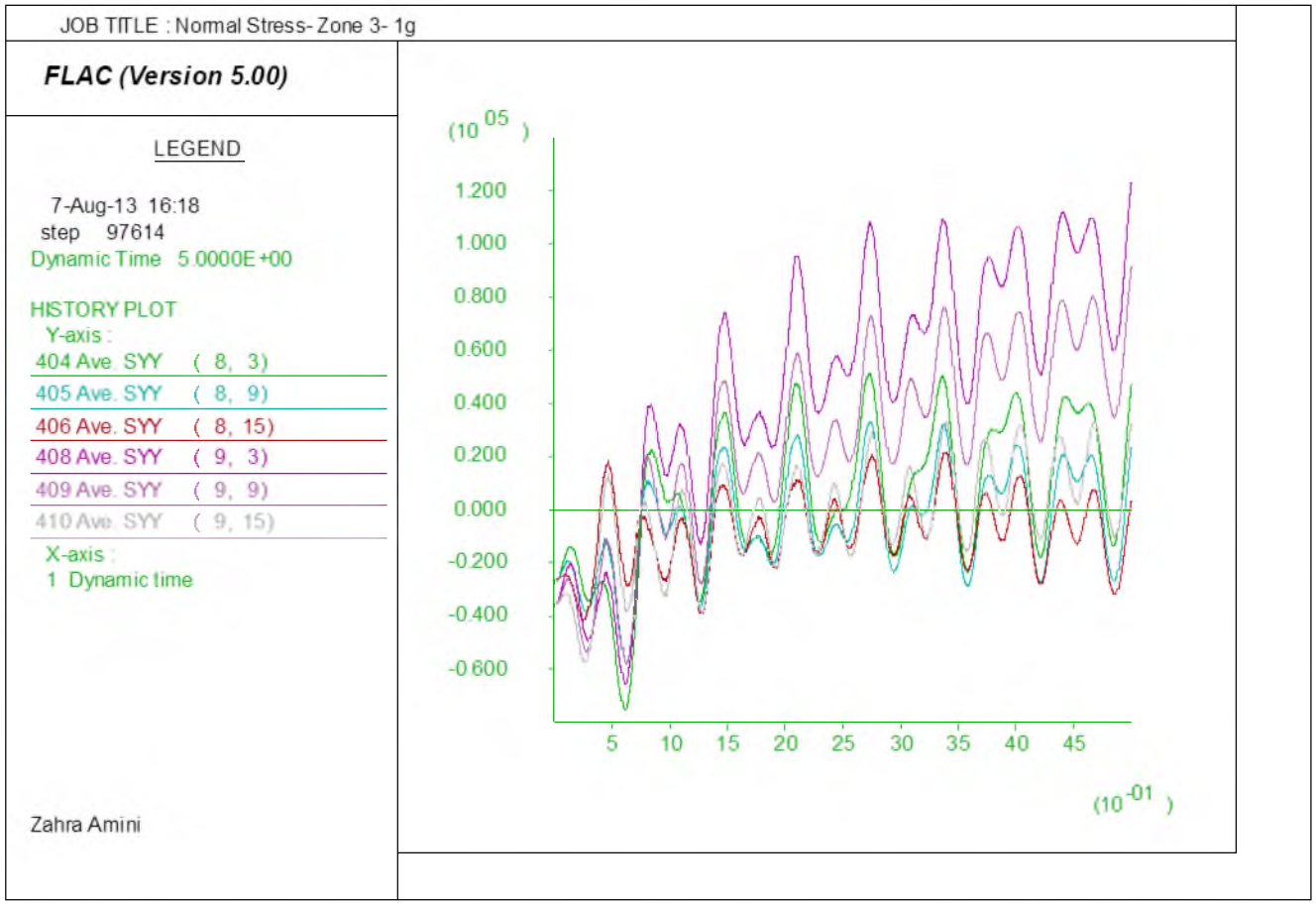

Figure D.25. Normal stress time histories at zone 4 due to horizontal acceleration amplitude of 1 g

REFERENCES

American Society of Civil Engineers (1987). "Seismic analysis of safety-related nuclear structures and commentary on standard for seismic analysis of safety related nuclear structures." *ASCE Standard 4-86*, New York, USA.

Arellano, D., Stark, T. D., Horvath, J. S., and Leshchinsky, D. (2011). "NCHRP project 24-11(02), guidelines for geofoam applications in slope stability projects: final report." NCHRP Project No. 24-11(02), Transportation Research Board, Washington, D.C.

ASTM C273 (2000). "Standard test method for shear properties of sandwich core materials." *Annual Book of the ASTM Standards*, American Society for Testing and Materials , PA, USA.

Athanasopoulos, G.A., Nikolopoulou, C.P., Xenaki, V.C., and Stathopoulou, V.D. (2007). "Reducing the seismic earth pressure on retaining walls by EPS geofoam buffers – numerical parametric study." *Proc., 2007 Geosynthetics Conference*, Washington DC, USA, p. 15.

Athanasopoulos, G. A., Pelekis, P. C., and Xenaki, V. C. (1999). "Dynamic properties of EPS geofoam: an experimental investigation." *Geosynthetics International*, 6(3), 171-194.

Barrett, J. C. (2008). "Effectiveness of connectors in geofoam block construction." MSc. Thesis, University of New Brunswick, Canada.

Barrett, J. C., and Valsangkar A. J. (2009). "Effectiveness of connectors in geofoam block construction." *Geotextiles and Geomembranes,* 27(3), 211 - 216.

Bartlett, S. F., and Lawton, E. C. (2008). "Evaluating the seismic stability and performance of freestanding geofoam embankment." *6th National Seismic Conference on Bridges and Highways,* Charleston, SC.

Bartlett, S.F., Negussey, D., Kimble, M., and Sheeley, M. (2000). "Use of geofoam as super-light-weight fill for I-15 reconstruction." *Transportation Research Board 79thAnnual Meeting*, Federal Highway Administration, Washington, D.C, 40-47.

Bathurst, R. J., and Alfaro, M. C. (1997). "Review of seismic design, analysis and performance of geosynthetic reinforced walls, slopes and embankments." *Earth Reinforcement*, 2, 887-918.

Das, B. M. (1993). "Principles of Soil Dynamics." Brooks/Cole, Pacific Growe, CA.

Duskov, M. (1991). "Use of Expanded Polystyrene (EPS) in flexible pavements on poor subgrades." *Proc., International Conference on Geotechnical Engineering for Coastal Development*, Yokohama, Japan, 1, 783–788.

Duskov, M. (1997). "Materials research on EPS20 and EPS15 under representative conditions in pavement structures." *Geotextiles and Geomembranes,* 15 (1–3), 147–181.

Elragi, A. (2000). "Selected engineering properties and applications of EPS geofoam." Ph.D. thesis, State University of New York, Syracuse, NY.

Horvath, J. S. (2004). "Geofoam compressible inclusions: the new frontier in earth retaining structures." In Geotechnical Engineering for Transportation Projects: *Proceedings of Geo-Trans 2004*, Jul 27-31 2004, Edited by American Society of Civil Engineers, Reston, VA 20191-4400, United States, Los Angeles, CA, USA, 1925-1934

Horvath, J. S. (1995). "Geofoam Geosynthetic." 1st Ed., Horvath Engr., P.C., Scarsdale, Ny.

Itasca Consulting Group, Inc. (2005). "*FLAC*: Fast Lagrangian Analysis of Continua: structural elements, Version 5." Minneapolis, MN.

Kramer, S.L. (1996). "Geotechnical Earthquake Engineering." Prentice-Hall, Inc., Upper Saddle River, N.J.

Kuroda, S., Hotta, H., and Yamazaki, F. (1996). "Simulation of shaking table test for EPS embankment model by distinct element method." *International Symposium on EPS Construction Method – EPS TOKYO '96*, Japan, 83-92.

Lingwall, B. N. (2011). "Development of an expanded polystyrene geofoam cover system for pipelines at fault crossings." Ph.D. thesis, University of Utah, Salt Lake City, UT.

Makdisi, F. I., and Seed, H. B. (1978). "Simplified procedure for estimating dam and embankment earthquake-induced deformations." *Journal of the Geotechnical Engineering Division*, Proceedings of the American Society of Civil Engineers, Vol. 104, No. GT7, July 1978, 849-867.

Negussey, D. (2006). "Design parameters for EPS geofoam." *Soils and Foundations,* Syracuse University, NY.

Negussey, D., and Anasthas, N. (2001). "Young's modulus of EPS geofoam by simple bending test." *EPS Geofoam 2001, 3rd International Conference on EPS Geofoam*, Salt Lake City, Utah, USA.

Negussey, D., Stuedlein, A., Bartlett, S.F., and Farnsworth, F. (2001). "Performance of a geofoam embankment at 100 south, I-15 reconstruction project, Salt Lake City." *Proc., 3rd International Conference on EPS Geofoam*, Salt Lake City, UT.

Ossa, A., and Romo, M. P. (2011). "Dynamic characterization of EPS geofoam." *Geotextiles and Geomembranes*, 29, 40-50.

Riad, H. L. and Horvath, J. S. (2004). "Analysis and design of EPS-geofoam embankments for seismic design." ASCE Geo-Trans 2004, July 27-31, Los Angeles, California.

Riad, H. L., Ricci, A. L., Osborn, P. W., and Horvath, J. S. (2003). "Expanded Polystyrene (EPS) geofoam for road embankments and other lightweight fills in urban environments." *Proc., Soil and rock America,* Cambridge, MA., 67-72.

Seed, H.B., Martin, G.R. (1966). "The seismic coefficient in earth dam design." *ASCE Journal of the Soil Mechanics and Foundations,* 92, 25-58.

Stark, T. D., Arellano, D., Horvath, J. S. and Leshchinsky, D. (2000). "Guidelines for geofoam applications in embankment projects." Interim (Phase I) Report - National Cooperative Highway Research Program Project No. 24-11, submitted to the Transportation Research Board by the University of Illinois at Urbana-Champaign in cooperation with Horvath Engineering, P.C. and ADAMA Engineering, Inc.

Stark, T. D., Arellano, D., Horvath, J. S., and Leshchinsky, D. (2004). "Geofoam applications in the design and construction of highway embankments." *National Cooperative Highway Research Program*, Project No. 24-11, Web Document 65.

Trandafir, A.C., Bartlett, S.F., and Lingwall, B.N. (2010). "Behavior of EPS geofoam in stress-controlled cyclic uniaxial tests." *Geotextiles and Geomembranes*, 28, 514-524.

Xenaki, V. C., and Athanasopoulos, G. A. (2001). "Experimental investigation of the interaction mechanism at the EPS geofoam-sand interface by direct shear testing." *Geosynthetics International*, 8(6), 471-499.

Zarnani, S., and Bathurst, R.J. (2007). "Experimental investigation of EPS geofoam seismic buffers using shaking table tests." *Geosynthetics International*, 14(3), 165–177.